Universidad de Valencia - CSIC

Departamento de Física Atómica, Molecular y Nuclear

Instituto de Física Corpuscular

UNIVERSITAT DE VALÈNCIA

Ground-state shape determination of N∼Z nuclei from beta-decay studies

Ana Belén Pérez Cerdán

Tesis Doctoral

Enero de 2012

UNIVERSIDAD DE VALENCIA - CSIC
INSTITUTO DE FÍSICA CORPUSCULAR

DEPARTAMENTO DE FÍSICA ATÒMICA, MOLECULAR Y NUCLEAR
MOLECULAR Y NUCLEAR

Ground-state shape determination of N∼Z nuclei from beta-decay studies

ANA BELÉN PÉREZ CERDÁN
TESIS DOCTORAL
ENERO DE 2012

Berta Rubio Barroso, Investigadora Científica del Consejo Superior de Investigaciones Científicas (CSIC)

CERTIFICA: Que la presente memoria **"Ground-state shape determination of N∼Z nuclei from beta-decay studies"** ha sido realizada bajo su dirección en el Instituto de Física Corpuscular (Centro Mixto Universidad de Valencia - CSIC) por **Ana Belén Pérez Cerdán** y constituye su Tesis Doctoral dentro del programa de doctorado del Departamento de Física Atómica, Molecular y Nuclear.

Y para que así conste, en cumplimiento con la legislación vigente, presenta ante el Departamento de Física Atómica, Molecular y Nuclear la referida memoria, firmando el presente certificado en Burjassot (Valencia) a 17 de Enero de 2012.

A mi familia.

Contents

List of Figures

List of Tables

Chapter 1

The Physics

1.1 β-decay process

Radioactivity was discovered in 1896 by Becquerel [1] and it became clear within a few years that unstable nuclei could decay with the emission of three types of radiation called α, β and γ-rays.

One outstanding puzzle related to the β-decay process was that the energies of the electrons emitted were observed to be non-discrete, in contrast with α- and γ-decay. This continuous energy distribution of β-decay electrons was a confusing experimental result in the 1920s since it seemed to contradict the law of conservation of energy. An example of such a β-decay spectrum is shown in figure 1.1. The energy distribution extends from zero to an upper limit (the beta endpoint energy) which is equal to the energy difference between the quantized initial and final nuclear states. This puzzle was solved by Pauli who suggested the existence of a new, very light uncharged and weakly-interacting particle, the neutrino, which is emitted in the β-decay process. In 1930 this was a revolutionary step as the neutrino was the carrier of the 'missing' energy. Another puzzle in understanding β-decay (β^-, β^+) was the emission of particles (electron, positron, neutrino) that are not present in the atomic nucleus.

Fermi assumed that in the beta process, the electron and antineutrino were created during the process of β-decay (Fermi 1934). He proposed that the act of creation is very similar to the process of photon emission in atomic and nuclear decay processes. By 1933 the quantum theory of radiation was well understood and Fermi constructed his theory of β-decay in this manner. In contrast to the electromagnetic interaction where a photon is exchanged between the charged particles, with zero rest mass (m_γ=0) and an infinite interaction range, the β-decay process appears to be short range. In quantum field theory, it can be shown that the range is inversely proportional to the mass of the exchange 'charge' carrier. Thus, a hypothetical par-

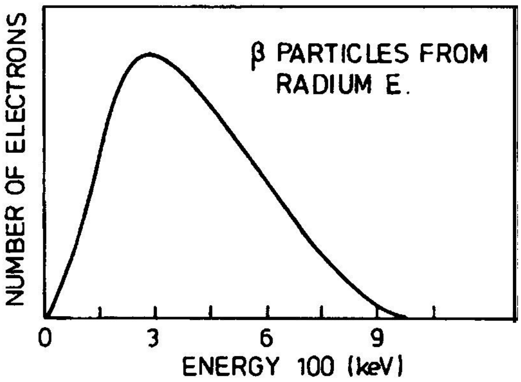

Figure 1.1: Simple example of beta spectrum. Figure taken from one of the classic papers; Ellis and Wooster (1927)

ticle, the intermediate boson ($W^{\pm}$) is exchanged. In this way, the symmetry aspects relating electromagnetic and weak interactions are introduced.

The two basic β-decay processes and one electron capture process are:

1. $$\beta^{-} decay : n \longrightarrow p + e^{-} + \bar{\nu}_e \tag{1.1}$$

   which takes the form in the nuclear media

   $$^{A}_{Z}X_N \rightarrow ^{A}_{Z+1} X_{N-1} + e^{-} + \bar{\nu}_e \tag{1.2}$$

   by which an electron is emitted from the nucleus leading to the conversion of a neutron into a proton and the increase of the nuclear charge Z in the final nucleus by one unit. This process takes place in neutron-rich nuclei which convert neutrons into protons in order to approach the valley of beta stability.

2. $$\beta^{+} decay : p \longrightarrow n + e^{+} + \nu_e \tag{1.3}$$

   which takes the form in the nuclear media

   $$^{A}_{Z}X_N \rightarrow ^{A}_{Z-1} X_{N+1} + e^{+} + \nu_e \tag{1.4}$$

   This process consists of the conversion of a proton into a neutron, consequently a positron is emitted and the nuclear charge Z of the final nucleus decreases by one unit.

3. $$Electron\ Capture\ (EC) : p + e^{-} \longrightarrow n + \nu_e \tag{1.5}$$

which takes the form in the nuclear media

$$ {}^A_Z X_N + e^- \rightarrow {}^A_{Z-1} X_{N+1} + \nu_e + \gamma_{X_{ray}} \tag{1.6}$$

This is a process, rather similar to β^+ decay, in which the nuclear charge also decreases by one unit. An atomic electron is 'captured' by a proton, thereby transforming it into a bound neutron and a neutrino is emitted. This process leaves the atom in an excited state as a vacancy has been created in one of the inner electron shells, usually the K-shell. Following the electron capture process, the atomic vacancy created is very quickly filled as electrons from less bound orbitals make downward transitions with the emission of characteristic X-rays.

These three processes can only occur when they are energetically allowed, that is to say, when Q, the energy released in the decay, is positive. These Q-values are defined as follows:

$$\begin{aligned} \beta^- : Q_{\beta^-} &= [M({}^A_Z X_N) - M({}^A_{Z+1} X_{N-1})]c^2 \\ \beta^+ : Q_{\beta^+} &= [M({}^A_Z X_N) - M({}^A_{Z-1} X_{N+1})]c^2 - 2m_e c^2 \\ EC : Q_{EC} &= [M({}^A_Z X_N) - M({}^A_{Z-1} X_{N+1})]c^2 - B_e \end{aligned}$$

where B_e is the electron binding energy, m_e is the electron mass, c is the velocity of light and M indicates atomic masses.
β^+-decay and EC both lead from the initial nucleus ${}^A_Z X_N$ to the final nucleus X^A_{Z-1} but both may not always be energetically possible as Q must be positive for any decay process. The atomic mass energy difference must be at least $2m_e c^2$=1022 keV to permit β^+-decay. When β^+-decay is energetically possible the nucleus may also undergo electron capture, but the reverse is not always true, and this leads to EC making the only contribution to the last 1022 keV of the Q_{EC}-window.

1.2 Fermi Theory of β-decay

Fermi developed his theory of β-decay based on Pauli's neutrino hypothesis and postulating the creation of the electron and neutrino in the process.Treating the β-decay as a transition that depends upon the strength of coupling between the initial and final states, Fermi developed a relationship, referred to as Fermi's Golden Rule [2], which led to the following expression for the decay rate:

$$\lambda = \frac{g^2 |M_{fi}|^2}{2\pi^3 \hbar^7 c^3} \int_0^{p_{max}} F(Z,p) p^2 (Q - T_e)^2 dp \tag{1.7}$$

where M_{fi} is the nuclear matrix element which describes the transition probability of the nucleus from initial to final states, g is a constant factor characteristic for β-decay and F(Z,p) is the so-called *Fermi function* which is due to the distortion of the electron wave function by the Coulomb field of the daughter nucleus. The integral in this equation depends ultimately on the maximum total energy, E$_{max}$, and the Z of the daughter nucleus, and thus it can be expressed as

$$f(Z, E_{max}) = \frac{1}{(m_e c)^3 (m_e c^2)^2} \int_0^{p_{max}} F(Z,p) p^2 (E_{max} - E_e)^2 dp \tag{1.8}$$

where the constants have been included to make f dimensionless. This function is known as the *Fermi integral* and has been tabulated for values of E$_{max}$ and Z [3]. Knowing that $\lambda = \frac{ln2}{t_{1/2}}$, it leads to

$$f t_{1/2} = \frac{2\pi^3 \hbar^7 ln2}{g^2 m_e^5 c^4 |M_{fi}|^2} \tag{1.9}$$

The quantity on the left side of eq. 1.9 is called the *comparative half-life* or *ft-value.* It provides a way to compare the β-decay probabilities in different nuclei so that differences in ft values must be due to differences in the nuclear matrix element and thus to differences in the nuclear wave functions. This ft-value only makes sense when it refers to a given transition, i.e., between one initial and one final level. However, the concept of ft is commonly extended over all transitions involved in the decay, ending up in the total ft or integral. This can be done by adding the inverse of the ft quantities for all the transitions involved

$$\sum \frac{1}{ft} = \frac{1}{f T_{1/2}} \tag{1.10}$$

β-decay half-lives encompass an enormous range which may vary from about 10^{-3} to 10^{20} s. Therefore, what is often quoted is the log$_{10}$ft value, where the units of t$_{1/2}$ are always in seconds.

In the decay the emitted particles can carry away angular momentum. Decays with smaller angular momentum are more probable than those with larger angular momentum. L=0 decays are called "allowed". Decays with L=1 are called "first forbidden", and so on.

The intrinsic spins of the emitted β-particle and the neutrino can couple to S=0 or S=1. In the case of allowed decay, the former is referred to as Fermi decay, and the latter as Gamow-Teller decay. An additional requirement for Fermi transitions is that they must occur between states belonging to the same isospin (T) multiplet (T$_z$)[1]. These selection rules can be summarized as follows:

---

[1] Although neutrons and protons are independent fermions, they have almost the same mass and behave in the same way in purely nuclear interactions. The concept of the isospin quantum number T is based on the observation of the charge independence of the nuclear interaction. The z component of the isospin, Tz, is defined as (N-Z)/2. In a nucleus characterised by Z and N, this means that the minimum value of T that any state can have is T=T$_z$.

$\triangle$J=0, ΔL=0,ΔS=0 $\triangle$T=0, ΔT$_z$=$\pm$1 in allowed Fermi transitions
$\triangle$J=0,$\pm$1, ΔL=0, ΔS=0,$\pm$1 J$_i$=J$_f$=0 excluded in allowed Gamow-Teller transitions

Table 1.1: Selection rules for β-transitions.

This has the consequence that g$^2|M_{fi}|^2$ in Eq. 1.9 can be split into two parts: one governing Fermi decays and the other governing Gamow-Teller decays. Hence, g$^2|M_{fi}|^2$ can be expressed as

$$g^2|M_{fi}|^2 = g_F|M_{fi}^F|^2 + g_{GT}|M_{fi}^{GT}|^2 \tag{1.11}$$

The former mode is driven by the vector operator O$_F$=$\tau^\pm$ which is isospin lowering (β^--decay) or isospin raising (β^+), independent of the nuclear spin and does not carry any angular momentum. In the Gamow-Teller decay the interaction is also driven by the Pauli operator O$_{GT}$=$\sigma\tau^\pm$ which causes the spin change in the nucleus whereas this is not possible in the Fermi decay. In this case this is an axial operator as the decay involves a transfer of one unit of angular momentum.

From several experimental results [4] the free neutron ratio of axial vector to vector coupling constants was determined to be

$$\frac{g_{GT}}{g_F} = \frac{g_A}{g_V} = -1.270 \pm 0.003 \tag{1.12}$$

Since g$_V$ is well known while g$_A$ is not, the expression for the ft-value is usually written in the following way

$$ft = \frac{D}{|M_{fi}^F|^2 + (\frac{g_A}{g_V})^2|M_{fi}^{GT}|^2} \tag{1.13}$$

where D=$\dfrac{2ln2.\pi^3\hbar^7}{m_e^5c^4g_V^2}$=6143.6(17) s from a relatively recent re-analysis of the experimental data [5] on $0^+ \rightarrow 0^+$ superallowed decays which depend uniquely on the vector part of the Weak interaction. This Fermi decay occurs between states of identical isospin, i.e. ΔT=0 and has a very fast decay time, as it requires no change in angular momentum, isospin or parity. Hence, the nuclear wave functions of the initial i and final states f are identical and the matrix element is M$_V^2$=2.

The reader should note that forbidden decays can also occur with a large reduction in the transition probability compared to the allowed cases. In these transitions a parity change can occur and large changes in spin have been observed. Table 1.2 summarizes these beta forbidden transitions.

1st-forbidden (l=1) π_i=-π_f	Fermi, |ΔJ|=0,1 Gamow-Teller, |ΔJ|=0,1,2
2nd-forbidden (l=2) π_i=π_f	Fermi, |ΔJ|=2 Gamow-Teller, |ΔJ|=2,3
3rd-forbidden (l=3) π_i=-π_f	Fermi, |ΔJ|=3 Gamow-Teller, |ΔJ|=3,4

Table 1.2: Selection rules for forbidden β-decays up to 3^+ forbidden. The rules for higher order processes follow the same pattern.

1.3 The GT-Strength and the Sum Rule

From the discussion in the previous section the transition rate for a given decay is characterized by its ft-value. The equation can be expressed in terms of the *total strength* or total rate B

$$ft = \frac{6143.6 \pm 1.7}{B}\frac{g_V^2}{4\pi} = \frac{6143.6 \pm 1.7}{B(F) + B(GT)}\frac{g_V^2}{4\pi} \tag{1.14}$$

where B(F) and B(GT) are the Fermi and Gamow-Teller strengths respectively. These probability rates can be defined as:

$$B(F) = \frac{1}{2J_i + 1}|\langle J_f \| \sum_k t_\pm^k \| J_i \rangle|^2 \equiv \frac{g_V^2}{4\pi}\langle \tau \rangle^2 \tag{1.15}$$

$$B(GT) = \frac{1}{2J_i + 1}|\langle J_f \| \sum_k \sigma^k t_\pm^k \| J_i \rangle|^2 \equiv \frac{g_A^2}{4\pi}\langle \sigma\tau \rangle^2 \tag{1.16}$$

For the particular case of pure Gamow-Teller decays we can define B(GT) as the dimensionless quantity

$$B = B(GT) = \langle \sigma\tau \rangle^2 \tag{1.17}$$

where the B(GT) is assumed to be given in units of $g_A^2/4\pi$. In this work we will use the convention established by Eq. 1.17.

Throughout most of the nuclear chart, Fermi decay is suppressed by the isospin selection rule. Since Fermi transitions only occur between states of an isomultiplet, the whole Fermi strength is concentrated in one single final state, the so called isobaric analog state (IAS). The situation of the GT transition is completely different though and its strength is spread in general over many possible final states as a result of both the possible spin-flip and the spin-dependent residual nuclear interaction which can mix many states. The study of the GT distribution and strength, either by charge-exchange reactions or weak decay, provides excellent tests for nuclear models as these parameters are extremely sensitive to the details of nuclear structure. Since in the region of interest in this work Fermi decay is isospin forbidden, in what follows only GT transitions will be considered.

There exists a very general model-independent sum rule [6] for the GT operator which states that the summed strength for a given initial state with N, Z is the following:

$$S^{-} - S^{+} = \sum_{f} \langle f|\sigma\tau^{-}|i\rangle^{2} - \sum_{f} \langle f|\sigma\tau^{+}|i\rangle^{2} = 3(N-Z) \qquad (1.18)$$

where i and f label the initial and final states respectively and the summation is over all the possible final states. This sum rule is derived by assuming nucleons are pointlike particles which interact via an effective two-nucleon interaction resulting from meson exchange, whereas explicit mesonic degrees of freedom are not considered.
The existence of this strong, model independent, sum rule for the total GT strength from a given initial state is of particular interest. This exact relation states that the difference between the total transition S^{-} and S^{+}, measured in β^{-} and β^{+} decay respectively, is independent of the structure of the parent state, whereas each quantity is strongly dependent.

Since most nuclei have more neutrons than protons, S^{+} is expected to be very small in many cases due to Pauli blocking, in particular for heavy systems with a neutron excess. On the other hand the lower limit obtained for S^{-} from [7] suggests that $S^{-} \geq 3$(N-Z). This leads to $S^{-} \approx 3$(N-Z) and it is expected that in many cases the experimental value, S^{-}_{ex}, should be close to the sum rule value.

1.4 Experimental probes for the study of the Gamow-Teller distribution

Since the paper published by G. Gamow and E. Teller [7], the determination of the so-called GT-matrix elements from β-decay and charge-exchange reactions has led to a series of discoveries concerning the structure of the nucleus and the properties of spin-isospin transitions in nuclei. As stated in the previous section, the study of these transitions gives valuable information on the spin-isospin excitations in nuclei which are also of importance in the extension and test of present nuclear models. Most of our present knowledge of collective spin-isospin excitation, in particular of the GT strength, comes from intermediate-energy charge-exchange reactions. Unfortunately, β-decay is not the best tool to map out the complete response function in the $\sigma\tau_{\pm}$ channels since it only has access to a small fraction of the nuclear states populated. Thus it misses the strongest transitions in the spectrum due to its limited energy window. Hence, one needs probes that allow the experimental survey of higher excitation energies where the dominant portion of the transition strength lies. This is possible with hadronic probes such as the (p,n) and (n,p) charge-exchange-type reactions, whose properties will be described in the following section.

1.4.1 Charge-exchange reactions and the Gamow-Teller resonance

The (p,n) and (n,p) reactions, which can also be driven by the $\sigma\tau$ operator, allow the independent variation of both momentum and energy transfer to the target. This offers the opportunity to examine a large excitation energy window in the final nucleus and thus a large fraction of the total GT strength. However, the study of the GT strength with such a probe is limited to nuclei of elements which make suitable targets, i.e. mostly stable nuclei. It has been proved that charge-exchange reactions at intermediate energies and zero degrees are dominated by G-T transitions. Therefore, in order to meet the condition of no angular momentum transfer (L=0) in the reaction, the angular distribution of neutrons and protons must be peaked at zero degrees and the bombarding energy must be very high.

In 1980 there was an experimental breakthrough in the understanding of spin-isospin excitation with the (p,n) experiments performed at the Indiana University Cyclotron Facility(IUCF) [8] which showed the existence of very collective spin-isospin modes in nuclei. The measured zero-degree (p,n) spectra of various neutron-rich target nuclei with an incident proton beam of 200 MeV showed a prominent peak(see Fig.1.2) which offers one of the most beautiful examples of a giant resonance in nuclei. This peak was interpreted as the giant Gamow-Teller resonance, already predicted by Ikeda, Fujii and Fujita in 1963 [6], which is a collective spin-isospin oscillation in which the excess neutrons coherently change the direction of their spins and isospins without a change in their orbital motion. This resonance is characterised by ΔS=1, ΔT=1 and ΔL=0 relative to the initial state, i.e. the ground state of the nucleus in the target. In the case of this experiment, the GT resonance is inferred from the absence of spin-isospin strength at low excitation energies. Already in 1975 there were experimental indications of this resonance having been observed in a 45-MeV ^{90}Zr(p,n) experiment by Doering et al. [9] and three years after in various low-energy ^{90}Zr(^{3}He,t) experiments by Galonsky et al. [10] and Ovazza et al. [11].

The experiments performed so far with (p,n) reactions for different nuclei where eq. 1.18 applies directly have shown that only 60% of this strength is observed in the region of the GT resonance peak: the remaining 40% is normally called *the*

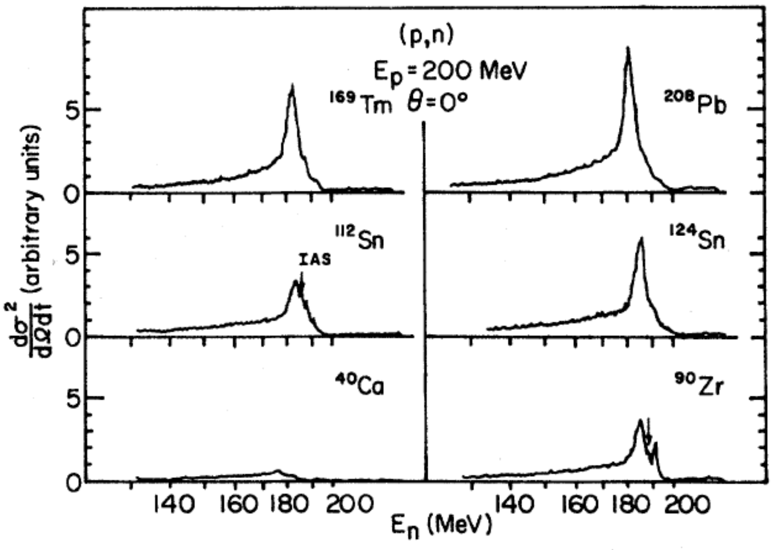

Figure 1.2: Differential cross sections of various target nuclei in the (p,n) reactions at E_p=200 MeV and 0^o scattering angle from Gaarde et al [8]. The spectra are normalized to show relative cross sections. With increasing neutron excess the GT cross section increases, indicating there are more neutrons taking part in the oscillation.

missing strength. This feature is found for many nuclei over the nuclear chart and a summary of the results obtained by Gaarde[8] from (p,n) data taken at 160 MeV is shown in Fig. 1.3. This has been the subject of many experimental studies since 1975 and the question regarding the quenching mechanism of the GT strength has not been fully clarified. A convincing explanation was presented in 1997 by Wakasa et al. [12]. The fact that in heavy nuclei the GT resonance lies on top of a large continuum due to background, whose shape and magnitude is not well known, was an experimental obstacle in the analysis of charge-exchange reactions for a proper determination of the GT strength at high energies. Two physically different explanations had been proposed for the solving of this missing strength dilemma. One was the Δ(1232)-hole admixture into the nucleon-hole excitation GT states which removes the GT strength lying at low excitation energy and shifts it to the Δ excitation region lying at ~300 MeV of excitation energy. The other possible mechanism is due to the classical configuration mixing which is based on the experiment performed at the Research Centre for Nuclear Physics (RNCP) by Wakasa et al. in 1997 in Osaka [12]. The experimental evidence indicates that (2p2h) correlations are chiefly responsible for shifting GT-strength to excitation energies higher than the GT resonance in the final nucleus. Excitations at higher energy of 2nucleon-2hole and 2nucleon-1hole character are mixed with the main 1nucleon-1hole states excited in G-T transitions which causes the shift in the strength [13] to higher excitation

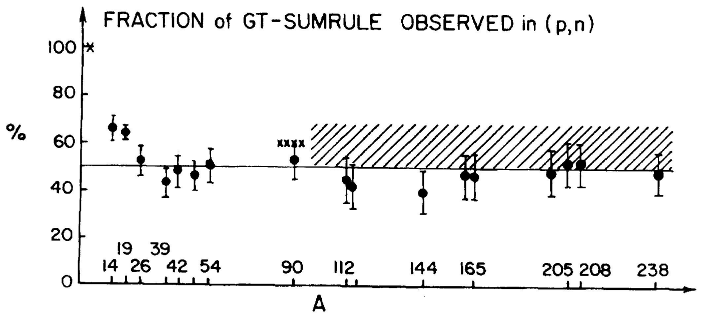

Figure 1.3: Fraction of Gamow-Teller sum rule strength observed in (p,n) reactions. The cross hatched region corresponds to the uncertainty in defining the background. Figure taken from reference [8]

energy regions. Therefore, the missing strength is distributed within the background around the GT resonance peak, which contains most of the strength, and is spread in the continuum up to 60 MeV. Supporting evidence for this view comes from the large fraction of the sum rule observed in ^{54}Fe [14][15], from the small amount of GT strength found at low excitation in the ^{90}Zr(n,p) reaction [12] and from the success of the model with (2p2h) corrections in reproducing large-angle spectra in (n,p) reactions on ^{54}Fe. A better evaluation of the background and the consideration of these (2p,2h) correlations in the experiment on a ^{90}Zr(n,p) reaction in Osaka led to a better and more accurate understanding of the quenching of the GT strength. It was also concluded that quenching due to the first mechanism described, the Δ(1232)-hole admixture into the nucleon-hole excitation GT state, seems to be very small, whereas the nuclear configuration mixing plays the major role.

1.4.2 β-decay studies

The β-decay, which is a weak-interaction process, brings invaluable complementary information on transitions to well-resolved states and allow the investigation of nuclei far from stability. However, in β-decay experiments, the number of measured transitions is limited by the β-decay window and the measured strength can only be compared with a model dependent calculation which predicts how much of the full strength should lie within the energy window defined by the Q_β-value . On the other hand, β-decay studies allow the understanding of nuclear structure and provide excellent tests for the existing theoretical models.

The advantage of the β-decay studies is that they are not affected by the huge experimental background observed in charge-exchange reactions and are therefore much cleaner probes. Using the β-decay process as a tool to measure the GT-strength is crucial to complement the results coming from charge-exchange reactions on nuclei far from stability, where this is the only way to study the spin and isospin structure of the nuclear response at present. The drawbacks of this process is the decay energy window, which limits the available final states to energies typically below 10 MeV.

Therefore the studies on β-decay are normally focused on those cases where most of the GT-strength lies within the energy decay window. It should be noted that the GT process is forbidden in most cases and is allowed only if the same orbital or the spin-orbit partner orbital of the initial proton(neutron) are free on the neutron(proton) side. If we restrict ourselves to the β^+ process, there are three regions in the nuclear chart where these conditions are fulfilled:

- The rare-earth region around mass 150, above the quasi-doubly magic nucleus ^{146}Gd.
- The nuclei around the doubly magic nucleus ^{100}Sn.
- The N≈Z nuclei up to A≈70-80.

It should also be highlighted that the spectacular experimental and theoretical development in the last years has improved the quality of the available data. The new facilities devoted to the production of radioactive beams (ISOLDE, GSI, RIKEN, CNRP, Louvain-La Neuve...) have opened the possibility to study nuclei far from the line of stability. The construction of new facilities in the near future, for instance the FAIR project in Darmstadt and SPIRAL2 in GANIL, will allow the survey of more exotic species. It is expected that secondary beams will be obtained with a higher intensity by orders of magnitude compared to what is presently available. The advanced intrumentation which has been developed will also permit spectroscopy studies with the low intensity exotic beams produced. On the other hand, the IGISOL technique available at the University of Jyväskylä has also allowed the production and study of refractory elements which were impossible to separate chemically with standard ion sources at Isol facilities. Measurements of the beta feeding distribution for the decay, Tc isotopes [16] for example, have proven their importance in the study of the decay heat in a nuclear reactor.

Chapter 2

The A$\simeq$80 region along the N$\sim$Z line

2.1 Deformed nuclei

The nuclear shape is a basic bulk property of the nucleus. In between closed shells, the large number of available valence nucleons in orbits with large single particle angular momentum often leads to nuclei with large deformations. The addition of a small number of particles and the accumulated p-n interaction strength may shift the equilibrium shape to a potential minimum corresponding to a prolate, oblate or spherical shape. The shapes range from spherical to super- [17] and, perhaps, even hyper-deformed spheroids [18] which are oblate or prolate. They can also have octupole deformations [19] and perhaps even more exotic shapes. Therefore, the study of deformed nuclei is a complementary endeavour to the exploration of nuclear shell structure in spherical nuclei and permits the extension of the theoretical models to such exotic regions.
Deformed nuclei possess features which are clearly different from spherical nuclei such as:

- The energy of the lowest 2^+ state in an even-even nucleus is considerably lower than the typical excitation energy of the first 2^+ state in spherical nuclei.

- Rotation bands exist and exhibit a behaviour similar to that of a rigid quantum mechanical rotor with energy E$\sim$I(I+1) where I is the nuclear spin. Therefore, the rotational motion is a possible mode of excitation whereas in spherical nuclei, the collective rotation about an axis of symmetry cannot be observed, since the different orientations are quantum-mechanically indistinguishable.

- The enhancement of the B(E2;$2^+ \rightarrow 0^+$) value over the single particle estimate implies large quadrupole deformations since this magnitude is related to the intrinsic quadrupole moment, Q_0, by the simple rotational formula:

$$B(E2;2^+ \longrightarrow 0^+) \propto Q_0^2 \tag{2.1}$$

The nuclear surface can be parameterised by an expansion in spherical harmonics with the length of the radius vector R pointing from the origin to the given surface. For an axially symmetric case, which is the assumption made in what follows, this parametrisation is given by:

$$R(\theta,\phi) = R_0 c(\beta_\lambda)[1 + \sum_{\lambda=2}^{\lambda_{max}} \beta_\lambda Y_{\lambda 0}(\theta,\phi) \tag{2.2}$$

Here c(β_λ)ensures the volume conservation enclosed by the surface defined. R_0 is the radius of the sphere, $R_0=r_0A^{1/3}$, with r_0=1.2 fm and A the atomic mass number. It has the same volume as the deformed nucleus, independently of the deformation parameters β_λ. $Y_{\lambda 0}$ is a spherical harmonic of order λ for which the lowest multipole, λ=2, corresponds to a quadrupole deformation and a spheroidal shape. Only a quadrupole distortion will be considered in the region studied in this work, since nuclei with quadrupole shapes abound through out the Periodic table in midshell region.

Hence, the deviation of the nuclear shape from spherical symmetry can be directly observed via the electric quadrupole moment. The relationship between the deformation parameter β_2 and the quadrupole moment, assuming a uniform charge distribution, is

$$Q_0 = \frac{3}{\sqrt{5\pi}} R_0^2 Z \beta_2 (1 + 0.36\beta_2) \tag{2.3}$$

where Z is the atomic number and Q_0 is the intrinsic quadrupole moment which would only be observed in a frame of reference where the nucleus is at rest. However, what is measured in the laboratory frame is a different quadrupole moment Q_s, hereinafter called the spectroscopic quadrupole moment, since the nucleus is rotating. This spectroscopic quadrupole moment is the expectation value of the quadrupole moment operator, defined as

$$Q_s(I) = \langle I, m = I | Q_2^0 | I, m = I \rangle = \sqrt{\frac{I(2I-1)}{(2I+1)(2I+3)(I+1)}} (I\|Q\|I) \tag{2.4}$$

The Q_s of a nuclear state with spin I=0 or 1/2 is zero, although the nucleus can possess an intrinsic deformation. By assuming the nuclear deformation is axially symmetric with the nuclear spin having a well-defined direction with respect to the symmetry axis of the deformation, the spectroscopic and intrinsic quadrupole moments can be related in the following way:

$$Q_s = \frac{3K^2 - I(I+1)}{(I+1)(2I+3)} Q_0 \tag{2.5}$$

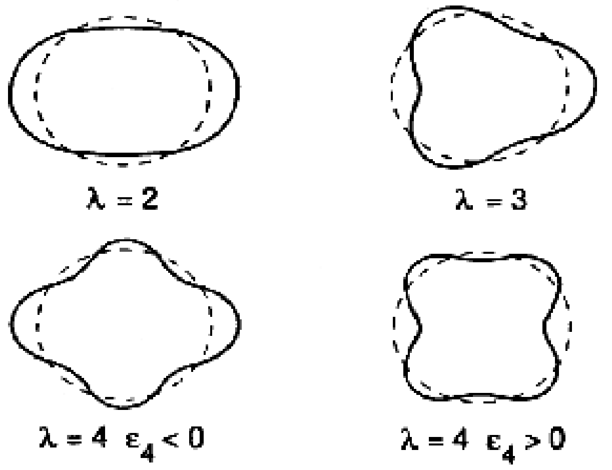

Figure 2.1: Selection of some modes of vibration of the nucleus which are allowed by the general expansion of the nuclear surface in equation 2.2. Dipole deformations, λ=1, correspond to a shift of the centre of mass. λ=2 shows the ellipsoidal vibration of the nuclear surface, whereas λ=3 corresponds to octupole deformations which is the principal asymmetric mode of the nucleus associated with negative-parity bands. For heavy nuclei, hexadecapole deformations, λ=4, play an important role in admixture to quadrupole excitations for the ground state [20]. In certain circumstances the deformation parameters ε_λ and δ are also used whose relation with β_λ can be found in [21]. Picture extracted from [22].

where K is the projection of the nuclear spin onto the symmetry axis. In fact, the observed quadrupole moment does have a sign opposite to the intrinsic one. Hence, when a prolate deformed nucleus rotates (Q_0 >0) about an axis perpendicular to the symmetry axis, having the form of a Rugby ball, the time averaged shape looks more like an oblate nucleus (Q_s <0), which would have an opposite sign in the value of the quadrupole moment.

Most of the presently available data on nuclear quadrupole moments has been obtained via collinear laser spectroscopy, where direct information on the magnitude of quadrupole moments can be inferred from the study of the hyperfine structure [23]. On the other hand, for the cases of spin I=0 or 1/2, the quadrupole deformation will not be accessible experimentally since no quadrupole moment will be observed and no indicators of deformation will exist. This is a clear limitation in even-even nuclei since the spin of their ground state is 0^+ and no quadrupole moments can be experimentally measured. One possibility is to use the empirical Grodzin's formula from which a measurement of the quadrupole deformation β_2 of even-even nuclei

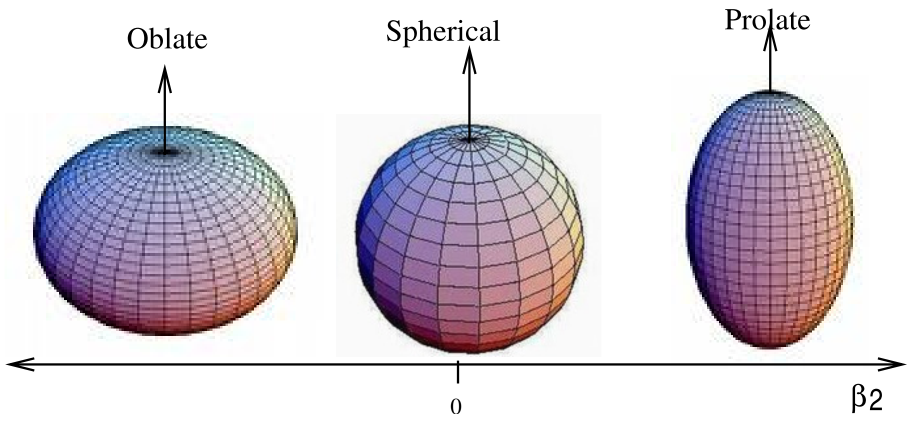

Figure 2.2: Schematic picture showing oblate, spherical and prolate shapes. The arrows for the oblate and prolate shapes indicate the symmetry axis.

may be obtained from the energies of the first excited 2^+ state:

$$\beta_2 = [\frac{204}{(\hbar^2/2I)A^{7/3}}]^{1/2} \tag{2.6}$$

where the rotational parameter $\hbar^2/2\mathrm{I}$ equals $(1/6)\mathrm{E}_{2^+}$ and I is the moment of inertia. However, the sign of this deformation cannot be determined by applying this formula and other methods must be used. They are addressed in the next section where an introduction is given to the region of our interest.

2.2 The region of interest

The nuclei with mass A=70-80 close to the N=Z line have provided a happy hunting ground for nuclear spectroscopists and theorists for some time [24]. The fact that the protons and neutrons are filling the same shells and that there are energy gaps at nucleon numbers 34, 36, 38 and 40, shown in Fig. 9.1, leads to a landscape where nuclear properties change rapidly with the addition or subtraction of a single nucleon. Thus the nuclear shape may change from nucleus to nucleus. We also find shape co-existence in these nuclei with oblate, spherical and prolate shapes all competing in terms of excitation energy. Such nuclei are also of interest because it is here that we might hope to observe the effects of neutron-proton pairing, an effect which is washed out by the much larger number of like-nucleon pairs as we move away from the N=Z line.

The variation in shape along the N=Z line has been explored [26, 27] and we see a steady change as we go from ^{64}Ge towards ^{100}Sn with a peak in deformation at ^{76}Sr and ^{80}Zr in the middle of the shell as one might expect from simple parametrisations such as the *P* scheme of Casten et al. [28, 29, 30]. Shape co-existence

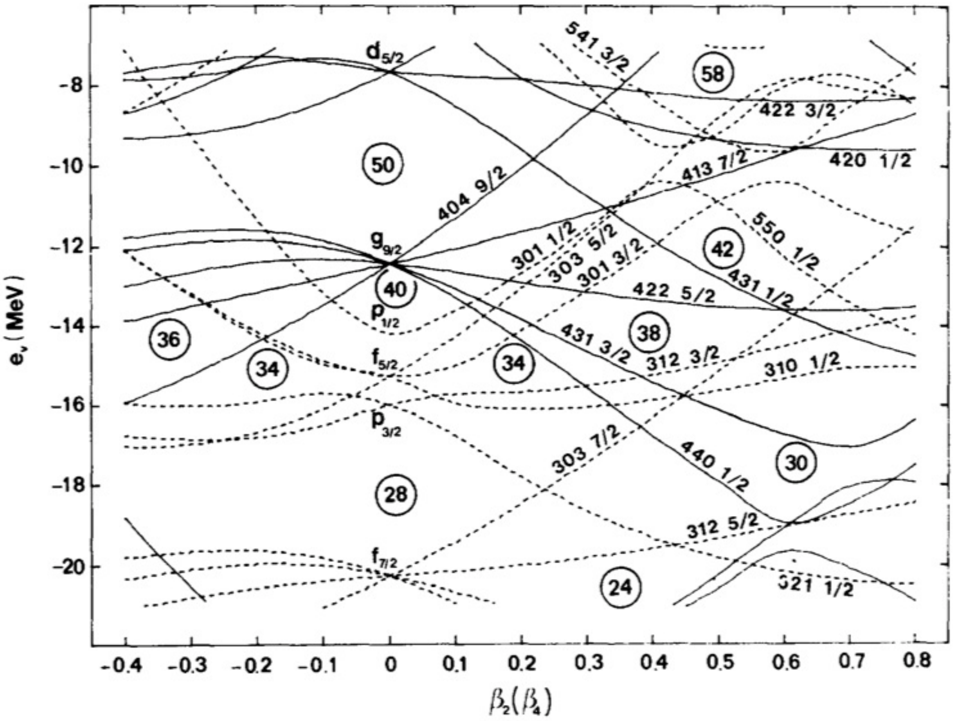

Figure 2.3: Single-particle levels in the region A=80 as a function of the quadrupole deformation β_2 calculated using the Woods-Saxon potential (figure extracted from [38]. The asymptotic quantum numbers $[Nn_z\Lambda\Omega]$ are given to simplify the identification of individual levels. The particle number is shown in circles.

was first reported by Piercey et al. [31] in the Se isotopes as early as 1981. More recently, studies of isomeric decays produced following fragmentation [32] and subsequent measurements of the Coulomb excitation of beams of radioactive ^{74}Kr and ^{72}Kr [33, 34] have shown that there are low-lying, excited 0^+ states in these nuclei. The mixing of these states with the ground state could be extracted in terms of simple two level mixing [35].

This rich diversity of shape and behaviour has attracted considerable attention from theorists, who have applied a variety of different approaches to try to explain what we observe. These include *inter alia* calculations in the configuration dependent shell correction approach with deformed Woods Saxon potentials [38], self consistent deformed Skyrme mean field calculations [39, 40], Hartree Fock Bogoliubov calculations with the Gogny force [41], relativistic mean field calculations [42] and the self consistent complex excited VAMPIR model [43].

In this region, Gamow-Teller decay is allowed since the free neutron orbitals have the same quantum numbers as the valence protons around the Fermi surface. As a

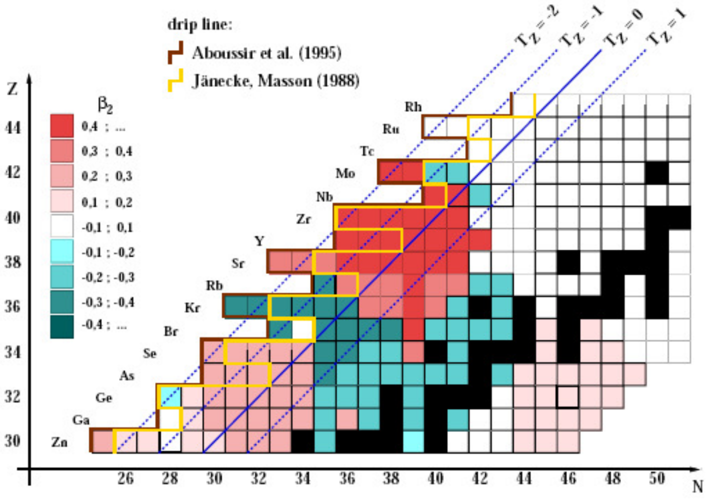

Figure 2.4: Theoretical calculations of the ground-state deformation for the region N∼Z and A∼80 [36][37].

consequence, a large part of the GT strength is contained within the Q_{EC} window. Therefore, the structure of the GT strength can be investigated directly by β-decay measurements without dealing with (p,n) and (n,p) charge-exchange reactions which have a huge experimental background and are not possible in these nuclei at present. As a result, recent studies of β-decay have been used to extract information on the shapes of various nuclei in the region [44, 45], namely ^{76}Sr and ^{74}Kr, using the Total Absorption Spectroscopy (TAS) method [46]. This kind of study is based on an idea originally put forward by Hamamoto et al [47] , namely that the deformation of the nuclear ground state can be determined by measuring the B(GT) distribution in its β-decay. Sarriguren et al [48] then implemented the required calculations in which the B(GT) is calculated for the deformations that minimise the ground state energy. Further details of these calculations are given in the next section. In some cases, in particular for the light Kr and Sr nuclei, the distributions are markedly different. This procedure is of particular interest since it can provide information on the shape for decaying 0^+ ground states. Figure 2.5 shows the result of these theoretical calculations for the Sr isotopes. A clear difference can be observed between the structure of the B(GT) distribution generated by the oblate(spherical) shape and that of the prolate case. However only a part of the B(GT) can be seen within the Q_{EC} window, yet it may be possible to determine the nuclear shape for the ground state using the experimental B(GT) distribution and comparing it with these theoretical calculations. The experimental results for ^{76}Sr and ^{74}Kr showed a good agreement when they were compared to these theoretical predictions.

Having this in mind, the primary aim of the present work is to determine the shapes

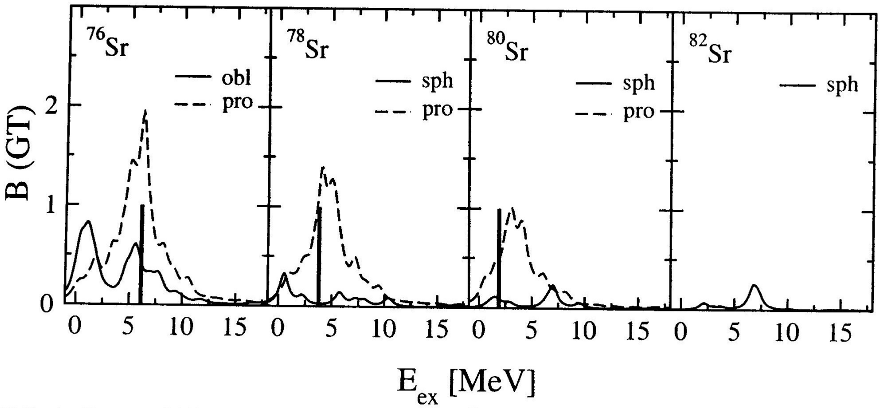

Figure 2.5: Gamow-Teller strength distributions $[g_A^2/4\pi]$ as a function of the excitation energy of the daughter nucleus [MeV] [49]. The theoretical calculation has been performed assuming different shapes for the ground state of the parent nucleus and is based on the QRPA. The vertical lines represent the Q_{EC}-window.

of the ground states of ^{77,78}Sr and ^{76,78}Rb. The B(GT) distributions of these nuclei will be obtained using a total absorption spectrometer (TAS). We only have theoretical calculations for the even-even case, ^{78}Sr, and the odd ^{77}Sr case. Although we do not have the calculations for the corresponding odd-odd cases we believe that we can also draw some conclusions about them from [50, 51] and from considerations on the even-even cases. It should be noted that the Grodzins formula allows us to extract the deformation but not the sign of 0^+ ground states while the comparison with the theoretical calculation allow us to distinguish between a prolate and oblate shape provided that their B(GT) distributions differ markedly.

2.3 HF+BCS+QRPA theory

A self-consistent approach based on a HF+BCS+QRPA method with density dependent Skyrme forces has been used by Sarriguren et al [48] to describe β^+-decay properties in even-even and even-odd(odd-even) deformed proton-rich nuclei. This theory [48, 49] can be compared with the experimental results obtained using high resolution techniques. The success of the phenomenological shell model in giving a microscopic description of nuclear properties favours the assumption that nucleons move independently in an average potential produced by all the nucleons. This idea is applied in the Hartree-Fock method which allows the derivation of a single-particle potential from a 2-body interaction using a variation principle with Slater determinants. The following approximation is made without taking into account a residual interaction

$$V(1,..A) = \sum_{i<j=1}^{A} V(i,j) \simeq \sum_{i=1}^{A} V(i) \qquad (2.7)$$

It is known that the Hartree-Fock theory with density dependent forces provides a very good description of fundamental properties of the ground state for spherical nuclei. Within the framework of this theory three types of density-dependent Skyrme forces will be considered. These forces are namely the SK3 force [52], which is the most frequently used and usually taken as a reference, the SG2 force [53], proposed by Van Giai and Sagawa which gives a good description of the GT excitation in spherical nuclei and on spin excitations in deformed nuclei, and the SLy4 force [54] which is one of the latest forces used. This theory alone cannot be applied to nuclei far from shell-closures as the level occupancies have a major effect on the solution of the HF equation. Therefore it is convenient to introduce pairing correlations in the ground state using the BCS approximation developed by J. Bardeen, L. Cooper and J. Schrieffer in 1957. The result of the HF-BCS calculation is the eigenfunction having the lowest energy, i.e., it provides an approximation to the ground state wave function.

In order to discuss the shape of the isotopes under study, a quadratic quadrupole constraint must be added to the HF theory. The procedure is to minimise the HF energy by fixing the nuclear deformation. This leads to a different solution for each value of the quadrupole deformation. As an example, Fig. 2.6 shows the total HF energy plotted as a function of the quadrupole moment for the even-even $^{76-82}$Sr isotopes. In the case of ^{78}Sr two minima are observed for each of the two Skyrme forces used in the calculation. The separation of these two minima is of the order of 2 MeV. This means that shape mixing in the ground state is expected to be very small.

Due to the importance of some collective excited states in the region, it is necessary to include the RPA approximation (Random Phase Approximation) which takes into account correlations in the excited states and also in the ground state. This theory can be generalized using the HF method and the BCS approximation and is called QRPA(Quasiparticle Random Phase Approximation) which introduces a separable spin-isospin residual interaction in both particle-hole and particle-particle channels in the mean field. The combination of these three microscopic models (HF+BCS+RPA) involves complex calculations which are believed to be the most accurate ones at present for the mass region under discussion.

2.4 Experimental techniques to measure the $I_\beta(E)$ distribution and extract the B(GT).

The main aim of this work is to determine the B(GT) from the β-decay of different Sr and Rb isotopes and extract the shape of their ground states. So far the

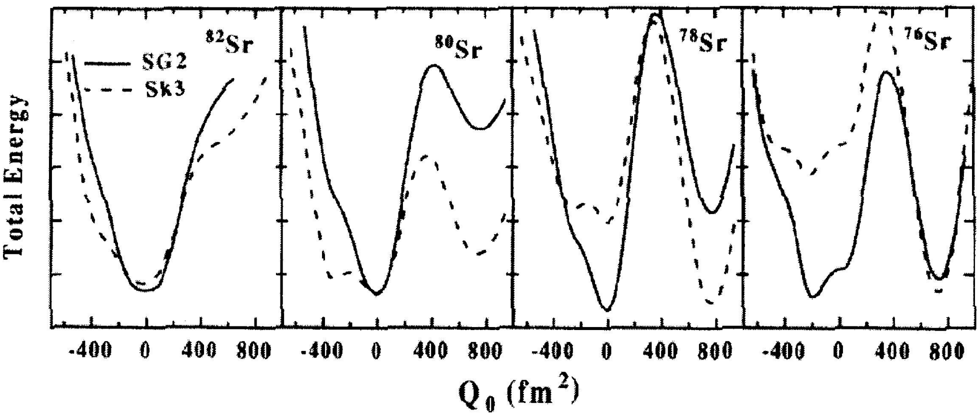

Figure 2.6: The HF energy as a function of the quadrupole moment (deformation) for the two interactions SG2(solid line) and Sk3(dashed line) in even-even Sr isotopes. The distance between two ticks on the vertical axes is 1 MeV, however the offset is different for each curve. Figure taken from reference [49].

B(GT) has been discussed within a theoretical framework. However, an experimental method is needed to measure this GT-strength distribution from β-decay measurements and to express it in terms of measurable quantities. The strength of the GT-transition to the state at excitation energy E_x in the daughter nucleus can be derived from the measurements of the β intensity $I_\beta(E_X)$ to this particular state, the parent β-decay half-life $T_{1/2}$ and the decay energy available, given by the Q-value and the excitation energy of the level, according to the following relation:

$$BGT(E) = \frac{K \quad I_\beta(E)}{(g_A/g_V)^2 f(Q_\beta - E) T_{1/2}} \tag{2.8}$$

where K=6143.6 (17) [5], f is the Fermi integral and g_A/g_V=-1.270(3) [4] is the ratio of axial-vector and vector coupling constants for the free neutron decay. The fermi integral depends on the energy available for the decay, namely (Q_β-E), as shown in Eq. 1.8 and can only be solved numerically. It becomes very small and approximately $\sim(Q_\beta\text{-E})^5$ for high excitation energies of the daughter nucleus. Due to this strong energy dependence of the Fermi integral and from equation 2.8, it can be deduced that only a small amount of feeding located at high excitation energies close to the Q-value would lead to a significant portion of strength. This will be of extreme importance from the experimental point of view since a very sensitive method is needed to take account of any small fraction of feeding that populates excited states lying at high energy close to the value of the available decay energy.

All the variables involved in equation 2.8 (Q-value, half-life and beta feeding intensity) can be measured experimentally. In what follows, our main experimental task will be the measurement of the beta feeding intensity of the nuclei under study. The rest of the variables involved in equation 2.8 (Q-value and half-life) will be assumed to be known or measurable by very well-established methods. In order to obtain the B(GT), it is necessary to measure the β-intensity, i.e., the probability of populating a level of energy E in the daughter nucleus when the β-decay process occurs. There are two possible ways to do this where the main objective is the detection of the β-delayed γ-rays: the traditional high-resolution spectroscopy and the total absorption gamma spectroscopy (TAS). The former method is based on the use of high-resolution germanium(Ge) detectors widely used in studying prompt radiation from reactions. A considerable effort has been devoted to the improvement of such detectors and the instrumentation associated in recent decades . The latter technique consists of the use of large scintillator crystals which act as γ-energy calorimeters with very high efficiency for γ-rays of all energies. Though already used in the early 70s by Duke [55], this latter technique has not been in widespread use due to certain difficulties that have been overcome in recent years.

2.4.1 High-resolution spectroscopy and the Pandemonium effect

Due to the continuum character of the beta spectra, the measurement of the β-decay to each individual state is not straightforward by means of beta particle detection. The beta-feeding to a particular state in the daughter nucleus can be measured by detecting the β-delayed gamma-rays of the γ-cascades which are emitted from that level to the ground state and by imposing an intensity balance with suitable corrections for internal pair production, internal conversion, etc. This will only be valid in cases not very far from the stability line when no levels fed in the decay lie above the particle separation energy, hence decaying by emitting a particle and not by electromagnetic transitions. Ignoring such decays, the β-feeding to a certain level would be the difference between the total γ-intensity which de-excites this level and the intensity which populates it from the other excited levels above.

$$I_\beta(E_i) = I_T^{OUT}(E_i) - I_T^{IN}(E_i) \tag{2.9}$$

This β-delayed electromagnetic radiation is usually registered by using high-resolution germanium detectors. Such studies can often reveal a wealth of nuclear structure data on individual levels at all excitations in simple decay schemes. They disclose some information about the structure of low-lying states in complex decays. However, the apparent simplicity of the method meets difficulties regarding the exact determination of I_β in complex decays.

At present even the best Ge arrays suffer from a low efficiency detection for γ-rays, with a maximum of 20% efficiency at 1332 keV achieved [56]. What makes the situation worse is the fact that this efficiency is strongly dependent on the energy. For very complicated decay schemes with many levels populated at high excitation energy and many de-excitation patterns for each level, such measurements fail to detect part of the gamma intensity. The reason is that some or many of the weak gamma transitions remain unobserved and cannot be placed in the decay scheme. As a consequence, the β-feeding is incorrectly determined. Since high energy and weak gamma transitions occur mostly at high excitation energy, most of the strength is wrongly assigned to levels at low excitation energy in complex decay schemes with high Q_β. Thus, the intensity obtained is misplaced and has a large systematic error, which is further emphasized by the re-normalization effect of the Fermi integral $f(Q_\beta\text{-}E)$. Its strong dependence on the transition energy ($\sim(Q_\beta\text{-}E)^5$) leads to the need for an accurate detection of even very weak β-decay branches to levels with excitation energy close to the Q_{EC} value. This effect can be summarised as the combination of the following factors:

- The low detection efficiency for primary γ-rays, usually those with high energy.
- The high fragmentation of the I_β strength function at high excitation energies as the upper part of the level scheme has a very high level density, in particular for medium mass and heavy nuclei. Thus, peaks in the γ-ray spectrum become less clearly defined and it is better to talk about a continuum of energy levels in this region of the scheme.
- Not only can the I_β be highly fragmented but also the de-excitation path of the cascade can follow different routes (further fragmentation of the γ-intensity).

This problem was already recognized by Hardy et al. in 1977 [57] who called it the *Pandemonium effect.* He drew the conclusion that *"every complex β-decay scheme based on γ-ray peak analysis and intensity balances must now be regarded as doubtful".* Even with a modern closely packed-array of germanium of 42 large Ge detectors, such as EUROBALL [58], it has been shown that a substantial part of the B(GT) remains undetected. This was accurately studied for the case of decay of the ^{150}Ho isomer with the CLUSTERCUBE at GSI [59] for which 50% of the strength was not observed. This rather general conclusion leads to the need to find an alternative technique to obtain a reliable B(GT) distribution over the whole decay energy window.

2.4.2 Total Absorption Spectroscopy (TAS)

The TAS technique has been conceived to overcome the limitations of the standard low-efficiency, high resolution γ-ray spectroscopy explained so far. The ideal tool would be a γ-energy calorimeter, hereinafter called TAS, with 100% full-energy

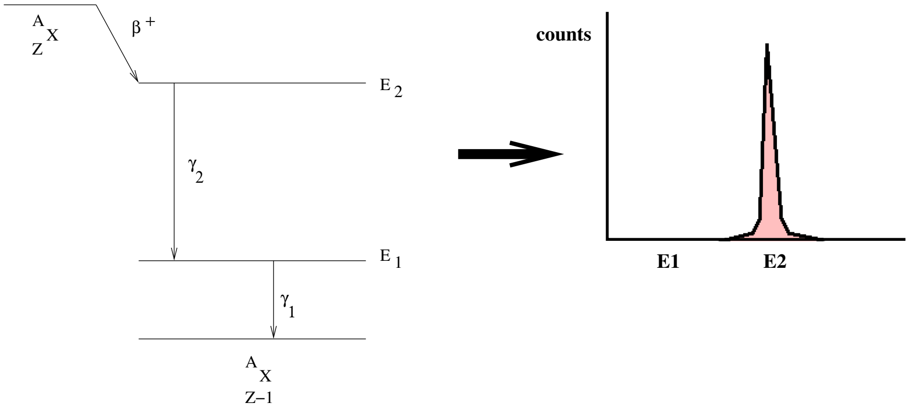

Figure 2.7: Example of a β-decay followed by a γ-ray cascade (left). The direct spectrum measured for an ideal TAS covering 4π around the source is plotted (right). No unfolding methods are needed to obtain the I_β distribution in this case.

peak efficiency for γ-rays of all energies. This kind of detector would register the sum energy of all the γ-rays in the γ cascade which de-excites a level fed initially in the β-decay (in contrast to the detection of each individual γ-ray on which the high-resolution spectroscopy is based). This feature is very important since it makes the detector efficiency independent of gamma-ray multiplicity. To illustrate schematically how an ideal TAS would work, a simple decay is represented in figure 2.7 on the left. A spectrum similar to what is shown on the right would be obtained with an ideal TAS.

Other features which a total absorption spectrometer must have are the following:

1. The light yield should be proportional to the deposited energy over as wide a range as possible, i.e, good efficiency for γ-rays of few MeV.

2. The decay time of the induced luminescence should be short so that fast signal pulses can be generated.

3. The medium should be transparent to the wavelength of its own emission for good light collection and the material should be of good optical quality.

4. The crystal should be manufactured in sizes large enough to be of interest as a practical detector.

Since an ideal TAS does not exist, this implies that the response of any spectrometer used for β-decay measurements will depend on the level scheme of the daughter nucleus populated in the decay. Therefore the relation between the feeding f_j to each level j and the measured TAS data d_i can be expressed in terms of a detector response function R_{ij} in the following form:

$$d_i = \sum_{j=0}^{jmax} R_{ij} f_j, i = 1, i_{max} \tag{2.10}$$

This implies that the matrix response of the detector must be known, which involves a lot of detailed measurements and simulations, and also unfolding methods must be applied to the TAS data . This complexity together with the fact that large scintillator crystals with a high efficiency cannot easily be fabricated were the main reasons why this technique did not become popular in the past. Many modifications were made to the total absorption spectrometers through the years in order to deal more accurately with the analysis of the data. A brief summary of these modifications is given below in order to describe the evolution till the up-to-date TAS detectors.

Duke [55] was the first who introduced the TAS technique applied to β^+/EC-decay measurements in the early 1970s. The spectrometer used consisted of two 15 cm diam. x 10 cm height NaI(Tl) crystals placed at a 1.5 cm distance with the source positioned at the mid-plane centre. However, the rather poor peak efficiency of these detectors (28% at 1 MeV) and the problems encountered in the unfolding of the data made the results not very reliable. Based on experimental tests using a large number of calibration sources, the response function to a γ-ray was approximated by a step function superimposed on a full-energy photopeak. The subsequent unfolding was then performed as a "peeling-off" procedure, starting from the high-energy end of the spectrum. The response function method obviously had serious limitations and was progressively abandoned when Montecarlo simulations started to give satisfactory results. Johansen et al. [60] started employing such Montecarlo simulations in 1973 to construct the response function of the detector. They modified the spectrometer used by Duke and used it at OSIRIS for β^- emitters in studies of fission-product decay isotopes. Since beta particles distort the gamma-sum spectrum by shifting it upwards in energy, they required a beta-gamma coincidence by placing a ring-shaped plastic detector around the two NaI(Tl) crystals. Due to the poor approximation of an ideal TAS with this arrangement, there were clear limitations in the analysis of the data. The beta strength function distributions obtained may be regarded as suspect for the nuclei studied.

In 1985, encouraged by the discussions on the validity of complex decays schemes from high resolution spectroscopy initiated by Hardy et al. in their paper, Alkhazov et al. [61] continued to investigate this Pandemonium effect. A new total absorption gamma spectrometer consisting of a large NaI crystal of ∅20 cm x 20 cm with a pit of 4 cm x 10 cm was used. Even though the crystal employed was considerably larger than the previous one, the TAS still differed too much from an ideal TAS. A

60% higher peak efficiency was achieved though. β^+/EC decay measurements were performed for which a thin Si(Li) detector was put in front of the source to take into account the annihilation radiation. The introduction of such a detector for the β^+ detection allowed them to obtain independent information on the EC feeding since this process competes with β-decay. By setting a β^+-gamma coincidence condition, the results derived from β^+(EC) feeding through the known EC/β^+ ratio values could therefore be checked separately. It was concluded that many beta intensities published in the past, in particular for nuclei with large Q-values, were substantially wrong. They claimed that *"a reevaluation of the usefulness of a whole class of experiments"* was necessary.

Greenwood et al. [62] employed a 25.4 cm diameter x 30.5 cm long NaI(Tl) well detector at the INEL on-line isotope separator facility with a 45% increase in peak efficiency. Although this was the best approximation to an ideal TAS so far, the analysis of the TAS data continued to be an inherent difficulty. The impossibility of giving an analytical method to account for the uncertainties assigned to the resulting beta feeding distribution was a clear limitation in the analysis procedure followed.

In the last 13 years, four larger spectrometers have been employed to measure beta strength distributions. The first one was constructed at the Nuclear Institute of St. Petersburg and was very similar to the one used by Alkhazov et al. It consists of two NaI(Tl) detectors and was used for the first TAS experiments at GSI and recently in Jyväskylä for the study of the β-decay of some refractory isotopes that were considered important contributors to the decay heat in reactors [16]. The second one was constructed at Berkeley and transported to GSI [63], with a high peak efficiency, from which very fruitful results in β-decay studies were extracted. The third one is LUCRECIA, the largest NaI(Tl) crystal in the world, which is still in use at ISOLDE with a permanent setup. It has been utilised for the determination of the shapes of the Sr [44], Kr [45] and Rb isotopes, some of which are presented in this work, and for some Pb isotopes [64]. Further detail of the geometry and features of this detector will be given in chapter 3, where the experimental set-up will be explained in detail. A fourth one, consisting of 12 BaF_2 crystals, has recently been used in Jyväskylä to study the decay of A$\approx$100 neutron rich nuclei [65]. The light output of each crystal is read independently and thus additional information on the multiplicity of the gamma-ray cascades can be extracted. In all these cases, the spectrometers cover a solid angle of $\approx 4\pi$ around the radioactive source and posses a very high intrinsic efficiency for γ-ray detection.

In Fig. 2.8 a typical configuration of a TAS for β^+/EC measurements has been schematically drawn in order to highlight the processes taking part in the detection

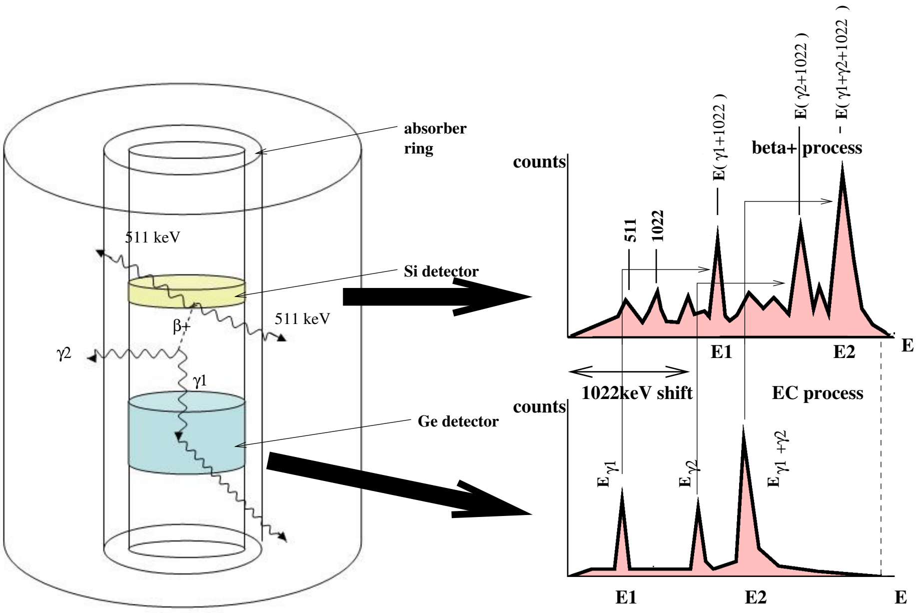

Figure 2.8: Schematic drawing of a real TAS with an absorber ring and ancillary detectors: a beta counter (Si detector) and a Ge detector. The addition of material (the ancillary detectors) leads to Compton background, escape peaks and in general, a decrease in the efficiency.

and the complexity of the spectrum obtained. An absorber ring (as used by Johansen et al.) can be placed in the inner part of the crystal, usually made of Be or polyethylene, to avoid the penetration of positrons into the spectrometer. Ancillary detectors are usually placed around the source in order to tag certain events. Since the EC process competes with β-decay, a beta counter must be placed in front of the source to tag the β^{+}-decays (first used by Alkahov et al.). This kind of set-up is usually complemented with a Ge detector to detect the X-rays and also tag EC-process. As should be noted, the addition of all the above material causes a reduction in the efficiency. However, the employment of the right configuration and a large crystal, such as those mentioned above, leads to an efficiency still close to 100% for γ-ray detection (Note:-not full energy peak). Therefore, the probability of detecting at least one gamma in the cascade is $\simeq$ 100%.

Since the peak efficiency is below 100%, it is possible that one γ-ray is fully absorbed in the crystal and the other escapes totally or partially. Another effect caused by the addition of dead matter is the increment of Compton background in the spectrum as a γ-ray can interact with the material (for instance with the Ge detector) and lose some energy before entering the crystal. The annihilation of the β^{+} produces two γ-rays in the configuration back-to-back which can also be detected in the TAS and summed in the the detection of the cascade. This causes a shift of 1022 keV in the TAS β^{+}-decay spectrum (TAS in coincidence with the beta counter) when comparing it to the spectrum obtained when an EC occurs (TAS in coincidence with the Ge detector gating on the X-rays). As can be seen in Fig. 2.8, the spectrum becomes very complex, specially in the β^{+} case, even for a very simple decay.

In the last years, not only has there been a great development in terms of growing scintillator crystals to large sizes but a very detailed study and optimisation on the analysis techniques employed to unfold the TAS data has been developed [66]. The unfolding algorithm taking into account the inherent statistical natural of the data and the means in Monte Carlo simulation for the construction of the response function of the TAS detectors will be described in detail in Chapter 6.

Chapter 3

The Experiment and setup.

The experiment IS398 was aimed at the production of N∼Z Sr and Rb isotopes in the framework of the investigation of nuclear shapes of nuclei in this region. In this work the decays of the ^{77,78}Sr and ^{76,78}Rb nuclei were under study. The results of these studies will be presented here. The measurements were carried out in three separate experiments at the isotope on-line separator (ISOLDE) in 2003, 2004 and 2006 at CERN. Both the experimental setup and measurements are described in detail in the following sections.

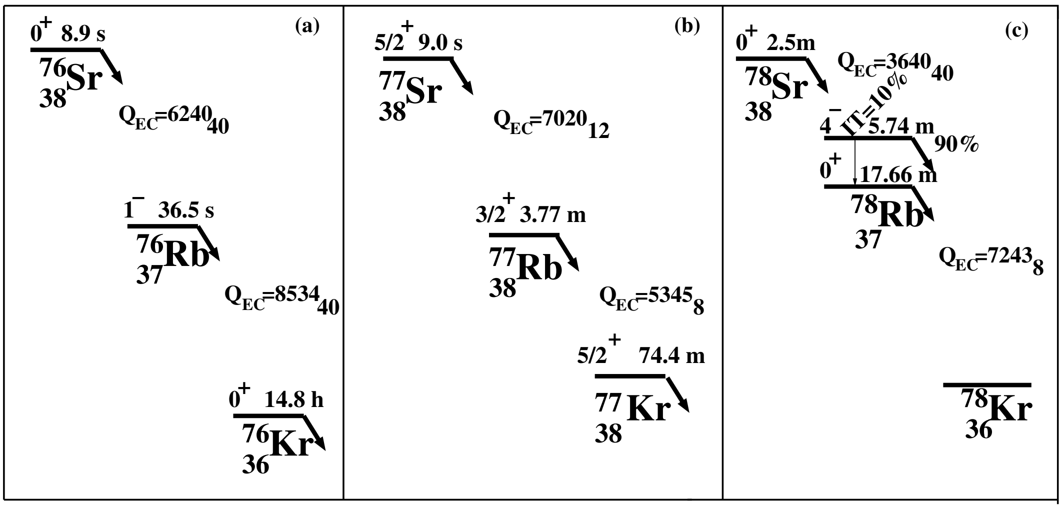

Figure 3.1: Schematic picture of the β^+/EC decays of a)^{76}Sr and ^{76}Rb, b) ^{77}Sr and ^{77}Rb and c) ^{78}Sr and ^{78}Rb. The Q$_{EC}$ values [67] and half-lives [68] have been extracted from the literature, except for the half-life of ^{78}Sr, where we performed a dedicated experiment.

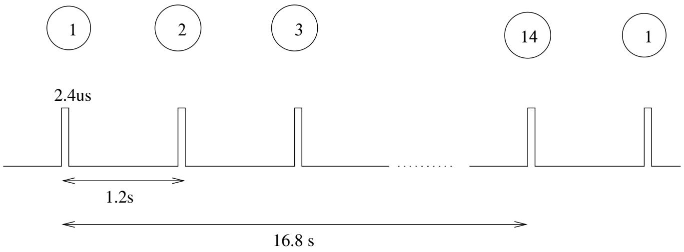

Figure 3.2: Time structure of the supercycle in the PS-Booster.

3.1 Sr and Rb isotope production

The ISOLDE(*Isotope Separator On Line Device*) facility is located at the Proton Synchrotron Booster (PSB), at CERN. It is dedicated to the production of radioactive nuclei produced via spallation, fragmentation or fission reactions in a thick target followed by ionisation and then mass separation.

The primary beam of 1.4 GeV protons is delivered by the PS-Booster, a stack of four small synchrotrons which pre-accelerate the 50 MeV protons injected by a linear accelerator (LINAC). The PS-Booster delivers pulses of 3.2 x 10^{13} protons per pulse every 1.2 s. Each pulse lasts for 2.4 μs thus leading to an instantaneous current of 2.1 A. At the time of our experiments the pulses were organised in a supercycle of 14 pulses (see fig. 3.2) with the flexibility to deliver a varying sequence and number of pulses to ISOLDE and other facilities. In the experiments described here different numbers and sequences of pulses in the supercycle were used at various times.

The Sr and Rb nuclei were produced in Nb targets (A=91, N=48) of thicknesses 52 g.cm^{-2} (masses 76, 77) and 37 g.cm^{-2} (mass 78) with a beam of 1.4 GeV protons injected through a transfer line from the PS-Booster into the ISOLDE target hall to produce a spallation reaction. The target was coupled to an ion source in order to ionise and extract the products of the reaction. Ideally, this combination of target-ion source should produce an ion beam preferably containing isotopes of only one chemical element. ISOLDE has 3 different target-ion sources available: laser ion-source, plasma ion source and surface ion source. The most appropriate ion source is chosen depending on the characteristics of the isotopes to be extracted. In this experiment a surface ion source made of tungsten, with a higher work function than the atoms which should be ionised, was used. This ion-source consists of a tube which is heated up to 2200 K to produce thermo-ionisation in the hot surface. Fluorine, in the form of CF_4, was added to the ion source carrier gas in order to extract the Sr isotopes of interest in the form of SrF^+ ions and suppress the ionization of other isobaric reaction products [70, 71], mainly Rb which do not form a fluoride. At room temperature CF_4 is a gas and is thus very easily added

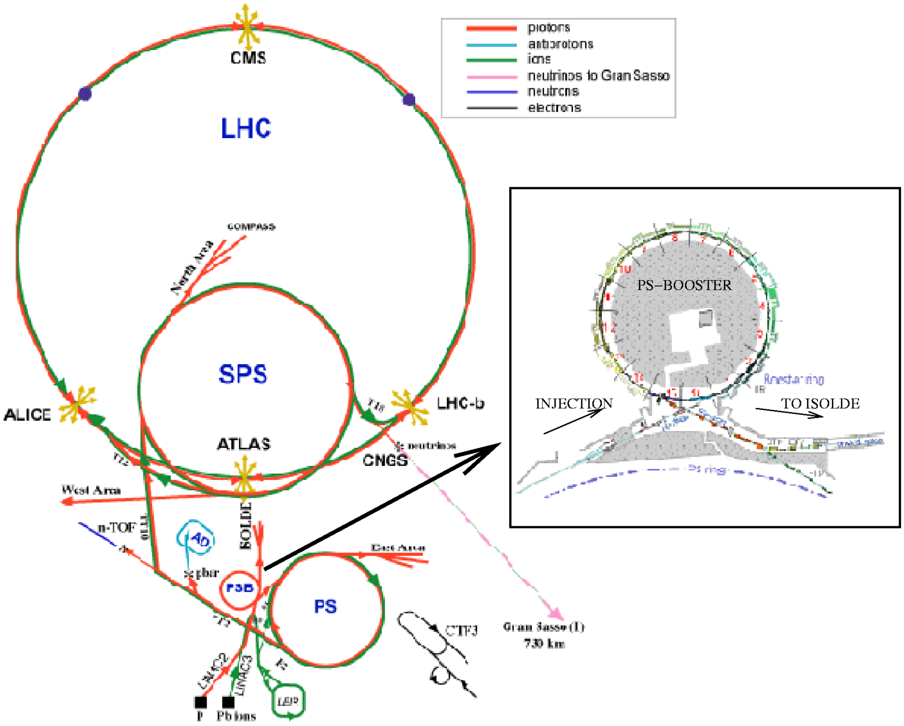

Figure 3.3: Layout of the CERN accelerators showing the PS-Booster [69].

to the ion-source in a controlled way. For the Rb production, with the exception of ^{78}Rb, CF_4 was not added in the ion source due to the high cross section production for Rb. In the particular case of ^{78}Rb, it turns out that it has two low-lying states which β-decay, namely the ground state and the 4^- state at 111.2 keV excitation. Both are produced in spallation. If this nucleus is made directly then both decays are present. Here we made the ^{78}Rb via the decay of ^{78} Sr exclusively, both when we studied ^{78}Sr and ^{78}Rb. As a consequence the 4^- isomeric state was not populated in our studies and our results only address the decay and hence the shape of the 0^+ ground state in ^{78}Rb.

The SrF^+ and Rb^+ ions were then extracted from the target-ion source unit with a 60 kV electric field potential [72]. This acceleration voltage is not constant at ISOLDE due to the varying load caused by the pulsed proton beam. The beam and the large cascade of high energy particles produced in the target lead to an intense air ionisation in the surroundings of the target. What is done in conventional isotope separators is that the target and the ion source are kept at a constant high voltage. However in this case this would cause a break down in the normal supply during beam impact. This has been solved by using a pulsed voltage supply which brings the 60 kV high voltage to zero in 35 μs before beam impact and restores it

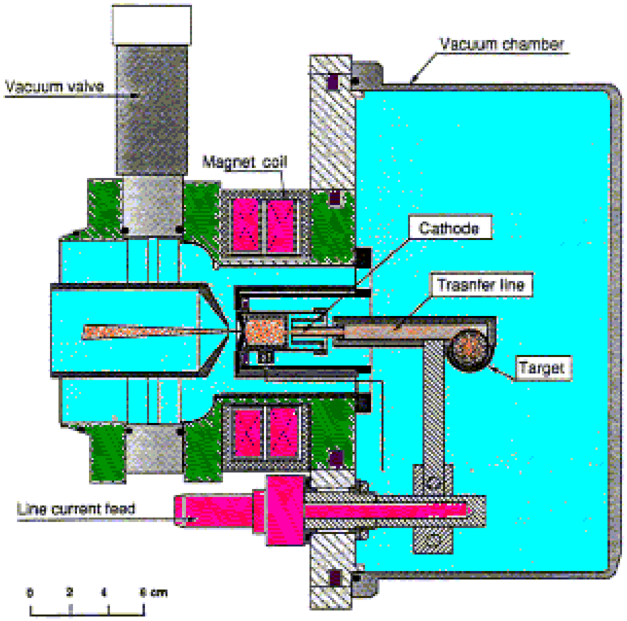

Figure 3.4: Configuration of the target-ion-source in ISOLDE.

to the regulated value after 6 ms with a precision of ±1 V. This recuperation time of 6 ms might have some effect in the extraction of some short-lived nuclei, however in our case this was not relevant since our cases under study have a relatively long half-life.

The ISOLDE isotope mass separator facility is provided with 2 magnetic mass separators: the GPS (General Purpose Separator) and the HRS (High Resolution Separator). The GPS consists of a system of quadrupole magnets which focus the beam parallel to the entrance of the dipole, which is an H magnet with 70° deviation, and separates the masses at the focal plane. Furthermore, there is also a mechanism to select three beams simultaneously within a mass range of 15 per cent, which makes the facility more versatile and efficient. The mass resolving power is $\frac{M}{\Delta M}$=2400. On the other hand, the HRS is a more complex combination of quadrupoles and two large dipole magnets of 90° and 60° deviation, which can achieve a better isobaric separation and a mass resolution of $\frac{M}{\Delta M}$=7000 [73]. Both separators are connected to the general beam line feeding the different installations but cannot be run simultaneously. In our case, once the ions were extracted from the target-ion source unit they were mass analysed in the HRS (masses 76,77) and in the GPS (masses 78).

The control of the target-ion source, the beam line and the vacuum system was

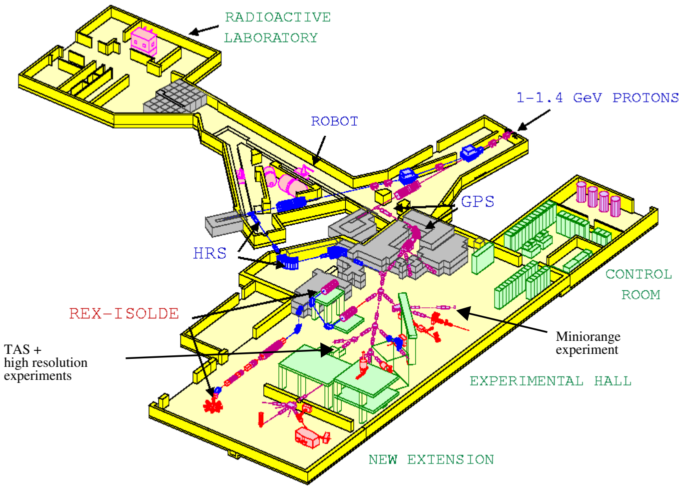

Figure 3.5: Layout of the experimental hall at ISOLDE. The placement of our different setups has been marked.

done in the control hall through PC programmes designed for this purpose [74]. After the isotopic mass separation of the ion beam performed with the GPS or the HRS, the secondary radioactive beam was directed into the beam line and carried to the different experimental setups under vacuum where it was implanted in a tape. The different setups used for the measurements will be described below and are marked in Fig. 3.5.

3.2 TAS experiment: setup and measurement for the determination of the B(GT) strength for masses 76, 77 and 78.

The primary aim of the present work is to determine the GT strength distributions as a function of the excitation energy of the daughter nucleus for the decays of ^{77,78}Sr and ^{76,78}Rb with the use of a TAS, in our case, LUCRECIA. The final goal will be to compare these distributions with theoretical calculations [49], when available, assuming different deformations for the parent ground state. The success in the application of the total absorption technique to the decays of ^{74}Kr [45] and ^{76}Sr [44] in previous experiments encouraged similar measurements for the remaining Sr isotopes which are reported in this work.

The measurements of mass 76, 77 and 78 were performed in two separate experiments which differed only slightly in the production method as described in section

3.1. The experiment involving masses 76 and 77 was carried out in 2003 while a second experiment was carried out in 2004 for mass 78 together with a high resolution experiment for γ-ray studies on the ^{78}Sr β^+/EC decay (see section 3.3). The setup was installed at the end of the RC3 beam line as shown in Fig. 3.5. The transmission from the output of the separator to the experimental setup was 78% for masses 76 and 77 and 46% for mass 78. In both experiments, the secondary beam was deposited on a tape transport system operated under vacuum called Desdemone. This system was designed and constructed by the Strasbourg members of the collaboration in the framework of the Sr and Kr experiments with the TAS. In the second experiment the TAS and the high resolution setups were interconnected with each other with this tape system. This device, shown in Fig. 3.6, is controlled remotely and enables the implantation of the radioactive ions on a thick 55 μm mylar aluminised tape which can be moved after a fixed time to carry the accumulated activity to the counting position and, at the same time, remove the residual activity. Every measurement cycle was divided into three parts: collection time T$_c$ to accumulate the radioactive nuclei on the tape; transport time T$_t$, during which the source is moved to the measurement point at a speed of 1.3 m/s; and measurement time T$_m$. In most cases a symmetric cycle was chosen in which the collection of the source is simultaneous with the measurement of the activity. This time is chosen on the basis of the half-life of the nucleus and its daughter involved and it is a compromise between the fraction of the saturation activity reached and the counting time. This time must also fit with the structure of the pulses from the PS-booster accelerator supercycle which provides the primary proton beam. These comments apply to all the measurements presented in this work.

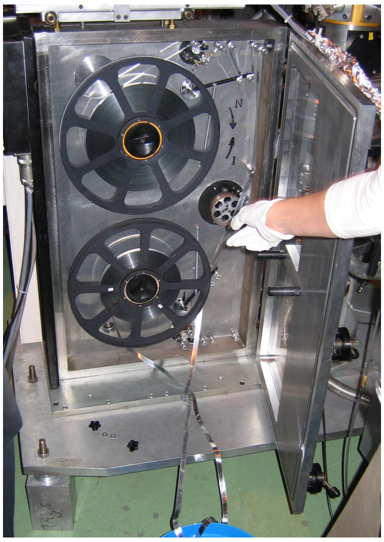

Figure 3.6: Photo of the tape transport system, Desdemone.

Due to the fact that the incoming proton beam is pulsed, the movement of the tape is synchronised with the signal given by the synchrotron which starts a cycle in Desdemone. Once this cycle has started, its duration can be controlled by the microprocessor included in the tape transport system. Since the proton bombardment on the target leads to a high neutron production which causes a high gamma and neutron background, the acquisition is inhibited for about 10-15 ms after the beam impact. After this, a beam-gate is opened for a certain time in the control hall (this time varies depending on the isotope and its production cross section), at which time the collection on the tape starts. This process continues until the time specified for the cycle of accumulation is complete. The tape is then moved and another proton beam pulse triggers the start of a new cycle and hence a new collection, as shown in Fig. 3.7.

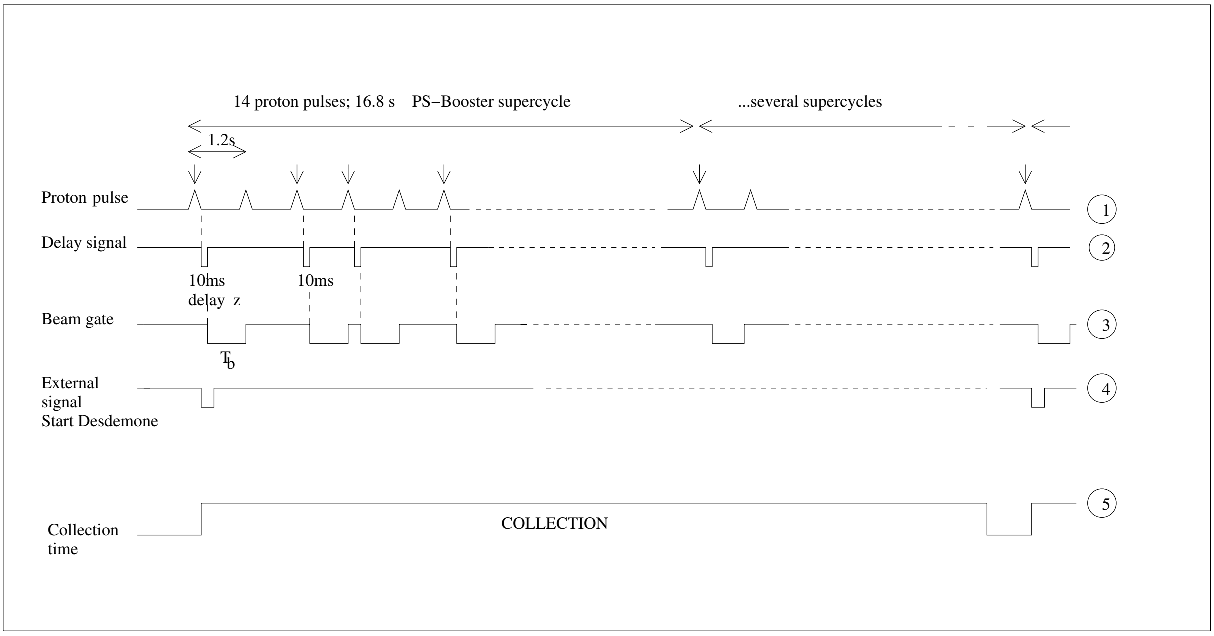

Figure 3.7: Chronogram of the proton supercycles, beam and collection cycle.

The beam line where the TAS setup was installed ends with a telescopic aluminium tube of 1.2 mm thickness and 68 mm diameter which is sealed by an 80 μm kapton window. A set of three collimators, one of 36 mm diameter and two of 4 mm diameter, were placed 950, 975 and 992 mm upstream respectively from the measurement point, located in the middle of the crystal. Their purpose is to suppress the beam halo and define a reduced beam spot on the mylar tape. The collection point was placed just behind the last collimator shown in Fig. 3.8. Of particular note is the fact that the source can also be collected in the middle of the crystal with the geometry displayed, thus enabling the measurement of short-lived exotic nuclei with half lives as short as 5 ms. Such possibility was not used for the cases under study in this work.

At the core of the setup is located the total absorption spectrometer, LUCRECIA. The TAS LUCRECIA was conceived and designed for the study of the β-strength function, in particular for β-decays with a large Q-value. It consists of a large cylindrical crystal of NaI(Tl), to our knowledge the largest NaI crystal in the world, 38 cm x 38 cm, covering a solid angle of $\approx 4\pi$ as shown in Fig. 3.8 and manufactured by *Saint Gobain Crystals and Detectors*. The light coming from the scintillator material is collected by eight 5 inch coupled photomultiplier (PMT) tubes. The crystal has a transverse hole (7.5 cm in diameter) which allows the beam pipe to enter up to the centre of the crystal and different ancillary detectors to be put for the detection of X-rays (EC decay) and positrons (β^+ decay). The crystal is encased in a 13 mm thick aluminium cylinder whose thickness gets reduced to 11 mm inside the radial hole in order to limit the gamma-ray absorption around the source. The inner side of the crystal is coated with a 2 mm thick Al_2O_3 layer to provide good light reflection. The whole spectrometer is isolated by a 4-layer shield of boron-polyethylene (10 cm), lead (5.1 cm), copper (1.5 cm) and aluminium (2 cm). This shielding reduces the counting rate coming from the room background, consisting mainly of neutrons and γ-rays after the target bombardment, by a factor of 3.5, with the shielding opened, down to 1 kHz with the shielding closed. The remaining activity mainly comes from the decay of ^{40}K present in the crystal. The stability of the PMT tubes is continuously monitored by a Light Emitting Diode (LED) triggered by a pulse generator. This allows the observation of possible shifts in gain of the PMT tubes due to a high counting rate or changes in the crystal temperature. An air conditioning system is also used to keep the temperature of the crystal stable within ±0.5 degrees.

This crystal has a large intrinsic efficiency for gamma detection. However, the introduction of ancillary detectors has an adverse effect on the efficiency which leads to a decrease in the photopeak value of 10 per cent. This is highlighted in Fig. 3.10 which shows the variation in the efficiency depending on the device placed in the hole: a NaI plug covering half of the hole in the crystal approximately or the ancillary detectors which will be described later. These numbers have been calculated by means of Monte-Carlo simulations with *GEANT4*. For such simulations an accurate description of the geometry of the scintillator crystal including the beam pipe, collimators, shielding, tape transport system, etc, as well as the characteristics of the materials involved was used. The total efficiency in both cases is close to 90 per cent in the range 300-3000 keV which means that for a cascade of two or more γ-rays in this range, the probability of detecting something is always $\geq$99 per cent. However, in terms of energy resolution the performance of a scintillator crystal, like the one used in this work, is not as good as the resolution of Ge detectors. For

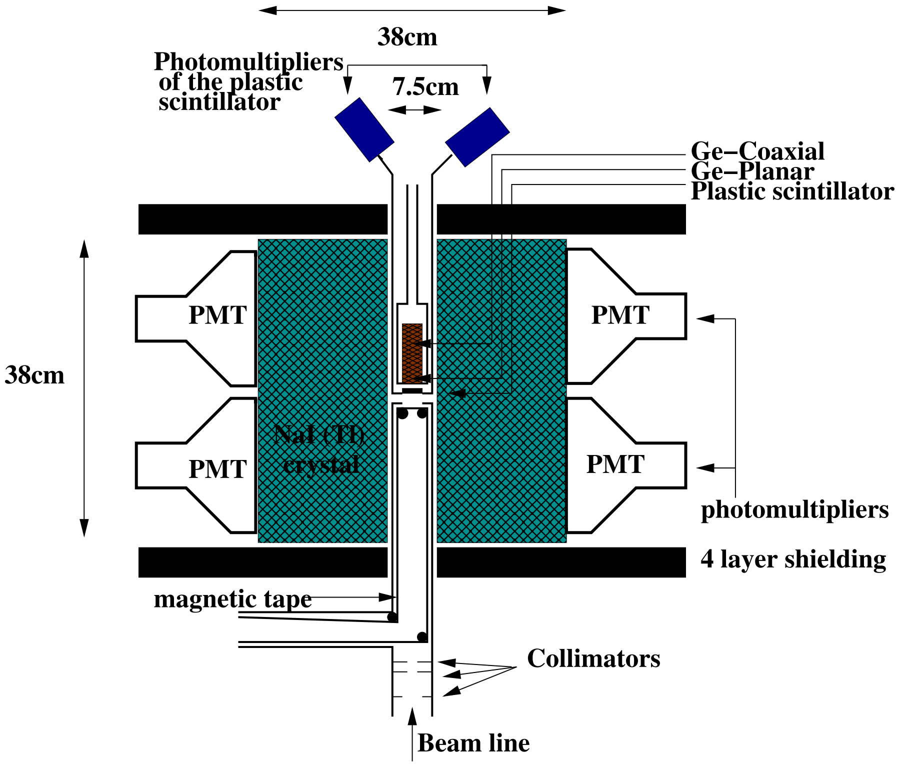

Figure 3.8: Schematic drawing of the LUCRECIA spectrometer.

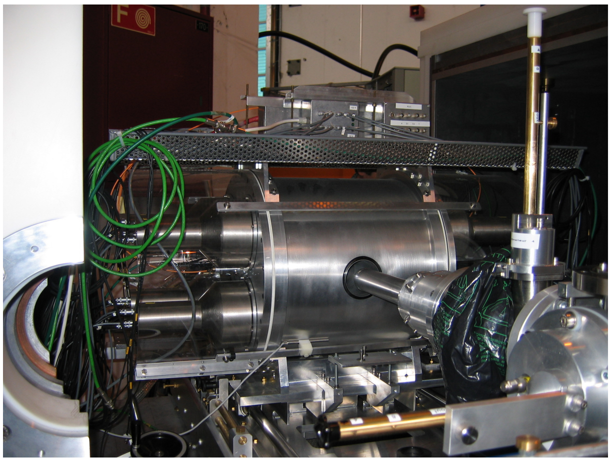

Figure 3.9: Photograph of the LUCRECIA spectrometer.

LUCRECIA, the energy resolution achieved was 8.4% at 661.6 keV and 4.3% at 2754 keV determined by using sources of ^{137}Cs and ^{24}Na respectively.

The ancillary detectors introduced into the hole were a beta counter for positrons

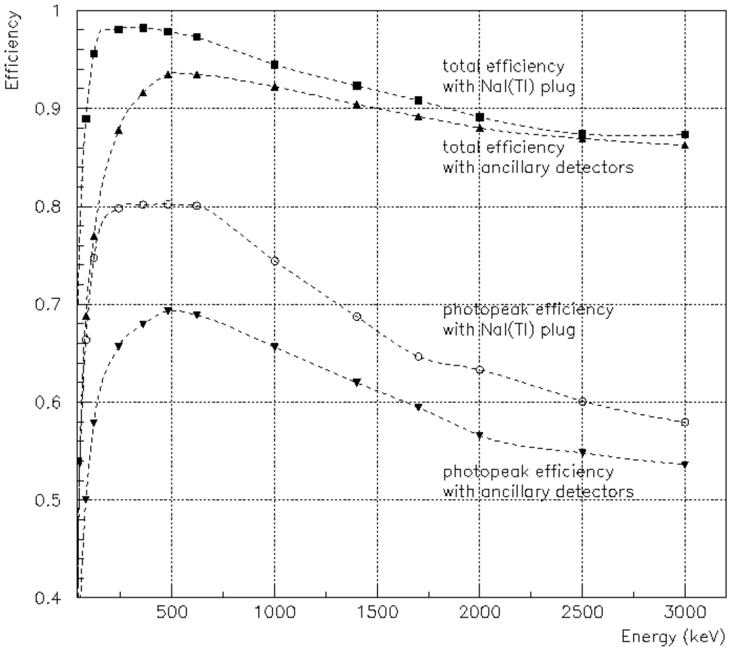

Figure 3.10: Total and photopeak efficiencies of Lucrecia simulated for the configurations with a NaI plug and with the ancillary detectors described in the text.

and a germanium telescope (planar+co-axial) for the detection of X- and γ-rays. The beta counter consisted of a 2 mm thick NE102 plastic scintillator material which is placed in front of the germanium detector and close to the radioactive source. The reason for choosing this material instead of Si is the low energy of the X-rays of Rb and Kr produced in the EC decay. The energy range of the X-rays of interest was approximately 11-15 keV and a Si material would absorb them before they could enter the planar germanium detector. This would make it impossible to use the X-ray coincidence technique to identify the Z of the isotopes and the possibility to obtain EC spectra of the nuclei of interest. In each of the experiments a different beta counter was used. In the first experiment a 2 cm diameter plastic scintillator covering a solid angle of 14.6% was used. In the second experiment a 3 cm diameter scintillator covering a 17.3 % solid angle replaced the previous one. The main difference between them lies in the collection of the light. In the first case the light was collected by two light wave guides and in the second the collection was done by 90 optical fibres. On the other hand, the germanium telescope consisted of a 1 cm thick planar Ge detector backed by a 5 cm thick co-axial Ge detector. The energy resolution for the planar was 0.66 keV at 59.5 keV and it covered an energy range up to 362 keV. The co-axial detector showed an energy resolution of 1.03 keV at 121.0 and 1.9 at 1112 keV and covered an energy range of 75-4300 keV. The end cap of the telescope cryostat was made of a thin Be window to reduce the X-ray absorption. The solid angle covered by the telescope was approximately 14 % of the

4π angle. This telescope was used specifically to detect low energy γ-rays with the planar detector as well as more energetic γ-rays with the co-axial detector.

Table 3.1 shows the measurement cycles chosen for the different isotopes of interest. In an experiment with a target-ion source of the type described in this work, the yield of ions with a fixed primary beam current generally decreases as a function of time. The activity registered inside LUCRECIA after collection in the early stages of the life of the target-ion source and the number of pulses used for the production are shown in table 3.1. Background measurements were performed, interspersed with the isotope measurements. Such measurements are very important from the point of view of background subtraction, essential for the application of the TAS analysis method. On the other hand, one of the main factors of contamination in a TAS measurement is the subsequent decay of the daughter nucleus produced in the parent decay. In order to proceed with a background subtraction in a later analysis offline, a part of the measurement was devoted to the daughter β-decay of each parent of interest. In some cases, namely ^{76}Rb and ^{78}Rb, such measurements were not needed since their daughters are very long-lived and stable respectively. A total of 780, 76, 218, 244, 276 and 284 min were devoted to the measurements of ^{76}Sr, ^{76}Rb, ^{78}Sr, ^{78}Rb, ^{77}Sr and ^{77}Rb decay respectively. Coincidence and singles spectra were recorded. Calibration measurements using standard sources, namely ^{241}Am, ^{137}Cs and ^{60}Co , were also carried out at the end of the experiment. ^{24}Na was produced and then directed to the TAS station in order to check how well the response function of LUCRECIA is reproduced with Montecarlo techniques. Such a procedure will be described in chapter 6.

Table 3.1: The half-life $T_{1/2}$ [68], and Q_{EC} [67] value for each isotope is shown. In the case of ^{78}Sr the half-life was determined in this work (see next chapter) and is included on the table. The time settings for the tape cycle given by T_c, collection time, T_d, delay time and T_m, measurement time, together with the number of proton pulses used for the production of the different isotopes, N_p are listed. The counting rate registered inside LUCRECIA after collection and the beamgate are also specified.

Isotopes	$T_{1/2}$ (s)	Q_{EC} (keV)	T_c (s)	T_d (s)	T_m (s)	N_p	Activity (counts/s)	beamgate (s)
^{76}Sr	8.9(3)	6240(40)	15	0	15	9	4500	15
^{76}Rb	36.5(6)	8534(4)	15	3	12	2	4000	0.006
^{77}Sr	9.0(2)	7020(12)	15	0	15	7	3800	1.1
^{77}Rb	226.2(24)	5345(8)	135	0	420	7	7200	135
^{78}Sr	155(3)	3762(11)	32	0	32	2	5400	0.6
^{78}Rb	1059.6(48)	7243(8)	16.8	750	1080	5	5300	16.8

3.3 High-resolution experiment: setup and measurement for γ-ray studies in ^{78}Sr.

In order to analyse the data from the TAS spectrometer LUCRECIA we require some knowledge of the low energy part of the level scheme in the daughter nucleus. Moreover the better our knowledge of the level scheme the higher the accuracy that can be achieved in evaluating the total absorption data. Here we can rely on published information on the discrete level on all of the decays [76, 77, 78] except ^{78}Sr and ^{77}Sr decays. Very little is known about the decay scheme of ^{78}Sr whose knowledge only goes up to 895 keV [79] while the Q_{EC} is 3762 keV [67]. A similar situation applies to ^{77}Sr β-decay where only 6 levels are known up to 1540 keV [80] and its Q_{EC} is 7020 keV [68]. Germanium spectroscopy is widely used for the detection of γ-rays and the construction of level schemes based on its good energy resolution. This type of spectroscopy is widely known as high-resolution spectroscopy. The measurement station, described in this section, was designed exclusively to study the level scheme of ^{78}Rb via the EC/β^+ decay of ^{78}Sr using this high-resolution technique. The experiment took place in 2004 and measurements on mass 78 using this high-resolution setup and the TAS LUCRECIA were made separately. As stated in the previous section, the two stations were interconnected by the Desdemone tape system. Due to limitations of time, a γ-ray study for ^{77}Sr β-decay was postponed for a third experiment in 2006, as described in the next section.

In these experiments a symmetric cycle was used in which the collection of the source and simultaneous measurement of the activity was 231 s. Together with the 4s used in moving the tape this equals the 235.2 s overall length of the supercycle. The activity of the source after the collection was typically ∼127 kBq and the beam-gate used 100 ms. The setup used in the experiment is shown schematically in Fig. 3.11 and on a photograph in Fig. 3.12. As can be seen in these figures, the γ-rays from the source can be detected by three germanium detectors, which are placed at right angles to each other. The geometry was chosen to minimise the possibility of coincidences between the annihilation quanta. One of the detectors is a planar Ge detector of 14 mm thickness and a front face of 35.7 mm diameter with a Be window of 300 μm thickness. The other two are co-axial Ge detectors of 40% (Dulcinea) and 70 % (Voltaire) efficiency. Voltaire also has a Si detector of 300 μm thickness in front of the Ge detector with a separation of 3 mm between the two. Table 3.2 displays the information about the volume, energy resolution and energy range covered of the three detectors used. Figure 3.11 shows the various distances from the source to the detector front faces as well as the thicknesses of the windows in front of the detectors and other dimensions. These numbers are important in order to allow us to perform Monte Carlo simulations of summing effects in the Ge detectors.

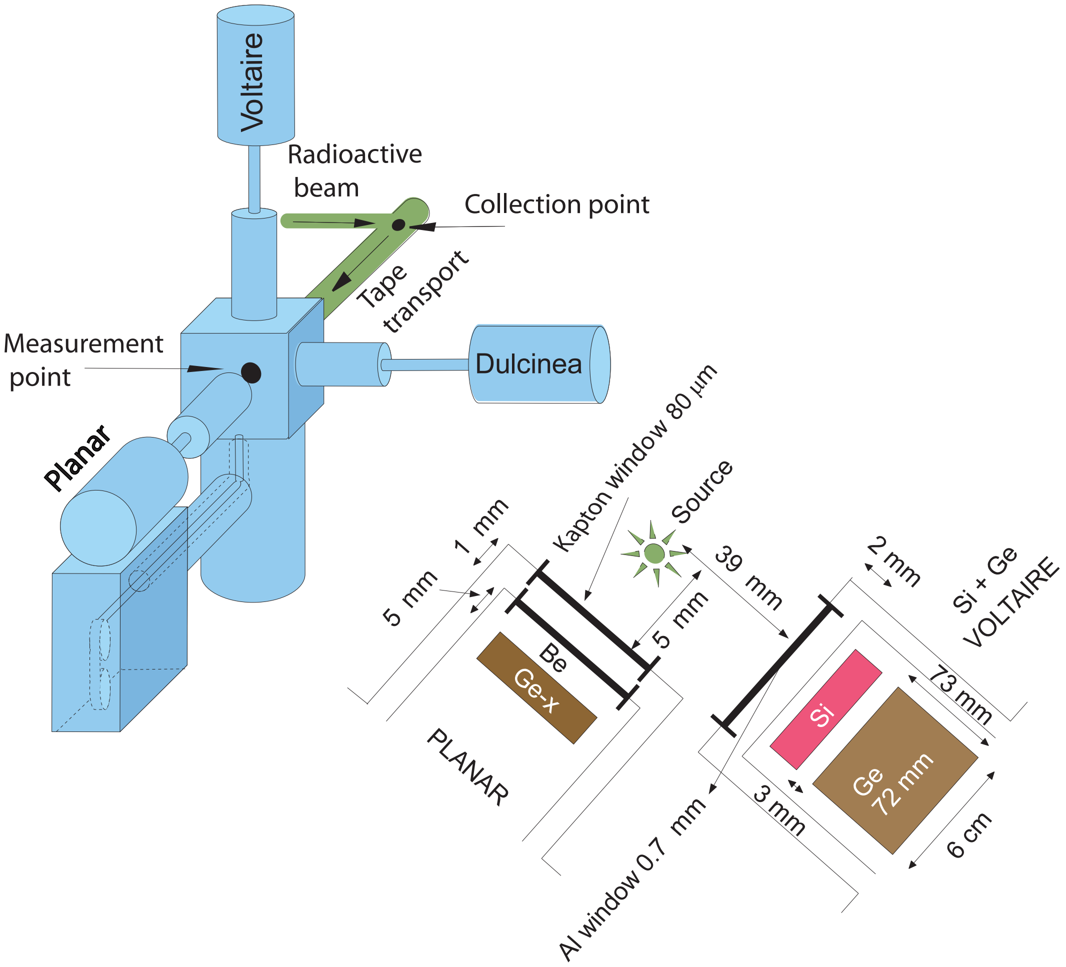

Figure 3.11: A sketch of the experimental setup for the gamma-ray singles and γ-γ and γ-X-ray coincidences. On the upper left we see the geometry with the three Ge detectors all at 90 degrees to one another. On the lower right we see a vertical cross-section through the apparatus. The figure is not to scale but the thicknesses of the various windows, the dimensions of the planar and Voltaire detectors and the distances from the source to the detectors are marked. It should be noted that Voltaire consists of a Si detector in front of a 70% efficiency Ge co-axial detector.

In this experiment, in the early stages of the life of the target-ion source, four of the pulses from the PS-Booster supercycle delivered sources which resulted in counting rates of 15 and 4.5 kBq in the planar detector and Voltaire respectively. The coincidence counting rate, where the three detectors were involved, was 2.4 kBq. The data acquisition system was inhibited for 10 ms after each impact of the PS-Booster beam on the target to eliminate any background from neutrons or γ-rays generated in the ISOLDE target. Overall this measurement lasted approximately

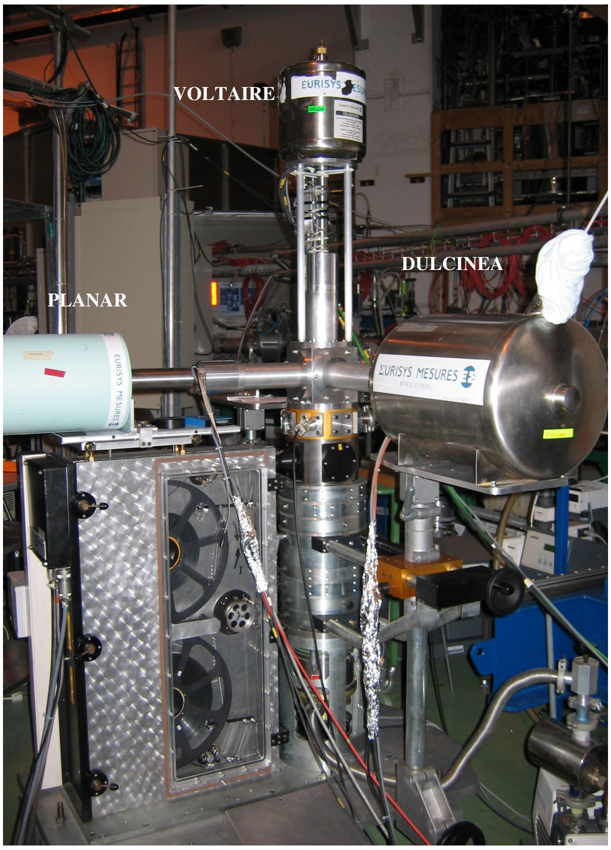

Figure 3.12: Photo of the High-Resolution setup with the three germanium detectors.

Table 3.2: Ge detectors used in the γ-ray studies of ^{78}Sr. Their volume, energy resolution and energy range covered are listed.

Detector	Volume	Resolution (keV)	Energy range
Planar	19.5 cm^3	0.6 at 121.8 keV	12-924 keV
Dulcinea 40	166 cm^3	1.6 at 121.8 keV	43-3340 keV
Voltaire 70	96 cm^3	2.0 at 121.8 keV	53-4390 keV

eight hours and the source activity was essentially constant over this timescale. Both singles and gamma-ray coincidences were recorded. Afterwards the detectors were calibrated for efficiency and energy using standard sources of ^{241}Am, ^{133}Ba and ^{152}Eu.

3.4 Mini-orange experiment: setup and measurement for internal conversion studies in $^{77-78}$Sr and γ-ray studies in ^{77}Sr

The analysis and construction of the level scheme of ^{78}Rb with the data acquired with the previous setup led to a number of ambiguities in the spins and parities of certain low energy transitions which were likely to be highly converted. On the other hand, the electron conversion is also important for the analysis of the TAS data since it contributes to the transition intensity. In order to determine the multipolarities of the β-delayed transitions assigned to ^{78}Rb, a third experiment was carried out at ISOLDE to measure their internal conversion coefficients. The experimental station was set in the branch LA1 after the HRS separator as shown in Fig 3.5. The measurements were made with a mini-orange spectrometer constructed and used by Barden at the GSI Mass Separator. It is described in detail in his thesis [81] and briefly in what follows. High resolution and internal conversion measurements were also carried out for ^{77}Sr since its level scheme had not yet been accurately determined. A photo of the whole setup is shown in Fig. 3.13.

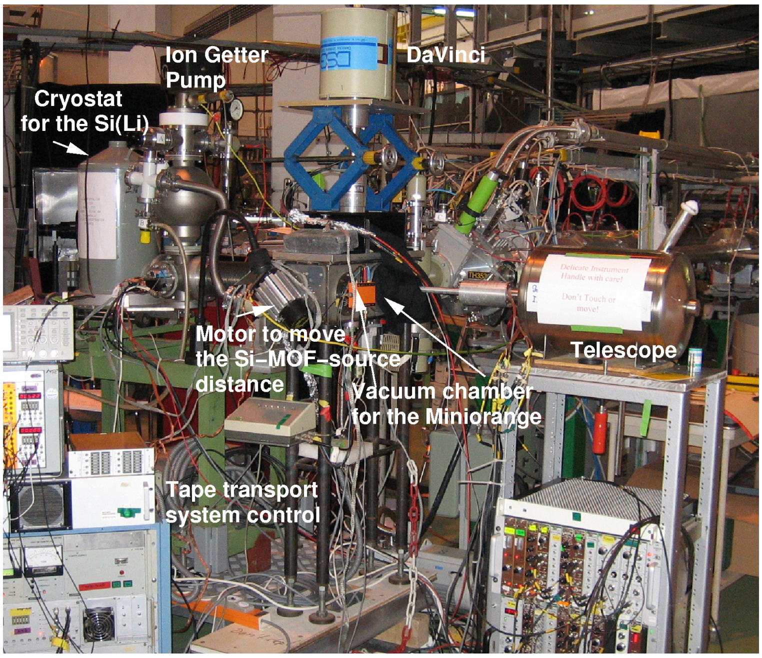

Figure 3.13: Photo of the setup used for electron conversion and γ-γ coincidence measurements.

With magnetic spectrometers one makes use of the different magnetic rigidity, Bρ, of the electron which is directly connected to its momentum. The spectrometer is used as a lens which focuses the electrons of interest on a focal plane where the electron detector is located, for instance a Si(Li) detector. Through changes of the intensity of the magnetic field generated by the spectrometer, the whole electron spectrum can be measured since only electrons with a certain energy emitted from the same source point will be focused and detected whereas the rest will be defocused. In addition, in β^+-decay experiments the positrons will be bent away from the detector thus avoiding a huge background otherwise.

This is the basis of how our mini-orange spectrometer (MOF) works [82, 83, 84] and is shown in the upper left part of Fig. 3.14. Electrons (positrons) from the source are bent towards (away from) a cooled Si(Li) detector by the toroidal magnetic field generated by wedge-shaped permanent magnets arranged symmetrically around a cylindrical plug, made of Tungsten with a density of 18 g.cm^{-2}. This plug prevents photons and particles from reaching the Si(Li) directly. The magnets are made of SmCo$_5$ and come in two shapes which are shown in the upper part of Fig. 3.14. The electron transmission is determined by the number and type of magnets, the distance from the source to the front face of the mini-orange and the distance from the source to the Si(Li) detector, all of which can be varied. This can be achieved with the use of a movable table along the z-axis built at GSI and connected to a motor which can change the position with a precision of 0.1 mm controlled by an electronic micro-chip. Each configuration can be classified by nX/d/f where n is the number of magnets of type X (see Fig. 3.14), d is the distance from the source to the mini-orange front face and f is the distance from the source to the Si(Li) detector as shown in Fig. 3.15. The distances are in mm. The transmission for each configuration must be determined empirically. Figure 3.15 shows a horizontal cross-section through the whole apparatus. The mass-separated beam from a mass separator, in this case the GPS at ISOLDE, is deposited on to a tape, which is moved at predetermined intervals to place the accumulated activity in front of the mini-orange. This tape transport system is part of the mini-orange setup and works similarly to Desdemone, the tape described previously. It was designed at GSI and adjusted to the beam line of ISOLDE to perform these measurements.

One of the principal features of this mini-orange system was that Barden went to some effort to ensure that the front face of the Si(Li) detector stays clean. In other words, that chemical contaminants in the vacuum do not condense on the cold face of the detector. This condensation is a typical problem in other spectrometers of this kind where the resolution deteriorates after a few hours of running. This improvement was achieved by the arrangement shown schematically in Figs. 3.15 and 3.16. As stated above, the details of how this was done are given in his thesis. Here only the essential elements of the apparatus are described. The main chamber housing the mini-orange, marked III in the figures, can be separated from the rest of the system by a valve marked V. The rest of the system is divided into two compart-

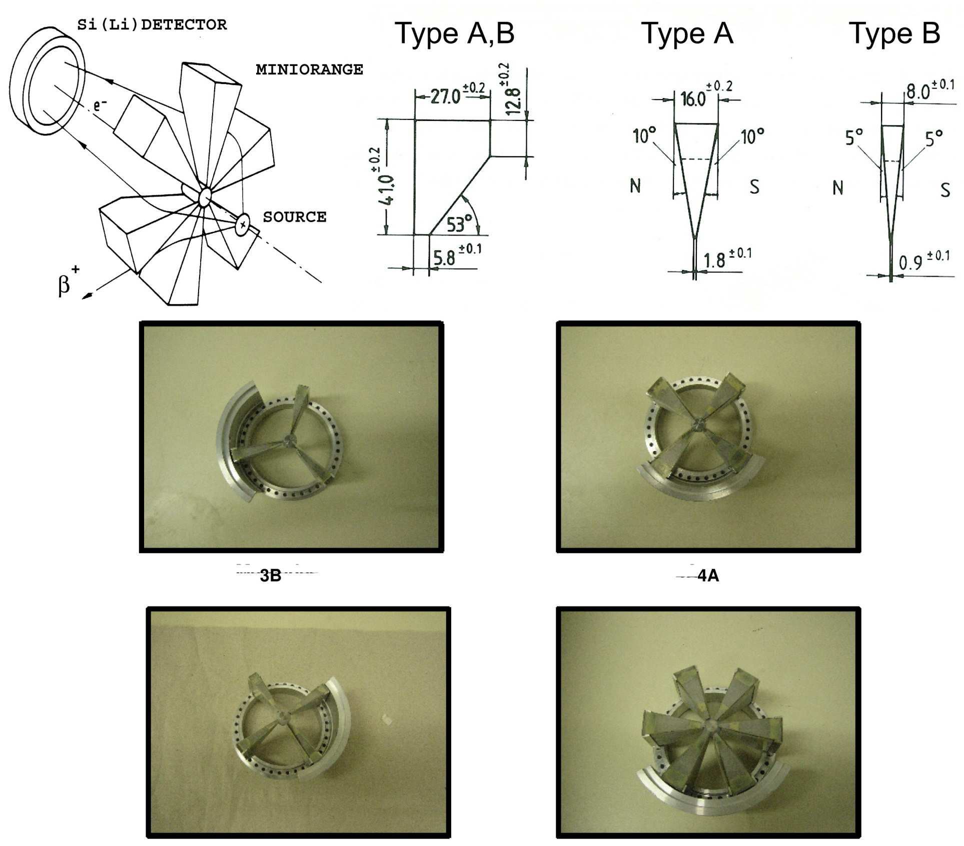

3B

4A

4B

6A

Figure 3.14: In the upper part of the figure an schematic picture of how the mini-orange works and the two types of magnets, A and B, are shown. The lower part of the figure shows a photograph of the different sets of magnets used in this work. The notation used is nX where n is the number of magnets and X is the type, A or B.

ments marked I and II. In the former the Si(Li) detector sits on the end of a cold finger held at liquid N_2 temperatures during operation. A window of polyethylene, aluminised on both sides, with a thickness of 260 μg cm^{-2} separates I and II. The Si(Li) detector is only cooled down once the vacuum in I has reached 10^{-7} mbar. This vacuum is achieved in two steps. Initially a vacuum of 10^{-4} mbar is established in the whole volume including I, II and III using a standard cryopump system. At this point I and II are connected by Valve W. Once the vacuum of 10^{-4} mbar is reached, this valve W is closed, an ion getter pump is started and a cold trap on the pumping line to I is filled. Now the vacuum of 10^{-7} mbar is established in I and this compartment is kept isolated during the measurements. Since the window in front of the Si(Li) is fragile it is important that the vacuum in II is maintained throughout the measurements. This could be done with the help of Valve V which was closed

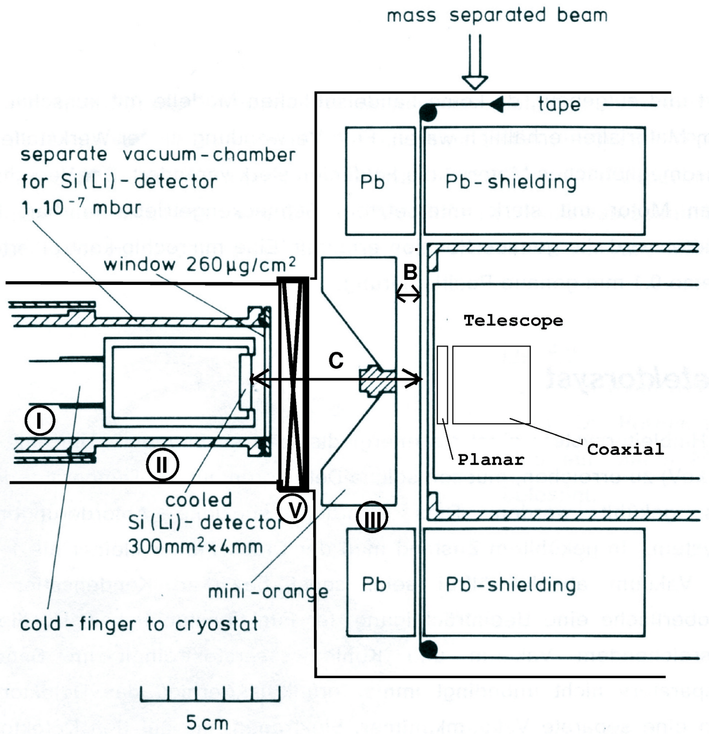

Figure 3.15: A sketch of a horizontal cross-section through the experimental setup for the conversion electron studies with the mini-orange spectrometer [81]. The mass-separated source is deposited on to a tape, which is moved periodically to place the accumulated activity in front of the mini-orange and the Ge telescope (see text). These two detectors sat at 180 degrees to one another with the source in between as shown. A co-axial Ge detector was positioned above the source at right angles to the telescope and is not shown in the figure. The distances B and C are the distances from the source to the front face of the mini-orange and the Si(Li) detector respectively. This nomenclature is used to classify the various mini-orange setups used in the experiments as can be seen in the text. It is consistent with other measurement carried out with the same spectrometer by Barden [81] and Bea et al [85]. The various independent volumes in the apparatus (see text) are marked I, II, and III respectively. There is a valve between I and II which is not shown in the figure and a valve marked V which is used to isolate II from III, the main mini-orange chamber.

every time the mini-orange chamber had to be opened. This was needed often in order to change the magnets or place calibration sources inside the chamber.

In this experiment, the transmission from the output of the separator to the experimental setup was 75%. Only one type of magnet was used, namely the B type

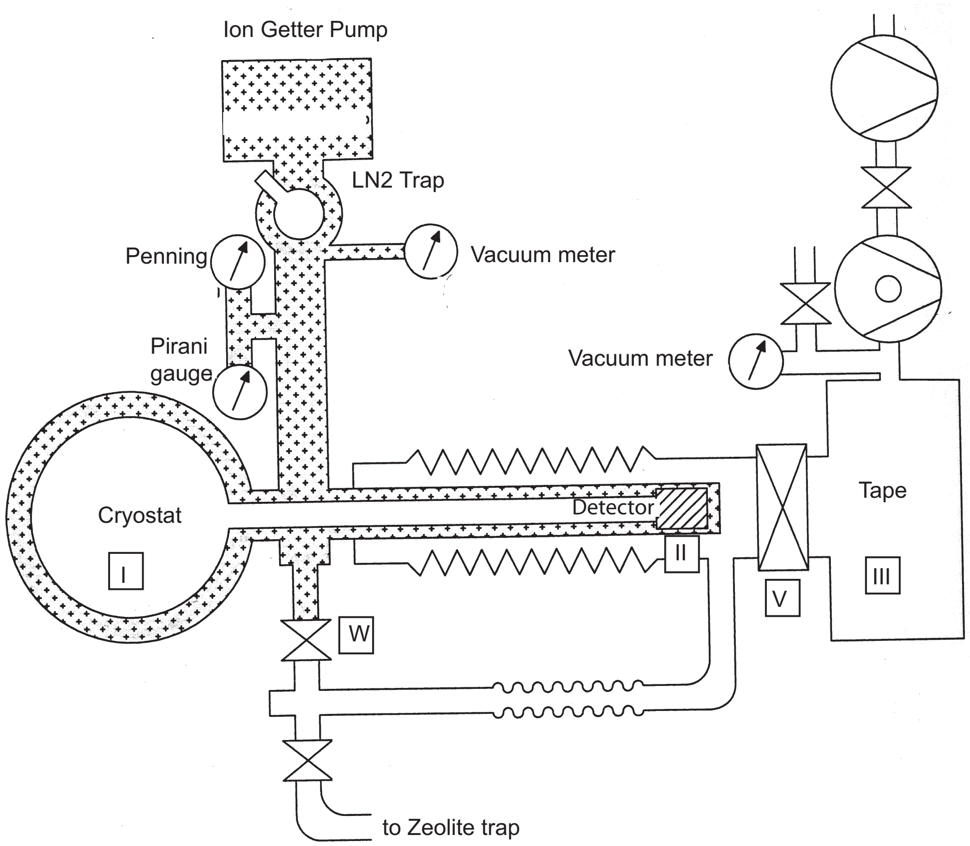

Figure 3.16: A schematic picture of the mini-orange and its associated vacuum system. The different independent volumes have been labeled as I, II and III. Valve V isolates the volume II from III, whereas Valve W is used to isolate the volume I from the rest of the system. This vacuum configuration (see text) ensures that the front face of the Si(Li) detector remains clean during the measurements since the volume I can be kept under a very high vacuum.

shown in Fig. 3.14. A Ge telescope was placed at 180 degrees to the mini-orange. This telescope consists of a planar Ge of 10 mm thickness and a front face of 50.5 mm diameter with a co-axial detector of 20% efficiency placed 12 mm behind it. This telescope has a Be window of 300 μm thickness in front of it to allow low energy photons to enter with the minimum absorption. In addition to the telescope a 70% efficiency co-axial Ge detector sat directly above the source and at right angles to the telescope. Table 3.3 shows the volume, resolution and energy range of the Ge detectors involved. Table 3.4 shows the cycles used for the measurement of each isotope. During the time that the tape was moving the counting was inhibited for 170 ms and the beam gate of the GPS closed to prevent activity being deposited along the tape.

Table 3.3: Ge detectors used in the third experiment in conjunction with the mini-orange spectrometer. Their volume, energy resolution and energetic range covered are listed. The Planar and the co-axial 20 are part of a telescope arrangement and have a common cryostat (see text).

Detector	Volume	Resolution (keV)	Energy range
Planar	19.5 cm^3	0.6 at 121.8 keV	7-980 keV
Co-axial 20	93 cm^3	1.9 at 1332 keV	35-4300 keV
Co-axial 70 (DaVinci)	166 cm^3	2.1 at 1332 keV	40-4100 keV
Si(Li)	300 mm^2 x 4 mm	1.2 at 121.8 keV	5-530 keV

Table 3.4: The half-life and the time settings for the tape cycle, where T$_c$ and T$_m$ are the collection and measurement times respectively, are listed. The number of protons used for the production of each isotope is also shown. The isotopes marked with * were used for calibration purposes since their conversion coefficients are well established [86][87][88]. The comments have the following criteria: (a) Measured with the magnet configuration 3/8/125.(b) Measured with the magnet configuration 4/8/125. (c) Measured with the magnet configuration 6/8/85. (d) Measured with the magnet configuration 6/8/125.

Isotope	Half-life (s)	T$_c$ (s)	T$_m$ (s)	N$_p$	Comments
^{77}Sr	9±2	15	15	6	b,d
^{77}Rb*	226.2±2.4	0.5	480	1	a
^{78}Sr	159±8	230	230	1	a,b,c,d
^{79}Sr*	135±6	120	120	2	a,d
^{79}Rb*	1374±30	0.3	2400	1	a,b,c,d

The electron spectrum and the corresponding γ-ray spectra were recorded simultaneously. Coincidences and direct spectra were recorded. ^{133}Ba and ^{152}Eu were used as standard sources for absolute efficiency calibrations of the γ-ray detectors.

3.5 Electronics

The electronics used for the three setups described previously is quite similar and consists of two complementary circuits which will be explained in detail below. In all the experiments the data were recorded in two different modes: directly without using any further conditions, the so-called singles, and in coincidence. The latter were recorded in a secuential event by event mode (Listmode) in a digital linear tape (DLT). We shall start with the high-resolution setup since it presents a simpler example from which the other two setups can be derived easily.

3.5.1 SLOW ELECTRONICS (ENERGY CIRCUIT)

High-resolution setup

A simple and identical circuit is used for the 3 germanium detectors consisting of a linear spectroscopic amplifier (SA) with high stability. The amplitude of the signal from the detector is proportional to the energy deposited by the γ-ray and after amplification by this module, it is used as an input for two Analogue to Digital Converters (ADC). The first ADC registers the direct spectra (singles). Its output is connected to the CAMAC histogramming memory where these data are stored on disk in 8 kBytes spectra. The other ADC only registers those events which are validated by a simultaneous activated signal, the master gate (GAI), which comes from the time circuit which will be explained in detail in the next section.

The Valencia group developed a data acquisition system control using ROOT graphical interface, which enables both the energy spectra of each validated event by the master gate and the singles stored on disk to be visualised on-line. This on-line control system is essential to check the counting rates, resolution and possible breakdowns of the voltage supply of the ISOLDE separator among other things.

TAS setup

The electronics were controlled from a Multi Instance Data Acquisition System (MIDAS) Control [89] designed by the Strasbourg group which uses a VME processor. The VME crate controller is commanded by a graphical user interface which in principle has the same functions as the system from Valencia and allows the recording of the spectra in the two different ways described before: a direct spectrum for each detector with no further conditions for the acquisition (singles) and coincidence events, where the data are stored continuously on tape requiring the validation of an event.

The slow electronics is similar to the previous setup. The TAS detector has three outputs. Two of them come from the dynode of the PMT which are used for energy measurements. One of these dynode outputs is summed with the other seven dynode signals coming from each of the PMTs of the TAS. The third output comes from the anode of the PMT and is also summed with the other 7 anode signals of the other PMTS for timing measurements, which are part of the fast electronics.

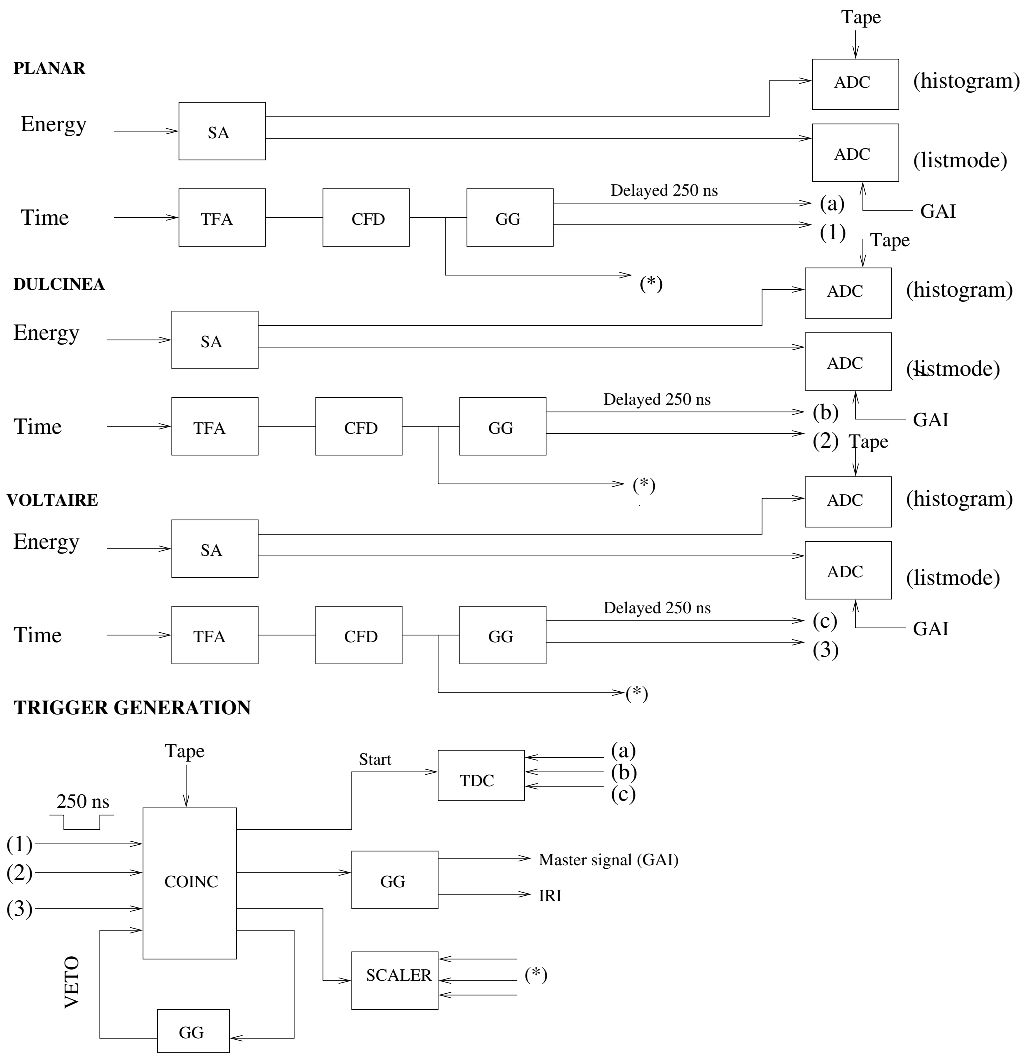

Figure 3.17: Schematic diagram of the slow and fast electronics circuit for the high-resolution setup. The labels that appear correspond to: constant fraction discriminator (CFD), Coincidence module (COINC), Fan-in/Fan-out module (FAN IN), Gate/Delay generator (GG), spectroscopy amplifier (SA), Time Digital Converter (TDC) and Timing filter amplifier (TFA).

Mini-orange setup

The data acquisition system developed by the Valencia group was used to perform the measurements in this experiment. The layout of the slow electronics circuit is similar to that of the high resolution setup but in this case there is an additional Si(Li) detector for electron detection.

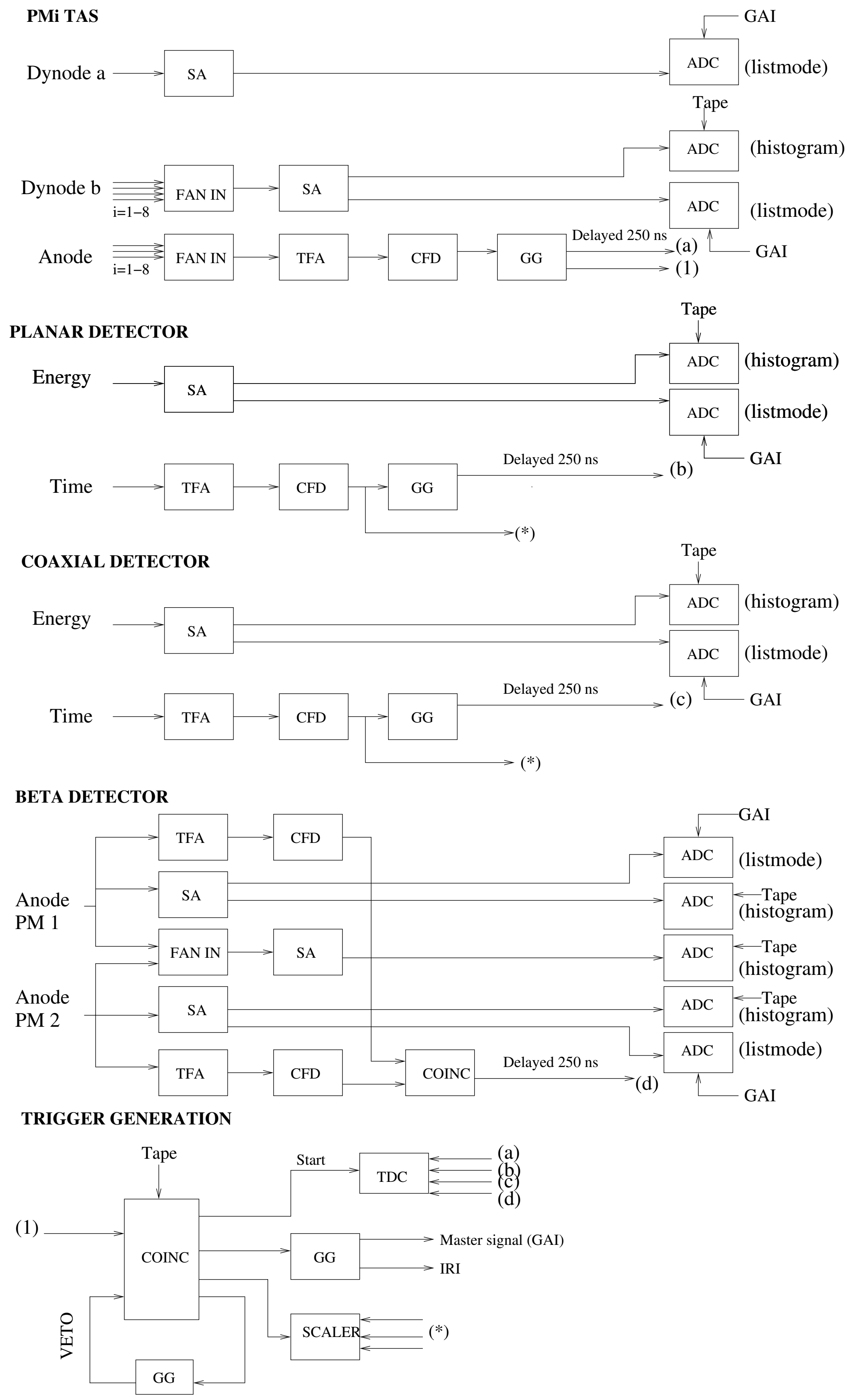

Figure 3.18: Schematic diagram of the slow and fast electronics circuit for the TAS setup. The labels are defined in Fig. 3.17.

3.5.2 FAST ELECTRONICS (TIMING CIRCUIT)

High-resolution setup

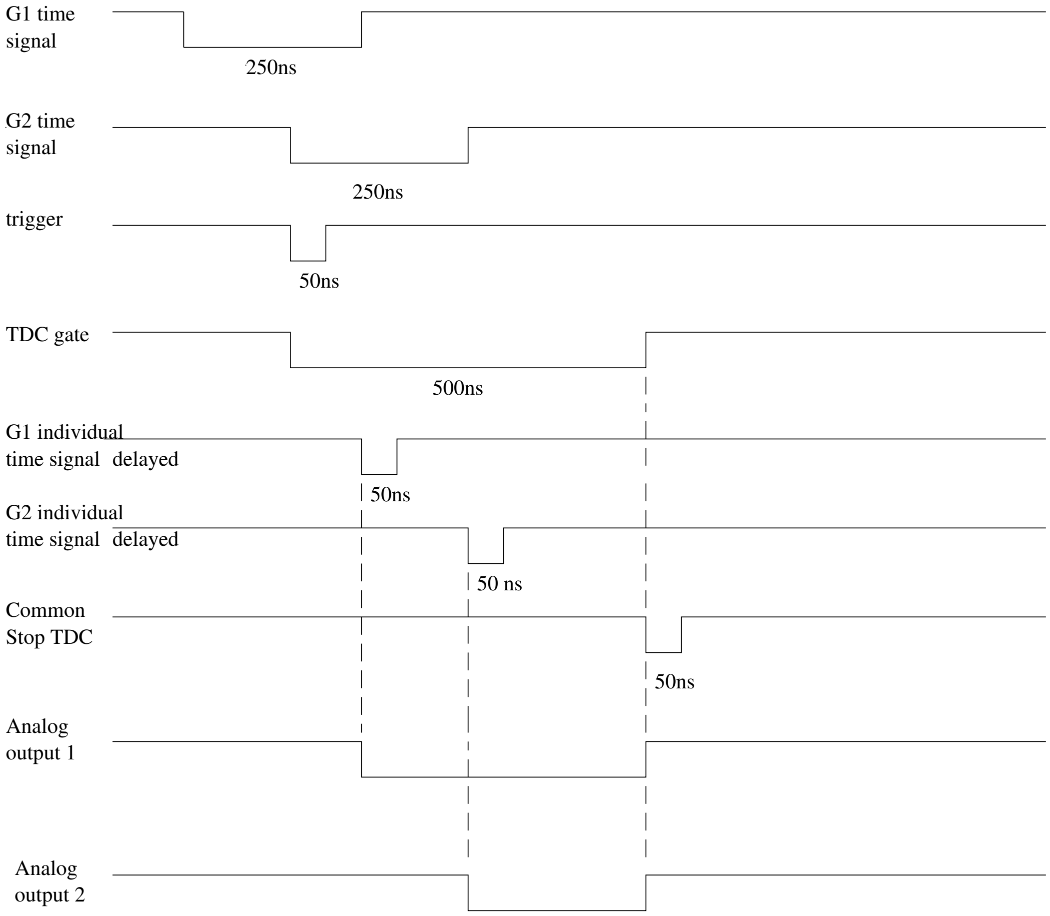

Figure 3.19: Time sequence of the pulses in the coincidence electronics.

This part of the electronics establishes the coincidence between 2 or more γ-rays which acts as a trigger for the start of the acquisition. Once there is a detection of a γ-ray in the germanium detectors a fast signal is generated and converted into a logic NIM signal with a width of 250 ns. The coincidence condition is fulfilled when one time signal of 250 ns (G_1 time signal in fig. 3.19) overlaps with a second time signal, also of 250 ns (G_2). A trigger signal is produced provided that the tape transport system is not moving and the system is not busy processing a previous validated cycle. The coincidence window is therefore 250 ns and when a coincidence has been detected and the event validated, a start signal is produced in the TDC (Time-to-Digital-Converter) at the time of the arrival of G_2 opening a TDC gate of 500 ns. The individual time signal for each detector is delayed 250 ns to make sure that they arrive within the time the TDC is open. This signal will be the input of

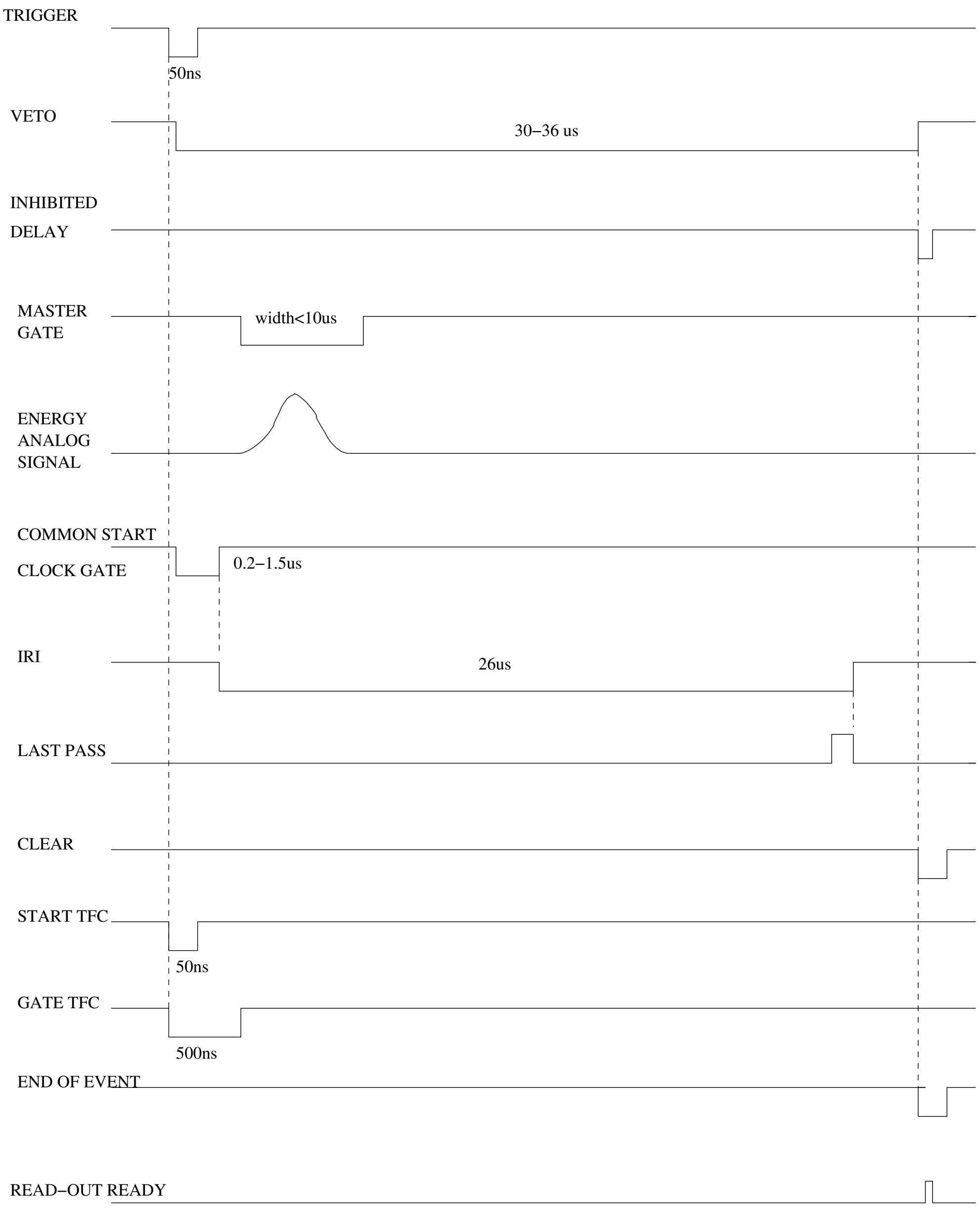

Figure 3.20: Chronogram of the sequence of an event.

the TDC which operates in common stop mode as shown.

Once there is a valid trigger, the encoding cycle is started without any further condition and a new trigger signal is immediately inhibited by a gate of $\approx 30\ \mu$s which acts as a veto for the system (VETO signal). This VETO must be adjusted so that all the CAMAC modules (ADCs and TDCs) have time to convert the data and go through the so called daisy chain in the protocol FERA(Fast Encoding and Readout ADC). It must also take into account the time it takes the system to write in memory, which depends on the number of parameters used in each event, and is the main responsible for the deadtime of the acquisition system. After the validation of the trigger, a master gate is generated (GAI) with an adjustable delay of a few microseconds so that all the analogue energy signals are within this gate.

For the tagging of the event, a start signal is sent to the clock and to the TDC, namely a TFC (TIME-TO-FERA converter), immediately after a trigger is received in order to time-stamp the event and start the time measurement respectively. The clock module is the fastest part of the system and it is read out almost immediately.

As soon as the master gate is generated, the FERA driver which controls the daisy chain sends a "readout request" (REO) through the bus control to the first module and the readout cycle is initialized. An additional gate called IRI is generated after this master gate to inhibit the writing in memory by the FERA driver before all the CAMAC modules have converted. The last PASS signal generates the CLI (Clear Input) in the FERA driver and the system is then ready to accept a new trigger. If, for any reason, there is no last PASS signal out of the TFC, a clear signal is automatically generated at the end of the VETO signal and resets the system to accept a new trigger. This clear signal is also sent to the clock module as an end-of-event marker in the data stream.

TAS setup

The electronics is almost identical to the one described above. In this case the number of input parameters is higher and the VETO signal is increased to 80 μs so that the readout cycle and the time it takes the Fera Driver to store the data in memory are within this gate. The IRI signal is also increased as there are more CAMAC modules which must process the data. The hardware sum of the anode signals of the 8 PMTs of the TAS acts as a trigger for the system in this case.

Mini-orange setup

The electronics is almost identical to the high-resolution setup and only the number of input parameters. A coincidence between the DaVinci detector with the co-axial detector or with the planar detector acts as a trigger for the system.

Chapter 4

The decay scheme of ^{78}Sr

In this chapter the results of the analysis of the measurements on the decay of ^{78}Sr with the high resolution and mini-orange setups in 2004 and 2006 respectively are reported. The information obtained can be summarised as follows:

- The half-life of the ^{78}Sr ground state.
- Energies and relative intensities of the γ-ray transitions observed in the β-decay of ^{78}Sr.
- Internal conversion coefficients obtained from the electron spectra measured with the mini-orange.
- Spin and parity assignments to levels in ^{78}Rb.
- The decay scheme of ^{78}Sr.
- Beta feeding and log ft values for transitions to levels in ^{78}Rb.

The extracted properties of the levels in ^{78}Rb have been compared with calculations based on deformed Hartree-Fock with Skyrme interactions and pairing correlations in the BCS approximation. This has allowed an interpretation of the nature of the observed sets of levels in the odd-odd nucleus ^{78}Rb.

4.1 The previous level scheme

Very little was known about the ^{78}Sr β-decay scheme prior to this work. The measurement of the half lives of different γ-ray transitions observed in the β-decay of the daughter nucleus ^{78}Rb by Bavaria et al. [78, 88] suggested that this decay proceeds both from an isomeric level, ^{78m}Rb ($T_{1/2}$=5.74±0.05 min), as well as from the ^{78g}Rb ground state ($T_{1/2}$=17.66±0.08 min) as shown in Fig. 4.1. The nuclear spins and magnetic moments of ^{78}Rb were measured by Ekström et al. [90] by atomic-beam magnetic resonance techniques at ISOLDE resulting in a spin of I=0 for the ground state and I=4 and μ_I=2.56 for the isomer. The β-decay measurements on ^{78}Rb by Bavaria et al. strongly favoured 0^+ and 4^- parity assignments for the ground state and isomer respectively, which were in good agreement with the Nilsson model configurations proposed by Ekström et al.

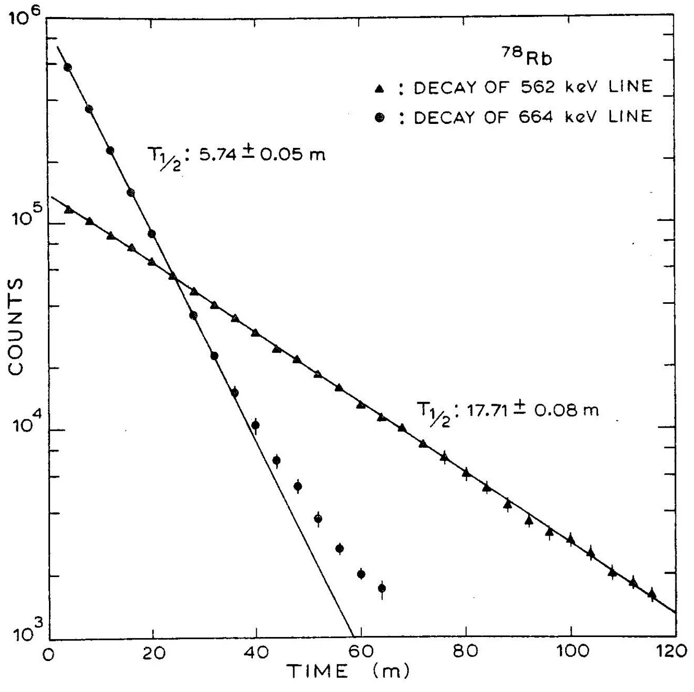

Figure 4.1: Two transitions in ^{78}Rb→^{78}Kr β^+-decay illustrating isomeric and ground state component lifetimes of 5.74(5) min and 17.71(8) min respectively. Data taken from Bavaria et al. [78].

There appears to have been only two previous studies [91, 79] of the β^+/EC decay of ^{78}Sr. The first study was carried out by Grawe et al [91]. ^{78}Sr was produced at ISOLDE following a similar reaction to the one in our work. The half-life of ^{78}Sr was measured and established as 159(8) s. Fifteen gamma-ray transitions, five of them already observed [92, 93], were identified using a Ge detector. Because of the lack of coincidence data, no definite decay scheme could be proposed for ^{78}Sr. A more comprehensive work was performed years later by Mukai et al [79]. They studied γ-ray singles and coincidence spectra in the beta decay of ^{78}Sr and also studied the in-beam γ-rays from the ^{54}Fe(^{28}Si,3pn)^{78}Rb reaction. Two Ge detectors for γ- and X-ray detection were used. Due to the small size of the X-ray detector, γ-γ coincidences involving transitions of high energy were not possible. In their β-γ experiment the recoil reaction products were accumulated on a lead-coated plastic tape transport system. Using the γ-γ coincidence technique, they constructed a simple decay scheme showing 15 γ-ray transitions and six excited states in ^{78}Rb populated in the decay. Their short paper indicates that the 5.74 min isomeric state in ^{78}Rb at 111.2 keV excitation energy was populated directly in their study since they observed that the measured decay curve for the 103.2 keV γ-ray is influenced by its being populated in the isomeric decay as well as in ^{78}Sr decay. They were not able to see the linking transition from the isomer. Some spin-parities were assigned based on the transition intensities and previously published papers [78, 90].

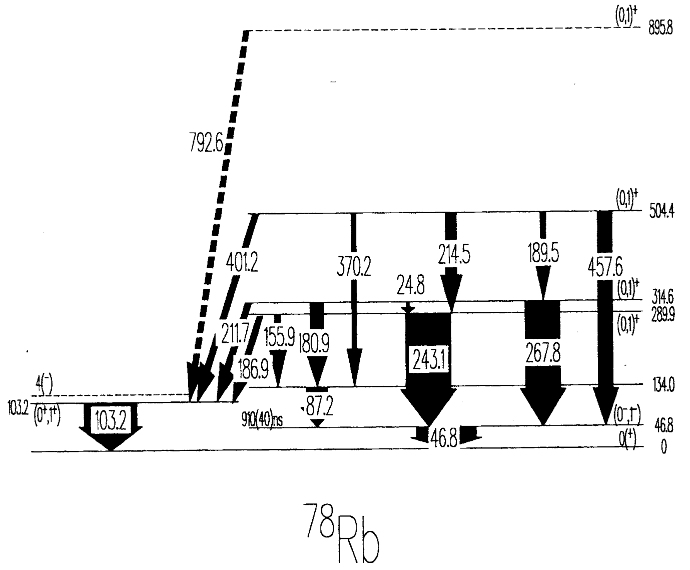

Figure 4.2: Low-lying level scheme of ^{78}Rb from Reference [79]. The authors have not included the information on the excitation energy of the isomer and it is given as "x". They predict the energy of this linking transition to be lower than the binding energy of the K$_\alpha$-shell (~13keV) since the K-conversion peak is not observed. McNeill et al. [94] have found the excitation energy of the isomer to be 111.2 keV with an 8.6 keV highly converted linking transition to the 103 keV level. The same authors have also observed a 64.4 keV transition to the 46.8 keV level from the isomer.

McNeill et al. [94] studied for the first time the isomeric decay of ^{78m}Rb with an in-beam spectroscopy study. They observed a 64.4 keV transition decaying into the 46.8 keV level and concluded that it has M3 character based on the measurement of its internal conversion coefficient (CE). They also observed a highly converted 8.6 keV linking transition between the isomeric state and the 103.2 keV level. Hence, the position of the isomer at an excitation energy of 111.2 keV was established based on these two parallel cascades. They also measured the CE for the 103 keV transition which gave an E1 or M1 multipolarity assignment. However these authors only consider an M1 multipolarity but no further arguments are given to support their statement since an E1 transition is not ruled out. An E1 multipolarity was assigned to the 46.8 keV transition based on the measurement of its CE.

The structure of ^{78}Rb was studied in-beam by Kaye at al. [95, 96]. They reported nine bands based on low-lying levels and also provided information on some of the levels at low spin which are populated in ^{78}Sr decay.

4.2 Data Analysis

As explained in the previous chapter, two different ways to record the data were used: directly, storing the data from each detector continuously (singles), and in list-mode, setting a coincidence window of 250 ns for the validation of an event. The singles from the high resolution setup (see Section 3.3 for full description of its geometry) were used to determine the energies and intensities of the gamma transitions observed in the decay of ^{78}Sr exclusively. Those registered with the mini-orange setup were used for internal conversion studies. On the other hand, the coincidence spectra registered with the high resolution setup were used to create gamma matrices to derive the level sequences and construct the level scheme of ^{78}Sr. A program called *Xtrackn* [97], written in Legnaro, was used for the entire analysis if not said otherwise. It enables the calculation of the area under each peak, the fitting of each peak with a background subtraction and the analysis of the γ-γ coincidence matrices.

4.2.1 Energy Calibration and Efficiency

High resolution setup

The energy and efficiency calibrations were performed using standard sources, namely ^{241}Am, ^{133}Ba and ^{152}Eu. The energy range covered was 26-1400 keV. The centroids of the highest photopeaks in the spectra were determined using a Gaussian fit with a first-order polynomial background subtraction. For the case of the planar detector, a more complex fit was needed since an exponential tail on the left part of the photopeak can be seen due to incomplete charge collection in the detector. In this case, the *TV* analysis program written at the University of Cologne was used [98].

In order to obtain the energies of the transitions, a calibration with energy versus channel is performed using the following expression:

$$E = a_0 + a_1 chan + a_2 chan^2 \tag{4.1}$$

This energy calibration function is a second order polynomial used to correct any possible non-linear behaviour of the electronics, though a_2 is very small in practice.

The intensities of the peaks can be obtained by applying the following relation:

$$Intensity = \frac{Area}{Efficiency} \tag{4.2}$$

The efficiency curve versus energy for a Ge detector is a combination of 2 different phenomenological functions namely:

- For E≥60 keV Jackel et al. [99] proposed the following function:

  $$ln\epsilon(E) = \frac{2}{\pi}.(b_1 + b_2x + b_3x^2).arctan(exp(b_4 + b_5x + b_6x^2)) \tag{4.3}$$

  with χ=lnE

- For E≤60 keV Debertin et al. [100] proposed the following:

  $$\epsilon(E) = b_1exp(b_2E^{b_3}(1 - exp(b_4E^{b_5}) \tag{4.4}$$

where the condition is that the final function must be continuous at E=60 keV.

For the efficiency calibration the standard sources were placed in exactly the same position as the ^{78}Sr source during the experiment. The relative intensities of the photopeaks, the source activity and the time of the measurement were known which allowed one to obtain an absolute efficiency calibration. In Fig. 4.3 the adjusted efficiency curve for Voltaire and Dulcinea is shown together with the experimental points and their error bars. The fit was made according to the proposed phenomenological functions.

The planar detector was strongly affected by the summing, which meant that it was impossible to calibrate it in absolute efficiency by means of standard sources. The coincidence summing occurs when the nucleus emits 2 or more simultaneous γ-rays which enter the same detector. The effect depends primarily on the characteristics of the detector, the geometry and the decay scheme. The summing effects are likely to happen in close geometries where the source-to-detector distance is small and when the detectors are large, which is the case for the planar detector in this set-up. The additional coincidence-summing effects due to X-rays (from electron capture or internal conversion) cannot be neglected when the detectors used are very sensitive to low energies. Other sorts of radiation, which could also be in

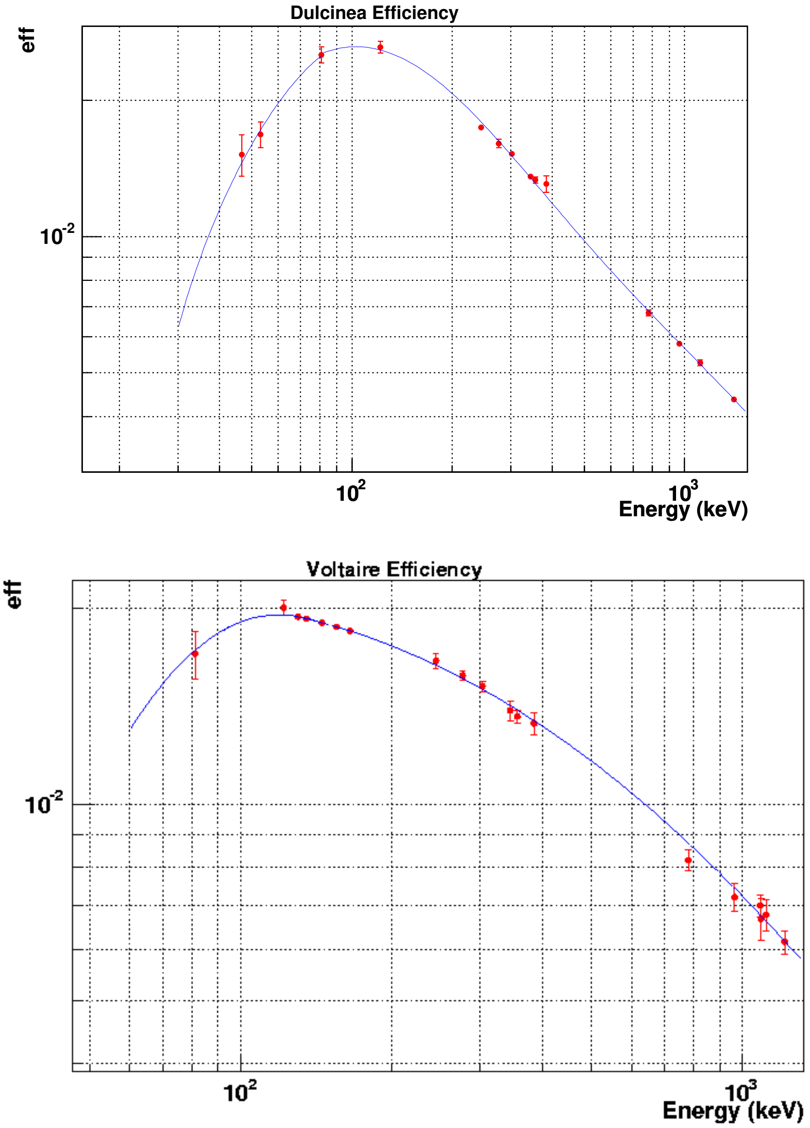

Figure 4.3: Photopeak efficiency as a function of energy for Dulcinea and Voltaire.

true coincidence, include the bremmstrahlung associated with beta particles and the annihilation radiation from positron decay. Therefore they must also be taken into account. In our case, other causes such as random summing effects were negligible since the counting rates were low.

An example of coincidence summing occurs when the first photon in a cascade from a level loses all its energy in the Ge detector and one of the following γ-rays from the same cascade is also detected leading to the recording of the sum pulse. This event will not be recorded in the full energy peak of the first photon but in the sum of the energies of the two photons. Therefore, if the efficiency of the detector has been determined as a function of energy by means of standard sources, coincidence-summing corrections must be applied in order to obtain accurate gamma intensities in the analysis of a level scheme.

The correction factors to the experimental intensities, when summing effects occur, were calculated by a Fortran code written by J.L.Tain. The method used is based on a general formula for complex decay schemes given by Andreev et al [101]. This formula takes into account coincidence summing of γ-rays with X-rays following internal conversion and the 511 keV emitted in positron annihilation. The assumptions made were the following: bremsstrahlung can be neglected, β-radiation is absorbed in the detector window and γ_1 and γ_2 with energies E_1 and E_2 respectively are emitted within the resolving time of the germanium detector with no angular correlations between them.

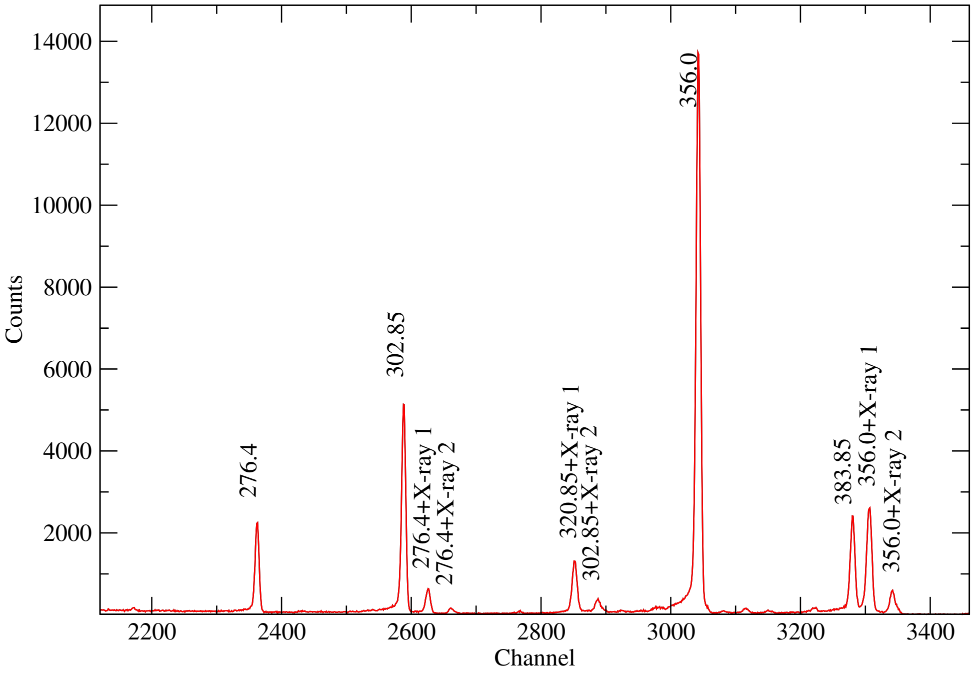

Figure 4.4: Illustrated summing effect for the measurement of ^{133}Ba with the planar detector.

In the case of our planar detector, the summing effect is around 20 per cent at 224 keV and it is shown in Fig. 4.4 for the measurement of ^{133}Ba. Correction for this effect was essential in order to determine accurately the intensities of the different γ-rays emitted in the decay of ^{78}Sr$\rightarrow$^{78}Rb. Therefore, the losses in the different emission lines must be taken into account. The following information must be known in order to apply the correction method described:

- The level scheme of the nucleus to be studied.
- The absolute total and photopeak efficiencies of the detector.
- The internal conversion coefficients for each transition.
- The β^+/EC ratio which establishes the probability of summing with a 511 keV photon coming from the positron annihilation or with an X-ray.

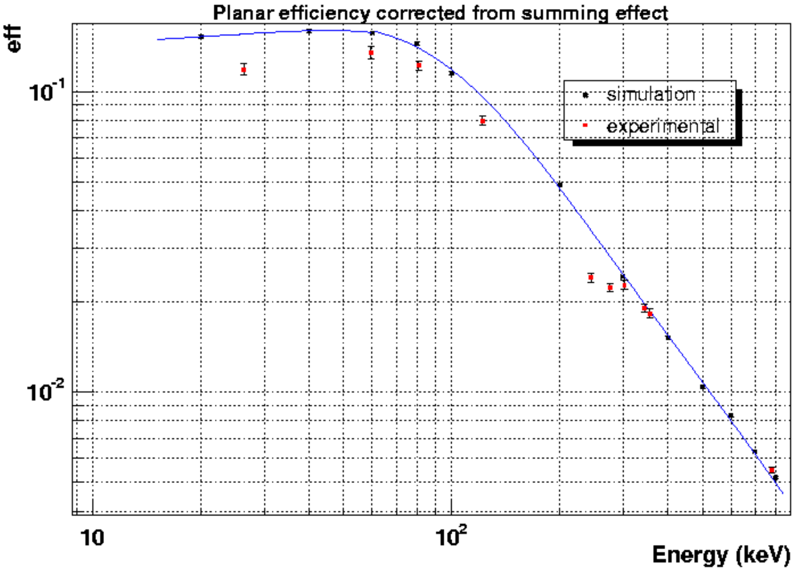

Figure 4.5: The continuous line is the simulated photopeak efficiency of the planar detector. The points correspond to the photopeak efficiency calculated by means of ^{133}Ba and ^{152}Eu sources without summing correction.

The absolute total and photopeak efficiencies were determined by simulating the response of the detector with *GEANT4*. Once obtained, the summing correction was done for ^{133}Ba, a well known γ-source, to check how well the intensities were reproduced. Table 4.1 shows the corrected intensities after the application of the summing correction. A 10% discrepancy appears between the values obtained and those from the literature [102].

Table 4.1: Gamma intensities of ^{133}Ba corrected from the summing effect in the planar detector. The values from the literature [102] are shown for comparison.

Emission lines (keV)	Uncorrected intensity	Corrected intensity	Literature value
81.0	49.746	50.931	51.20
79.6	3.646	3.925	3.77
383.9	18.082	15.319	14.50
302.9	26.128	26.635	29.20
356.0	100	100	100
276.4	9.505	10.133	11.30

Mini-orange setup

A similar procedure was performed in terms of energy calibration for the electron and gamma spectra registered with the mini-orange setup (see Section 3.4 for details on this specific setup). Open standard sources of ^{133}Ba and ^{152}Eu were used and placed at the measurement position covering a range of 81-1410 keV in total. The determination of the centroids and area under the peaks was rather complex in the case of the Si(Li) detector. A fit using an exponential tail in combination with a Gaussian and a linear background was performed in the simplest cases using the *TV* program. In many other cases the overlap of different peaks and the background lead to the need to use a more sophisticated fit. In those cases a fitting program designed for such a purpose by L.M Fraile [103] was used.

In terms of efficiency calibration several problems were encountered. The planar detector suffered from fluctuations in its detection and stopped acquiring data randomly without an apparent cause. In what follows the planar detector will not be used for the CE measurements. This is discussed further in Section 4.5. On the other hand, it is strongly affected by summing and an efficiency calibration can be only obtained via Montecarlo simulations. Figure 4.2.1 shows the efficiencies of both the planar and the co-axial detectors. The former has been calculated using *GEANT4*. In the case of the third Ge detector, DaVinci, it could not be calibrated in absolute efficiency since the data file saved for such a purpose was corrupted. In the analysis of the CE measurement the data from this detector were not used.

4.2.2 γ-γ coincidence matrix

The knowledge of level sequences and transition relations requires gamma-coincidence measurements with two or more germanium detectors exposed to the same radioactive source. The acquisition of this coincidence data is done in list-mode where every event is recorded continuously on tape. The large event samples

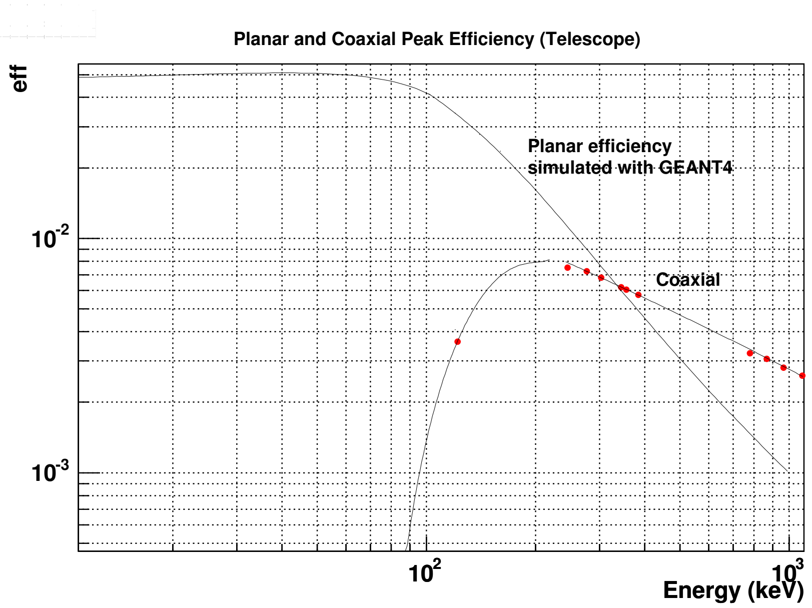

Figure 4.6: Efficiency of the telescope used at the mini-orange station.

(several hundreds of Mbytes) make necessary the use of a particular data storage mechanism. This can be achieved by using the so called NTuples or Ttrees which have been designed to substantially improve access time and facilitate compression of the data, thereby permitting the different events to be interactively processed. In particular, a Ttree is a data structure used by the ROOT Analysis Toolkit designed at CERN [104], which is used in this work. A Ttree can be compared to a table in which each event is a row with different columns representing the different variables. This is much more useful than storing the variables in histograms directly, which would lead to the loss of the exact values of the variables for each event and their correlations. Once the data are stored in this form, 1- or more dimensional projections of any of the n-variables of the events can be made setting different conditions with ROOT. The different variables stored were:

- Clock: used to time stamp the event during the acquisition and reseted after each tape movement.
- Dulcinea: energy signal of the detector Dulcinea.
- Voltaire: energy signal of the detector Voltaire.
- Planar: energy signal of the planar detector.
- TDC-Dulcinea: output signal of Dulcinea from the TDC.
- TDC-Voltaire: output signal of Voltaire from the TDC.

- TDC-planar: output signal of planar from the TDC.

Bi-dimensional spectra called "matrices" are then created, whose axes correspond to the energies (channels) of 2 different detectors and whose height is the number of coincidence events which have occurred. The procedure for the study of the coincidences is the following: all events in one of the detectors (one of the axes of the matrix) are inspected and peak and background gates are set on all peaks of interest. It should be noted for example that a coincidence between $\gamma 1$ and $\gamma 2$ can be detected as $\gamma 1$ in detector1 and $\gamma 2$ in detector 2 or viceversa, allowing the coincidence relations to be found. Once the efficiency of each detector is precisely known, both the analysis of the coincidence spectrum for each γ-ray transition and the knowledge of the gamma intensity enable the level scheme of the daughter nucleus in the decay to be built up. The data used for this procedure came exclusively from the high-resolution setup.

The energy peaks identified were assigned to the decay of ^{78}Sr if a coincidence between them and the Rb X-rays in the planar detector occurred. This removed any γ-rays present in the spectra which belong to the ^{78}Rb→^{78}Kr decay or simply came from background contaminants.

4k⊗4k matrices
Dulcinea⊗Voltaire
Dulcinea⊗planar
Voltaire⊗planar

Table 4.2: γ-γ coincidence matrices built up for the construction of the level scheme of ^{78}Rb.

4.3 The Half-life of ^{78}Sr

The half-life of ^{78}Sr decay was determined with the use of the list-mode data in the experiment with the high resolution setup. The γ-ray spectra from the Ge detectors were recorded with a time stamp which was reset after each tape movement. The step time of the clock used was 65 ms. The data were divided into time bins corresponding to 20 steps of the clock. The peak area of the strongest transitions in ^{78}Rb were measured for each bin in the planar detector and fitted with an exponential function, $e^{-\lambda t}$, where λ is the decay constant and t the time. The resulting curve of the peak area versus time is shown in Fig. 9.9 for the 103.1 keV transition. A value of 155(3) s was obtained for the half-life. Fits to peak areas of weaker gamma lines in the ^{78}Sr decay were also consistent with this value. This agrees with the values of 150(20) s, 170(30) s and 159(8) s given by Liang et al. [92], Hagebø et al. [105] and Grawel et al. [91], respectively.

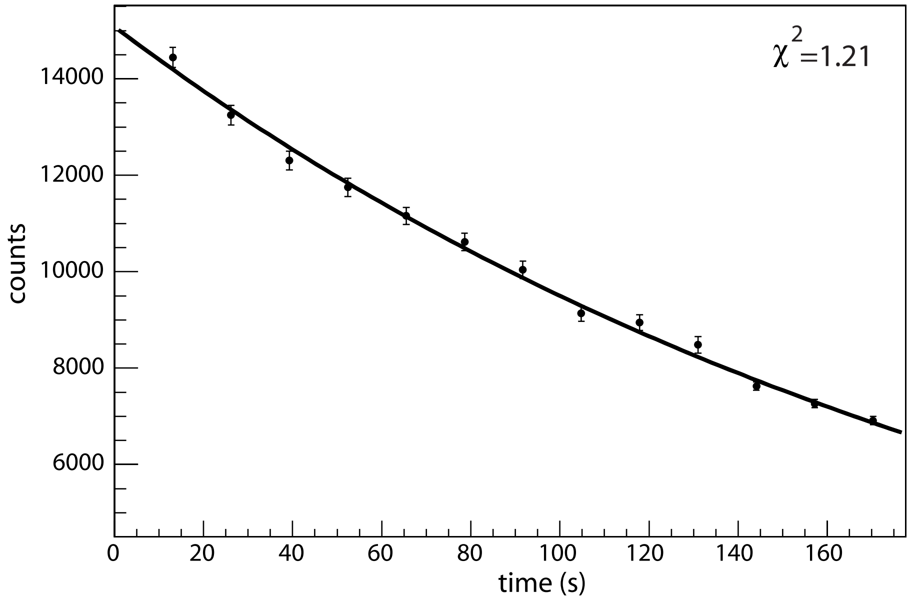

Figure 4.7: A plot of the peak area of the strong 103 keV γ-ray as a function of time measured with the planar detector. The line indicates the best mean-square fit to the data and the reduced χ^2 obtained. This leads to a half-life of 155(3) s.

4.4 Determination of the levels populated in the decay of ^{78}Sr and their γ-ray transitions

The construction of the level scheme is based on the three γ-γ coincidence matrices from the high-resolution setup: Dulcinea$\otimes$Voltaire, Dulcinea$\otimes$planar and Voltaire$\otimes$planar. Figures 4.8 and 4.9 show examples of the recorded coincidence spectra from the planar and Dulcinea detectors. The energies and intensities observed in the decay of ^{78}Sr are listed in Table 4.3 together with the energies of the levels they de-excite. In general the energies and intensities are the weighted mean values derived from the singles spectra from the 3 Ge detectors under the following conditions:

- The transitions with E>800 MeV are only observed in the coaxial detectors.
- Voltaire has a poorer energy resolution, therefore the peak fitting is affected by a larger error in those cases where the contamination with ^{78}Rb is higher. The data from this detector are ignored in the calculation of the weighted mean value for those specific transitions.
- The summing correction, which mainly affects the planar detector, results in a 10% deviation in the intensity. When a high deviation in the intensity of one particular transition measured by this detector is observed in comparison with those given by the other two, it is not taken into account.
- Several γ-ray peaks in the singles spectra that appear to be single transitions are shown by the coincidence data to be complex peaks. The relative intensities of the multiple components are estimated from the coincidence spectra. They are marked with an asterisk in Table 4.4. The energies of the different components are extracted from level energy differences.

The level energies were obtained using a program [106] which uses as an input the energies of all the γ-rays feeding and de-exciting each level. The transition intensities in Table 4.3 are normalised to that of the 103.3 keV γ-ray. Table 4.4 lists the gamma-rays coincident with each γ-ray transition placed in the level scheme of ^{78}Sr β-decay. We have confirmed the 7 excited levels observed by Mukai et al. [79] and the 15 transitions observed by Grawel et al [91]. Moreover, ten of the levels seen in the present work were also observed in the in-beam study by Kaye et al. [96]. In total 16 new levels and 44 new γ-ray transitions have been identified. The decay scheme for ^{78}Sr to levels in ^{78}Rb based on the present work is shown in Figs. 4.13 and 4.14. The figures summarise our knowledge of the γ-ray transition energies and multipolarities as well as the measured feeding in the β-decay and the log ft values deduced from them. It should be noted that the transition intensities are normalised assuming that the total intensity of all transitions feeding the ground state, suitably corrected for internal conversion, is equal to 10,000. The normalization factor between the transition intensities given in Table 4.3 and Figs. 4.13 and 4.14 is 31564.75.

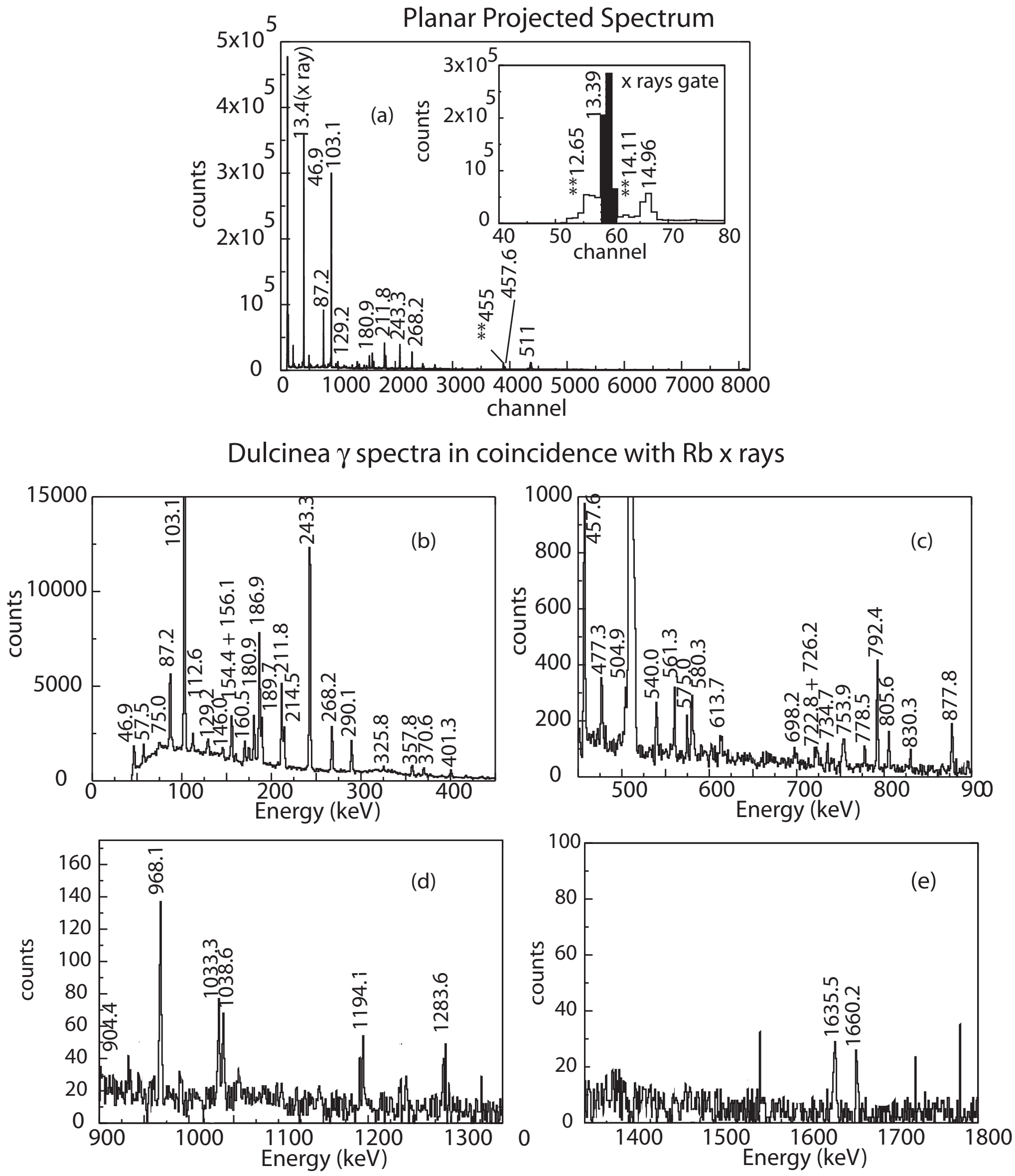

Figure 4.8: In the upper half of the figure is shown a projected spectrum of the γ-rays observed in the planar detector. The peaks are labelled with their energies in keV. Those marked ** are from the decay of the daughter nucleus ^{78}Rb. The inset indicates the gate set on the Rb X-rays which reveals the coincident γ-ray spectrum in Dulcinea shown below. Some random spikes appear on the projected spectrum due to a non-perfect background subtraction. They do not correspond to any γ-ray in ^{78}Rb and are therefore not labelled. Note that the spectrum from Dulcinea is plotted in sections, which are continuations of one another.

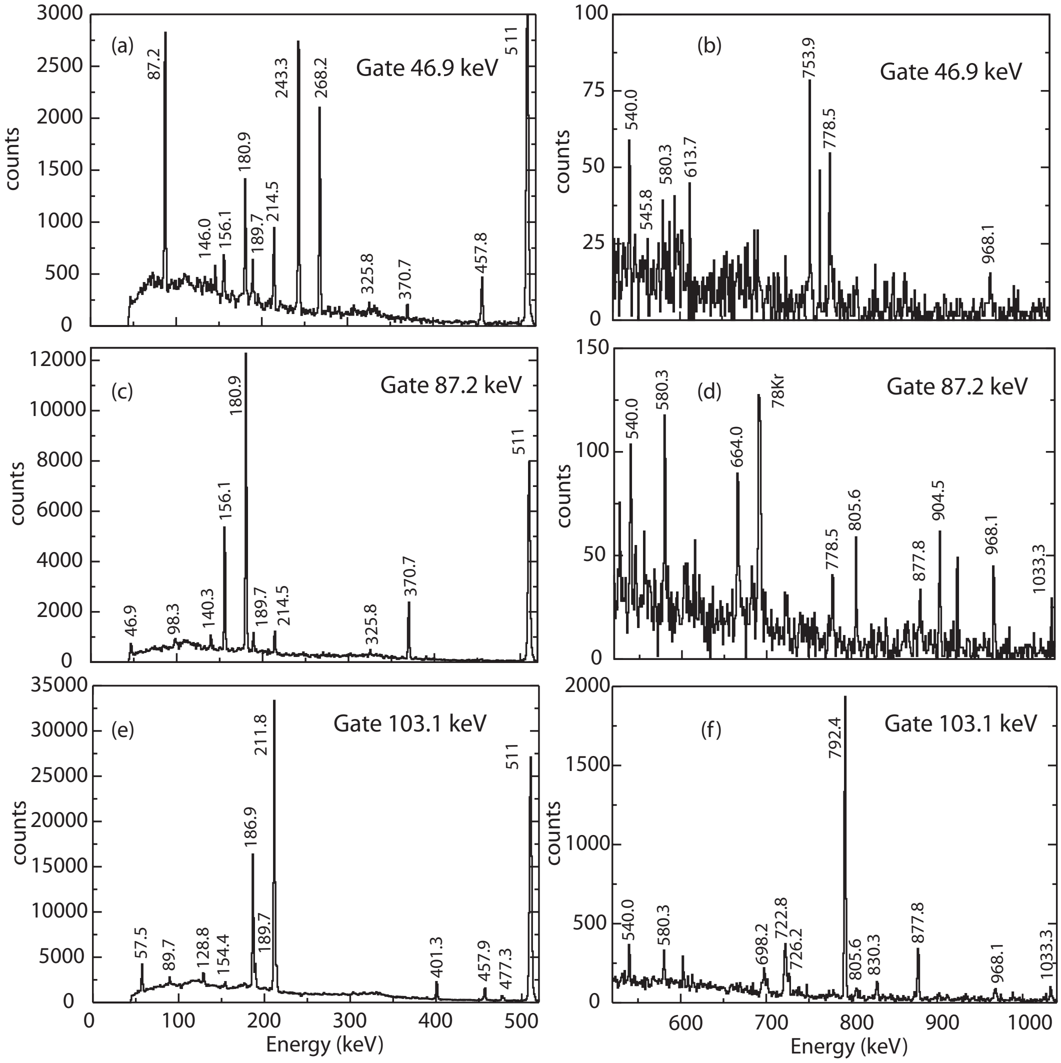

Figure 4.9: Projection of the spectra in Dulcinea obtained by gating on the 46.9 keV (a and b), 87.2 keV (c and d) and 103.1 keV transitions (e and f) in the planar detector. The peak labelled ^{78}Kr in d) is the 693 keV line in ^{78}Kr. This line is in coincidence with Kr X-rays and a previously unreported 87 keV transition in ^{78}Rb decay.

E_γ (keV)	Relative Intensity	E_{level} (keV)	E_γ (keV)	Relative Intensity	E_{level} (keV)
25.0(2)	720(40)	315.2	401.3(3)	570*(40)	504.7
46.9(2)	8900(300)	46.9	457.8(2)	1800*(140)	504.7
57.5(4)	483(8)	160.8	457.9(2)	450*(40)	561.3
62.4(2)	80(14)	255.3	477.3(3)	356(12)	1038.5
75.0(3)(a)	120(30)		504.9(2)	410(30)	504.7
87.2(5)	3030*(90)	134.0	540.0(4)	445(10)	830.1
89.7(3)	96(4)	193.0	545.8(7)	33(7)	801.6
98.3(3)	84(7)	232.3	561.3(2)	1110(40)	561.3
103.1(3)	10000(180)	103.3	575.0(2)	114(6)	830.1
112.6(9)	140(8)	232.3	580.3(2)	305(12)	895.7
128.8(3)	140*(18)	232.3	613.7(4)(a)	517(14)	
129.3(4)	110*(18)	290.2	664.0*(3)	70*(30)	895.7
133.8(2)	156(11)	134.0	698.2(2)	76(6)	801.6
140.2(2)	74(12)	274.2	722.8(2)	389(14)	826.3
146.0(4)	298(8)	193.0	726.2(2)	178(10)	830.1
154.4(4)	144(5)	315.2	734.7(2)	89(6)	895.7
156.1(2)	795(15)	290.2	753.9(3)(a)	318(18)	
160.5(4)	300(12)	160.8	778.5(3)	290(17)	1283.4
170.4(3)(a)	390(30)		792.4(2)	878(17)	895.7
175.6(4)(a)	340(20)		805.6(5)	210(20)	1038.5
180.9(3)	1980(30)	315.2	830.3(2)	191(9)	933.7
186.9(6)	2360(30)	290.2	845.5(3)	59(15)	1038.5
189.7(4)	1255(12)	504.7	877.8(3)	309(8)	1038.5
211.8(2)	4450(50)	315.2	895.7(2)	146(7)	895.7
214.5(3)	2560(40)	504.7	904.5(2)	52(3)	1038.5
243.3(2)	6490(120)	290.2	968.1(2)	311(16)	1283.4
255.3(2)	140(20)	255.3	1033.3(4)	69(4)	1194.1
268.2(2)	4490(110)	315.2	1038.7(2)	194(10)	1038.5
290.1(2)	795(15)	290.2	1194.1(2)	141(6)	1194.1
325.8(2)	391(15)	830.1	1283.6(3)	98(7)	1283.4
357.8(2)(a)	520(20)		1635.5(9)	64(6)	1738.9
370.7(2)	689(13)	504.7	1660.2(5)	108(7)	1950.4
400.5(5)	45*(15)	561.3			

Table 4.3: List of the γ-ray energies and relative intensities from the β-decay of ^{78}Sr with their uncertainties and the level they decay from. In general the energies and intensities are the weighted mean values derived from the singles spectra from the 3 Ge detectors (see text). The intensities are normalized to that of the 103.3 keV γ-ray. The γ-ray energies and intensities obtained from coincidences have been marked with an asterisk. The γ-rays which could not be placed in the level scheme but belong to the β-decay of ^{78}Sr have been marked with an (a).

Table 4.4: List of observed coincident gamma-ray lines for each gamma transition observed in the ^{78}Sr β-decay. The gamma-ray transitions which have been marked with an (a) correspond to transitions which belong to the ^{78}Sr β-decay but have not been placed in the level scheme. The coincident gamma-ray lines which correspond to ^{78}Rb β-decay have been marked with a double asterisk.

E_γ(keV)	Coincident lines
25.2	46.9, 57.5, 87.2, 103.1, 129.3, 133.8, 156.1, 160.5, 170.4(a), 175.6(a), 186.9, 189.7, 243.3, 290.1, 325.8, 580.3 753.9(a), 778.5, 968.1
46.9	Rb-X, 25.0, 62.4, 87.2, 98.3, 140.2, 146.0, 156.1, 180.9, 189.7, 214.5, 243.3, 268.2, 325.8, 370.7, 457.8, 540.0, 545.8 575.0, 580.3, 664.0, 753.9(a), 778.5, 845.5, 904.5, 968.1, 1660.2
57.5	Rb-X, 25.0, 103.1, 129.3, 154.4, 189.7, 214.5, 325.8, 400.5, 477.3, 540.0, 580.3, 613.7(a), 734.7, 778.5, 877.8, 968.1 1033.3, 1660.2
62.4	Rb-X, 46.9, 89.7, 103.1, 146.0, 545.8, 575.0
75.0(a)	Rb-X, 211.8
87.2	Rb-X, Kr-X, 25.0, 46.9, 98.3, 140.2, 156.1, 180.9, 189.7, 214.5, 325.8, 370.7, 540.0, 580.3, 664.0, 693.0**, 778.5 805.6, 904.5, 968.1, 1660.2
89.7	Rb-X, 62.4, 103.1, 545.8, 575.0, 845.5
98.3	Rb-X, 46.9, 87.2, 133.8, 664.0, 805.6
103.1	Rb-X, 25.0, 57.5, 62.4, 89.7, 128.8, 129.3, 154.4, 175.6(a), 186.9, 189.7, 211.8, 214.5, 325.8, 400.5, 401.3, 457.9 477.3, 540.0,545.8, 575.0, 580.3, 664.0, 698.2, 722.8, 726.2, 734.7, 778.5, 792.4, 805.6, 830.3, 845.5, 877.8, 968.1 1033.3, 1635.5, 1660.2
112.6	Rb-X, 664.0, 805.6
128.8	Rb-X, 103.1, 664.0, 805.6
129.3	Rb-X, 25.0, 57.5, 103.1, 160.5, 189.7, 214.5, 325.8, 540.0, 580.3, 778.5, 968.1, 1660.2
133.8	Rb-X, 25.0, 98.3, 140.2, 156.1, 180.9, 189.7, 214.5, 325.8, 370.7, 540.0, 580.3, 664.0, 778.5, 805.6, 904.5, 968.1

Table 4.4 – Continued on next page

Table 4.4 – continued from previous page

E_γ(keV)	Coincident lines
	1660.2
140.2	Rb-X, 46.9, 87.2, 133.8
146.0	Rb-X, 46.9, 62.4, 545.8, 575.0, 845.5
154.4	Rb-X, 57.5, 103.1, 160.5, 189.7, 325.8, 357.8(a), 580.3, 778.5, 968.1
156.1	Rb-X, 25.0, 46.9, 87.2, 133.8, 189.7, 214.5, 325.8, 540.0, 580.3, 778.5, 968.1, 1660.2
160.5	Rb-X, 25.0, 129.3, 154.4, 189.7, 214.5, 325.8, 400.5, 477.3, 540.0, 580.3, 734.7, 778.5, 877.2, 968.1, 1033.3, 1660.2
170.4(a)	Rb-X, 25.2, 214.5, 540.0, 805.6
175.6(a)	Rb-X, 25.2, 214.5, 540.0
180.9	Rb-X, 46.9, 87.2, 133.8, 189.7, 325.8, 580.3, 778.5, 968,1
186.9	Rb-X, 25.0, 103.1, 189.7, 214.5, 325.8, 540.0, 580.3, 613.8(a), 778.5, 968.1, 1660.2
189.7	Rb-X, 25.0, 46.9, 57.5, 87.2, 103.1, 129.3, 133.8, 154.4, 156.1, 160.5, 180.9, 186.9, 211.8, 243.3, 268.2, 290.1, 325.8 778.5
211.8	Rb-X, 75.0(a), 103.1, 189.7, 325.8, 580.3, 613.7(a), 778.5, 968.1
214.5	Rb-X, 46.9, 57.5, 87.2, 103.1, 129.3, 133.8, 156.1, 160.5, 170.4(a), 175.6(a), 186.9, 243.3, 290.1, 325.8, 613.7(a) 753.9(a), 778.5
243.3	Rb-X, 25.0, 46.9, 189.7, 214.5, 325.8, 540.0, 580.3, 778.5, 968.1, 1660.2
255.3	Rb-X, 545.8, 575.0
268.2	Rb-X, 46.9, 189.7, 325.8, 580.3, 778.5, 968.1
290.1	Rb-X, 25.0, 189.7, 214.5, 290.1, 540.0, 580.3, 778.5, 968.1, 1660.2
325.8	Rb-X, 25.0, 46.9, 57.5, 87.2, 103.1, 129.3, 133.8, 154.4, 156.1, 160.5, 180.9, 186.9, 189.7, 211.8, 214.5, 243.3, 268.2 290.1, 370.7, 401.3, 457.8, 504.9
357.8(a)	Rb-X, 154.4, 561.3, 805.6
370.7	Rb-X, 46.9, 87.2, 133.8, 325.8, 778.5
400.5	Rb-X, 57.5, 103.1, 160.5, 477.3
401.3	Rb-X, 103.1, 325.8, 778.5
457.8	Rb-X, 46.9, 325.8, 778.5

Table 4.4 – Continued on next page

Table 4.4 – continued from previous page

E_γ(keV)	Coincident lines
457.9	Rb-X, 103.1, 477.3
477.3	Rb-X, 57.5, 103.1, 160.5, 400.5, 457.9, 561.3
504.9	Rb-X, 325.8, 778.5
540.0	Rb-X, 46.9, 57.5, 87.2, 103.1, 129.3, 133.8, 156.1, 160.5, 170.4(a), 175.6(a), 186.9, 243.3, 290.1
545.8	Rb-X, 46.9, 62.4, 89.7, 103.1, 146.0, 255.3
561.3	Rb-X, 477.3, 357.8(a)
575.0	Rb-X, 46.9, 62.4, 89.7, 103.1, 146.0, 255.3
580.3	Rb-X, 25.0, 46.9, 57.5, 87.2, 103.1, 129.3, 133.8, 154.4, 156.1, 160.5, 180.9, 186.9, 211.8, 243.3, 268.2, 290.1
613.7(a)	Rb-X, 57.5, 186.9, 211.8, 214.5
664.0	Rb-X, Kr-X, 46.9, 87.2, 98.3, 103.1, 112.6, 128.8, 133.8, 455.0**
698.2	Rb-X, 103.1
722.8	Rb-X, 103.1
726.2	Rb-X, 103.1
734.7	Rb-X, 57.5, 103.1, 160.5
753.9(a)	Rb-X, 25.2, 46.9, 214.5
778.5	Rb-X, 25.0, 46.9, 57.5, 87.2, 103.1, 129.3, 133.8, 154.4, 156.1, 160.5, 180.9, 186.9, 189.7, 211.8, 214.5, 243.3 268.2, 290.1, 370.7, 401.3, 457.8, 504.9
792.4	Rb-X, 103.1
805.6	Rb-X, 87.2, 98.3, 103.1, 112.6, 128.8, 133.8, 170.4(a), 357.8(a)
830.3	Rb-X, 103.1
845.5	Rb-X, 46.9, 89.7, 103.1, 146.0
877.8	Rb-X, 57.5, 103.1, 160.5
904.5	Rb-X, 46.9, 87.2, 133.8
968.1	Rb-X, 25.0, 46.9, 57.5, 87.2, 103.1, 129.3, 133.8, 154.4, 156.1, 160.5, 180.9, 186.9, 211.8, 243.3, 268.2, 290.1
1033.3	Rb-X, 57.5, 103.1, 160.5
1038.7	Rb-X

Table 4.4 – Continued on next page

Table 4.4 – continued from previous page

E_γ(keV)	Coincident lines
1194.1	Rb-X
1283.6	Rb-X
1635.5	Rb-X, 103.1
1660.2	Rb-X, 46.9, 57.5, 87.2, 103.1, 129.3, 133.8, 156.1, 160.5, 186.9, 243.3, 290.1

4.5 Determination of the electron conversion coefficients in the decay of ^{78}Sr

In addition to the emission of photons, there exists a process by which the nucleus 'transfers' its excitation energy to a bound electron, causing electrons to move into an unbound state with an energy balance of

$$T_{e^-} = (E_i - E_f) - B_n \tag{4.5}$$

where E_i-E_f is the nuclear excitation energy difference between levels i and f, B_n the corresponding electron binding energy and T_e the electron kinetic energy which can be measured with an electron spectrometer. This electromagnetic process competes with γ-ray emission and should be taken into account in the total intensity balance.

The contribution of this process to the transition between two nuclear levels is normally expressed in terms of the internal conversion coefficient α defined as follows:

$$\alpha = \frac{I_e}{I_\gamma} \tag{4.6}$$

where I_e is the electron intensity and I_γ the γ-ray intensity. The exact determination of the α coefficients is not only important from the point of view of the total transition intensity but also for the determination of the I^π of the levels. These coefficients depend strongly on the character (electric or magnetic) and multipolarity of the transition (L=1,2,..). The electrons are emitted directly from the inner atomic shells K, L, M ... and α represents the sum of all the partial coefficients which correspond to the different shells

$$\alpha = \alpha_K + \alpha_L + \alpha_M + ... \tag{4.7}$$

The values of these coefficients have been calculated theoretically and are tabulated [107]. They depend strongly on:

- The atomic number Z
- The energy of the transition
- The multipolarity.

Large K-shell conversion coefficients are expected for low energy and high-multipolarity transitions in heavy nuclei, with smaller values for higher atomic shells, higher transition energies, lower multipoles and lighter nuclei.

The mini-orange spectrometer focuses the internal conversion electrons emitted from the source into the Si(Li) detector (see chapter 4 for further detail). In Fig. 9.7

a conversion electron spectrum measured with the Si(Li) detector using one of the magnet configurations is shown for ^{78}Sr. The different conversion electron lines and the atomic shell in which conversion occurred have been marked. It should be noted that only the K- and the L- (or L+M) component for the strongest electromagnetic transitions can be resolved in the spectrum. As shown in Eq. 4.6, the conversion coefficient for the K- and L- components observed can be extracted from the ratio of the absolute electron intensity of the atomic shell involved and its absolute gamma intensity. In section 4.2.1 it was mentioned that the planar detector of the mini-orange setup suffered from fluctuations and stopped randomly during the data acquisition. Therefore an absolute gamma intensity could not be extracted for the gamma transitions of interest with the planar. In what follows only the co-axial detector of the telescope will be considered for such a purpose. One could argue that for energies lower than ~250 keV there are not enough calibration points to extract a very accurate photopeak efficiency curve for the co-axial detector, as shown in Fig. 4.2.1. A *GEANT4* simulation was performed for this detector in order to establish a precise efficiency curve for such low energies. However a big discrepancy appeared between the simulation and the experimental points for low energies while both curves matched well for energies higher than 250 keV. Based on these results, the simulation could not be used for low gamma transitions. This problem was thus overcome by using the relative gamma intensities previously obtained with the high resolution setup for the measurement of ^{78}Sr. They were used to derive the absolute gamma intensity for those low energy gamma transitions observed with the co-axial detector.

Another key point is to determine the electron intensity for each of the conversion lines observed. A knowledge of the electron transmission versus the energy of the electron is needed for each magnet configuration. The known conversion coefficients for several lines of the sources produced in situ, namely ^{77}Rb, ^{79}Sr and ^{79}Rb, and of the standard sources of ^{133}Ba and ^{152}Eu were used to derive the transmission curves shown in Fig. 4.11. Since the singles spectra were used for the analysis, the deadtime for the electron and gamma spectra was negligible. In case of discrepancy between the transmission given by the standard and the internal sources, the latter were favoured when plotting the transmission curve. This discrepancy was caused by the difficulty of placing the standard sources at precisely the same point where the transport tape places the mass-separated beam for the measurement. In general if there is a large discrepancy between the internal and the external lines this region is not used for the determination of conversion coefficients.

Table 4.5 shows the mean value of the conversion coefficients obtained from different magnet settings. The error associated with the use of the various curves in Fig. 4.11 was estimated by eye. The multipolarities of the transitions were

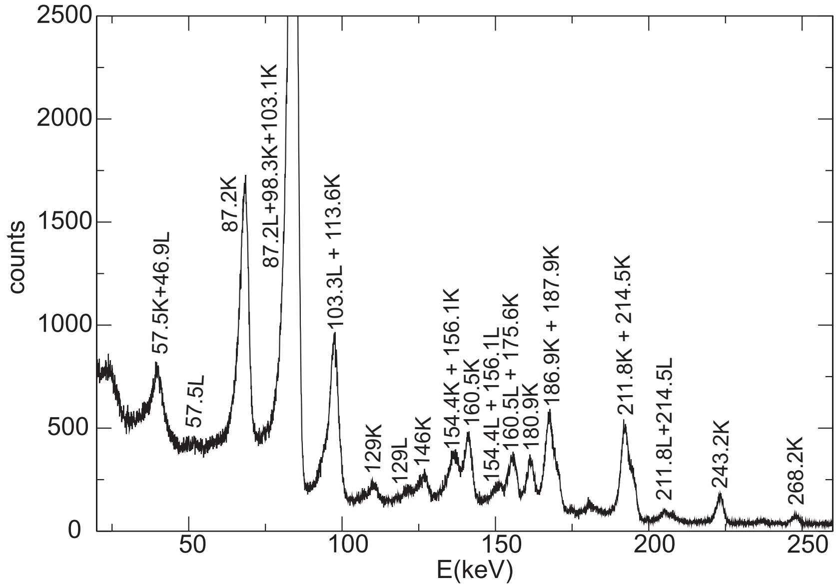

Figure 4.10: A conversion electron spectrum measured with the arrangement 6/8/125. The conversion electron lines are marked with the energies of the electromagnetic transition involved and the atomic shell in which conversion occurred. All of them are assigned to transitions in ^{78}Rb. Note that the binding energies for the K-, L1- and L2- shells are 15.2, 2.07 and 1.87 keV respectively.

then deduced from a comparison with the theoretical values [108] as shown in Fig. 4.12. No conversion electron lines were observed that could be identified as an E0 transition from a possible excited 0^+ at low energy.

4.6 Beta feeding and log ft values

The total intensity for each transition can be obtained from the following expression:

$$I_T = I_\gamma + I_e = I_\gamma(1 + \alpha_T) \tag{4.8}$$

where I_T is the total intensity, I_γ the gamma intensity, I_e the electron intensity and α_T the sum of all the partial conversion coefficients of the different atomic shells. For those transitions for which an experimental CE was not derived, the theoretical values were used [108]. For transitions with an energy ≥700 keV, the approximation $I_T \simeq I_\gamma$ would be considered to be valid since the CEs are $<5e^{-4}$ for an E1 transition and $<1e^{-3}$ for an M1 or E2 transition.

The beta feeding to a certain level E_i will be the difference between the total intensity which de-excites this level and the total intensity which feeds it from the

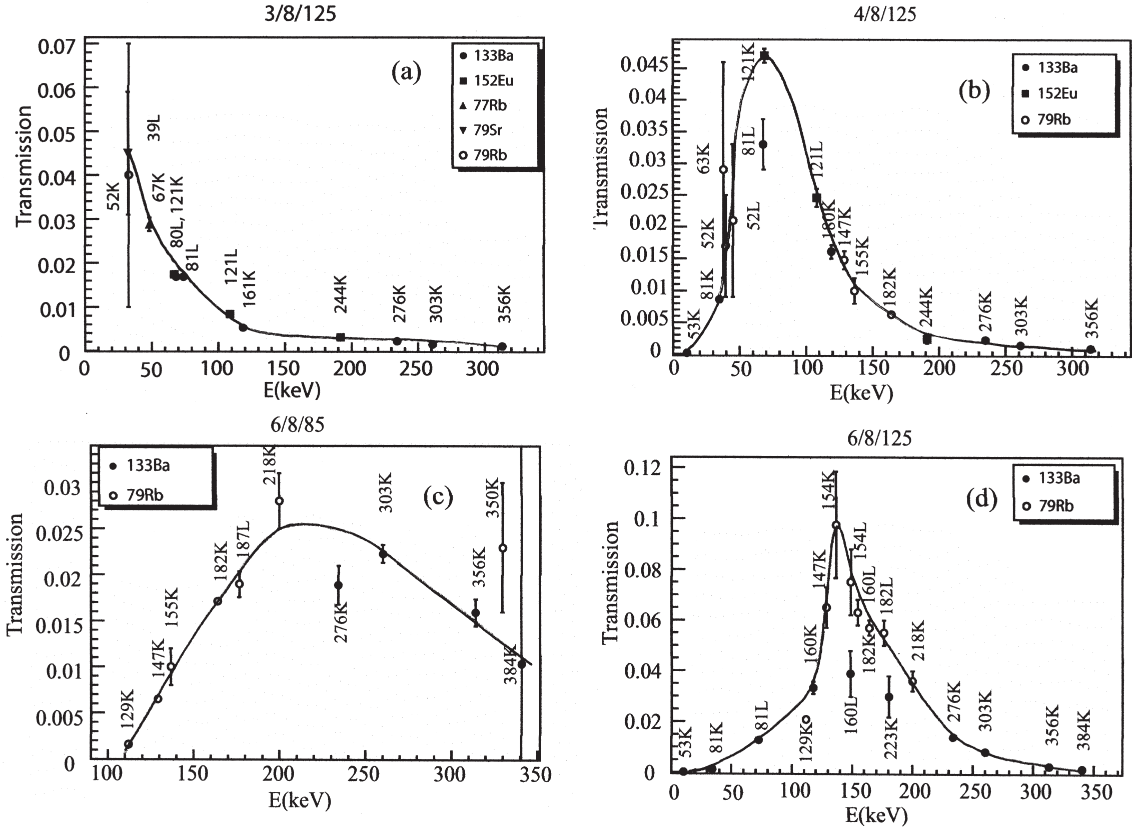

Figure 4.11: Measured transmission points for the four separate arrangements of the mini-orange used. They are classified by A/B/C where A is the number of magnets, B is the distance from the electron source to the front face of the mini-orange and C is the distance from the source to the Si(Li) detector (see Fig. 3.15 and text). Since only one type of magnet was used in the present work there is no need to specify the magnet type (see Section 3.4). The measurements were made with both standard sources of ^{133}Ba and ^{152}Eu and with sources prepared in situ of ^{77}Rb, ^{79}Sr and ^{79}Rb (see text).

other excited levels above. This can be written explicitly as:

$$I_{\beta}(E_i) = I_T^{OUT}(E_i) - I_T^{IN}(E_i) \tag{4.9}$$

In addition to the beta feeding to excited levels, it is important to determine the direct feeding to the ground state. We have adopted spin and parity 0^+ for the ^{78}Rb ground state. The spin was determined by the atomic beam resonance measurements of Ekström et al. [90]. Initially positive parity was assigned because it is difficult to find any suitable configuration which gives 0^- spin and parity. Similar arguments have been advanced in earlier publications [78, 90] on this topic. More convincingly McNeill et al. [94] showed that the isomeric spin 4 state at 111.2 keV

E_γ(keV)	α_K	$\alpha_{L+M..}$	Multipolarity	Comment
57.5		0.0846(17)	M1	a,b
87.2	0.21(3)		M1	a
98.3	0.55(11)		M1/E2	a
103.1		0.014(2)	M1	a
112.6(9)	0.11(5)		E1 or M1	a
128.8(3)	0.032(11)		E1	b
146.0(4)	0.054(12)		M1	c
154.4(4)	0.063(18)		M1/E2	c
156.1(2)	0.017(5)		E1	c
160.5(4)	0.08(2)		M1/E2	c,d
180.9(3)	0.013(2)		E1	c
186.9(6)	0.023(5)		M1	b,c
189.7(4)		0.024(9)	M1	d
211.8(2)	0.020(3)	0.0027(7)	M1	b,c,d
214.5(3)	0.023(8)	0.0027(7)	M1	a,c

Table 4.5: Conversion coefficients measured for different transitions in ^{78}Rb. The comments have the following criteria: (a) Measured with the configuration of magnets 3/8/125. (b) Measured with the configuration of magnets 4/8/125. (c) Measured with the configuration of magnets 6/8/85. (d) Measured with the configuration of magnets 6/8/125. (*) Although the CE obtained is compatible with an E1 and M1, the latter has been adopted after being deduced from other spins assigned.

and the ground state have opposite parities. Earlier Ekström et al. [90] had shown that the measured magnetic moment of the isomeric state is in close agreement with the theoretical value for the $\pi[422]5/2^+ \times \nu[301]3/2^-$ configuration. In other words it is of negative parity. No available configuration of positive parity can reproduce the large measured value of the magnetic moment for the isomeric level. Thus we believe that the I^π of the isomeric state is 4^- and consequently the parity of the ground state is positive.

Since the decay of the ground state of ^{78}Sr to the ground state of ^{78}Rb does not involve γ-ray emission alone, but β^+ or EC, γ-ray spectroscopy cannot be used to determine the fraction of the direct beta feeding which populates ^{78g}Rb. A β-decay between the parent and daughter ground states would be a Fermi isospin-forbidden transition and would then be strongly hindered. Several papers have reported $0^+ \rightarrow 0^+$ isospin forbidden beta transitions [109], however these transitions have only been observed in the decay of odd-odd parent nuclei. Although the measurements reported here were not sensitive to any ground state to ground state feeding, the Total Absorption studies of the same decay addressed in chapter 7 show that there is little or no such feeding. This is just what one would expect for an

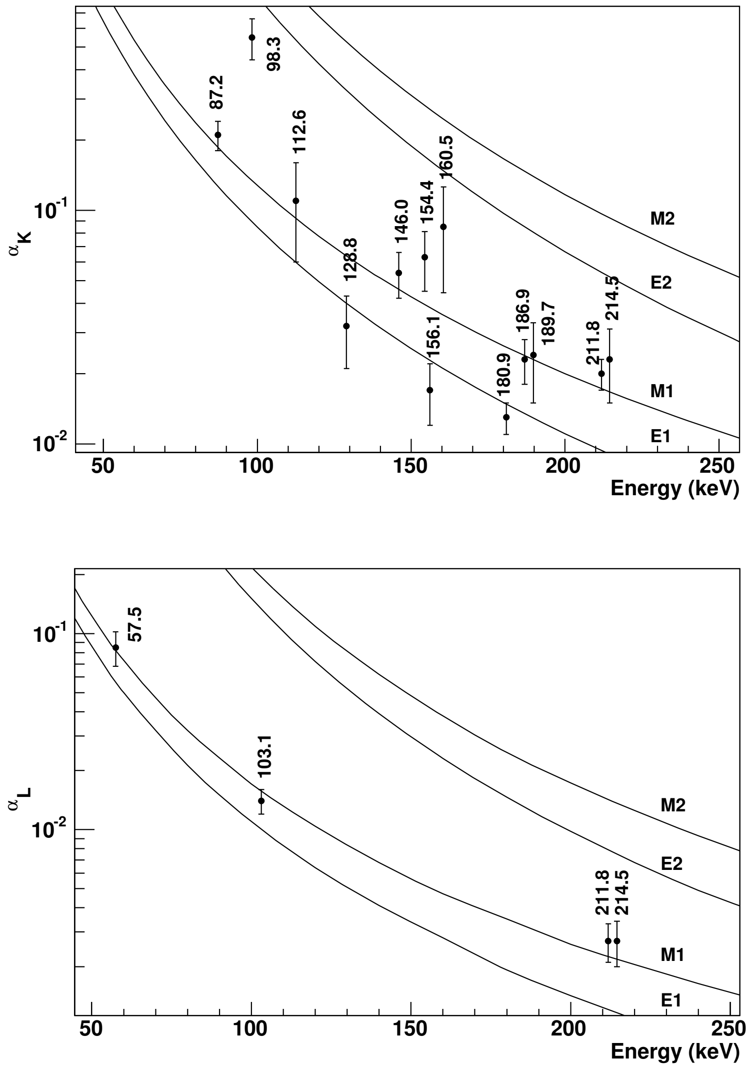

Figure 4.12: The measured conversion coefficients for transitions in ^{78}Rb measured in studies of the decay of ^{78}Sr. The upper graph shows the K-component of the conversion coefficients and the lower one the L- or the L+M component if they cannot be resolved. The points are labelled with the shell in which conversion occurs and the energy of the transition.

isospin-forbidden 0^+ to 0^+ β-decay. Table 4.6 shows the results of the beta feeding for all the excited states deduced from an intensity balance calculation with no feeding to the ground state considered.

For a better interpretation of the results, it is convenient to introduce the log

E_{level} (keV)	I^π	$\beta_{feeding}$ %	log ft	BGT $\times 10^2$
0	0^+	0		
46.9	1^-	0(2)	8(2)	0.002(8)
103.3	1^+	1.6(6)	6.15(19)	0.27(12)
119.6	(3^+)			
134.0	1^-	0.1(4)	7.3(18)	0.02(8)
160.8	1^+	1.16(11)	6.17(5)	0.25(3)
193.0	0^-,1^-,2^-	0.82(10)	6.37(6)	0.16(2)
232.3	$(2)^-$	0.47(14)	7.91(14)	0.0047(15)
255.3	1^+,1^-,2^+	0.33(10)	6.72(14)	0.07(2)
274.2	2^-	0.25(4)	8.14(8)	0.0027(5)
290.2	1^+	3.9(12)	5.63(14)	0.9(3)
315.2	1^+	49.5(12)	4.50(2)	12.1(5)
504.7	1^+	21.2(5)	4.72(2)	7.3(3)
561.3	1^+	3.96(19)	5.40(3)	1.50(10)
801.6		0.35(3)	6.26(4)	0.21(2)
826.3	1^+	1.23(5)	5.69(3)	0.77(5)
830.1	1^+	3.58(7)	5.22(2)	2.27(9)
895.7	1^+	4.71(12)	5.05(2)	3.42(15)
933.7	1^+	0.61(3)	5.90(3)	0.48(3)
1038.5	1^+	3.76(10)	5.02(2)	3.66(17)
1194.1	1^+	0.67(2)	5.62(2)	0.92(5)
1283.4	1^+	2.22(7)	5.01(2)	3.70(19)
1738.9	1^+	0.20(2)	5.61(5)	0.93(11)
1950.4	1^+	0.34(2)	5.20(3)	2.39(19)

Table 4.6: Measured β-decay feedings, the log ft and the B(GT) values obtained for each energy level. The I^π values for the energy levels are also listed.

ft value since it is intimately related to the β-decay transition rate. A small value of this quantity for a certain level means a strong beta feeding. Spin and parity assignments for nuclear energy levels can be also made on the basis of the log ft values and will be discussed in the next section. The probability that a nucleus decays and populates a level i in the daughter nucleus is inversely proportional to the partial half-life of this level

$$t_i = \frac{T_{1/2}}{I_\beta(i)} \tag{4.10}$$

with $T_{1/2}$ the half-life of the parent nucleus, and I_β(i) the beta feeding to the level i.

In order to know the beta transition rate between the ground state of the parent nucleus and an excited state populated in the daughter, it is necessary to include the dimensionless factor f(Z,E$_{max}$(i)), the Fermi integral. This depends on the Z of the daughter nucleus and the maximum energy E$_{max}$(i) for a given β-decay transition, (Q$_{EC}$-E(i)). The theoretical values for the Fermi integral are tabulated in [3]. Therefore, the ft value for a given transition is defined as

$$ft = f(Z, E_{max}(i))t_i \tag{4.11}$$

Another important magnitude is the β-decay strength for each excited state, which can be derived from the log ft values using the following expression and assuming no Fermi transitions involved :

$$B(GT)_i = \frac{\lambda}{ft} \tag{4.12}$$

where $\lambda = 3809.0 \pm 1.0$ [5]. In the present work, only the Gamow-Teller decay is considered since the isospin-forbidden Fermi transition is hindered from the selection rules. The log ft and B(GT) values obtained for each level populated in the β^+/EC decay of ^{78}Sr are shown in table 4.6. As can be observed, most of the strength goes to the 290.1, 315.1, 504.7 and 561.3 keV levels.

The total Gamow-Teller strength observed in the β-decay of ^{78}Sr is the sum of the strength for all the individual levels in the level scheme obtained. This results in the following:

$$B(GT) = (0.42 \pm 0.02)\frac{g_A^2}{4\pi} \tag{4.13}$$

The result obtained will be discussed and compared to that obtained by total absorption spectroscopy in chapter 7. From these high resolution measurements no clear conclusions can be drawn as most of the B(GT) strength may lie outside the window of energy sensitivity. The level scheme obtained goes only up to 2 MeV while the Q$_{EC}$ value is 3762 keV [67]. However a knowledge of the low-lying part of the scheme, obtained in this part of the experiment, is a prerequisite for the subsequent analysis based on unfolding procedures for our TAS measurement.

The decay scheme for ^{78}Sr to levels in ^{78}Rb based on the present work is shown in Figs. 4.13 and 4.14 . The figure summarises our knowledge of the γ-ray transition energies and multipolarities as well as the measured feeding in the β-decay and the log ft values deduced from them. The Q$_{EC}$ value is taken from [67].

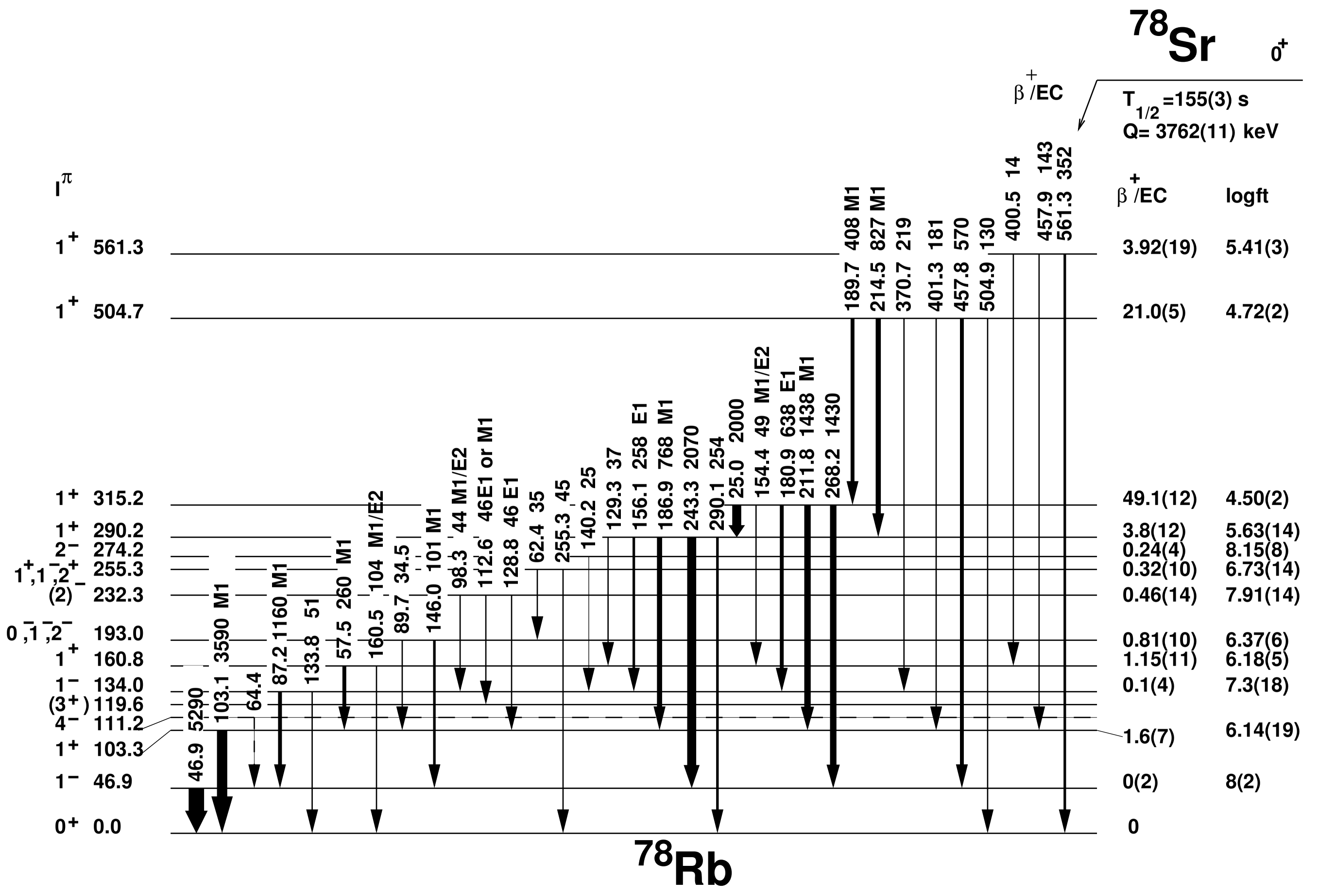

Figure 4.13: Here we see part of the decay scheme for ^{78}Sr deduced in the present work. The assigned I$^{\pi}$ values and level energies in keV are shown on the left. The percentage feeding in the β-decay and corresponding log ft values are shown on the right. The γ-ray energies and multipolarities measured in the present work are marked on the figure. It should be noted that the transition intensities are normalised to a total intensity of 10,000 units feeding the ground state. The ^{78}Sr half-life and the Q$_{EC}$ [67] are also shown. For completeness the isomeric level at 111.2 keV and the 64.4 keV de-exciting transition (dashed line) [94] are included although the level is not populated in the decay. Note that McNeill et al. [94] observed the conversion electrons from the 46.9 and 64.4 keV transitions. They assigned multipolarities of M1 and M3 character to the two transitions. This establishes the fact that the 111.2 keV level and the ground state have different parities.

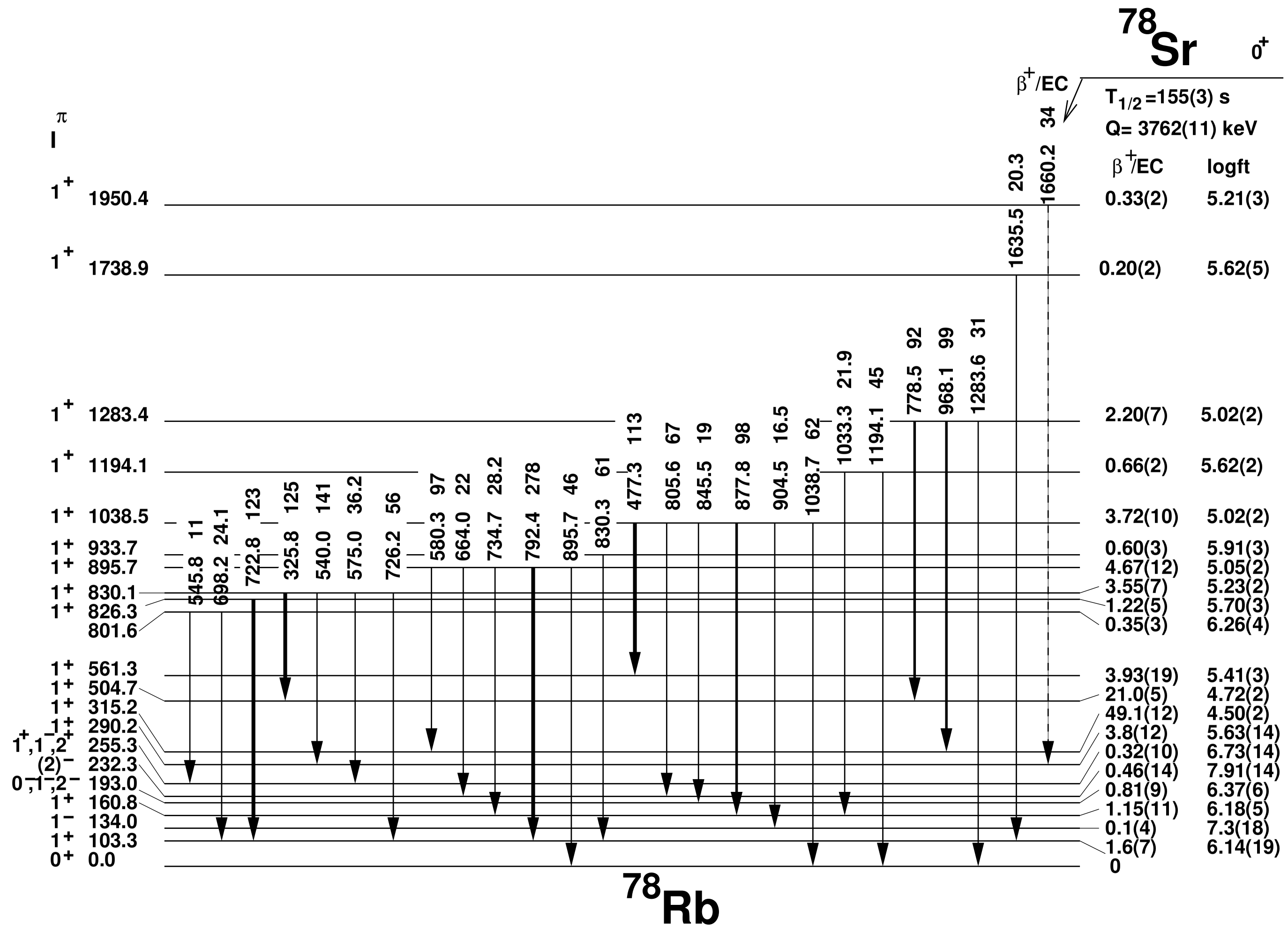

Figure 4.14: Same as for Fig. 4.13 but now including levels above 600 keV. Note that the levels at 46.9, 111.2, 119.6 and 274.2 keV have been omitted since we do not see transitions feeding them from higher levels.

4.7 Discussion of the parity and spin assignments to the levels

In this chapter the spins and parities, I^π, of the energy levels listed in Table 4.6 will be discussed and supporting arguments for these values will be given.

Our starting point is as follows. It seems clear that the levels at 290.2, 315.2, 504.7 and 561.3 keV all have spin and parity 1^+ since they are fed strongly in the β-decay of the ^{78}Sr ground state with log ft values fully consistent with allowed Gamow-Teller character [110]. We have also adopted spin and parity 0^+ for the ^{78}Rb ground state and supporting arguments are given in Section 4.6.

With the above in mind we will now review the I^π assignments we have made to the levels in ^{78}Rb. The levels found will be treated in order of increasing energy. Spins and parities will be assigned when possible according to their calculated beta feeding, logft value and the way the level de-excites and is fed, including the nature and multipolarity of the radiation when CE information is available.

46.9 keV level : This level is fed by an M1 transition of energy 87.2 keV (see Fig. 4.13) de-exciting the 134.0 keV level, which has a firm assignment of 1^- (see the later discussion of this level), and decays to the ground state. It is thus firmly established as $I^\pi = 1^-$. This is in accord with the reported measurements of McNeill et al. [94] where the 46.9 keV transition was determined to have E1 multipolarity. The lifetime of this level has been measured by Mukai et al. [79] as 910(40) ns and by Kaye et al. [95] as 610(100) ns. In broad terms the transition rates obtained from these lifetimes are consistent with electric dipole multipolarity in the region [110]. In the case of Kaye et al. the value was cross-checked with a measurement they made of the lifetime of the 66.5 keV level in ^{77}Kr.

103.3 keV level: As shown in Fig. 4.13 the 103.3 keV level decays by an M1 transition to the ground state. This establishes its spin and parity as 1^+. It is fed by M1 transitions with energies 186.9 and 211.8 keV from 1^+ levels, which agrees with this assignment.

111.2 keV level: This isomeric level is not populated in the ^{78}Sr β-decay and is included here and in Fig. 4.13 for the sake of completeness. As mentioned earlier 4^- is the most reasonable choice for the spin and parity of this level in view of the results of Ekström et al. [90] and McNeill et al. [94].

119.6 keV level: Kaye et al. report a level at this energy, which decays by an unseen low energy transition. Our results are consistent with its existence through the observation of coincidences between the 112.6 keV and the 664.0 and 805.6 keV transitions. This level is fed by an E1 or M1 112.6 keV transition from a level at 232.3 keV which we believe is a $(2)^-$ (see below). A 170.4 keV line observed in coincidence with the 25.2, 214.5 and 540.0 keV gamma-ray lines could possibly feed this level from the 290.0 keV level. However, the coincidence of this 170.4 keV line with the 805.6 keV gamma-ray is in disagreement with its suggested placement and no firm conclusions have been drawn. A possible explanation would be the existence of a doublet at an energy of 170 keV which would resolve this inconsistency. No de-exciting transitions were observed from this level to either the 0^+ g.s. or the 1^- level at 46.9 keV. It is likely that the de-excitation proceeds through a highly converted transition to one of the other lower-lying levels. The planar detector threshold in our case is too low to observe a transition of 8.4 keV to the 111.2 keV level. A 16.8 keV E2, if it exists, is below our sensitivity. This explains why there is no value of feeding for this level in Fig. 4.13.

134.0 keV level: This level is fed by the 156.1 keV E1 transition from the 1^+ level at 290.2 keV. It decays to the ground state, which establishes it as a 1^- state. As mentioned above the M1 character of the transition of 87.2 keV to the 46.9 keV level fixes that state as a 1^- state. The level at 134.0 keV was seen in the heavy-ion fusion-evaporation study by Kaye et al. [95]. They assign spin and parity 2^- on the basis of the measured Directional Correlations de-exciting Oriented states (DCO) ratios for the 87.2 keV transition. The reported DCO ratios appear to be consistent with either E1 or M1 multipolarity, which is consistent with our M1 assignment from the K conversion coefficient. Not surprisingly they did not see the 133.8 keV transition to the ground state since it appears to be below their sensitivity limit. We believe that the correct I^π is 1^- and this has the consequence that the levels in both band 5 and band 6 in their paper would have spins lower by one unit.

160.8 keV level: The 160.5 keV transition to the ground state has a multipolarity of mixed M1/E2 character. This fixes the I^π of the 160.8 keV level as 1^+. This is corroborated by the fact that it is fed by an M1/E2 transition from the 1^+ level at 315.2 keV. We have determined that the 57.5 keV de-exciting transition to the 103.3 keV level is of M1 character. It should be noted that our assignments are in disagreement with those of Kaye et al. [95] who, on the basis of DCO ratio measurements in a heavy ion, fusion-evaporation reaction study, assign E2 and stretched M1 character to the 160.5 and 57.5 keV transitions respectively. Our assignment would lower the spin of their band 9 by one unit.

193.0 keV level: This level decays by an M1 transition of 146.0 keV to a 1^- level. This makes it of negative parity with a spin of 0, 1 or 2. This is consistent with the small amount of feeding in the β-decay (see below).

232.3 keV level: This level was observed in-beam by Kaye et al [95]. Although we also observe three de-exciting transitions of roughly the same energies the branching ratio they report for the 129.2 keV transition is clearly inconsistent with our observations. Instead we see a much weaker 128.8 keV transition de-exciting this level. The fact that we see another 129.3 keV transition de-exciting the 290.2 keV level, a level not observed by Kaye et al., does not resolve this inconsistency. Here we observe an M1/E2 transition of 98.3 keV to a firm 1^- state and an E1 transition of 128.8 keV energy to a firm 1^+ state. This fixes negative parity and allows spins 0, 1 or 2. The 1^- assignment is unlikely because we do not see the transition to the ground state. On the other hand, considering the earlier discussion in relation to the 119.6 keV level, 2^- is clearly favoured.

255.3 keV level: The 255.3 keV level decays to the ground state and to the 193.0 keV level. Thus it can have $I^\pi = 1^-$, 1^+ or 2^+. The reader may object to the fact that we have not ruled out the 2^+ and 2^- assignments to the 255.3 and 193.0 keV levels on the basis of the relatively large log ft values, which would agree with first forbidden transitions, but not with second forbidden transitions (as would be the case for spins and parities 2^+ and 2^-). However, in these two cases the feeding, based on the intensity balance into and out of the levels, is only 0.3 and 1.0% respectively. These values are low enough that they could be attributed to indirect feeding by unobserved transitions from higher-lying levels. This is a manifestation of the so-called *Pandemonium* effect [57].

274.2 keV: A level at this energy is populated strongly in the in-beam studies of Kaye et al [95]. In their work and based on DCO ratios, they see a 140 keV stretched M1 transition to the 134 keV level, which they assigned as a 2^- level. From our data we deduce that the 134 keV level has spin and parity 1^- and using their information we assign 2^- to the 274.2 keV level.

290.2, 315.2, 504.7 and 561.3 keV levels: We remind the reader that at the beginning of this discussion we assumed that all of these levels have $I^\pi = 1^+$ based on the log ft values. Nothing in the decay scheme we have constructed contradicts this assumption. It should be noted that Kaye et al. [95] also report the levels at 290.2 and 504.7 keV with the latter decaying to the former. Two of the de-exciting transitions from the 290.2 keV level observed by us were not seen and the 214.5 keV transition was the only line seen from the 504.7 keV level. We would judge that the other transitions were not seen because they are below the level of sensitivity in their experiment. The branching ratios they report for the 290.1 keV level are in poor agreement with those reported here. Kaye et al. also report the 315.2 keV level as decaying via the 211.8 and 180.9 keV transitions but do not see the other transitions reported here. Since the 268.2 keV transition has an intensity comparable to the 211.8 keV transition this is surprising. They assign $I^\pi = (2^+)$ to this level which is ruled out by the small log ft value.

Levels above 600 keV: All of these levels have log ft values less than 5.9. Conse-

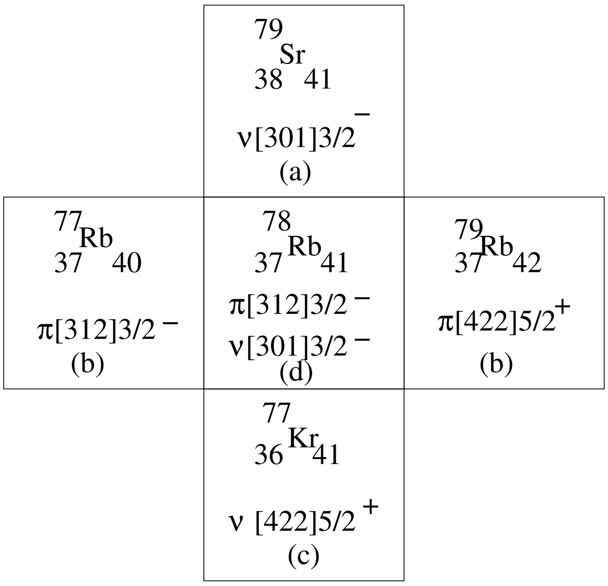

Figure 4.15: Part of the nuclear chart showing ^{78}Rb and their neighbour nuclei. The asymptotic numbers associated with the ground state for each nucleus are shown. They have been extracted from references (a) [120], (b) [111] ,(*c*) [90] and (d) this work.

quently based on the compilation of Raman and Gove [109] of log ft values for allowed Gamow-Teller transitions, they are all assigned as 1^+ states. This assignment is in accord with all the transitions de-exciting these levels to the levels discussed above.

Finally it is worth noting that the levels observed by us and discussed in this section up to 505 keV energy were also seen in the in-beam experiment reported by Kaye et al. [95] with the exception of the levels at 193.0 and 255.3 keV.

4.8 Interpretation of the level structure of ^{78}Rb

The complexity found in the decay schemes of deformed odd-odd nuclei arises naturally from the several modes of excitation, both single-particle and collective, that can occur in these nuclei, from the many possible interactions between these modes and from the many possible configurations of the valence proton and neutron. In this section, we will try to discuss the structure of the levels in the odd doubly nucleus ^{78}Rb observed in the present experiment. We will include in our discussion the 4^- isomeric level since its properties are germane to the discussion although it is not populated in this decay. We will restrict ourselves to the levels in Fig. 4.13, the lower part of the level scheme, because at higher energies the levels are probably too mixed to allow us any clearcut interpretation.

It is convenient for this purpose to group the levels into four "families" or categories, which we will discuss in turn. The first of these, family A, consists of the four 1^+ levels which have small log ft values. They lie at 290.2, 315.2, 504.7 and 561.3 keV in excitation energy. Family B are the observed negative parity states at 46.9 (1^-), 134.0 (1^-), 193.0 (0^-,1^-,2^-), 232.3 (2^-) and 274.2 (2^-). The 255.3 keV (1^+,1^-,2^+) level and the 4^- isomeric state at 111.2 keV will also be included in family B (see below). Family C has the two 1^+ levels with very small beta strength at 103.3 and 160.8 keV. Finally we will treat the ground state as being of a separate family D. Note that our present knowledge of the 119.6 keV level does not allow us to place it in any of these families.

The starting point for our understanding of the structure of ^{78}Rb lies in the nature of the ^{78}Sr ground state. This is because the deformation of the parent state can be related to the states populated in the daughter nucleus, as discussed in several papers [47, 48].

A number of measurements are relevant here. Firstly Lister et al. [26] have measured the B(E2;$2^+ \rightarrow 0^+$) for the ground state band in ^{78}Sr and from this they derived $Q_0(2^+)$= 3.29(19) b. This is consistent with the prediction of Möller and Nix [112] of $Q_0 = +3.2$ b. Lister et al. [26] also pointed out that this large prolate deformation is supported by the quadrupole moment they extract for ^{79}Sr from the ground state band in that nucleus. The isotope shift measurements of Buchinger et al. [113] support a large $\delta\langle r\rangle^2$ for ^{78}Sr from which one can derive a large deformation of $\sqrt{\beta}^2 \simeq$0.38. All of this information is consistent with a large deformation.

Theoretical calculations of the beta feeding to the states in ^{78}Rb from the ^{78}Sr ground state have been published in reference [50]. A detailed description of those calculations is done in chapter 2. The minima in a plot of the total HF energy versus deformation give the possible deformations of the ground state. For ^{78}Sr two minima are found, one prolate with $\beta = 0.42$ and the other spherical. The quasiparticle orbitals in the vicinity of the Fermi level predicted by our Skyrme (SG2) HF+BCS calculations are [422]$5/2^+$, [431]$3/2^+$ and [312]$3/2^-$ in the case of proton states and [431]$1/2^+$, [301]$3/2^-$, [422]$5/2^+$, and [431]$3/2^+$ in the case of neutron states, where $[Nn_z\Lambda]\Omega^\pi$ stands for the asymptotic quantum numbers [25]. These predicted states are consistent with Rb isotope shifts measurements by Thibault et al. [111] that established $\pi[312]3/2^-$ and $\pi[422]5/2^+$ as the ground states of the odd-proton nuclei ^{77}Rb and ^{79}Rb, respectively. In addition, the state $\pi[312]3/2^-$ is known to be only 39 keV apart from the ground state in the latter nucleus [114] and the proton orbital $\pi[431]3/2^+$ is also proposed to be nearby. Overall, the proton orbitals expected close to the Fermi level are $\pi[312]3/2^-$, $\pi[422]5/2^+$ and $\pi[431]3/2^+$, in accord with our HF+BCS calculations. Analogously, hyperfine structure and magnetic moment measurements for a number of Kr and Sr isotopes [115] place the ordering of neutron orbitals as [301]$3/2^-$ and [422]$5/2^+$, which are also consistent with our calculations.

Prolate			Spherical		
E_x (MeV)	Nilsson configuration	spin	E_x (MeV)	spherical shell	spin
0.76	$\pi[431]3/2^+$ $\nu[431]1/2^+$	$1^+(2^+)$	0.79	$\pi p_{3/2} - \nu p_{1/2}$	$1^+(2^+)$
0.74	$\pi[312]3/2^-$ $\nu[301]3/2^-$	$0^+(3^+)$			
0.57	$\pi[312]3/2^-$ $\nu[422]5/2^+$	$1^-(4^-)$			
0.33	$\pi[422]5/2^+$ $\nu[301]3/2^-$	$4^-(1^-)$	0.44	$\pi f_{5/2} - \nu p_{1/2}$	$3^+(2^+)$
0.17	$\pi[431]3/2^+$ $\nu[301]3/2^-$	$3^-(0^-)$			
0.16	$\pi[422]5/2^+$ $\nu[422]5/2^+$	$5^+(0^+)$			
0.0	$\pi[431]3/2^+$ $\nu[422]5/2^+$	$4^+(1^+)$	0.0	$\pi p_{1/2} - \nu p_{1/2}$	$1^+(0^+)$

Table 4.7: Two-quasiparticle excitation energies and their associated asymptotic numbers $[Nn_z\Lambda]\Omega^\pi$ (spherical shells) in ^{78}Rb for prolate (spherical) shapes. Also shown are the spins resulting from the Gallagher-Moszkowski [116] coupling rules, as well as the spins obtained from the opposite sense of the rules (within parentheses) for the prolate shape. Similarly, the Nordheim coupling rules [117] have been applied to the spherical shape and the spins are also listed. The results correspond to Skyrme HF+BCS calculations with the Skyrme force SG2.

Table 4.7 shows the low proton and neutron two-quasiparticle configurations in the odd-odd daughter nucleus ^{78}Rb. In the spherical case, we have considered the so-called Nordheim rules [117] to extract the possible spins of the odd-odd configurations. According to the shell model, in the case of two particle excitations the net nuclear spin I comes from combining the net angular momenta of the odd proton j_p and of the odd neutron j_n . In particular, quantum mechanics allows any integer value for j in the range

$$|j_p - j_n| \leq I \leq j_p + j_n \tag{4.14}$$

However, of all possible final states the one which lies at lowest excitation energy depends strongly on the alignment of the intrinsic spin of the two odd particles. The Nordheim rules are based on the idea that nuclei like to align the spins of the two odd nucleons, just like the deuterium nucleus does since it has S=1. The corresponding state will probably be the lowest in energy. The total angular momentum j of an odd nucleon and its spin s will be called parallel if j=l+s, with l being the orbital angular momentum. The idea is that in this case the spin acts to increase j, so it must be in the same direction as l considering a simplistic one dimensional picture. Similarly, the total angular momentum and spin are called opposite if j=l-s. If we make the assumption that the spins of the proton and the neutron are parallel, based on the properties of the deuteron that makes it favorable for the intrinsic spins to add, we can conclude the following:

- The lowest state will correspond to the coupling where angular momenta j_p and j_n of the odd proton and neutron will be opposite to each other if one is

			prolate	spherical
Family	E_x	spin	Nilsson configuration	spherical shell
D	0	0^+	$\pi[312]3/2^-$-$\nu[301]3/2^-$	
B	46.9	1^-	$\pi[312]3/2^-$-$\nu[422]5/2^+$	
C	103.3	1^+		$\pi p_{1/2} - \nu p_{1/2}$
B	111.2	4^-	$\pi[422]5/2^+$-$\nu[301]3/2^-$	
	134.0	1^-	$\pi[422]5/2^+$-$\nu[301]3/2^-$	
C	160.8	1^+		$\pi p_{3/2} - \nu p_{1/2}$
B	193.0	0^-	$\pi[431]3/2^+$-$\nu[301]3/2^-$ or $\pi[312]3/2^-$-$\nu[431]3/2^+$	
	232.2	2^-	$\pi[312]3/2^-$-$\nu[431]1/2^+$ or (i)	
	274.2	2^-	$\pi[312]3/2^-$-$\nu[431]1/2^+$ or (i)	
A	290.2	1^+	$\pi[431]3/2^+$-$\nu[422]5/2^+$	
	315.2	1^+	$\pi[431]3/2^+$-$\nu[431]1/2^+$	
	504.2	1^+	(ii)	
	561.3	1^+	(ii)	

Table 4.8: Correspondence of the low-lying excited states in ^{78}Rb grouped into families and the interpretation in terms of associated quasiparticle configurations (spherical shells) using HF+BCS calculations with the Skyrme force SG2. (i) member of a rotational band built on 0^- or 1^- bandheads. (ii) Nilsson configurations producing an 1^+ state and at higher energy than those shown in Table 4.7.

parallel to its spin, and the other is opposite to its spin:

$$I = |j_p - j_n| \tag{4.15}$$

- Otherwise the lowest state will correspond to the coupling where the angular momenta will be parallel to each other and the total spin of the nucleus will be I=$j_p + j_n$.

These rules can then be summarised as follow:

$$I_{lowest} = j_p + j_n \quad when \quad j_p = l_p \pm 1/2 \quad and \quad j_n = l_n \pm 1/2, \tag{4.16}$$

$$I_{lowest} = |j_p - j_n| \quad when \quad j_p = l_p \pm 1/2 \quad and \quad j_n = l_n \mp 1/2, \tag{4.17}$$

The case of deformed nuclei is similar in the sense that the most favourable coupling will correspond to the configuration with the intrinsic spin of the odd proton and neutron aligned (deuteron-type coupling) [116]. One important difference in relation the spherical case is that in this case the asymptotic-quantum-number description of particle states must be used. Table 4.7 shows the two-possible particle odd-odd configurations, i.e. the values of the band quantum number K, according to the Gallagher-Moszkowski (G-M) rules [116] for deformed nuclei. K denotes the projection of the total angular moment and is a valid quantum number in the Nilsson model. Since we are considering axial symmetry for this nucleus, K=Ω, where Ω is the sum of the components of angular momenta of the two particles along the nuclear symmetry axis. Gallagher et al. found that it was possible to determine Ω on the basis of the coupling of the last odd proton and neutron in odd-odd nuclei using the assigned values to Ω_p and Ω_n based on the Nilsson quasiparticle configurations. The G-M rules were derived based on the effect of the residual neutron-proton interaction in doubly odd deformed nuclei. These rules are based on the assumption that the components Σ_p and Σ_n of proton and neutron spin always couple parallel along the nuclear symmetry axis. Similarly to the Nordheim rules, the G-M rules are the following:

$$I_{lowest} = \Omega_p + \Omega_n \quad if \quad \Omega_p = \Lambda_p \pm 1/2 \quad and \quad \Omega_n = \Lambda_n \pm 1/2 \tag{4.18}$$

$$I_{lowest} = |\Omega_p - \Omega_n| \quad if \quad \Omega_p = \Lambda_p \pm 1/2 \quad and \quad \Omega_n = \Lambda_n \mp 1/2 \tag{4.19}$$

with both couplings being possible. Table 4.7 shows the low energy proton-neutron two quasiparticle configurations in the odd-odd daughter nucleus ^{78}Rb. We have considered the possible odd-odd configurations according to the Gallagher-Moszkowski (G-M) rules for deformed nuclei. Similarly, in the spherical case the Nordheim rules have been applied. Thus, for each two-quasiparticle configuration we show in Table IV the spin of the lowest energy state corresponding to the G-M rule. We also show within parentheses the spin corresponding to the antiparallel spin coupling, which is expected somewhat higher in energy.

The results in Table 4.7 correspond to the force SG2, which has proved to be very successful in describing spin-isospin nuclear properties. Results for other Skyrme forces, SK3 and SLy4, are qualitatively similar to these although they differ in the details. We should also mention that although the B(GT) strengths are calculated at the end within QRPA, it is worth analysing the present decay scheme with this simple and intuitive approach which allows us to get a straightforward interpretation of the underlying excitation mechanism. Although we consider that ^{78}Sr is prolate, we will use these calculations to identify spherical states in the daughter nucleus as well since they can be fed in our experiment via higher excited states or from small admixtures of spherical configurations in the parent ground state. The theoretical excitation energies that appear in Table 4.7 for each configuration, E_x, have been calculated summing the quasiparticle energies of the proton, E^p_{qp}, and the neutron, E^n_{qp}, namely E_x=E^p_{qp}+E^n_{qp}. The quasiparticles of both the proton and the neutron can be obtained using the following expression:

$$E^i_{qp} = \sqrt{(E^{HF}_{sp}(i) - E_F)^2 + \Delta_i^2} \quad i = n \quad or \quad p \tag{4.20}$$

where $E^{HF}_{sp}(i)$ is the single particle energy obtained from the HF calculation, E_F is the energy of the Fermi level and Δ_i is the energy of the gap for the proton and the neutron. In this case the values used for Δ_p and Δ_n were 1.330 and 1.240 MeV respectively. In addition, E_F takes the values of -3.622 and -12.426 MeV for the protons and the neutrons respectively in the prolate case. In the spherical case the values used were -4.004 and -13.162 MeV. Once the excitation energies of the different configurations are obtained, an excitation energy of 0 keV is assigned to the configuration with the lowest energy and the rest are calculated with respect to this minimum energy state. Although these calculations should not be taken literally in terms of the excitation energies associated with each particular configuration, they can be taken as a guide to interpret the nature of the observed states if we characterise them in terms of I^π assignments.

Turning first to family B since there are not many configurations that can contribute to producing negative parity states at low energy, Table 4.7 indicates that only the prolate calculation predicts the existence of negative parity states at low energy. We can identify the 1^- states at 46.9 and 134.0 keV with the predicted 1^- states with configurations $\pi[312]3/2^- - \nu[422]5/2^+$ and $\pi[422]5/2^+ - \nu[301]3/2^-$. The latter is the partner of the 4^- state and lies at higher excitation energy as expected. The 193.0, 232.3, and 274.2 keV levels also belong to this family. The fact that the 193.0 keV level was not observed in beam and the other two were, favours a 0^- assignment to this level and 2^- to the 232.2 and 274.2 keV levels. We also place the 255.3 keV level into this family. Since it was not observed in-beam a 2^+ assignment is not favoured. The fact that it decays into the 193.0 keV level via an E1 transition instead of decaying via an M1 into 1^+ states of family C favours a 1^- assignment and prolate character. The 0^- state could arise from the $\pi[431]3/2^+ - \nu[301]3/2^-$ configuration or from $\pi[312]3/2^- - \nu[431]3/2^+$, not shown in Table 4.7 because it appears at higher energy. The 2^- states could arise from $\pi[312]3/2^-$ $\nu[431]1/2^+$, which also appears at higher energy, or as a member of the rotational band built on 0^- or 1^- bandheads. We include the 4^- isomeric level here, where we are on much stronger ground. The coupling of $\pi[422]5/2^+$ and $\nu[301]3/2^-$ gives us a 4^- state according to G-M rule and a state 1^- at a higher energy. This 4^- state is interpreted as the 4^- isomer observed at 111.2 keV. The assignment of this configuration for the 4^- isomer is confirmed by the observed magnetic moment $\mu = 2.56\ \mu_N$, measured in an atomic beam magnetic resonance experiment by Ekström et al. [90]. The large positive value measured could only be reproduced by assuming a large $\pi[422]5/2^+ - \nu[301]3/2^-$ component in its wavefunction. This relies on a large prolate deformation which was confirmed in the isotope shift measurements of Thibault et al. [111]. As seen in Table 4.7, such a prolate deformed state of $I^\pi = 4^-$ can be accommodated in the calculations at low energy, where one level with $I^\pi = 4^-$ and the same configuration as proposed by Ekström [90] is found. Note that the alternative $\pi[301]3/2^- - \nu[422]5/2^+$ assignment for this state would result in $\mu = 0.479\ \mu_N$, deduced from the following expression derived by Bohr and Mottelson [118] assuming the validity of the asymptotic-quantum number description:

$$\mu = (g_\Omega \Omega + g_R) I/(I+1) \tag{4.21}$$

$$g_R = 0.8 Z/A \tag{4.22}$$

and using the values $g_k(\pi[312]3/2^-)$=0.32 and $g_k(\nu[422]5/2^=)$=-0.10.

Based on the small observed beta feeding we conclude that the states at 103.3 and 160.8 keV have a rather different shape from the ^{78}Sr ground state and must therefore be spherical. If we look at Table 4.7 we see several possibilities for spherical 1^+ states and we can only say that they probably belong to one of these configurations.

Turning now to the 0^+ ground state we find that Thibault et al. [111] also measured the isotope shift for this state. They conclude that it has a large prolate deformation. The 0^+ ground state and the observed 3^+ excited state at 119.6 keV can be interpreted as arising from the $\pi[312]3/2^-$ and $\nu[301]3/2^-$ configuration $((|\Omega_p - \Omega_n|)$ and $(\Omega_p + \Omega_n)$ respectively). A different possibility for the 0^+ ground state that should be considered corresponds to the $\pi[422]5/2^+$ and $\nu[422]5/2^+$ coupling. Although the G-M rule predicts in this case a 5^+ state below the 0^+ state, a violation of the G-M rule cannot be discounted. This interpretation would agree with the expectation based on the assigned ^{79}Rb ground state configuration of $\pi[422]5/2^+$ and the $\nu[422]5/2^+$ configuration for the ^{77}Kr ground state, shown in Fig. 4.15, as proposed by Ekström et al. [90]. One should also note that the 0^+ deformed ground state will generate a rotational band with an odd-even Newby shift [119] [1] in the rotational energy levels.

The main characteristic of the states in family A is the small log ft values which link them closely to the ^{78}Sr parent state structure. Thus we see them as prolate-deformed states. From table 4.7 we see that two prolate states are predicted at low excitation energy with configurations $\pi[431]3/2^+ - \nu[422]5/2^+$ and $\pi[431]3/2^+ - \nu[431]1/2^+$ and can therefore be assigned as possible configurations for the two lowest states. In the first case a 4^+ state is expected below the 290.0 keV 1^+ level which could be identified with the 4^+ level observed at 115 keV energy in the in-beam experiments [95].

This part of the work which involves the study of the β-decay of ^{78}Sr with high resolution spectroscopy has been published in Phys. Rev. C84, 054311 (2011).

---

[1] The expected level spacing predicted by the nuclear collective model for rotational states is given by

$$E(I) = \frac{\hbar^2}{2\zeta} I(I+1) \quad (K \neq 1/2) \tag{4.23}$$

where ζ is the effective moment of inertia. However the experimental data for odd-odd nuclei show that this rule is not always valid. The levels of odd spin I present an energy shift relative to those of even I within a K=0 rotational band. One clear example of this so-called Newby shift is present in ^{241}Am. The I=1 state can be observed to be shifted downward and lying below the I=0 state in the K=0 band. This effect is due to residual n-p interaction.

Chapter 5

The decay scheme of ^{77}Sr

In this chapter we report the results of the analysis of the data on the decay scheme for ^{77}Sr from our experiments at CERN. Both γ-γ coincidence and electron conversion measurements were carried out with the mini-orange setup in 2006.

5.1 The previous level scheme

There has been only one previous study of the β^+/EC decay of ^{77}Sr carried out by Lister et al [80] in 1983. ^{77}Sr was produced in a ^{40}Ca(^{40}Ca,2pn) reaction with the use of an oil vapour helium-jet transfer system. The decay scheme of the levels in ^{77}Rb was established from γ-γ coincidences. For such measurements. a Ge planar detector for low energy gamma and X-rays and a Ge co-axial detector for higher energy photons were used. The half-life of ^{77}Sr was measured as $T_{1/2}=9.0\pm0.2$ s, from 4 of the strongest γ-ray transitions observed in the decay. Beta end-point measurements were performed in a beta-gamma coincidence setup and a Q_{EC} value of 6986±227 keV was deduced. In total 4 levels and 5 γ-ray transitions were firmly placed in the level scheme. 2 other levels and 2 γ-ray transitions were also tentatively placed as shown in Fig. 5.1.

The same authors reported an in-beam experiment on ^{77}Rb in the same publication. They established 2 bands based on low lying-levels. In 1993 a very detailed in-beam study was performed by Harder et al. [121] where 7 bands and information on many of the levels at low spin was obtained based on DCO ratio measurements. Their results confirmed the measurements of Lister et al.

On the other hand the spin and parity of ^{77}Rb g.s. has been extensively studied by Ekström et al. [90] and Thibault et al. [111]. Their results show a spin of I=3/2 and nuclear moment μ=0.65(3) μ_I. A negative parity assignment has been made since ^{77}Rb decay proceeds mainly to negative parity states in ^{77}Kr. This is in agreement with a configuration of [312]$3/2^-$ in the Nilsson diagram.

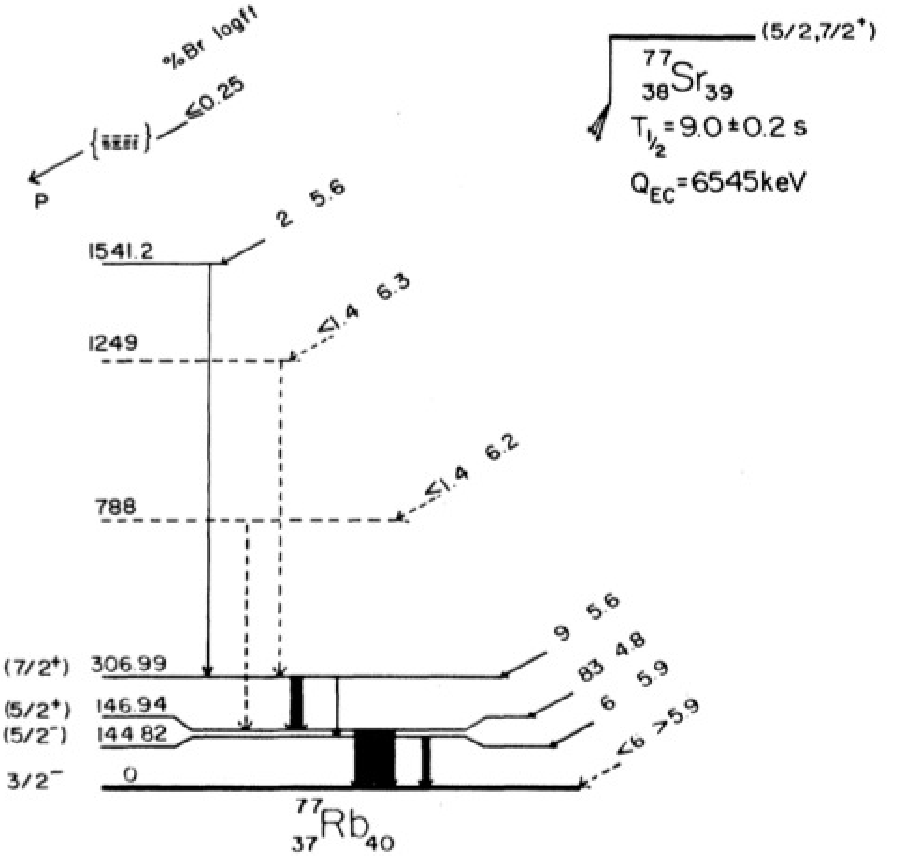

Figure 5.1: Previous level scheme of ^{77}Rb by Lister et al.

Turning now to the ground state of ^{77}Sr, Lievens et al. [122] measured a spin I=5/2 and μ=-0.348(4) based on hyperfine splitting and isotope shift measurements. The values deduced in their work agree with an assignment of [422]$5/2^+$ for the ground state unambiguously, thus setting a positive parity. Since the decay of ^{77}Sr to the ground state of ^{77}Rb is parity changing, ΔJ=1 or 2, the systematics of β-decay in the region [109] limit the log ft to >5.9. Therefore the beta feeding to the ground state is limited to < 6%. No measurements have been performed to estimate its value.

5.2 Data analysis

The procedure for the data analysis is the same as that described for the decay of ^{78}Sr. The singles spectra were used to determine the energy and intensity of the gamma-ray transitions. γ-γ coincidence matrices were built in order to extract the level sequences and the relations among the different gamma-transitions observed. In this case two matrices of 4k$\otimes$4k were built, namely planar$\otimes$DaVinci and co-axial⊗DaVinci. The reader is referred to section 4.2 for details of the energy and efficiency calibration of the different detectors and the level scheme construction.

5.3 Determination of the levels in the decay of ^{77}Sr and their γ-ray transitions

Figure 5.2 shows the two main coincidence spectra gated on the gamma transitions at 144.8 and 146.9 keV in the planar detector. The experiment suffered from very poor statistics and hence not many details on the level structure of the decay of ^{77}Sr could be deduced. The energies and intensities were extracted from the weighted mean values derived from the singles spectra of the 3 detectors used. The following conditions were followed when deducing the gamma energies and intensities:

- The transitions with E>820 keV are only observed in the co-axial and DaVinci detectors.
- Only the two detectors of the telescope were used for the determination of the gamma intensities since no efficiency calibration was available for DaVinci (see text in Sec. 4.2).
- The planar is affected by the summing. The intensities observed with this detector are thus corrected using the procedure discussed in section 4.2. In case of a high deviation in the intensity of one particular transition measured with this planar with respect to that measured with the co-axial, the latter only is considered.

Table 5.1 shows the energy of the γ-ray transitions and relative intensities obtained from the analysis. The intensities of the transitions in this table have been normalised to the 146.9 keV line. Table 5.2 shows the lines coincident with each gamma-ray observed in the decay of ^{77}Sr. The decay scheme for ^{77}Sr to levels in ^{77}Rb deduced from the present work is shown in Fig. 5.6. It should be noted that the γ-ray transition at 24.5 keV was not observed in the coincidence spectra since it is below our sensitivity limit. However it appeared as a clear peak in our singles and electron spectra. In the early work by Lister et al [80] they already inferred the existence of this transition from the coincidence data in their in-beam studies. The energy they assigned to this transition was based on level energy difference. On the other hand they calculated its intensity from intensity balance assuming no side feeding to the level it de-excites. A similar procedure was carried out by Harder et al. in relation to this transition and they assigned an M1/E2 multipolarity. No further arguments are given to support this assignment. Based on the above, we have added this γ-ray de-exciting the level at 331.7 keV to the level scheme in Fig. 5.6. On the other hand, the γ-ray transition at 59.8 keV was highly contaminated by the Tungsten X-rays. Its energy has been deduced based on level energy differences and its intensity extracted from the analysis of the γ-γ coincidences. Figure 5.3

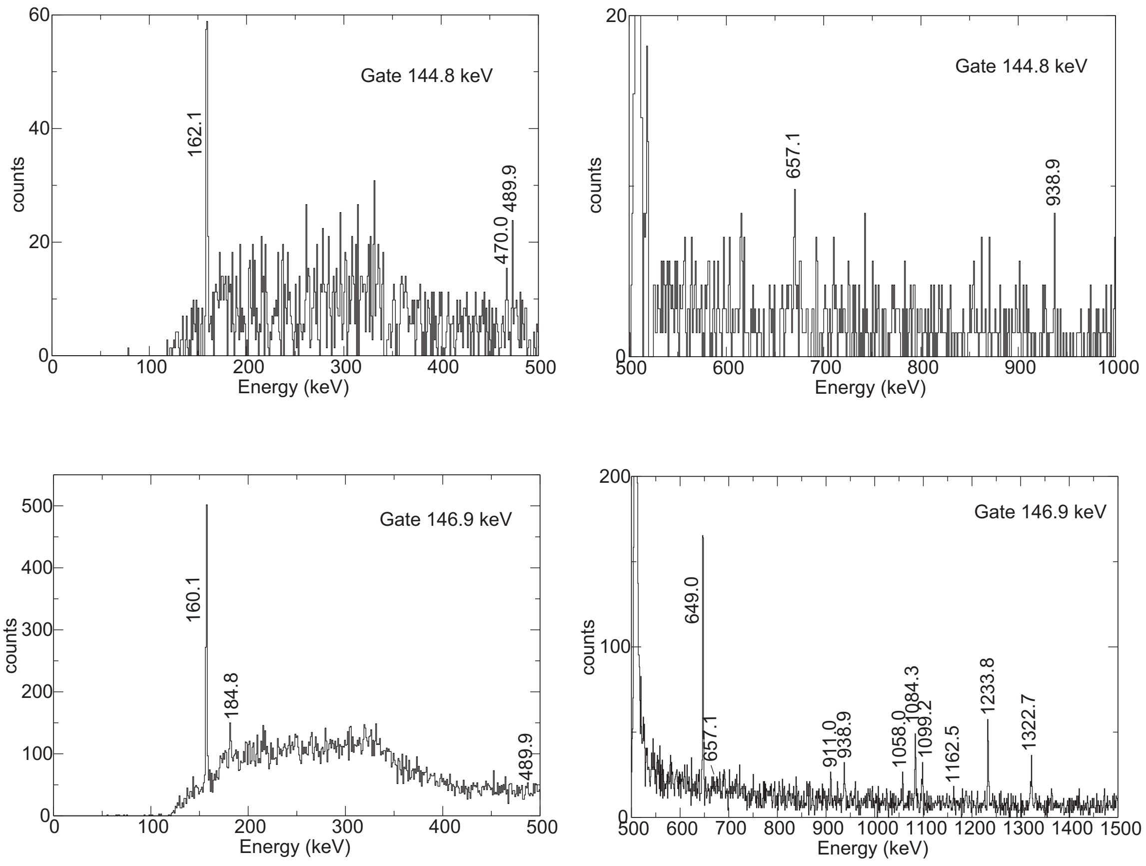

Figure 5.2: Projection of the spectra in DaVinci obtained by gating on the 144.8 keV (a and b) and 146.9 keV (c and d) in the planar detector.

shows the gate on the 160.1+162.1 KeV lines in DaVinci projected on the planar detector where this transition can be clearly observed. This is the first evidence of the existence of this line, which was not observed in previous studies [80, 121].

In summary we have confirmed 3 of the levels and 5 of the gamma-ray transitions observed by Lister et al. It should be noted that we have placed the 1234 keV transition in a different place in the level scheme than Lister et al. Moreover, we were not able to confirm the 942.0 and 641.2 keV gamma-rays as belonging to the decay of ^{77}Sr. In addition, 8 of the gamma-ray transitions and 6 of the levels observed in the present study were also seen in the in-beam experiment by Harder et al. The relative intensities deduced in this work are in complete accord with these previous 2 works. In total 9 new levels and 15 new gamma-ray transitions have been identified. The normalization factor between the transition intensities given in Table 5.1 and

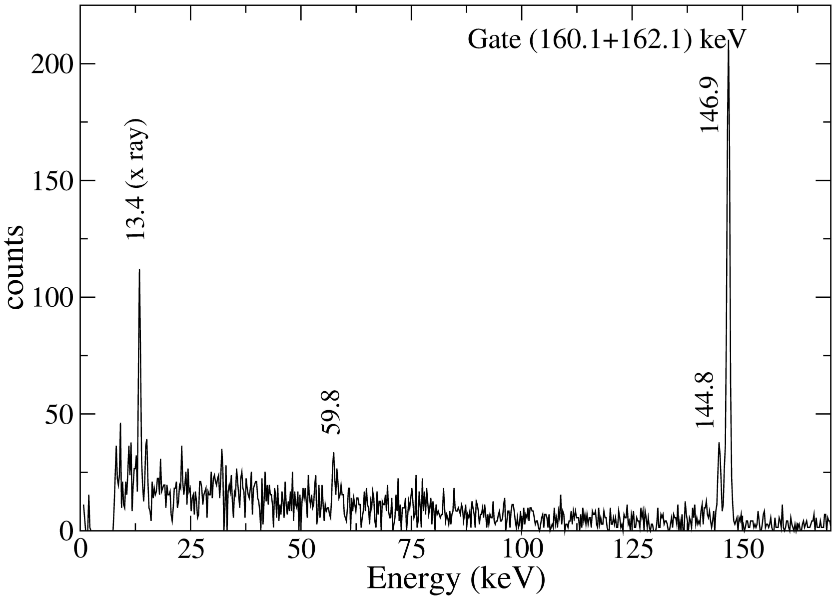

Figure 5.3: Projection of the spectra in the planar detector obtained by gating on the 160.1+162.1 keV lines in Davinci. This gate shows the existence of the 59.8 keV line in the level scheme of ^{77}Rb, firstly seen in this work.

Fig. 5.6 is 0.8576.

5.4 Determination of the electron conversion coefficients in the decay of ^{77}Sr

The same procedure described in the previous chapter for the decay of ^{78}Sr has been followed to determine the electron conversion coefficients in ^{77}Rb. The transmission curves in Fig. 4.11 are also valid in this case. Figure 5.4 shows the conversion electron spectrum with one of the two arrangement of magnets used. The different conversion lines and the atomic shell in which conversion takes place are marked. The CE of the line at 24.5 keV could not be extracted since it can only be seen with the planar which was affected by fluctuations in its acquisition. In addition, the transmission curve is not well determined for such low energies. This latter problem also occurs with the line at 59.8 keV with the additional difficulty of resolving the gamma transition in the the co-axial detector spectrum since it is highly contaminated by the W X-rays as stated above. Harder et al. derived the multipolarity of the lines at 144.8, 146.9, 160.1, 162.1, 184.8, 368.1 and 470.0 keV based on DCO ratios. They assigned an M1/E2 character to the 144.8 and 160.1 keV lines but no information on the multipole mixing, δ, could be provided for the 144.8 keV line. We intend to extract such information from the electron spectra measured in this work in order to determine their total intensities more

E_γ(keV)	Relative Intensity	E_{level}(keV)
24.5(2)	21(7)	331.7
59.8*(4)	38*(12)	368.1
144.8(4)	870(60)	144.8
146.9(3)	10000(700)	146.9
160.1(2)	1120(70)	307.2
162.1(3)	233(13)	307.2
184.8(3)	140(30)	331.7
368.1(2)	97(10)	368.1
470.0(4)	38(3)	614.8
489.4(3)	52(11)	795.7
649.0(2)	480*(50)	795.7
657.1(2)	172(16)	963.4
911.0(2)	199(17)	1055.8
938.9(2)	154(14)	1245.2
964.1(3)	61(9)	963.4
1058.0(3)	22(7)	1202.8
1084.3(2)	300(30)	1231.8
1099.2(3)	184(17)	1245.2
1162.5(3)	63(9)	1469.6
1233.8(3)	380(30)	1378.6
1237.6(3)	85(10)	1381.2
1322.7(3)	86(10)	1469.6
1378.1(3)	54(7)	1378.6
1381.0(3)	166(15)	1381.2

Table 5.1: List of the γ-ray energies and relative intensities from the β-decay of ^{77}Sr with their uncertainties and the level they decay from. The intensities are normalised to the 146.9 keV γ-ray. The gamma-ray energies and intensities obtained from coincidences have been marked with an asterisk.

accurately and extract the conversion coefficients. As observed in Fig. 5.4, it is difficult to resolve the 144.8K- and 146.9 K-lines in the peak at ~125 KeV and the 144.8L-, 146.9L-, 160.1K- and 162.1K-lines in the peak at ~140 KeV in the electron spectrum. The transition at 146.9 KeV is known to be an E1 transition [121]. For the analysis of the first peak, we have used the α_K of this transition to obtain the α_K for the 144.8 keV line. For the analysis of the second peak, the α_K and α_L of the 146.9 and 162.1 lines respectively, both with E1 character [121], and the α_L of the 144.8 keV line, whose CE was deduced previously, have been used in order to derive the α_K of the 160.1 keV K-line. A multipole mixing ratio of δ=0.470±0.019 is extracted for this transition in accord with the value 0.39(6) obtained in [80] based on angular distribution measurements. In addition, the CE of the 184.4 keV line has

E_γ(keV)	Coincident lines
59.8	144.8, 146.9, 160.1, 162.1
144.8	59.8, 162.1, 470.0, 489.9, 657.1, 938.9, 1162.5, 1237.6
146.9	59.8, 160.1, 184.8, 489.9, 649.0, 657.1, 911.0, 938.9, 1058.0, 1084.3 1099.2, 1162.5, 1233.8, 1322.7
160.1	59.8, 160.1, 489.9, 657.1, 938.9, 1162.5
162.1	59.8, 146.9, 489.9
184.8	59.8, 144.8, 489.9
470.0	144.8
489.4	144.8, 146.9, 160.1, 162.1
649.0	146.9
657.1	144.8, 146.9, 160.1, 162.1
911.0	146.9
938.9	144.8, 146.9, 160.1, 162.1
1058.0	146.9
1084.3	146.9
1099.2	146.9
1162.5	144.8, 146.9, 160.1, 162.1
1233.8	146.9
1237.6	144.8
1322.7	146.9

Table 5.2: List of observed coincident gamma-ray lines for each gamma transition observed in the decay of ^{77}Sr. Note that the gamma transition at 24.5 keV does not appear on the table since it was not observed in the coincidence spectra (see text).

been deduced from this work. It is in agreement with the E2 multipolarity reported by Lister et al. [80] and Harder et al. [121]. Table 5.3 shows the results of the CEs obtained in this work in conjunction with the multipolarities deduced from a comparison with the theoretical values [108] shown in Fig. 5.5.

E_γ(keV)	α_K	Multipolarity	Comment
144.8	0.11±0.06	M1+E2	a
160.1	0.061±0.011	M1+E2	a
184.8	0.073±0.016	E2	b

Table 5.3: Conversion coefficients measured for different transition in ^{77}Rb. The comments correspond to the following: (a) Measured with the configuration of magnets 4/8/125.(b) Measured with the configuration of magnets 6/8/125.

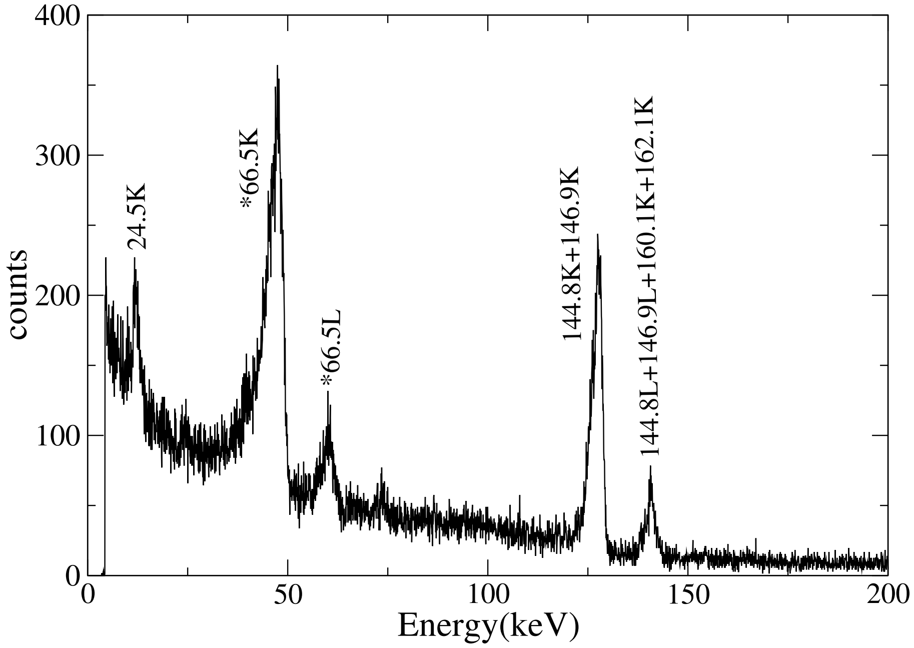

Figure 5.4: A conversion electron spectrum measured with the arrangement 4/8/125. The conversion electron lines are marked with the energies of the electromagnetic transition involved and the atomic shell in which conversion occurred. All of them are assigned to transitions in ^{77}Rb, except the 66.5 K- and L- lines that belong to ^{77}Kr. Note that the peaks marked as L- correspond to the L+M component since they cannot be resolved.

5.5 Beta feeding and log ft values

The total intensity for each transition was obtained and the beta feeding to each level observed in the level scheme of ^{77}Rb deduced from a simple intensity balance (see Eq. 4.8). The beta feeding, log ft and B(GT) values extracted from this work are given in Table 5.4. As can be observed, most of the strength, namely 62 %, goes to the level at 146.9 keV. Figure 5.6 summarises all the knowledge we have derived from this experiment for the decay of ^{77}Sr. The total Gamow-Teller strength in the β-decay of ^{77}Sr results in the following value:

$$B(GT) = (0.29 \pm 0.04)\frac{g_A^2}{4\pi} \tag{5.1}$$

This result will be compared to the value obtained from measurements with LUCRECIA in order to account for the relevance of the pandemonium effect with high resolution measurements in this nucleus. The poor statistics of this experiment have only allowed us to obtain information up to 1470 keV while the Q$_{EC}$ is 7020 keV [67]. This means there might be an important part of the Gamow-Teller strength lying at higher energies which cannot be seen in this type of experiment. The information

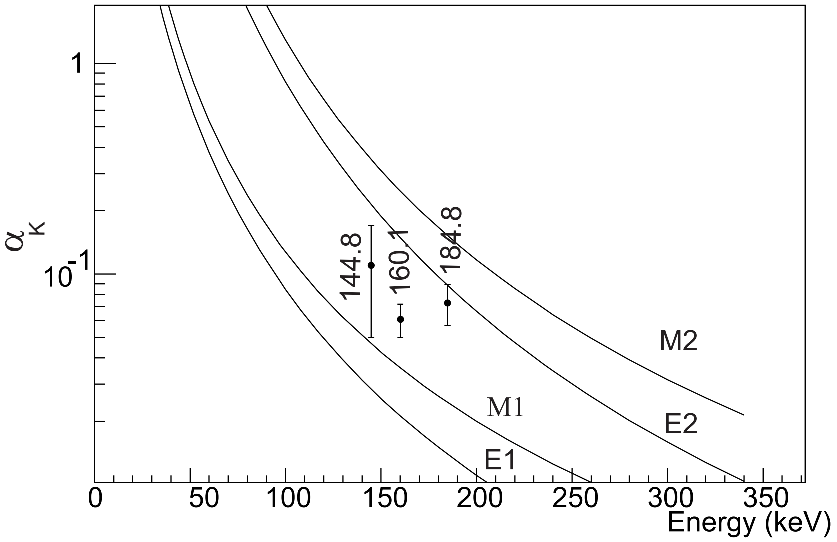

Figure 5.5: The measured conversion coefficients for transitions in ^{77}Rb measured in studies of the decay of ^{77}Sr. The graph shows the K-component of the conversion coefficients. The points are labelled with the shell in which conversion occurs and the energy of the transition.

extracted in this part of the work will be used for the construction of the response matrix for the decay of ^{77}Sr in order to analyse the TAS data for the same decay.

5.6 Discussion of the parity and spin assignments to the levels

In this section the parities and spins of the different energy levels listed in Table 5.4 will be discussed. As mentioned before, the spin and parity of the ground state of ^{77}Rb has been studied by Ekström et al and Thibault et al. They report I=3/2 and a negative parity consistent with the measured nuclear moment. On the other hand, the spin of the ground state of ^{77}Sr was measured with isotope shift measurements which resulted an I=5/2. A positive parity is set unambiguously and further arguments are given in their publication and summarised in section 5.1. The following discussion is based on these two assigments.

- *144.8 keV level*: it decays by an M1/E2 transition to the ground state. This establishes a firm negative parity and possible spins I=1/2, 3/2 and 5/2. It

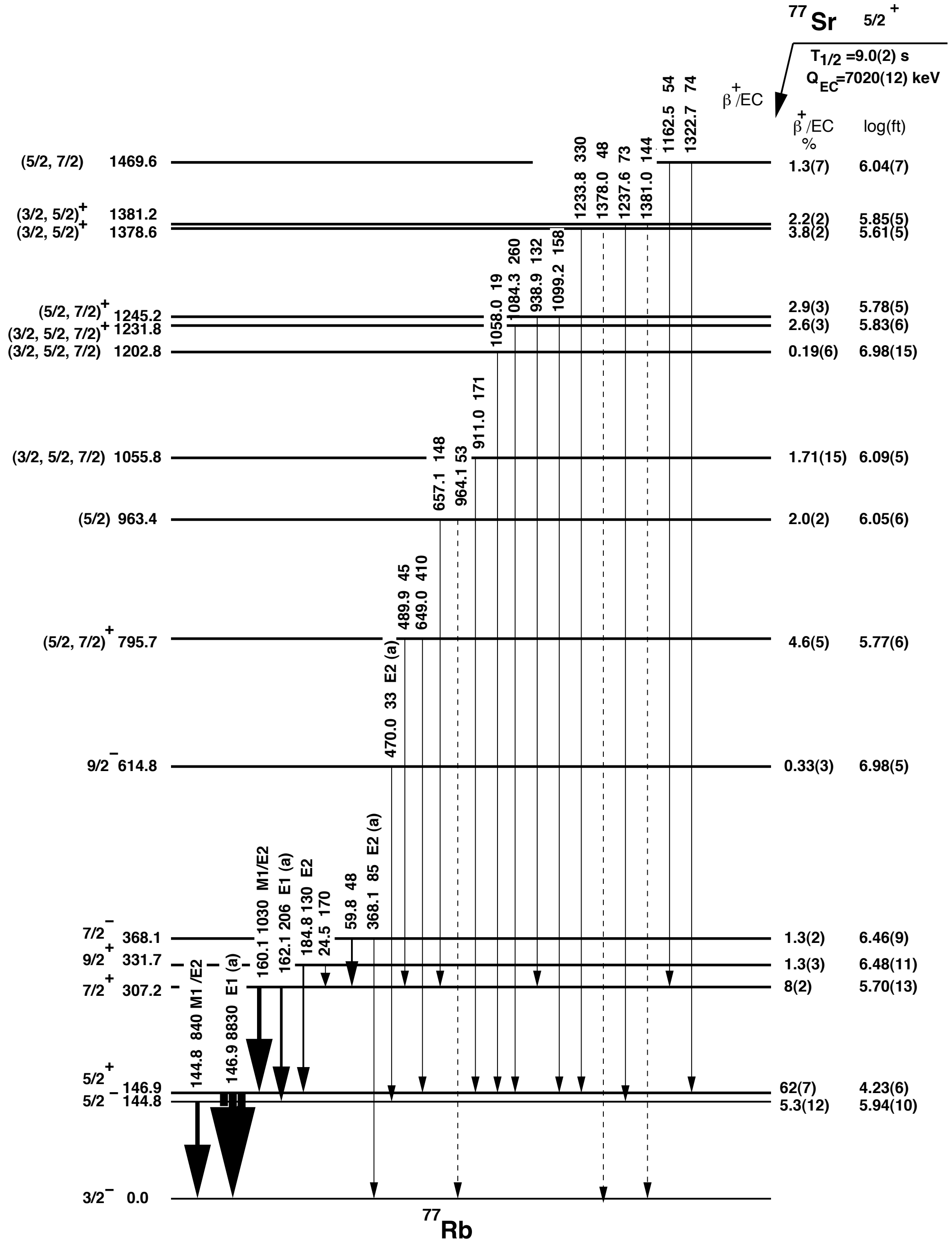

Figure 5.6: Level scheme of ^{77}Rb. The transition intensities are normalised to a total intensity of 10,000 units feeding the ground state. The assigned I^{π} values and level energies in keV are shown on the left. The percentage feeding in the β-decay and corresponding log ft values are shown on the right. The γ-ray energies and multipolarities measured are marked on the figure. It should be noted that those multipolarities marked with an (a) have been extracted from reference [121] where the CEs were deduced from angular distribution measurements in an in-beam study of ^{77}Rb. The half-life and Q_{EC} value of ^{77}Sr [67, 68] are also shown.

E_{level} (keV)	I^{π}	$\beta_{feeding}$ %	log ft	BGT $\times 10^2$
0	$3/2^-$	<6	-	-
144.8	$5/2^-$	5.3(12)	5.94(10)	0.44(11)
146.9	$5/2^+$	62(7)	4.23(6)	22(3)
307.2	$7/2^+$	8(2)	5.70(13)	0.8(2)
331.7	$9/2^+$	1.3(3)	6.48(11)	0.13(3)
368.1	$7/2^-$	1.3(2)	6.46(9)	0.13(3)
614.8	$(9/2)^-$	0.33(3)	6.98(5)	0.040(5)
795.7	$(5/2,7/2)^+$	4.6(5)	5.77(6)	0.65(8)
963.4	(5/2)	2.0(2)	6.05(6)	0.34(4)
1055.8	(3/2,5/2,7/2)	1.71(15)	6.09(5)	0.31(3)
1202.8	(3/2,5/2,7/2)	0.19(6)	6.98(15)	0.040(13)
1231.8	$(3/2,5/2,7/2)^+$	2.6(3)	5.83(6)	0.56(8)
1245.2	$(5/2,7/2)^+$	2.9(3)	5.78(5)	0.63(7)
1378.6	$(3/2,5/2)^+$	3.8(2)	5.61(5)	0.94(11)
1381.2	$(3/2,5/2)^+$	2.2(2)	5.85(5)	0.54(7)
1469.6	(5/2,7/2)	1.3(7)	6.04(7)	0.35(5)

Table 5.4: Measured β-decay feedings, log ft values and B(GT) values obtained for each energy level. The beta feeding to the ground state has not been considered in the calculations. The I^{π} values of the levels are also listed.

is fed by an E1 transition from the level at 307.2 keV. This latter level does not decay to the ground state and we can thus assign a spin of $I \geq 7/2$ with positive parity. Therefore this establishes a spin of 5/2 for the level at 144.8 keV and a spin and parity of $7/2^+$ for the 307.2 keV level.

- *146.9 keV level*: it decays by an E1 transition to the ground state. The dipole character of this transition is extracted from angular distributions [80] and DCO ratios [121] and thus assigned based on the fact that it is not mixed. A positive parity is then confirmed. It is fed by an M1/E2 transition from the level at 307.2 keV with spin $7/2^+$ (see text above). It is thus firmly established as $I^{\pi}=5/2^+$.

- *307.2 keV level*: it is established as a $7/2^+$ state based on earlier arguments (see discussion of level 144.8 keV).

- 331.7 keV level: Since it does not decay to the ground state via an E1 or M1 transition, its spin must be $I \geq 7/2$. It feeds the $5/2^+$ level at 146.9 keV with an E2 gamma transition which thus sets a spin-parity of $9/2^+$ for this level. The relatively strong 24.5 keV gamma transition between this level and the level at 307.2 keV indicates a difference in spin of $\Delta I=1$ which agrees with

$9/2^+$. It is also consistent with the small beta feeding observed.

- *368.1 keV level*: It decays via an E2 transition, also observed by Lister et al. [80] and Harder et al. [121], to the 3/2− g.s. This establishes a spin-parity of $7/2^-$. A transition of 59.8 keV is observed to de-excite this level into the level at 307.2 keV, which has not previously been reported by the latter authors. They observe an additional 223 keV transition decaying into the level at 144.8 keV which we do not see since it is is below our sensitivity.

- *614.8 keV level*: We see this level only through the existence of a 470 keV transition which is also assigned an E2 character by Harder et al. This makes this level a $9/2^+$. The existence of this level is further confirmed by an E1 transition to the $7/2^+$ level at 307.2 keV, observed in-beam by Harder et al., and a E2/M1 transition to the $7/2^-$ level at 368.1 keV, observed both by Harder et al. and Lister et al. in their in-beam work. We do not see these transitions since they are below our sensitivity.

- *Levels above 615 keV*: The levels observed above 615 keV have not been seen in previous in-beam works [80, 121] and therefore, the information on them is very limited since angular distributions or DCO ratios are not available. Based on the beta feeding observed in our work and taking into account the compilation of Raman and Gove of logft values for allowed GT transitions [109], we assign a positive parity to those levels with a log ft value less than 5.9. Tentative spins have been assigned assuming that M1 gamma transitions are favoured.

5.7 Interpretation of the level structure of ^{77}Rb

In this section, we will discuss the structure of the levels in ^{77}Rb observed in the β-decay of ^{77}Sr in this work. We will use the same type of HF+BCS calculations as for ^{78}Sr. In this particular case, the parent nucleus ^{77}Sr (Z=38, N=39) will be described by removing one neutron from the self-consistent mean field derived for the close even-even nucleus, ^{78}Sr (Z=38,N=40). The same is done for the daughter nucleus ^{77}Rb (Z=37, N=40) but removing one proton. Therefore both the parent and daughter are described by the same mean field. These calculations are performed for the two equilibrium shapes for which we obtained minima in the energy surfaces in ^{78}Sr (see Sec. 4.8), namely a prolate deformation with β=0.42 and a spherical shape. The reader should find more details of how these microscopic calculations are performed for odd-A nuclei in Ref. [123]. For a prolate ground state in ^{77}Sr, a spin of $5/2^+$ is found whereas for a spherical shape the calculations result in a spin $I=1/2^-$ [51]. The former agrees with the experimental value for the spin of the ground state in ^{77}Sr [122] and is also consistent with the predicted deformation of $\beta \approx 0.4$ in the same publication based on the measured spectroscopic quadrupole moment. Therefore, in what follows we will restrict ourselves to only the results obtained from the converged mean fields of the ^{78}Sr at a prolate equilibrium shape using the SG2 force. Results with other Skyrme forces differ only slightly and will not be presented here. In summary, our calculations for a prolate deformation suggest that the structure of ^{77}Rb must be governed by the $\pi[431]3/2^+$ and $\pi[312]3/2^-$ proton (hole) orbits and the $\nu[422]5/2^+$, $\nu[303]5/2^-$ and $\nu[301]3/2^-$ neutron (particle) orbits. These are consistent with the single-particle spectrum predicted by Nazarewicz et al [38] and shown in Fig. 5.7. It also agrees with the measured spins of the ground state in ^{77}Sr and ^{77}Rb [111] since adding a neutron-hole or a proton-hole to the ^{78}Sr core, results in I^π=5/2$^+$ in ^{77}Sr and 3/2$^-$ in ^{77}Rb.

Once the single-particle energies, wave functions and occupation probabilities are derived from the HF+BCS calculations, a separable spin-isospin residual interaction is introduced in both particle-hole and particle-particle channels and treated in the QRPA approximation to describe Gamow-Teller transitions. In order to interpret the energy spectrum of ^{77}Rb we will only use the mean field approximation since then we can associate each calculated level to a clear configuration. Firstly we will try to deduce from a qualitative point of view which kind of levels we can expect in ^{77}Rb from the decay of ^{77}Sr.

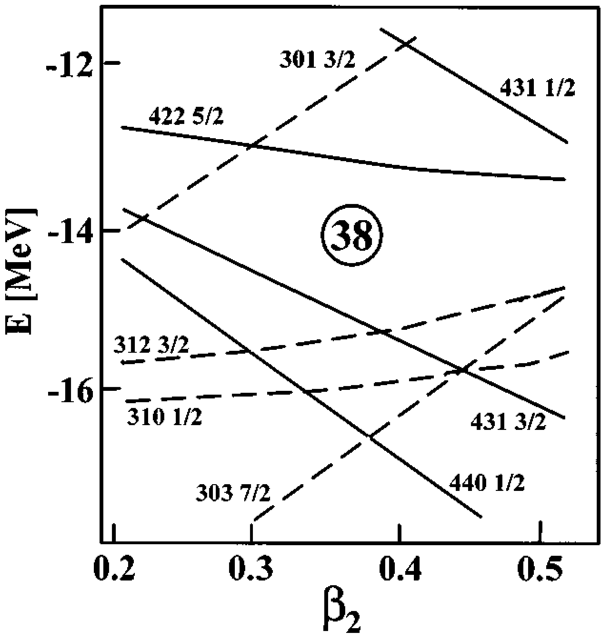

Figure 5.7: Single-particle spectrum near the N=Z=38 deformed shell gap calculated by Nazarewicz [38].

The ground state of ^{77}Sr can be expressed as a one-quasiparticle (qp) nucleon (neutron) occupying the lowest single-particle state in energy, as shown on the left of Fig. 5.8. Two type of transitions can occur, represented schematically in the same figure, and are expected at different excitation energies:

- 1qp type: this transition involves only the proton which is transformed into a neutron occupying the same orbital as that of the odd neutron in the parent, as shown in Fig. 5.8. Therefore we call the final state a 1 qp state (proton). The excitation energy can be calculated as:

  $$E^*_{1qp} = E^{\pi}_{qp} - E^{\pi_0}_{qp} \tag{5.2}$$

  where E^{π}_{qp} is the quasiparticle energy of the only proton involved in the transition and E_{π_0} is the lowest quasiparticle energy for protons. For the calculation of the quasiparticle energy we can use Eq. 5.2. In this case, the energy for the Fermi level obtained from the HF+BCS calculations is -3.188 and -13.57 MeV for protons and neutrons. The proton and neutron gap used in the calculations is 1.5 MeV for both protons and neutrons.

- 3qp type: in this transition the odd neutron acts only as a spectator and thus we end up with a 3 qp excitation, as shown in Fig. 5.8. The decay is basically the same as in the even-even case but with the blocked neutron orbital excluded from the calculation. The excitation energy of this state with respect to the ground state in the daughter nucleus is given by:

  $$E^*_{3qp} = \omega + E^{\nu,spect}_{qp} - E^{\pi_0}_{qp}; \quad with \quad \omega = E^{\pi}_{qp} + E^{\nu}_{qp} \tag{5.3}$$

  in order words, ω is the energy needed to produce a 1proton - 1neutron excitation in the decay of the even-even case. $E_{\nu,spect}$ is the quasiparticle energy of the neutron which acts as an spectator in the decay. As in the previous case, the lowest quasiparticle energy for the proton, $E^{\pi_0}_{qp}$, needs to be subtracted in the calculation.

From Eq. 5.3, it can be concluded that the lowest excitation energy of a 3qp type must be of the order of twice the neutron pairing gap, which is around 1-1.5 MeV (it should be noted that the theoretical calculations have used a value of 1.5 MeV for the pairing gap of the proton and neutron). Therefore, all the strength observed below approximately 2-3 MeV can be attributed to transitions of 1qp type only. The measurements performed in this work with high resolution spectroscopy only provides us with information on the low lying states up to an energy of 1400 keV. Consequently, we only have access to 1qp type transitions which basically tells us about the proton spectrum.

In an odd-A nucleus like the one under study, there is a set of rotational members built on each K_f bandhead, with K_f the total angular momentum projection on the

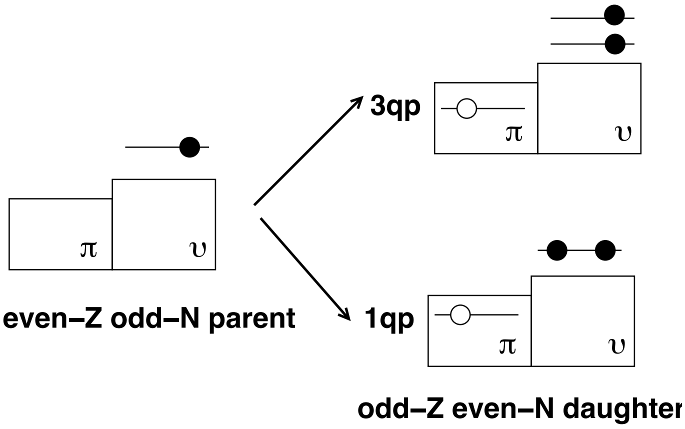

Figure 5.8: Possible β-decays in an even-Z odd-N nucleus shown in an schematic way.

symmetry z-axis for the final state. Therefore, for each allowed GT transition to a particular K_f bandhead, the strength gets distributed through the different members of the rotational band for which the allowed GT rules apply. The strength within a band to its rotational states will decrease as the excitation of the rotational states increases. The rotational nature of the final states that can be reached by GT transitions has thus been taken into account in the calculations. Therefore for a given K_i=I_i initial state from the parent, with I the parent g.s. spin, we have the following possibilities of final states populated in the daughter:

- (a) K_f=K_i-1: I_f=K_i-1, I_f=K_i and I_f=K_i+1
- (b) K_f=K_i : I_f=K_i and I_f=K_i+1
- (*c*) K_f=K_i+1: I_f=K_i+1

Consequently, by considering the different rotational states we are providing a more accurate fragmentation of the GT strength and also a more realistic density of excited states in the daughter nucleus.

Table 5.5 shows the different GT allowed transitions which involve only 1qp transitions obtained from our model. For each K_f banhead, only the rotational states which receive strength according to the selection rules are shown. The third column reports the Nilsson orbitals of the odd proton involved in the decay which is transformed into a neutron occupying the [422]5/2$^+$ forming a Cooper pair with the parent odd neutron and leaving an unpaired proton. The excitation energies and the GT strength derived from the calculation for each of the rotational state are also shown. The reader should note that we have added to the excitation energies

Allowed GT transitions					
K_f	I_f	π orbital	E_{exc} (MeV)	$B(GT)_{th}$ ($g_A^2/4\pi$)	$B(GT)_{exp}$ ($g_A^2/4\pi$)
$3/2^+$	$3/2^+$	$[431]3/2^+$	0.0514	0.0683	
	$5/2^+$		0.2226	0.0293	
	$7/2^+$		0.4623	0.0049	
$5/2^+$	$5/2^+$	$[422]5/2^+$	0.2390	0.0449	0.22(3)
	$7/2^+$		0.4788	0.0179	0.008(2)
$7/2^+$	$7/2^+$	$[413]7/2^+$	3.1607	0.0016	
First forbidden GT transitions					
$3/2^-$	$3/2^-$	$[312]3/2^-$	0.5573		-
	$5/2^-$		0.7285		0.0044(11)
	$7/2^-$		0.9682		0.0013(3)

Table 5.5: Rotational states populated in the decay of ^{77}Sr according to the results from HF+BCS calculations with the Skyrme force SG2 for the proton orbital assuming a prolate shape. The table is divided into two sections corresponding to the allowed GT and first forbidden transitions respectively. The bandhead of the rotational bands K_f and the associated rotational members populated in the decay are shown with their spins. The asymptotic quantum number $[Nn_z\Lambda]\Omega^\pi$ for the proton orbital involved in the transition, the excitation energies and the theoretical and experimental B(GT) from high resolution spectroscopy values are also given. Note that no theoretical B(GT) values are shown for the first forbidden transitions since they are not calculated in the model.

given by Eq. 5.2 the standard rotational energy [124]:

$$E_{rot} = \frac{1}{2\zeta_{cranking}}[I(I+1) - K^2] \tag{5.4}$$

where $\zeta_{cranking}$ is the moment of inertia calculated with the cranking model [125]. The value derived for our nucleus is $\zeta_{cranking}$=14.6 MeV. There is also an added section in the lower part of table 5.5 which shows the lowest first forbidden transitions of 1qp type obtained from the calculations. For these transitions, the B(GT) has not been calculated.

Based on this table, we will try to make an interpretation of the levels observed in the decay scheme of ^{77}Sr by comparison with the microscopic calculations. We will only consider levels up to an excitation energy of 620 keV since the spin and parities of higher levels are not well defined. The result of the excitation energies associated with the different configurations from the microscopic calculations should not be taken literally and will be used as a mere guide to the interpretation of the levels observed.

The levels at 0, 144.8, 368 and 614.8 keV with negative parity in our level scheme can be interpreted as the rotational members of the $K_f = 3/2^-$ band. They were also observed in the in-beam experiment by Harder et al. [121]. These states are also predicted by the theory which results in a 3/2- rotational band at low excitation energy as shown in Table 5.5. The 9/2- state does not appear in the table but it is also a member of the rotational band. These states are forbidden from the point of view of the β-decay since a change in parity occurs. Although these rotational states seem to receive a significant B(GT), the experimental values are not reliable due to the modest efficiency of the detectors which shift the strength to lower excitation energies [57] (see Sec. 2.4.1), namely the typical Pandemonium effect.

On the other hand, the theory predicts a rotational band built on the $3/2^+$ bandhead and associated to the configuration $\pi[431]3/2^+ \times \nu^2[422]5/2^+$. In fact, the $\pi[431]3/2^+$ orbital is the one predicted to lie closest to the Fermi surface in our calculations and also in the ones performed by Nazarewicz as shown in Fig. 5.7. However, this band could not be observed in our experiment nor in the in-beam work by Harder et al [121]. Their paper assigns the configuration $\pi[431]3/2^+ \times \nu^2[422]5/2^+$ to the $5/2^+$ band observed, which they call P1/P2, but this in contradiction with the fact that there should be a $3/2^+$ rotational band below. This suggests that there must be some mechanism that moves further away the predicted $[431]3/2^+$ and thus, it does not intervene in the 1qp type decay. It is worth noting that this predicted orbital has been observed in the decays of other odd-A neighbour nuclei such as ^{75}Kr [85] which present a rotational band built on the $3/2^+$ at low excitation energies and a similar deformation. Based on the arguments above, we believe that the positive parity states observed at 146.9, 307.2 and 331.7 keV with spin-parity $5/2^+$, $7/2^+$ and $9/2^+$ are the rotational members of the band built on the $\pi[522]5/2^+$ bandhead. Both the $5/2^+$ and $7/2^+$ can be populated in the decay. The calculated and experimental B(GT) values for both states are shown in Table 5.5. As can be seen, there are marked differences in the two B(GT) values for the $5/2^+$ state which can be a case of a strong Pandemonium effect.

Since high resolution spectroscopy does not provide reliable values for the strength and part of the decay has not been observed, in particular that at high excitation energies where 3qp type transitions play a role, we will leave the comparison of the predicted strength with the experimental one for Chapter 7 where the TAS results are discussed.

Chapter 6

Total absorption spectroscopy analysis

Chapters 4 and 5 present the level schemes deduced for $^{77-78}$Sr based on γ-γ coincidence and electron conversion measurements. We can rely on already published information found in the literature for the other nuclei of interest, ^{76,78}Rb [76, 77, 78]. With all this information available, we can proceed with the analysis of the TAS data. This chapter presents a detailed description of the analysis procedure. An unfolding method based on the Bayes theorem will be applied to the data from which the feeding distribution and hence, the B(GT) strength, can be obtained.

6.1 The sorting of the data

The list-mode data stored on DLT tapes were read event-by-event and saved in ASCII files. In order to improve access time and facilitate compression, the data of the different ASCII files were stored in Ttrees. Each Ttree contained the following variables:

- Clock: used to time stamp the event during the acquisition
- TAS_i with i=1-8: Energy signal of the PMT_i of the TAS.
- SumTAS: hardware sum of the signals of the 8 PMTs of the TAS.
- Betacounter_i with i=1-2: Energy signal of the PMT_i of the beta counter.
- Co-axial: energy signal of the co-axial detector.
- Planar: energy signal of the planar detector.

Using the analysis toolkit ROOT [104] and setting a particular condition, a projection of one or more dimensions of any of the 14 variables of the events stored could be obtained. Figure 6.1 shows examples of the projections of the TAS sum signal, beta counter sum signal and planar detector spectra in the measurement of the β-decay of ^{78}Sr.

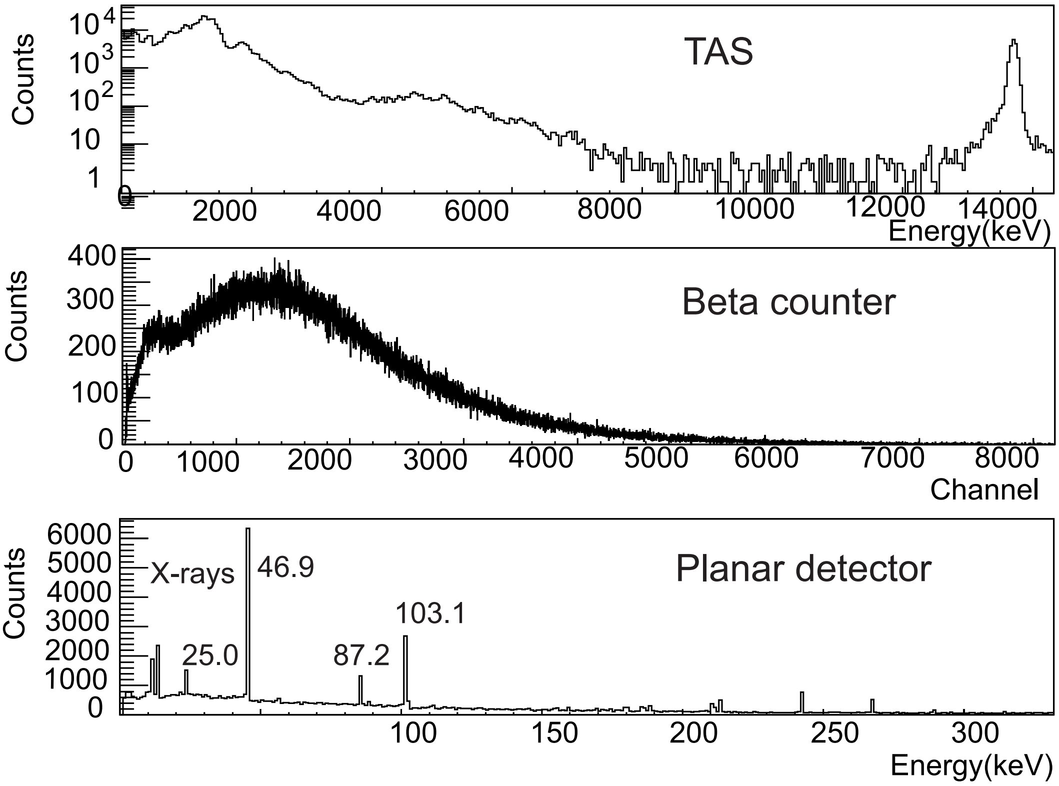

Figure 6.1: Projections of the list-mode spectra of LUCRECIA, the beta counter and the planar detector registered during the measurement of ^{78}Sr at the TAS station. Some of the most prominent gamma peaks have been marked in the planar detector spectrum. Note that the peak at the end of the TAS spectrum is caused by the light pulser which is used to check the stability of the crystal response.

In principle there are three possible philosophies for analysing the TAS spectra, namely in coincidence with the X-rays (EC-component), in coincidence with the positrons (β^+-component) or to use the singles spectra as a whole (β^++EC-component). The first and second options are cleaner since room background contamination does not need to be considered since it is very small, while the third option provides higher statistics. In the particular case of coincidences with the X-rays, the isobaric contamination is eliminated. This is especially important in cases where there is strong daughter contamination. In the case of ^{77,78}Sr the X-γ-ray coincidences are highly contaminated by the X-rays produced in the internal conversion of some highly converted, low energy transitions. The panel of Fig. 6.2 shows the TAS projection whereas the middle and lower panels show the energy spectrum of the TAS obtained when one requires a coincidence with the beta counter and the

Rb K$_\alpha$-peak in the planar detector respectively. Both spectra belong to the decay of ^{78}Sr. The energies of the peaks in the β^+ coincidence spectrum should be shifted by 1022 keV with respect to the same peaks in the X-ray coincidence spectrum. This situation does not always occur since most of the counts in the K$_\alpha$-peak in the planar detector result from the internal conversion of some highly converted low energy transitions. This is not only the case for the nucleus ^{78}Sr but also for ^{77}Sr. The other nuclei of interest, namely ^{76}Rb and ^{78}Rb, present X-ray coincidence spectra with poor statistics. Accordingly these spectra were not used in the present analysis. On the other hand, the analysis of the β^+ component implies that no information can be obtained in the last 1022 keV below the Q-value. The last 1022 keV are of extreme importance since in the cases under study it is expected that an important part of the β-strength lies in that region. Hence, the analysis of the TAS data without any coincidences (β^++EC-component) was chosen based on the arguments above. The consistency of the various forms of the analysis has been investigated by Nacher [126].

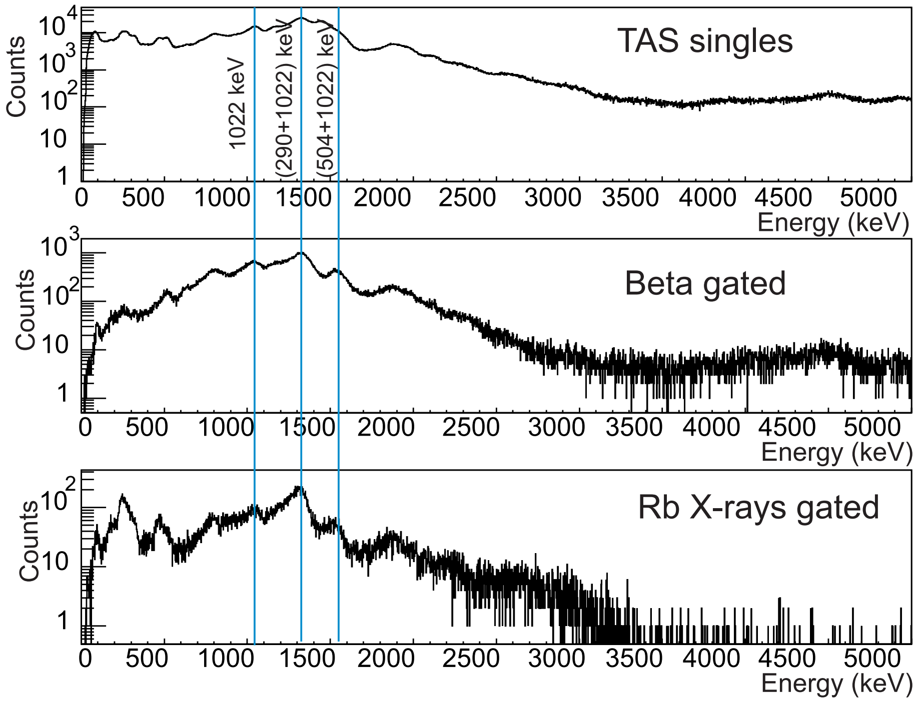

Figure 6.2: Energy spectrum of ^{78}Sr measured with LUCRECIA without requiring any condition (upper panel), requiring a coincidence with the beta detector (middle panel) and requiring a coincidence with the Rb K$_\alpha$-peak in the planar detector (lower panel).

6.2 Calibration

Standard sources, namely ^{137}Cs, ^{60}Co and ^{24}Na, were measured for energy calibration purposes. They were placed at the same position as the radioactive sources produced in the reaction and moved to the measurement position. In the case of ^{24}Na, it was produced in situ at ISOLDE after our Sr and Rb isotope production runs were completed and then steered up to the TAS station. Measurements of this particular decay play an important role in the validation of the Montecarlo simulations performed in the construction of the response matrix of the detector. Further details are given in Section 6.4.1.

6.2.1 Non-proportional light yield in a NaI(Tl) crystal

A NaI(Tl) crystal produces, for photons of energy E>200 keV, a non-proportional but approximately linear scintillator light yield L(E) given by

$$L(E) = a + bE \tag{6.1}$$

Regarding this behaviour, two photons in a cascade with energies E_1 and E_2 will produce a higher light yield than that from a single photon with energy E_1+E_2,

$$L(E_1) + L(E_2) = a + bE_1 + a + bE_2 = L(E1 + E2) + a \tag{6.2}$$

This causes an upward shift when dealing with sum peaks in a Na(I) crystal which depends mainly on the multiplicity of the cascade. We cannot speak of an energy calibration in a usual sense since the counts registered in a specific channel of the spectrum may come from different deposited energies.

This phenomenon was discovered in the late 50s [127] when the assumption of proportionality between the measured pulse height and the energy deposited by a γ-ray was found to be invalid. An intensive search resulted in order to understand the cause of such non-proportionality in the energy response of NaI(Tl) and the observation of an intrinsic resolution in the measured spectrum. Iredale [128] connected both things by saying that the non-proportional response of the crystal was mainly responsible for the intrinsic resolution observed. Three effects associated with the non-proportional light yield cause the spread in the total light produced: the full absorption of γ-rays following multiple Compton interactions, the cascade of secondary X-rays and Auger electrons following photoelectric absorption and the statistics related to the formation of δ-rays, i.e. low energy electrons produced by electron scattering in the crystal. In the end, the contribution to the amount of light corresponding to a full energy deposition of gammas in the crystal is due to numerous secondary electrons that have a variety of energies produced in the interaction of photons with matter.

This non-proportionality, for a long time forgotten in TAS measurements with NaI(Tl) crystals, was later exhaustively studied by D. Cano-Ott et al [75]. They found that the shift which is observed for the double γ-ray sum peaks is $\sim$30 keV and constant. These studies were performed in the late 90s to apply Monte Carlo simulations of the response of a NaI(Tl) TAS for beta-decay studies. Since the entire TAS spectrum is affected by this phenomenon and not only the position of the full absorption peaks, this effect cannot be considered as a simple energy recalibration of the energy deposition. Therefore it becomes of vital importance to implement the non-proportionality of the light yield in our Monte Carlo simulation. It should also be taken into account in the energy calibration.

6.2.2 Energy calibration

The centroids of the peaks in the experimental TAS spectra were determined using a fit that combines a Gaussian with an added tail [100], a step function and a linear background. Table 6.1 shows the peaks from the different gamma sources used for the energy calibration. The double gamma-ray sum peak of ^{24}Na was also used since it is the highest in energy (4152.66 keV). The $\sim$30 keV shift in energy [75] with respect to a single γ-ray of the same energy was taken into account.

Table 6.1: Experimental energy calibration points obtained from standard sources. Note that the peak corresponding to the ^{40}K decay, a contaminant present in the crystal, has also been used for the calibration.The sum peak corresponding to the decay of ^{24}Na has been marked with the superscript (a).

Source	Energy (keV)
^{137}Cs	661.66
^{60}Co	1173.2 1332.5
^{40}K	1460.85
^{24}Na	1368.7 2754.028 4152.661^{a}

The energy calibration was obtained using two different functions:

- For low energies:

$$Energy = a + b.channel + c.channel^2 \tag{6.3}$$

- For high energies:

$$Energy = a + b.channel \tag{6.4}$$

A similar procedure was used for the energy calibration of the Montecarlo simulations of the TAS crystal which are explained in Section 6.4. Here we had more flexibility in terms of calibration points since different gamma energies interacting with the TAS crystal could be simulated. In this case the centroids were fitted with the ROOT function *GetMean* [104].

Note that the energy calibrations of both the experimental data and simulations differ in the experiments carried out in 2003 and 2004 since the geometry of the TAS detector was not exactly the same. The main difference was due to the use of a different beta counter.

6.3 Subtraction of the contaminants

The raw experimental data suffered from various distortions, namely the room background, electronic pile-up and daughter activity, which introduced undesired counts in the spectra. In order to apply unfolding methods to the TAS data, the contributions of these unwanted components must be known a priori.

6.3.1 Room background

The room background consisted mainly of neutrons and γ-rays produced after the impact of the proton pulse on the target. A shielding involving four layers was built to reduce its contribution to the counting rate in the TAS. However, there was still some remaining activity registered mainly coming from the decay of ^{40}K present in the crystal. Background measurements were performed, interspersed with the measurements on the various isotopes. The room background was approximately 1.5 KHz during the measurement with the shielding closed. Since the counting rate of the room background was relatively low it did not produce any significant electronic pile-up. In what follows the background spectra will be treated as free of distortions.

6.3.2 Electronic pile-up

The electronic pile-up consists of the overlap of two or more pulses due to the statistical nature of the radiation registered in the detector and to the finite pulse width of the electrical signal generated. This source of distortion is unavoidable in our measurements and has been treated extensively by Cano-Ott et al [129]. A simple numerical method, based on a knowledge of the pulse shape, was introduced by these authors and applied successfully to the measurement with a TAS. The overlap of only two pulses is considered, the so-called first order pile-up, since the contribution of any more pulses is negligible under normal TAS measurement conditions, such as ours. This numerical method was used to determine the electronic pile-up in our spectra.

6.3.3 Daughter activity

The decays of the successive daughters of the nuclei under study introduced an important source of contamination in our measurements. Part of the beam time was devoted to measuring their spectra by changing the cycle of the tape transport system.

6.3.4 Determination of the contaminant factors

Once the different contaminants have been identified, the following step is to derive their contributions to our measured TAS spectra. In order to express this in mathematical terms the following equation can be used:

$$M_i = C_i + \lambda_B \times B_i + \lambda_P \times P_i + \sum_j (\lambda_{D_j} \times D_i); \qquad i = 1, n; j = 1, m \tag{6.5}$$

where M is the measured spectrum with contaminants, C is the clean unknown spectrum, B is the background spectrum, normalised by a factor λ_B, P is the electronic pileup contribution, normalised by a factor λ_P, and D_j are the successive j daughter activity contributions, normalised by a factor λ_{D_j}.

In order to explain how the different factors have been calculated we will use as an example the decay of ^{78}Sr. First we will concentrate on the daughter activity contamination due to the decay of ^{78}Rb, measured separately. The continuous black line in the upper part of Fig. 6.3 shows the raw spectrum of ^{78}Rb with contaminants. λ_B can be calculated using the end of the spectrum where only room background contributes, R_B. λ_B would then be the integral value of the raw spectrum of ^{78}Rb in R_B divided by the integral value of the room background spectrum, defined as (b) in the figure, in the same region. λ_P can be obtained by using a region beyond the largest Q_{EC}-value, R_P. Once the raw spectrum of ^{78}Rb is free of background, the only contribution to the counts in the region R_P is the pileup. λ_P will be the integral value of the spectrum of ^{78}Rb free of background in region R_P divided by the integral value of the pileup spectrum, defined as (c), in the same region. Since the daughter nucleus in the decay of ^{78}Rb is stable, it does not need to be taken into account as a contaminant in this case. The lower part of Fig. 6.3 shows the ^{78}Rb spectrum free of contaminants which have been subtracted as described.

The procedure for the determination of the background and pileup factors in the decay of ^{78}Sr is similar to that described above. The factor corresponding to the daughter activity, λ_D, can be calculated using the region above the Q_{EC} value of the decay of the parent, as shown in the upper part of Fig. 6.4. It would then be the integral value of the ^{78}Sr spectrum (free of background and pileup) divided by the integral value of the ^{78}Rb spectrum free of distortions (lower part of Fig. 6.3). The result of the subtraction of all contaminants is shown in the lower part of Fig. 6.4. The fact that the end-point of the clean TAS spectrum in this lower panel agrees with the Q_{EC}-value of 3762 keV from the last Mass-evaluation by Audi et al. [67], provides a good test of the subtraction method since it shows the subtraction has been done correctly.

The determination of the daughter activity contribution can be more complex in those cases where the Q_{EC}-value of the parent is larger than that of the daughter. What is done is to determine the amount of contamination introduced by the daughter based on the observed intensities of some particular known γ-ray transitions. For this purpose, the spectra from the Ge detectors were used. This procedure was carried out for the decay of ^{77}Sr.

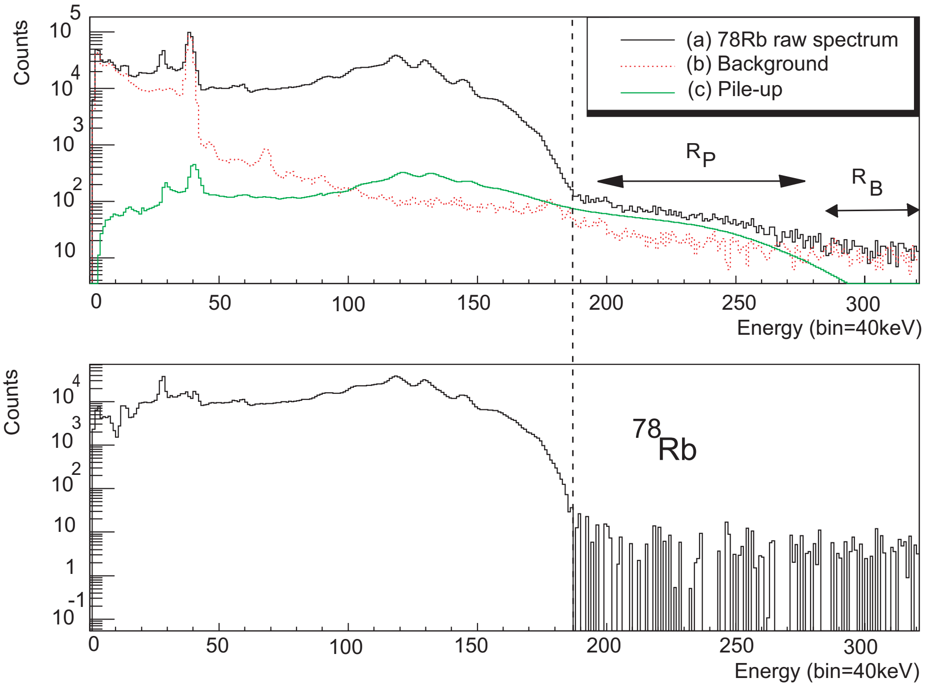

Figure 6.3: The upper part of the figure shows (a) the total recorded spectrum in the TAS for the total ^{78}Rb β-decay. (b) indicates the background activity recorded with no source inside LUCRECIA but in otherwise identical conditions. The background measurements were interspersed with the real measurements. (c) calculated pile-up (see text). The regions for the determination of the pileup and background contributions have been marked as R_P and R_B respectively.The lower part of the figure shows the result of (a) minus (b) and (c).

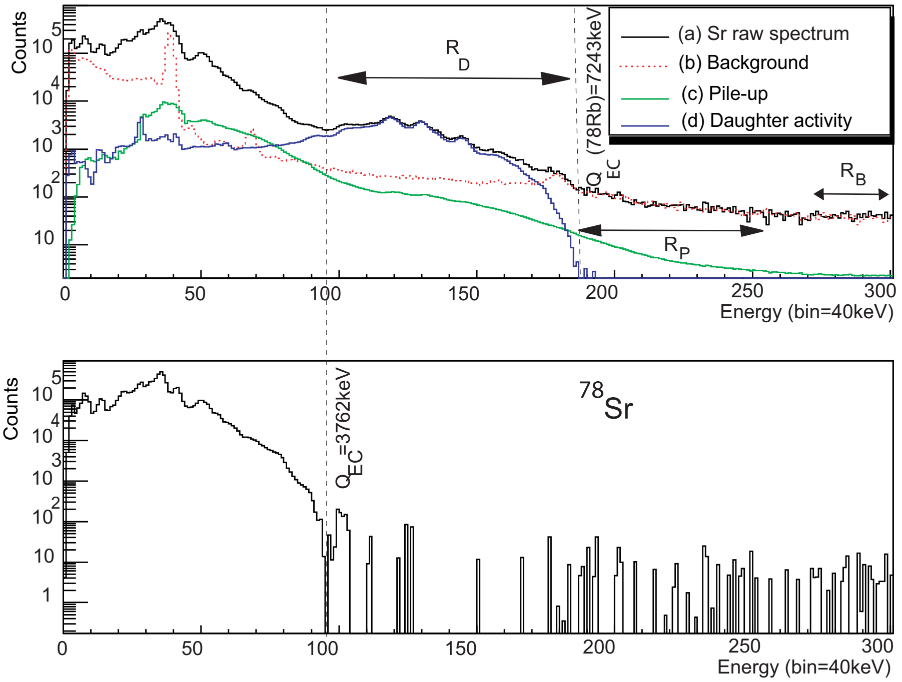

Figure 6.4: Same as in Fig. 6.3 but for the case of ^{78}Sr β-decay. d) corresponds to the daughter activity obtained in Fig. 6.3. The regions for the determination of the pileup, daughter activity and background contribution have been marked as R_P, R_D and R_B respectively. The lower part of the figure shows the result of (a) minus (b), (c) and (d).

6.4 Construction of the response function of the TAS

Since LUCRECIA has a photopeak gamma efficiency lower than 100%, its response to the decay emission and the subsequent electromagnetic de-excitation must be taken into account in unfolding the measured data. The relation between the measured TAS spectrum d and the level feeding distribution f can be represented in the following form:

$$d_i = \sum_{j=0}^{jmax} R_{ij} f_j; \qquad i = 1, i_{max} \tag{6.6}$$

where d_i is the number of counts in the spectrum for channel i, f_j is the decay feeding to the level labelled j and R_{ij} is the probability that the feeding to level j gives a count in the i channel. This probability is called the response of the spectrometer to the decay into level j.

In a β^+/EC-decay the daughter nucleus is fed at an excited state with a certain energy E(i). In such a process, the decay emission could be a positron for a β^+ decay or a cascade of X-ray and Auger electrons when the EC decay takes place. It should be noted that in the particular case of the EC process, only the response to the K X-ray emitted will be considered in this work. The reason is that Auger electrons and X-rays produced from filling higher atomic shells do not have enough energy to be able to reach the sensitive part of the scintillator crystal after traversing the dead material surrounding the source. Ignoring the beta-delayed particle emission (protons, neutrons or alphas) which will be neglected here, the daughter nucleus de-excites into the ground state by a cascade consisting of photons or internal conversion electrons. Thus, the response function of the spectrometer to a certain decay can be built up by successive convolution of the individual response distributions to all the emitted quanta in the β-decay process [75].

What should be noted is that for each β-decay, the response of the detector is unique and must be constructed taking into account the level scheme of the daughter nucleus. Therefore, a knowledge of the decay scheme is needed. In chapters 4 and 5 we have addressed this task for ^{77,78}Sr nuclei where γ-γ coincidence and electron conversion measurements were performed to deduce their level schemes. Regarding the other nuclei, we can rely on the literature [76, 77, 78]. Consequently, the problem of the construction of the response matrix can be reduced to the problem of obtaining all the responses to the individual quanta responses, i.e., the response to all the gamma and K,L,... conversion electron transitions and to the e^+ emission in the β-decay. A more detailed description of such a procedure can be found in [75]. For the particular case of EC/β^+ decay, the EC and β^+ processes compete. Therefore, what should be taken into account is the fact that the ratio between them depends on the atomic number Z of the daughter nucleus and the decay energy Q_β-E_j, where E_j is the excitation energy of level j. Hence, the total response function simulated will be the combination of the response to the EC and β^+ processes respectively for each level j using their corresponding EC/β^+ intensity ratio.

In the past, the determination of the individual response functions to monoenergetic quanta was performed experimentally by using a large number of calibration sources. Response functions for the available radioactive sources were tabulated and when not available, they were constructed by interpolation of the experimental ones [130]. However serious limitations arose since it was not possible to have appropriate sources for all the energy ranges needed. This method was progressively abandoned as soon as Montecarlo simulations started to give satisfactory results. In this work the individual response functions have been simulated with the Montecarlo code *GEANT4*. The non-proportional light yield of the TAS and the instrumental width of our experiment (see Section 6.4.1) were included in the simulation.

6.4.1 Validation of the Montecarlo simulation

Prior to the construction of the response matrix of the TAS for each decay, we need to verify how well our Montecarlo simulations reproduce the interaction of particles with it. For such simulations an accurate description of the physical processes, the materials and the geometry of the setup is needed. This involves highly detailed descriptions of the scintillator crystal including ancillary detectors, beam pipe, collimators, shielding, tape transport system, etc. Note that the relevant feature of the light yield non-proportionality of a NaI(Tl) scintillator crystal must also be implemented in the code.

^{24}Na was produced at CERN after the production of our nuclei of interest and measured in the same conditions. The β-decay of ^{24}Na is rather simple and well-known with a large Q_β window. It consists basically of 2 γ-ray cascades, as shown schematically in Fig. 6.5. In order to compare the simulated spectrum with the experimental one the following steps must be followed:

- Both spectra need to have the same calibration in energy. In what follows the criteria will be to recalibrate all the experimental spectra in energy to the energy calibration of the simulation.
- It is necessary to include the instrumental resolution σ_{exp} in the simulation. This resolution takes into account the resolution broadening due to the statistical nature of the light production and collection in the spectrometer, the conversion of the light into a signal in the photomultiplier tubes and the extra broadening introduced through the electronic chain. The instrumental width can be considered as the difference of the squares of the experimental and simulated widths and be fitted with a quadratic function of the form:

  $$\sigma^2_{instr} = \sigma^2_{exp} - \sigma^2_{sim} = a.E + b.E^2 \tag{6.7}$$

  where E is the energy and a and b are parameters which must be determined for each TAS configuration (note that there were two different experiments with different beta counters). This instrumental width is then added to the simulation by the convolution of the simulated spectrum with a Gaussian distribution dependent on the energy according to equation 6.7.

Figure 6.5 shows the simulated and experimental spectra of the ^{24}Na. A good match can be observed between the spectra. This confirms how well our Montecarlo simulations reproduce the experimental data.

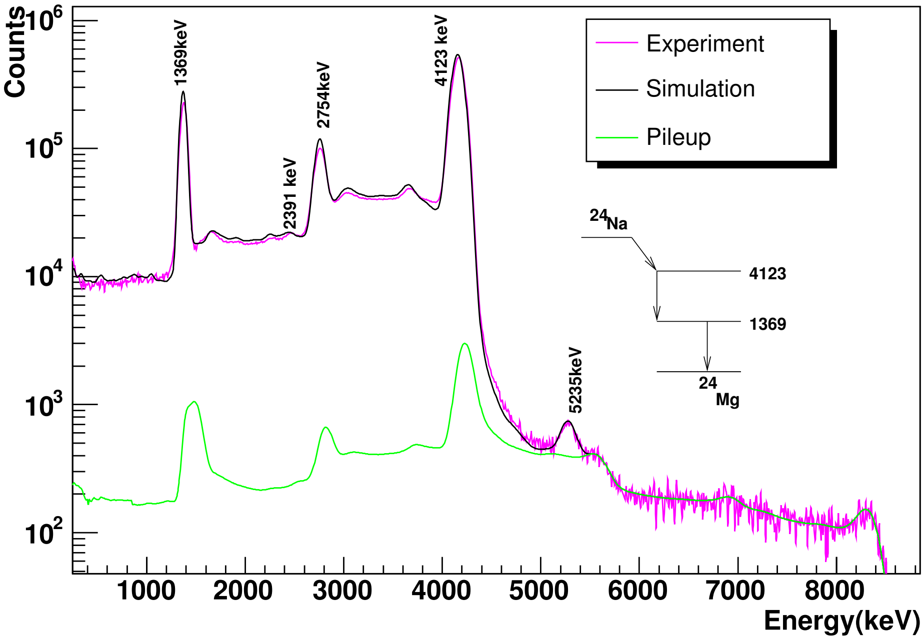

Figure 6.5: Simulation of the spectrum of the ^{24}Na source (pink line) with the *GEANT4* code overlaid with the experimental spectrum (black line). The dot-dash line represents the calculated electronic pile-up contribution.

6.4.2 The unknown de-excitation pattern at high excitation energies

For complex decay schemes with large Q-values, one can only obtain accurate information on low-lying excited states with high resolution spectroscopy. The relevant but very fragmented strength to states at high excitation in the daughter nucleus often remains undetected due to the modest efficiency of Ge detectors. However, it is necessary to have a knowledge as accurate as possible of the the decay scheme up to the Q$_{EC}$ value in order to construct the response matrix function to each particular decay. This problem can be overcome by using a model which averages, called the statistical model, which describes the electromagnetic de-excitation for the corresponding part of the level scheme where no experimental data are available. This statistical model uses average quantities such as level densities and strength functions:

- The level excitation energies, parities and spins are derived using a parametrisation of the back-shifted-Fermi-gas (BSFG) formula [131], with a (MeV^{-1}), the level density parameter, and $\triangle$(MeV), a fictitious ground-state. The model describes the dependence of the averaged density of levels of a given spin-parity on the excitation energy. The parameters a and $\triangle$(MeV) are nucleus-dependent and are usually adjusted in order to reproduce experimental level densities. They can be retrieved from the Reference Input Parameter Library (RIPL) [133] for many nuclei. However, these data were not available for the nuclei of our study. We calculated a and $\triangle$ using a program [132] which fitted the parameters of the BSFG formula from a set of cumulative numbers of levels at different excitation energies taking also into account the deformation parameter β. These numbers of levels were obtained from total nuclear level densities based on the realistic microscopic single-particle level schemes determined within the HF-BCS [133].

Table 6.2: Deformation and level density parameters of the nuclei under study. The latter have been extracted using the BSFG formula and a set of cumulative numbers of levels at different excitation energies derived from HF-BCS calculations(see text) [133].

Isotope	β	a (MeV^{-1})	$\triangle$(MeV)
^{76}Kr	0.38 [134]	11.480	0.228
^{77}Rb	0.38 [121]	9.9411	-0.441
^{78}Rb	0.391 [112]	10.613	-0.877
^{78}Kr	0.35 [135, 136]	11.561	0.024

- The branching ratios are obtained from gamma-strength functions related to the nuclear giant resonance excitation modes by the Axel-Brink hypothesis [137]. These strength functions have a Lorentzian shape except for M1 where a generalised Lorentzian shape is used. They depend on a, the level density parameter introduced before, B_n (MeV) the neutron binding energy, and E_0 (MeV), Γ_0 and σ_0, the giant resonance parameters. These last three parameters can be extracted from the systematics [138, 139, 140] [1] and are listed in Table 6.3. Only transitions of E1, M1 or E2 type were considered in our work. In the case of E1 transitions, two possible parametrisations are available for deformed nuclei with A>50. This explains the two possible values given for the giant resonance parameters in Table 6.3.

Here we have simply summarised very briefly the key points of the statistical model. A very detailed description is given in [142]. The branching ratios can then be handled as external parameters and our problem, expressed in Eq. 6.6, is reduced to the determination of the feeding distribution.

Taking into account all of these points, the branching ratios up to the last level determined with high-resolution measurements were assumed to be known. For the

---

[1] The document kopecky.dat available on the RIPL webpage [141] contains a summary of global systematics derived from experimental strength function data for the calculation of the giant resonance parameters

Table 6.3: Giant resonance parameters for the E1, M1 and E2 transitions of the nuclei under study.

	E1			M1			E2		
Isotope	E_0 (MeV)	Γ_0 (MeV)	σ_0 (mb)	E_0 (MeV)	Γ_0 (MeV)	σ_0 (mb)	E_0 (MeV)	Γ_0 (MeV)	σ_0 (mb)
^{76}Kr	13.863 19.887	3.944 7.857	220.236 110.541	9.693	4	137.641	14.895	5.198	1.962
^{77}Rb	13.819 19.826	3.920 7.810	224.742 224.742	9.651	4	7.780	14.829	5.186	2.049
^{78}Rb	13.697 19.84869	3.854 7.827	321.302 113.892	9.609	4	24.656	14.766	5.174	2.028
^{78}Kr	14.000 19.541	4.019 7.598	221.095 116.944	9.609	4	79.181	14.766	5.174	1.920

unknown part, the branching ratios were derived from the statistical model. In order to do this, we grouped into bins of 40 keV the levels in the unknown part up to the Q_{EC} value. This made it possible to overcome the problem of the convolution of the different quanta in the region of high level density, which can reach the order of 10^4-10^6 levels. The β^+ particles were simulated with the corresponding end-points for each nucleus. We used the exact energies of the gamma-ray transitions for the known part of the level scheme. Average energies (multiples of the energy bin width of 40 keV) were used in the Montecarlo simulations of the gamma response functions for the unknown part. All these approximations introduce systematic errors in our results. Tain et al. extensively investigated their effects [142] in the determination of the beta-strength with TAS measurements.

On the other hand, we have constructed several different level schemes, which translates into different response matrices, for each nucleus under study. The variables under play have been the two possible parametrisations for the strength of an E1 transition (the reader should note that for M1 and E2 transitions there is only one possible parametrisation to calculate the giant resonance parameters), the last level considered for the known part and those spin/parities which are undefined in the known level scheme. The TAS results will be sensitive to all of these elements and we will study their effects. Specific details of the value that these variables take will be given for each nucleus in the next chapter.

6.5 Application of the EM algorithm

Once the response matrix function of the spectrometer is determined, the next task is to solve the linear inverse problem, shown in Eq. 6.6, in order to obtain the feeding distribution **f**, with **d** and **R** known. However, inverting the **R** matrix is not a simple task. The **R** matrix is nearly singular since the feeding to contiguous energy bins in regions of high excitation energy, with very high level density, is very similar. Therefore, the nearly degenerate columns in **R** leads to computer overflows and round-off errors when one tries to calculate the inverse matrix. In the case of round-off errors, the calculated inverse matrix amplifies the statistical variations of the data and as a result, solutions which oscillate in an unphysical manner are obtained. Such a problem is said to be *ill-conditioned* or *ill-posed.*

The numerical treatment of such problems is a challenge since there is no unique solution. Different sets of solutions, including unreasonable ones with no physical meaning, can reproduce the same data profile. In addition, small changes in the data such as a perturbation caused by noise can cause arbitrarily large deviations in the results. This ill-posed problem is not unique to the unfolding of the TAS data but it is also found in many disciplines such as computer tomography, financial and environmental modeling, astronomy, etc. Therefore, selection methods need to be imposed in order to limit the solution to a reasonable set of possible solutions. This can be done by the inclusion of *a priori* information. In reference [66] three different algorithms applied to the solution of the linear inverse problem of the TAS have been explored. Their suitability and systematic uncertainties have been studied and their different characteristics explained in detail. In what follows, we will only refer to the Expectation-Maximisation algorithm (EM) which will be applied to the unfolding of the TAS data in this work. This algorithm is a method for iterative computation of maximum-likelihood estimates. The same algorithm can also be obtained by the application of the Bayes theorem on conditional probabilities, which can be stated in terms of several independent causes (f_j, j=1,2,..,m) which can produce effects (d_i, i=1,2,...,n).

The Bayes formula can be written as follows:

$$P(f_j|d_i) = \frac{P(d_i|f_j)P(f_j)}{\sum_{j=1}^{m} P(d_i|f_j)P(f_j)} \tag{6.8}$$

where the feeding, *f*, can be identified as cause and the counts registered, *d*, as effect in our case. Therefore the Bayes theorem can be read as: if a count is found in channel i of the measured spectrum, the probability that it has been caused by a feeding to a level within an energy bin j is proportional to the probability of having feeding to a level within the energy bin j times the probability that the feeding to a level within energy bin j produces a count in channel i. The denominator in equation 6.8 ensures the normalization of the probability to 1. The term

P(f$_j$) (P(f$_j$)=$\frac{f_j}{\sum_{j=1}^m f_j}$) represents the feeding f$_j$. On the other hand, the expression P(d$_i$|f$_j$) is in fact the matrix element R$_{ij}$.

In terms of probabilities, the inverse problem of equation 6.6 can be written as:

$$f_j = \frac{1}{\sum_{i=1}^n R_{ij}} \sum_{i=1}^n P(f_j|d_i)d_i, \qquad j = 1, ..., m \tag{6.9}$$

where $\sum_{i=1}^n$R$_{ij}$ is the probability of observing the feeding into j. This can also be interpreted as the efficiency of the detector and appears in the equation for normalisation reasons. The second term $\sum_{i=1}^n$P(f$_j$|d$_i$) can be identified with the inverse of the response matrix but written in terms of probabilities. By inserting 6.9 into 6.6, the following iterative expression is obtained:

$$f_j^{p+1} = \frac{1}{\sum_{i=1}^n R_{ij}} \sum_{i=1}^n \frac{R_{ij} f_j'^p}{\sum_{k=1}^m R_{ik} f_k'^p} d_i, \qquad j = 1, ..., m \tag{6.10}$$

where f' is normalized to 1 whereas f$_j$ on the left is not. The closer the initial distribution of feeding f^p is to the true distribution, the better the agreement is and fewer iterations are needed.

At this point it should be noted that the EM algorithm only deals with positive counts in the spectrum. As can be seen in the lower panel of Fig. 6.4, after the subtraction of the undesired components the TAS spectrum there is a region, close to the Q$_{EC}$-value, of low statistics with channels with zero and even negative counts. This region is also quite critical in the strength distribution determination since the Fermi integral takes values close to zero here due to its strong dependence on transition energy E, namely (Q$_{EC} - E)^5$. Therefore, this part of the TAS spectrum is subject to large systematic errors, i.e, small statistical fluctuations in the data could lead to an unphysical feeding distribution in this region. As a consequence, in what follows the algorithm will be applied using the raw spectra, taking into account the different contaminant components and their contributions. Hence, Eq. 6.6 will then be replaced by Eq. 6.11 for which a solution will be found using the EM algorithm described:

$$\mathbf{d'} = \mathbf{R}(b).\mathbf{f} + \sum_{k=1}^n \lambda_k \times contaminant_k, \qquad k = 1, n \tag{6.11}$$

where **d'** are the raw experimental data and λ_k are the factors for the contaminants, obtained as described in Section 6.3.4. The effect of avoiding the subtraction of the contaminants in the TAS data when applying the EM algorithm has been studied in detail by Nacher [126].

The following steps are performed to unfold the data:

1. A uniform flat feeding distribution is used for the feeding, namely f'$^{p}_{j}$=1/j, in order to start with the iterative method.
2. A number of iterations is chosen based on two requirements:
    - The resulting feeding should not show any unphysical oscillations.
    - The solution does not improve significantly in terms of χ^2 with a higher number of iterations.

   Based on these requirements, an upper value of 250 iterations was used.
3. f$^{p+1}_{j}$ is calculated using Eq. 6.10.
4. A χ^2 comparison between R$_{ij}$f$^{p+1}_{j}$ and the original spectrum d$_i$ is made after each iteration. The value of the χ^2 obtained is shown as an output.
5. f'$^{p}_{j}$ is replaced in Eq. 6.10 by f$^{p+1}_{j}$ and the procedure starts again. If a reasonable value of χ^2 is obtained, the iteration will stop. Otherwise it will continue from step 3.

From Eq. 6.10 , one could write the same expression as:

$$f^{p+1} = M^p.d \tag{6.12}$$

When convergence has been achieved, the above relation allows the treatment of the uncertainties of the distribution f obtained by making use of the error propagation theorem:

$$V_f = M.V_d.M^T \tag{6.13}$$

where V$_f$ is the covariance matrix of the f distribution and M^T is the transposed matrix M. Note that the feeding distribution obtained is normalised to unity.

6.6 Determination of the B(GT) distribution

The application of the EM algorithm to the TAS data allows us to obtain the beta feeding distribution, f, which is called the beta intensity, I$_\beta$. Equation 2.8 in Chapter 2 establishes the relationship between the beta feeding to an excited state and the strength of the GT-transition to this state. Since for the unknown part of the level scheme the levels are grouped into bins of 40 keV, we can interpret S$_\beta$ as an average quantity and express it in the following form:

$$S_\beta = \frac{K}{T_{1/2}} \sum_{E_x \epsilon \triangle E_x} \frac{1}{\triangle E_x} \frac{I_\beta(E_x)}{f(Q_\beta - E_x)} \tag{6.14}$$

where K=3809.0 ± 1.0 [5] and E_x is the central energy of the energy bin. The error in the strength is given by the error propagation formula where the uncertainty of the half-life, Q_{EC}, ft value and the statistical uncertainty of the feeding distribution must be considered. The reader should note that the pure statistical uncertainties of the feeding distribution obtained from 6.13 are rather small and unrealistic. This is due to the high correlation between the f_β values of the different channels. On the other hand, the B(GT) distribution is also very sensitive to the following components :

- The normalisation factors for the different contaminants.
- The parameters of the strength functions of gamma radiation. In our work we have considered two possible parametrisations for the E1 electromagnetic radiation, as shown in Table 6.3, whereas only one parametrisation is used for M1 and E2 transitions. The two parametrisations for E1 transitions result in slightly different level schemes for the unknown part obtained with the statistical model and consequently, different B(GT) distributions that only differ slightly.
- The last known level considered for the known part of the level scheme. Due to the low gamma-efficiency of Ge detectors some excited levels can be missing even within the known level scheme. This causes an error in the de-excitation branching ratios derived for the levels in this part of the level scheme. Therefore we need to be realistic in terms of determining the level at which our known level scheme is not affected by possible missing levels or γ-rays.
- The spins and parities of some undefined known levels.

Various combinations of these 4 factors have been used in order to construct different response matrixes for each nucleus and hence, derive their corresponding B(GT). The error in the strength will be given by the error derived from the propagation formula applied to Eq. 6.14 plus the error introduced by the 4 factors explained above. Note that the error on the latter factor is much higher.

Chapter 7

Results of the TAS data and discussion

This chapter reports the results of the TAS analysis for each nucleus under study. Firstly, the particular assumptions made for the construction of the response matrix of the detector for each case are presented. In terms of determining the contaminant factors in the TAS spectra, the procedure followed is the one described in the previous chapter. No further comments related to this point have been made unless some particular considerations were needed. Results of the feeding and the strength distribution are presented after the application of the EM algorithm. The distributions obtained are compared with the results from high resolution spectroscopy. From this comparison we can evaluate the importance of the Pandemonium effect for each nucleus which shifts the beta strength to lower energies in high resolution measurements.

Secondly, the measured B(GT) of ^{78}Sr are compared with QRPA calculations in order to derive the deformation of the ground state of the parent nucleus. The accumulated B(GT) distribution from the ground state of the daughter nucleus to a particular excitation energy has been plotted in order to perform the comparison between the experiment and the theory. The same kind of comparison with the theory is done for the decay of ^{77}Sr.

Although there are no theoretical calculations available for the odd-odd ^{76,78}Rb isotopes, conclusions have been drawn based on their measured B(GT) distributions. The results for the ^{76}Sr decay, already published by Nácher et al [44], are also used in the discussion in order to extract a general picture of the nuclear structure properties of the region.

7.1 ^{78}Sr decay results

Figure 7.1 shows schematically the A = 78 decay chain starting with ^{78}Sr. Since ^{78}Kr is stable, one needs only consider the contamination caused by the decay of the ^{78}Rb daughter nucleus. The determination of the different contaminants in this decay has been discussed in the previous chapter. There are uncertainties in the spins and parities of some of the levels deduced in the high resolution analysis included in this work. We have considered the levels at 193.0, 255.3 and 801.6 KeV to be 0^-, 1^+ and 1^+ respectively for the purposes of this analysis. The spins of the first two are based on our discussion in section 4.8 which favours those spin assignments. For the construction of the unknown part of the level scheme, we have applied the statistical model starting at 3 possible excitation energies up to the Q$_{EC}$ value. Two different parametrisations of the gamma-strength function for an E1 transition (see table 6.3) were used. These two parametrisations have also been used for the rest of the nuclei under study. Overall six different level schemes were constructed which were used to build up 6 detector response matrices.

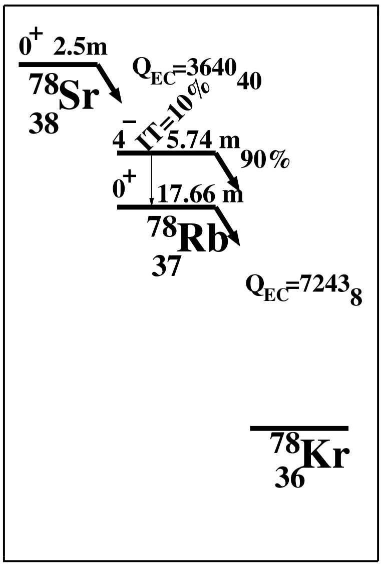

Figure 7.1: Schematic picture of the β^+/EC decay of ^{78}Sr and its consecutive daughter decays.

The construction of the response function of the detector for this particular nucleus needs special treatment. The occurrence of the 46.9 keV isomer in the de-excitation level scheme introduces a temporary break in the development of the gamma cascade which alters the measured spectrum. For a very long-lived isomer it is equivalent to the termination of the cascade and can be easily taken into account

last known level assumed (keV)	start unknown part (keV)
1283.4	1500
1738.9	1800
1950.4	1960

Table 7.1: Assumptions made for the construction of the unknown part of the level scheme of ^{78}Rb using the statistical model. The first column gives the last level considered to be known in our knowledge of the level scheme. The second column shows the starting energy from which the statistical model is applied up to the Q$_{EC}$ in order to generate the de-excitation pattern for the unknown part of the level scheme at high energies.

by setting the branching ratio from that level to zero. However, for this particular case the half-life is comparable with electronic processing times and some care must be taken. The 46.9 keV gamma transition below the isomer (see the level scheme of ^{78}Sr decay in Figs. 4.13 and 4.14) contributes to the rest of the detected cascade depending on the time delay and the pulse processing. The basic mechanism is conceptually the same as for the electronic pulse pileup distortion since the time distribution is governed by the same law, the Poisson time distribution. In this case, the difference in the heights of the two signals is not randomly selected but has specific values. Two different basic quantities need to be considered to address this problem: the decay rate α and the electronic pulse distribution, which is characterised by the peaking time τ_p and the width of the signal τ_w. It should be noted that there are clear differences between the typical electronic pileup and the occurrence of an isomer in a decay. In the electronic pile-up the counting rate is of the order of 10 kHz under normal conditions and is a global quantity given by the characteristics of the experiment. Therefore the rate is of the order of $\sim 10^4$ s^{-1}. In addition, the general peaking times in spectroscopy work range from 0.3-3 μs. This leads to a probability of electronic pileup, namely $\alpha\tau_p$, which varies between 0.5-3 %. The resulting time interval distribution is rather flat within the time duration of the pulse. On the other hand, the decay rate in an isomeric decay , which we will refer to as λ, varies within a very large range and depends exclusively on the nucleus under study. It is related to the half-life of the isomer by the expression $\lambda = \frac{ln2}{T_{1/2}}$. If the half-life of the isomer is very large, no summing between the lower part of the cascade below the isomer and the rest will occur, i.e. $\lambda\tau_p$ is very small. The opposite occurs when the half-life is very short which always results in summing. The case addressed here is an intermediate situation and special care must be taken. We have considered the half-life T$_{1/2}$=920±40 ns by Kaye et al [95] which results in a decay rate λ=0.753 μs^{-1}. The amplifier peaking time was τ_p=2.1 μs and therefore $\lambda\tau_p$=1.58. As discussed above, the decay is governed by the Poisson law and thus the differential probability that the de-excitation proceeds after a time t is given by the following expression:

$$dP = \lambda e^{-\lambda t} \tag{7.1}$$

If we assume a peak sensing ADC, which is applicable to the type of measurements we performed, the pulse generated once the isomer de-excites will be summed if it occurs within the peaking time τ_p. Therefore the probability of summing occurrence is given by:

$$\int_0^{\tau_p} \lambda e^{-\lambda t}\, dt = 1 - e^{-\lambda \tau_p} = 0.794 \tag{7.2}$$

In summary, this probability has been considered in order to alter the gamma response function of the 46.9 keV gamma transition obtained with the Montecarlo simulation. This gamma response has then been convoluted with the rest of the quanta responses for the construction of the total response of the detector.

Figure 7.2 shows the comparison between the reconstructed spectrum and the experimental one including the contaminants after the application of the EM algorithm. Here we only show the results concerning the analysis that leads to the smallest χ^2 once the unfolding method has been applied. As an aid to seeing the differences more clearly, since the upper graph of Fig. 7.2 is in log scale, the deviation between the reconstructed spectrum and the experimental one relative to the latter has been plotted in the lower part. The existing larger differences in the low energy part of the spectrum are caused by a possible mismatch between the energy calibrations of the two spectra. The limited energy resolution of the TAS makes it difficult to follow the variation of the feeding for such low energies where the density of levels is low. This is also a feature common to the results for the other nuclei under study. However, an excellent agreement can be observed in the rest of the spectrum which implies that our method is reliable. The resulting feeding distribution as a function of the excitation energy is shown in Fig. 7.3. The graph has been split into two parts in order to show the feeding near the Q_{EC} value in more detail. As can be observed, the feeding to the levels in the right panel has been calculated within bins of 40 keV while for lower energies, the feeding is calculated for each of the discrete levels observed in high resolution measurements. A shift in the feeding distribution can be observed when compared to the values obtained with high resolution spectroscopy, marked with dots in Fig. 7.3. However the results from both techniques differ only slightly for low energies. We can observe that the levels at 290.2, 315.1, 504.7 keV receive most of the strength in both cases. Regarding the gs to gs transition, the results from the TAS analysis show no feeding, which is expected for an isospin forbidden transition.

The strength distribution can be calculated by using Eq. 6.14. Figure 7.4 shows the B(GT) as a function of the excitation energy obtained from our TAS measure-

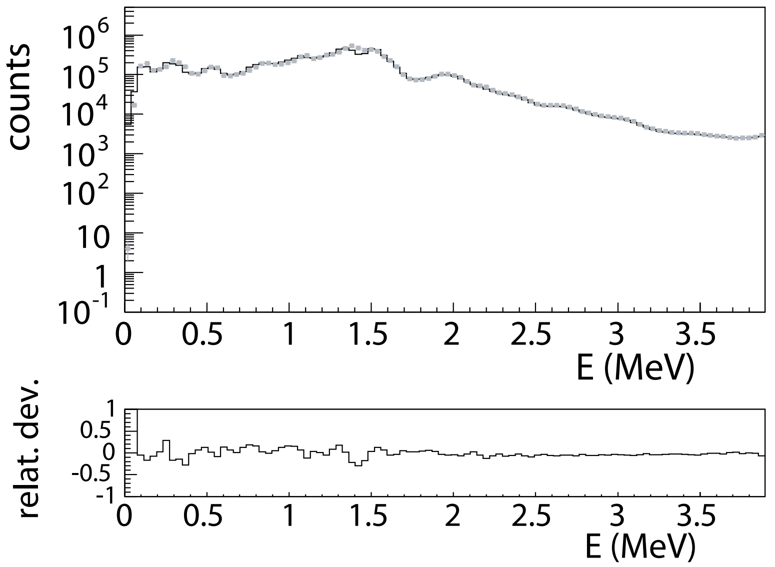

Figure 7.2: Upper panel: Experimental TAS spectrum of ^{78}Sr (black continuous line) with contaminants. The reconstructed spectrum obtained from our analysis appears overlaid (grey dashed line). Lower panel: difference of the reconstructed spectrum from the experimental one relative to the latter.

ments. The B(GT) obtained with high spectroscopy appears dotted in the same figure. The shaded area corresponds to the uncertainties derived from the different analyses made using the six different response matrix and different contamination factors. The upper and lower errors have been calculated based on the deviation between the analysis that results in the lowest χ^2 (which appears as a solid line in Fig. 7.4) and those which produce the highest but still acceptable χ^2. The error associated with the uncertainty in the half-life, Q_{EC} and the statistical error obtained from the application of the EM algorithm are also taken into account. For more details, the reader is referred to section 6.6.

Figure 7.5 shows how sensitive the determination of the B(GT) distribution is to the level scheme assumption for the case of ^{78}Sr. The B(GT) strength is shown accumulated in order to illustrate the problem more clearly. The decay scheme of ^{78}Sr has a gap with no levels between 1283.4 and 1738.9 keV. If we assume we know the level scheme up to an excitation energy of 1283.4 keV, the statistical model would build up a de-excitation pattern where no gap would exist within the region at 1283-1738 keV. This would result in strength within the 500 keV gap as shown in Fig. 7.5. This example stresses the importance of knowing the level scheme very well in detail at low energies where the level density is low. However, the total strength obtained with both assumptions differs only slightly and the strength

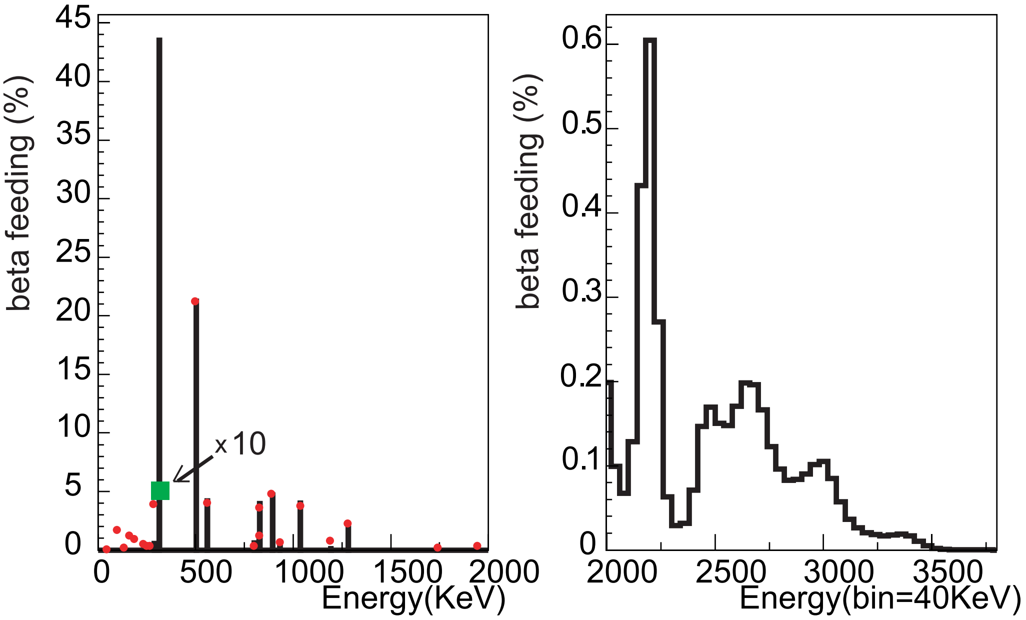

Figure 7.3: Comparison of the beta feeding obtained after the TAS analysis (continuous line) and that from the high resolution experiment (red dots) for the β-decay of ^{78}Sr. The beta feeding which appears as a square, corresponding to the level at 315.2 keV with a feeding of 49.5(12)% in high resolution, has been reduced by a factor of 10 so that it appears in the comparison. The closest dot on the left from this excitation energy corresponds to the beta feeding for the level at 290.2 keV with a value of of 3.9(2)% in high resolution.

distribution at high excitation energies shows a similar pattern. This is due to the high gamma efficiency of LUCRECIA and the fact that at high-level density the fluctuations in the strength obtained due to different assumptions for the branching ratio matrix are smoothed. What can be concluded is that the better our knowledge of the low-energy part the better determination of the strength in this part we can obtain. On the other hand, for high-level density there is no much dependence on the assumptions of the branching ratios. All these effects have been extensively studied by Tain et al [142].

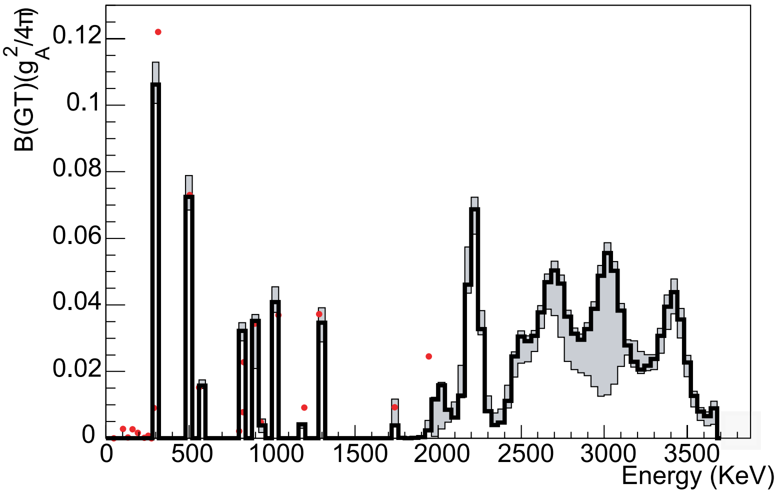

Figure 7.4: B(GT) distribution in the beta-decay of ^{78}Sr as a function of the excitation energy in the daughter nucleus (solid line) using the TAS method. The B(GT) distribution using high resolution spectroscopy (red dots) is also shown.

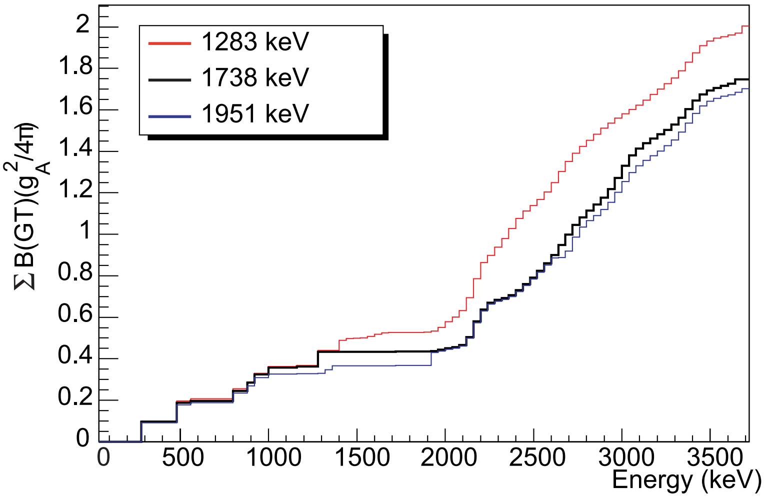

Figure 7.5: Accumulated B(GT) for ^{78}Sr obtained from different assumptions for the last level supposed to be known in the level scheme.

7.2 ^{77}Sr decay results

Figure 7.6 shows schematically the A = 77 β-decay chain starting with ^{77}Sr. Since the measurement of the β-decay of ^{77}Rb only lasts for 420 s while the collection time was 135 s, the contamination due to the decay of ^{77}Kr, with $T_{1/2}$=74.4m, can be neglected. Figure 7.7 shows the subtraction of the different contaminants in the decay of ^{77}Sr, namely the pile-up, the room background and the activity of ^{77}Rb already free of contaminants. Since the Q_{EC} value of ^{77}Rb is smaller than that of ^{77}Sr, the subtraction of the contamination caused by the decay of ^{77}Rb is more complex. In this case the γ-ray spectrum registered with the coaxial detector was used in order to determine the contribution of ^{77}Rb in the ^{77}Sr decay. A contamination of 5.3% caused by ^{77}Rb was then deduced based on the known relative intensities of certain γ-ray transitions in both decays. Table 7.2 lists the four starting levels which have been used for the application of the statistical model to deduce the branching ratios for the unknown part of the level scheme in ^{77}Rb.

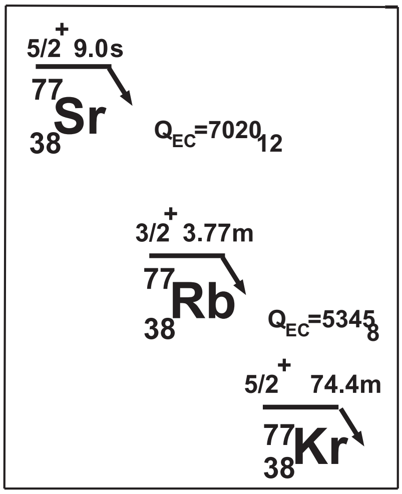

Figure 7.6: Schematic picture of the β^+/EC decay of ^{77}Sr and its consecutive daughter decay.

In Fig. 7.8 is shown the comparison between the reconstructed spectrum and the experimental one where a good agreement can be observed. Figure 7.9 shows the feeding distribution as a function of the excitation energy in ^{77}Rb obtained with the TAS (continuous line) and high resolution spectroscopy (dots). The squared dot represents the 62% of the apparent beta feeding observed with high resolution spectroscopy for the level at 146.9 keV. As can be observed, the TAS results show a feeding distribution remarkably different, specially in the low energy region where there is high resolution data available. In fact, at this 146.9 keV level the TAS results show a ~25% feeding which is less than half of what was observed in our spectroscopy work. This is a clear evidence of the Pandemonium effect which appears more dramatically in the plot of the B(GT) in Fig. 7.10. The B(GT) predicted at the 146.9 keV level by high resolution means is 0.22(3) ($g_A^2/4\pi$) (not plotted in Fig. 7.10 since it is off the y-axis scale) while the one obtained with the TAS is only

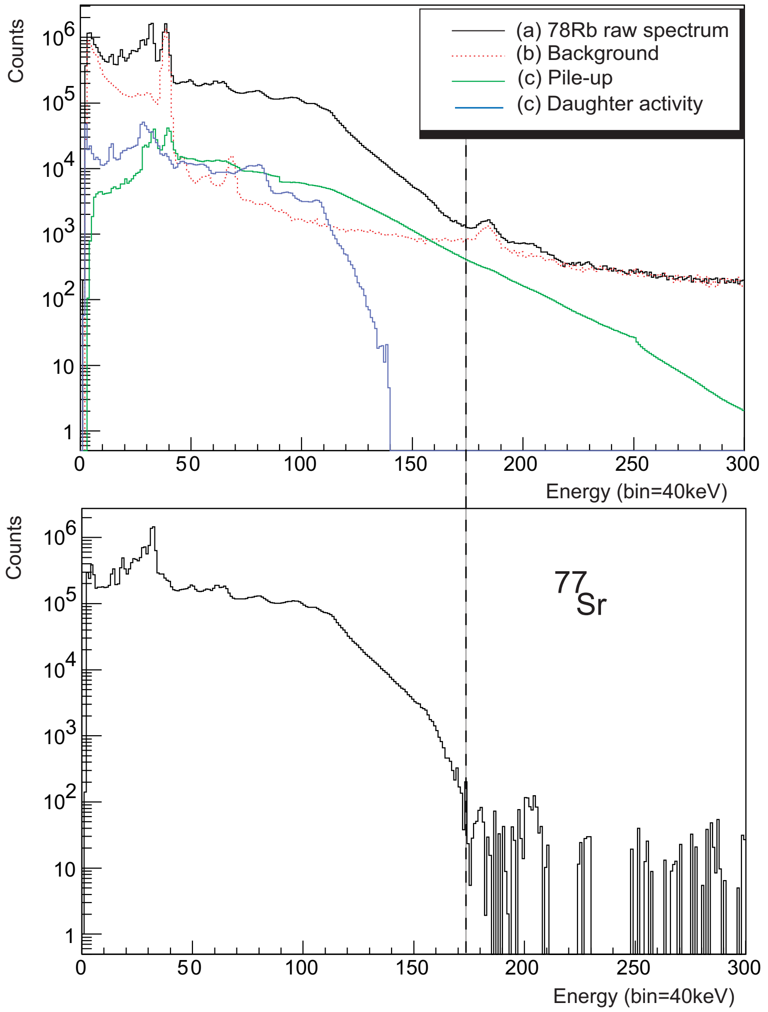

Figure 7.7: The upper part of the figures shows (a) the total recorded spectrum in the TAS for ^{77}Sr β-decay. (b) indicates the background recorded activity with no source inside LUCRECIA but else in identical condition. The background measurement was interspersed with the real measurement. (c) calculated electronic pile-up. d) corresponds to the daughter activity from the decay of ^{77}Rb. The lower part of the figure shows the result of (a) minus (b), (c) and (d).

$\sim$0.038(3) $(g_A^2/4\pi)$. This shows a clear example of the need for a TAS if the aim is to obtain a reliable B(GT). In addition, we can see that most of the strength lies above 2.5 MeV, a region which could not be observed in high resolution. This region is mainly due to 3qp transitions which were discussed in Sec. 5.7 when the level structure in the decay of ^{77}Sr was interpreted. This high energy region will be discussed in more detail in Sec. 7.6 below. In addition, the results of the B(GT)

last known level assumed (keV)	start unknown part (keV)
795.7	840
963.4	1000
1245.2	1280
1469.6	1480

Table 7.2: Assumptions made for the construction of the unknown part of the level scheme of ^{77}Rb using the statistical model. The first column gives the last level considered to be known in our knowledge of the level scheme. The second column shows the starting energy from which the statistical model is applied up to the Q_{EC} to generate the de-excitation pattern for the unknown part at high energies.

will be interpreted in terms of HF+BCS+QRPA calculations for this nucleus.

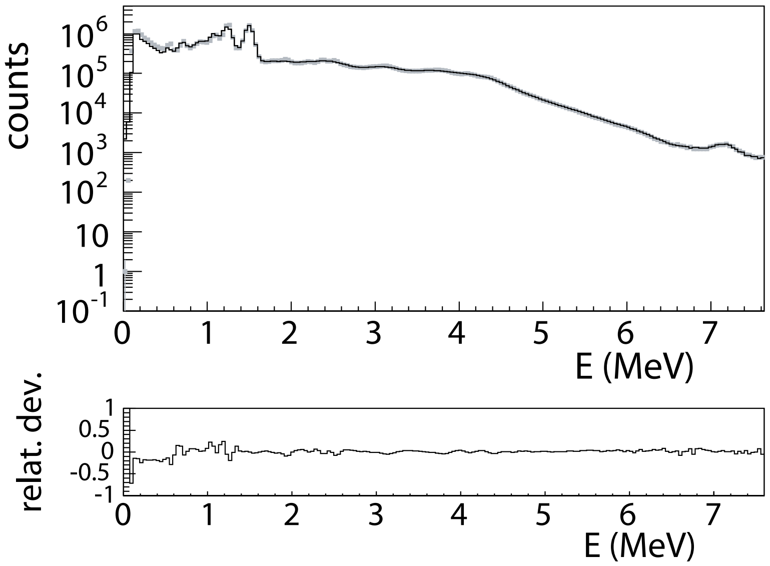

Figure 7.8: Upper panel: Experimental TAS spectrum of ^{77}Sr (black continuous line) with contaminants. The reconstructed spectrum obtained from our analysis appears overlaid (grey dashed line). Lower panel: difference of the reconstructed spectrum from the experimental one relative to the latter.

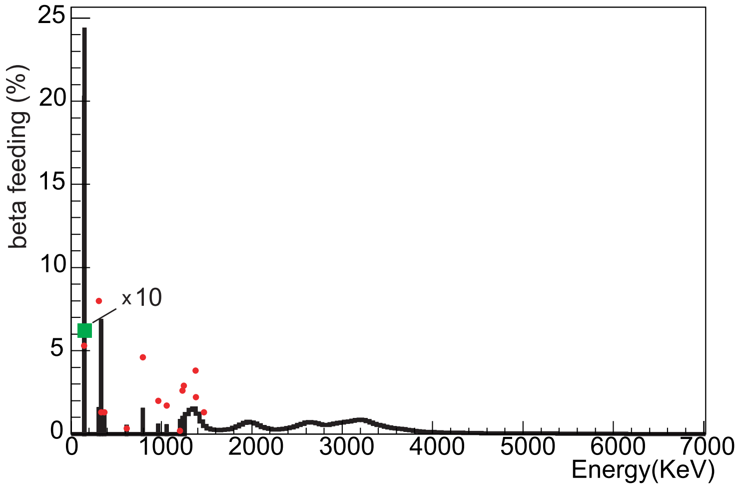

Figure 7.9: Comparison of the beta feeding obtained after the TAS analysis (continuous line) and that from the high resolution experiment (red dots) for the β-decay of ^{77}Sr. The beta feeding which appears as a square has been reduced by a factor of 10 so that it appears in the comparison.

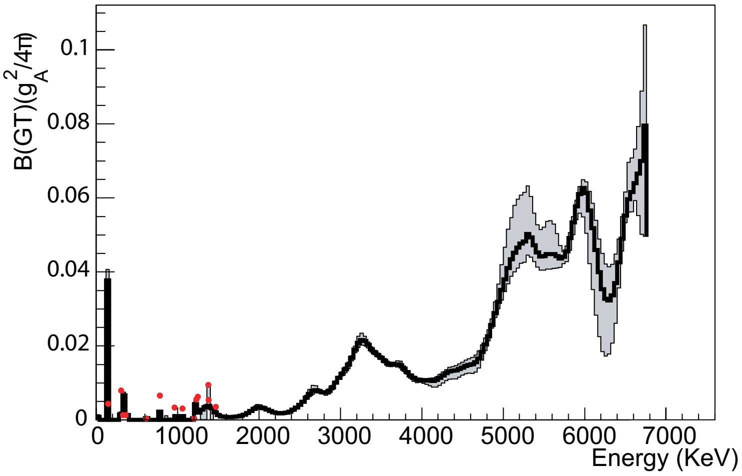

Figure 7.10: B(GT) distribution in the beta-decay of ^{77}Sr as a function of the excitation energy in the daughter nucleus (solid line) using the TAS method. The B(GT) distribution using high resolution spectroscopy (red dots) is also shown. Note that the B(GT) of the 146.9 keV level resulting from the high resolution experiment is 0.22 ($g_A^2/4\pi$) which does not appear on the graph since it is off scale.

7.3 ^{76}Rb decay results

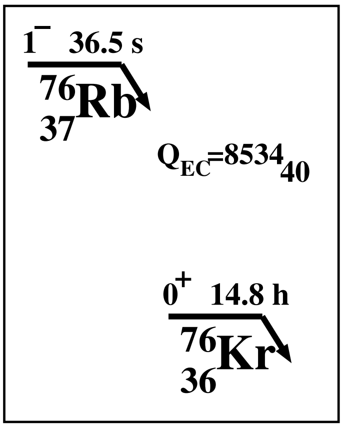

Figure 7.11: Schematic β^+/EC decay of ^{76}Rb and its consecutive daughter.

In Fig. 7.11 it can be seen that the half-life of the decay of ^{76}Rb is 2 orders-of-magnitude shorter than that of its daughter decay. Since the time of the measurement was 66.8 s, the contamination caused by the activity of ^{76}Kr is negligible. Only the electronic pileup and room background have been considered as contaminants in the ^{76}Rb decay data. The level scheme used for the construction of the detector response matrix has been extracted from the study of the decay of ^{76}Rb by Giannatiempo et al. [77]. Table 7.3 lists the two sets of spins and parities assumed in the TAS analysis for the levels of ^{76}Kr for which no definite spin-parity assignments were deduced in their paper. Those spin-assignments are in accord with the limitations imposed on the possible spins and parities for certain levels based on some measured conversion coefficients given by the same authors. The statistical model has been applied with 4 possible starting excitation energies, listed in Table 7.4, up to the Q$_{EC}$ value.

Figure 7.12 shows the comparison between the reconstructed spectrum and the experimental one including the contaminants. The feeding distribution obtained as a function of the excitation energy is shown in Fig. 7.13. It can be seen that apparent feeding is observed at low energies with high resolution spectroscopy whereas this feeding is not observed with the TAS measurements. This is a very clear example of the Pandemonium effect which stresses the need for a TAS for this kind of measurement. The levels at 2571.0, 2926.5 and 3602 keV clearly receive most of the strength in both analyses. A beta feeding of 34% is obtained for the level at 2571.0 keV, the most highly populated level in the decay, with high resolution spectroscopy while we only obtain ~15.5 % with the TAS. Figure 7.14 shows the corresponding B(GT) as a function of the excitation energy. As can be observed,

Level energy (keV)	I_1^π	I_2^π
2140.1	2^+	1^-
2192.4	1^-	1^-
2742.3	1^+	2^-
2774.9	0^-	0^-
2816.7	1^-	1^-
2926.5	0^-	1^-
2970.0	0^+	1^-
3242.2	1^+	1^-
3275.9	1^+	2^-
3421.5	0^+	1^-
3455.9	1^+	1^-
3636.2	1^+	1^-
3672.2	0^+	1^-
3977.9	1^+	1^-
3986.4	1^+	1^-
4289.3	0^-	1^-

Table 7.3: The two sets of spins and parities used for the TAS analysis of ^{76}Rb for the levels for which there is no definite spin-parity assignment in [76].

last known level assumed (keV)	start unknown part (keV)
2332.6	2571
3242.2	3300
3672.2	3700
4289.3	4320

Table 7.4: Assumptions made for the construction of the unknown part of the level scheme of ^{76}Kr using the statistical model. The first column gives the last level considered to be known in the level scheme. The second column shows the starting energy from which the statistical model is applied up to the Q_{EC} in order to generate the de-excitation pattern for the unknown part of the level scheme.

most of the beta strength lies at high excitation energy, which is missed with high resolution measurements.

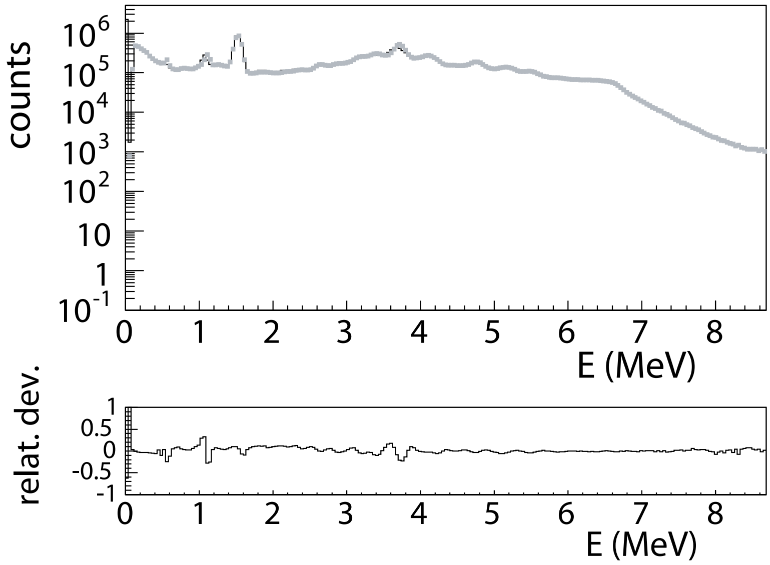

Figure 7.12: Upper panel: Experimental TAS spectrum of ^{76}Rb (black continuous line) with contaminants. The reconstructed spectrum obtained from our analysis appears overlaid (grey dashed line). Lower panel: difference of the reconstructed spectrum from the experimental one relative to the latter.

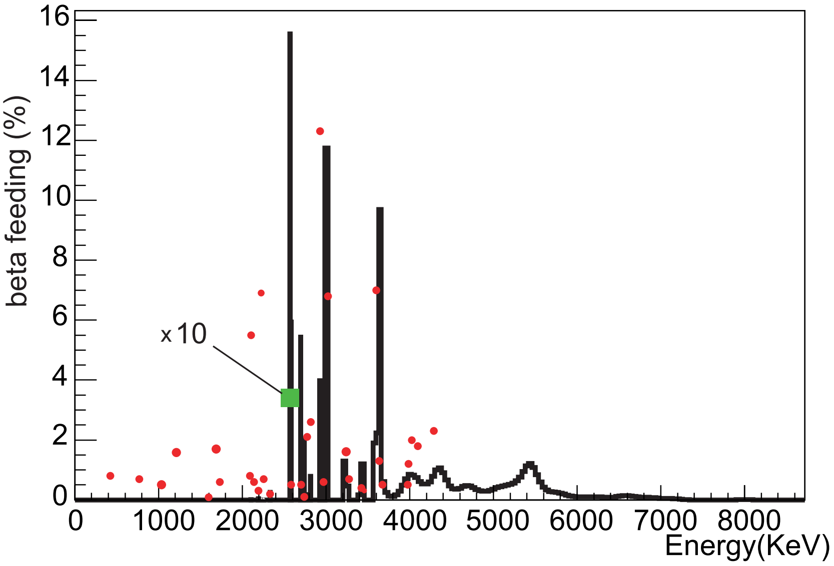

Figure 7.13: Comparison of the beta feeding obtained after the TAS analysis (continuous line) and that from the high resolution experiment (red dots) for the β-decay of ^{76}Rb. The beta feeding value which appears as a square has been reduced by a factor of 10 so that it appears in the comparison.

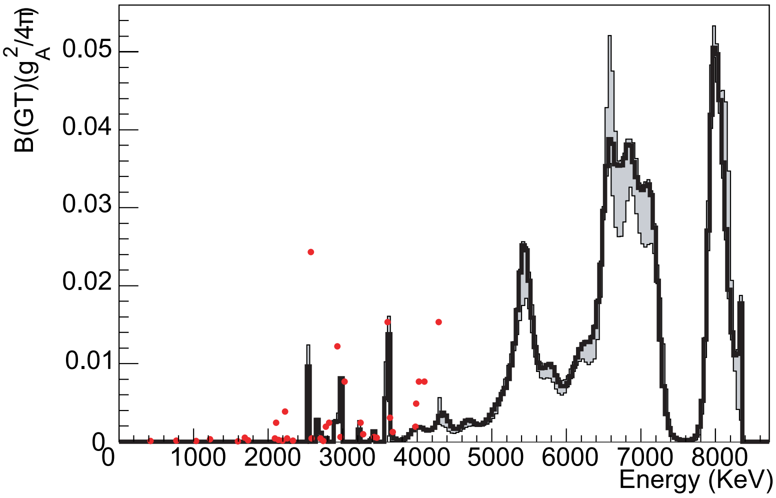

Figure 7.14: B(GT) distribution in the beta-decay of ^{76}Rb as a function of the excitation energy in the daughter nucleus (solid line) using the TAS method. The B(GT) distribution using high resolution spectroscopy (red dots) is also shown.

7.4 ^{78}Rb decay results

In our experiment, ^{78}Rb was produced via the decay of ^{78}Sr only. As a consequence the 4^- isomeric state was not populated and these results address only the decay of the 0^+ ground state. Since ^{78}Kr is stable, no daughter contamination was considered. In the previous chapter, Fig. 6.3 shows the contaminant subtraction from the raw TAS spectrum. Further details of how the subtraction was done are given there. Information on the low-lying levels populated in the decay of ^{78}Rb was extracted from reference [78] but only the levels populated in the decay of ^{78}Rb ground state have been considered in this work. The conversion coefficients derived for several transitions by Giannatiempo et al. [143] have also been used. In summary, for those levels with no spin-parity assignment in these references, a 1^+ spin-parity has been used with the only exception being the level at 2573.3 keV, for which we have assumed a 1^- spin-parity. These spin-parity assigments are in accord with the suggestions by Giannatiempo et al. for certain levels based on the α_k values reported in their paper. Table 7.5 shows the 4 starting excitation energies used for the application of the statistical model.

last known level assumed (keV)	start unknown part (keV)
5585.9	5620
4420.7	5020
4420.7	4620
3662.1	3700

Table 7.5: Assumptions made for the construction of the unknown part of the level scheme of ^{78}Kr using the statistical model. The first column gives the last level considered to be known in our knowledge of the level scheme. The second column shows the starting energy from which the statistical model is applied up to the Q_{EC} in order to generate the de-excitation pattern for the unknown part of the level scheme at high energies.

Bavaria et al. [78] extracted a beta feeding to the ground state of ^{78}Kr of 8%. They interpreted this feeding as arising from an admixture of the ^{78g}Kr analogue state (T=3, T_3=2) into ^{78g}Rb (T=T_3=2). However their measurements are based on γ-γ coincidence, β^+ singles and $\beta^+-\gamma$ coincidence with the use of Ge and Si(Li) detectors and a β-spectrometer. Therefore their studies are also subject to the Pandemonium effect. The gs-gs feeding in the decay of ^{78}Rb has been studied carefully in this work although the inherent properties of the TAS limit its sensitivity. This is due to the fact that only the penetration of the β^+ in the gs-gs decay can be detected with the TAS. Different analyses have been made assuming different values of the gs-gs feeding ranging from 0-8%. The smallest value of χ^2 was obtained when no feeding to the ground state was considered. This is consistent with the fact that the gs-gs transition in this case is isospin-forbidden and should be zero.

Figure 7.15 shows the comparison between the reconstructed spectrum and the experimental one including the contaminants. In addition, Figs. 7.16 and 7.17 show the beta feeding and B(GT) obtained with the TAS analysis. The beta feeding obtained with high resolution spectroscopy results in a predominant 'apparent' beta feeding at low excitation energies within the range 0-2.5 MeV, which is not observed with the TAS. This is again a clear example of the Pandemonium effect which results from the use of Ge detectors and their modest efficiency.

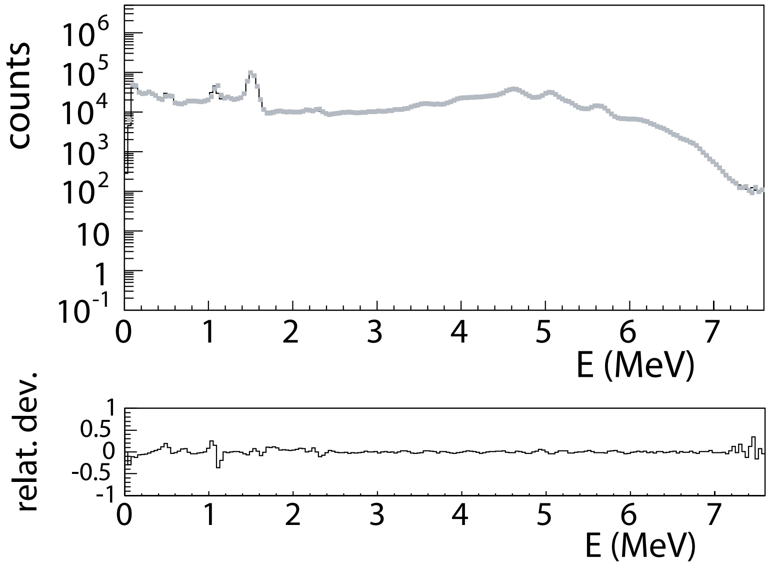

Figure 7.15: Upper panel: Experimental TAS spectrum of ^{78}Rb (black continuous line) with contaminants. The reconstructed spectrum obtained from our analysis appears overlaid (grey dashed line). Lower panel: difference of the reconstructed spectrum from the experimental one relative to the latter.

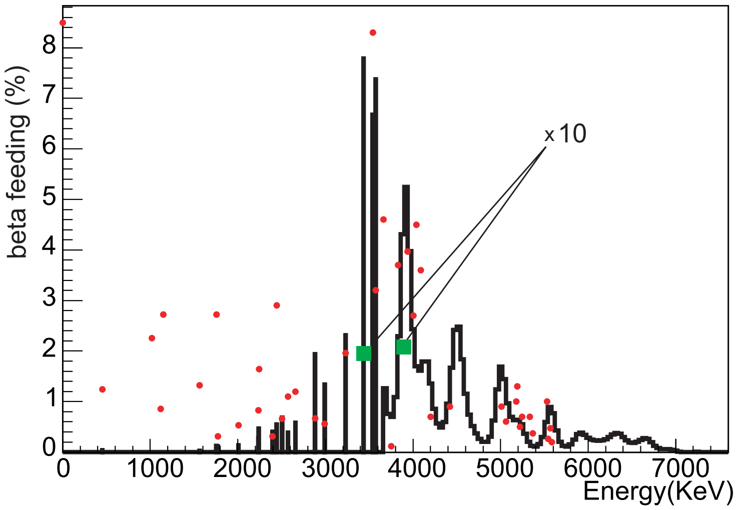

Figure 7.16: Comparison of the beta feeding obtained after the TAS analysis (continuous line) and that from the high resolution experiment (red dots) for the β-decay of ^{78}Rb. The beta feeding values which appear as squares have been reduced by a factor of 10 so that they appear in the comparison. No gs-gs feeding has been considered (see text).

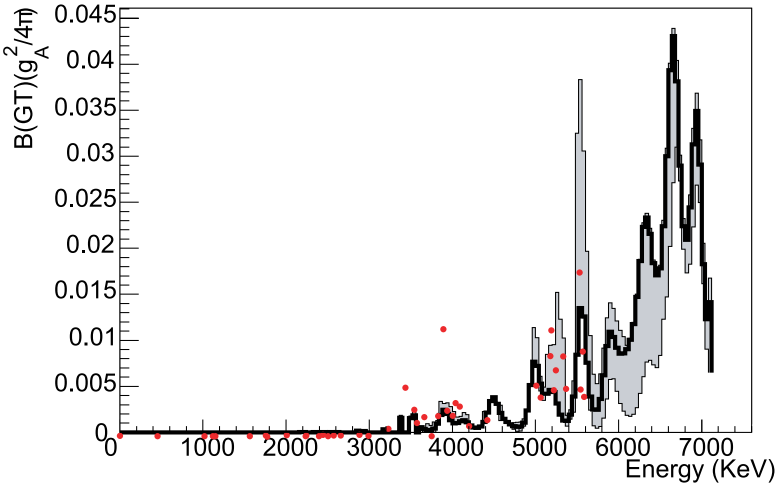

Figure 7.17: B(GT) distribution in the beta-decay of ^{78}Rb as a function of the excitation energy in the daughter nucleus (solid line) using the TAS method. The B(GT) distribution using high resolution spectroscopy (red dots) is also shown.

7.5 Deformation of the ^{78}Sr ground state

The main aim of these experiments was to determine the shape of the ^{78}Sr ground state. Since the spin of the ground state is I=0, no experimental quadrupole moment can be measured. Previous studies based on the measured B(E2;$2^+ \rightarrow 0^+$) for the ground state band in ^{78}Sr [26] and isotope shift measurements [113] support a large deformation for the ground state of ^{78}Sr. They are in agreement with theoretical calculations which predict a large prolate deformation reported by Möller and Nix [112]. However, the experimental studies cannot give conclusive evidence on the sign of the deformation.

Challenged by the success in deducing the deformation of the ground state of the even-even ^{74}Kr [45] and ^{76}Sr [44] nuclei using the TAS method, we used a similar approach for ^{78}Sr comparing our data with the existing theoretical calculations [50] for the B(GT) distribution as a function of energy. As mentioned in Chapter 2, these calculations use a self-consistent formalism based on a deformed Hartree-Fock (HF) mean field obtained with a Skyrme interaction including pairing correlations in the BCS approximation. The minimisation of the HF energy by fixing the nuclear deformation leads to a different solution for each value of the deformation. In the case of ^{78}Sr two minima are observed, one spherical and another prolate with $\beta \sim 0.42$. Three different Skyrme forces, namely SG2, SK3 and SLy4, have been used. They predict similar minima in the plot of the total HF energy versus deformation. Of particular note is the fact that the calculations using a SG2 and SLy4 interaction predict a spherical shape for the ground state, whereas the Sk3 interaction predicts a prolate shape. A separable spin-isospin residual interaction is then added to the mean field and treated in the Quasi-Random Phase Approximation (QRPA) formalism to obtain the B(GT) distribution which is compared with our data. The parent state and the states populated in the decay are assumed to have the same deformation when performing these B(GT) calculations.

We are interested in the comparison between the experimental B(GT) results and the theoretical B(GT) calculations. This comparison is difficult when done level by level since the positions of the levels reproduced by the theory seldom agree exactly with the experimental levels. An appropriate way to compare the experimental results with the theoretical calculations is to use the accumulated B(GT). The comparison is illustrated in Fig. 7.18. It shows the accumulated B(GT) strength for ^{78}Sr β^+/EC decay as a function of the excitation energy in the daughter nucleus. We also show in grey the error bars taking into account the different contributions to the uncertainty for the strength determination, addressed in Chapter 6. On the left of the figure, the B(GT) is compared with the accumulated strength calculated with the SG2, SK3 and SLy4 forces for prolate deformation. On the right hand side the experimental results are compared with similar calculations for the spherical case. The three Skyrme forces show a similar pattern for the B(GT) for both shapes, only differing slightly in the details. From this comparison it becomes very clear that the parent state is prolate since a similar trend is found between the experimental data and the calculations for the prolate shape. In contrast, the spherical shape fails to reproduce the B(GT) strength, in particular at high excitation energy. The minimum of β ~0.42 resulting from the prolate shape calculations is in agreement with the large deformation provided by the literature [26, 112, 113, 111]. In conclusion, this comparison gives a definitive evidence of the prolate character of the ground state deformation for ^{78}Sr. It also provides another example, in addition to the ^{74}Kr and ^{76}Sr cases, that confirms that this kind of comparison can be used to deduce ground state deformations in the region.

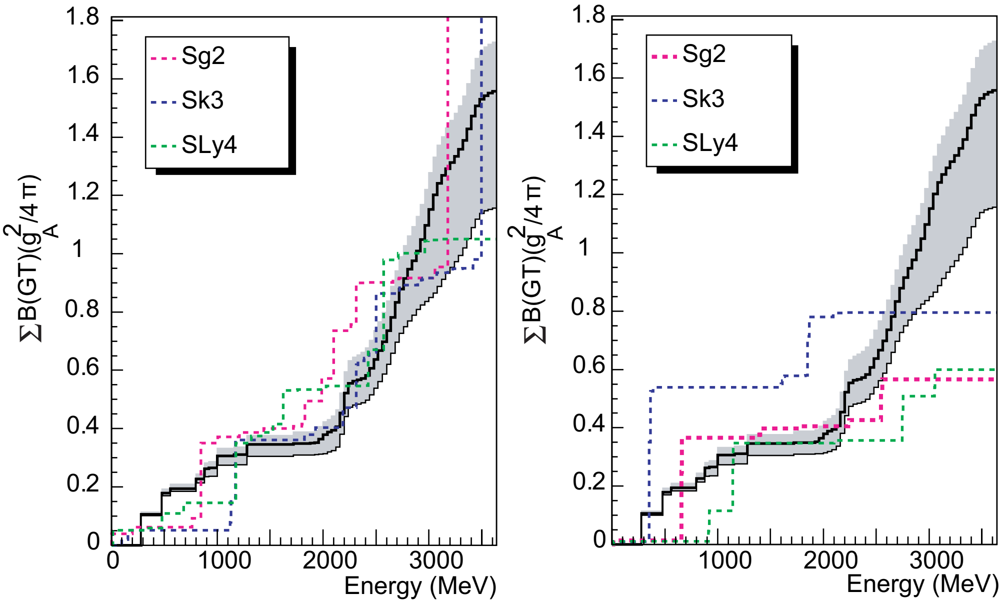

Figure 7.18: Accumulated B(GT) distribution resulting from this work (solid line) compared with QRPA calculations for prolate (left) and spherical (right) shapes of ^{78}Sr using the SG2, SK3 and SLy4 Skyrme forces [50].

7.6 Discussion of the B(GT) distribution for ^{77}Sr

In Fig. 5.8 in chapter 5 it was discussed that two distinct regions can be expected in the B(GT) distribution for ^{77}Sr β-decay, which is also a common feature for odd-A nuclei. The first region at low energy corresponds to 1qp excitations where the excitations are determined by the unpaired proton state. A second region, at energies above twice the pairing gap (2×1.1-1.5 MeV), results from 3qp excitations

I	E_{exc}^{exp} (keV)	$B(GT)_{th}$ $(g_A^2/4\pi)$	$B(GT)_{TAS}$ $(g_A^2/4\pi)$	$B(GT)_{hr}$ $(g_A^2/4\pi)$
$5/2^+$	146.9	0.0449	0.038(3)	0.22(3)
$7/2^+$	307.2	0.0179	0.0067(9)	0.008(2)

Table 7.6: GT strength predicted by the theory, $B(GT)_{th}$, obtained with the TAS, $B(GT)_{TAS}$, and with high resolution spectroscopy, $B(GT)_{hr}$, for the rotational members $5/2^+$ and $7/2^+$ built up on the $5/2^+$ band head corresponding to 1qp excitations of the proton in the $\pi[422]5/2^+$ orbital. The experimental excitation energy of those members is also listed.

where the odd neutron acts as an spectator and one proton-hole and one neutron-particle are created in the decay. Only a limited number of excitations can occur in the case of 1qp excitations at low energy whereas, in the part above ~2.5 MeV, the strength is much larger since more possible configurations can contribute. In Fig. 7.19 the strength distribution obtained with the TAS is plotted and compared with HF+BCS+QRPA calculations performed with the SG2 Skyrme force for a prolate shape. The rotational nature of the final states reached in ^{77}Rb has also been taken into account in the calculations (see more details in Sec. 5.7). In the lower energy part, it can be seen that two states observed experimentally receive most of the strength. They correspond to 1qp excitations with the proton in the $\pi[422]5/2^+$ orbital. The first peak corresponds to the $5/2^+$ level lying at 146.9 keV and the second one to the $7/2^+$ at 307.2 keV, both members of the positive-parity rotational band built on the $5/2^+$ band head (see Sec. 5.7). These excitations are also predicted by the theory as shown by the two dots that appear at low energy. They agree well with the experimental results obtained with the TAS which provide a reliable strength. The squares in the same figure represent the predicted strength assigned to 1qp excitations with the proton in the $\pi[431]3/2^+$ orbital. This configuration was already discussed in Sec. 5.7 concerning the level structure of ^{77}Sr. It was concluded that these predicted states are clearly not present in our experimental results. This statement is further reinforced by the TAS results. It can be observed that apart from those two experimental peaks at very low excitation energy, there is hardly any strength below 2.5 MeV as a result of the limited possibilities for 1qp proton excitations. Above 2.5 MeV is where most of the experimental GT strength lies. This is also in accord with the results of the calculations and with what one would expect from the arguments given in Sec. 5.7. It should be noted that this relevant region at high energy was not observed with high resolution spectroscopy due to the inherent properties of Ge detectors.

In order to make a better comparison with the theory, the theoretical GT strength has been convoluted with a gaussian of Γ=1 MeV which transforms the discrete the-

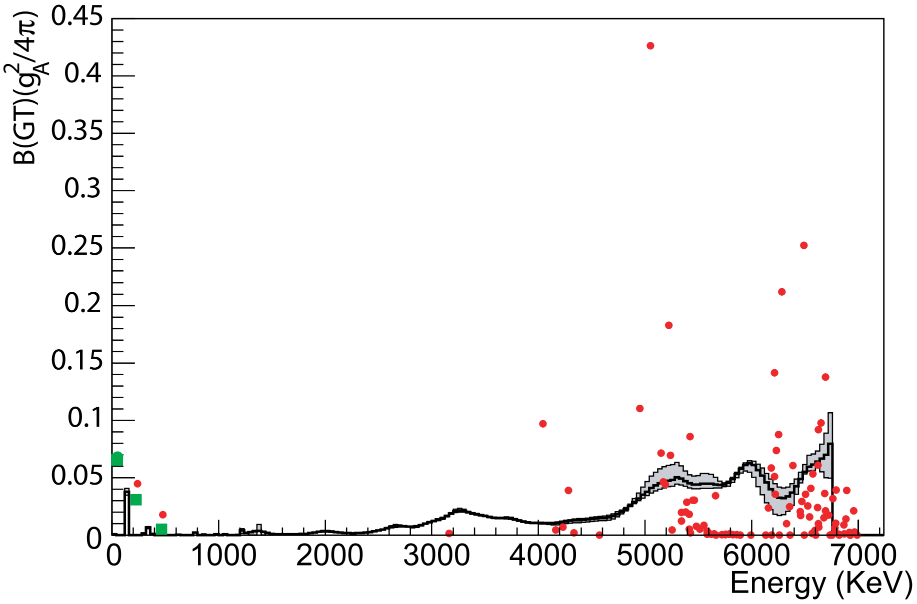

Figure 7.19: Gamow-Teller strength transitions in the beta-decay of ^{77}Sr as a function of the excitation energy of the daughter nucleus. The continuous line corresponds to the TAS results whereas the dots show the HF+BCS+QRPA calculations for the strength. The squared dots correspond to 1qp excitations with the proton in the $\pi[431]3/2^+$ orbital obtained with the theory for which no correspondence with the experimental results has been found (see text).

oretical spectrum in Fig. 7.19 into a continuous one in the upper panel of Fig. 7.20. The results obtained with the use of other Skyrme forces, namely SK3 and SLy4, are also shown. This representation is a better approximation since it incorporates a more reliable fragmentation of the strength and smoothing effects due to other coupling modes which are not taken into account in the QRPA. The lower panel of Fig. 7.20 shows the same but for the case of a spherical g.s. in ^{77}Sr. In this latter case, it is clear that the theory does not reproduce the experimental results since it predicts a very large part of the strength at low energy. This in in accord with the prolate deformation expected based on the measured quadrupole moment by Lievens et al [122]. In fact, the calculations using a prolate shape are in very good agreement with what is observed. Although the bump at 3 MeV in the strength is not reproduced by the theory it should be noted that one cannot expect so much detail in this type of calculation when done level by level. In general the trend is reproduced as is the total B(GT) expected within the Q_{EC} window. This can be seen in a better way if the accumulated strength is plotted, as shown in Fig. 7.21.

On the other hand, the decay involving 3qp type excitations (see Fig. 5.8)

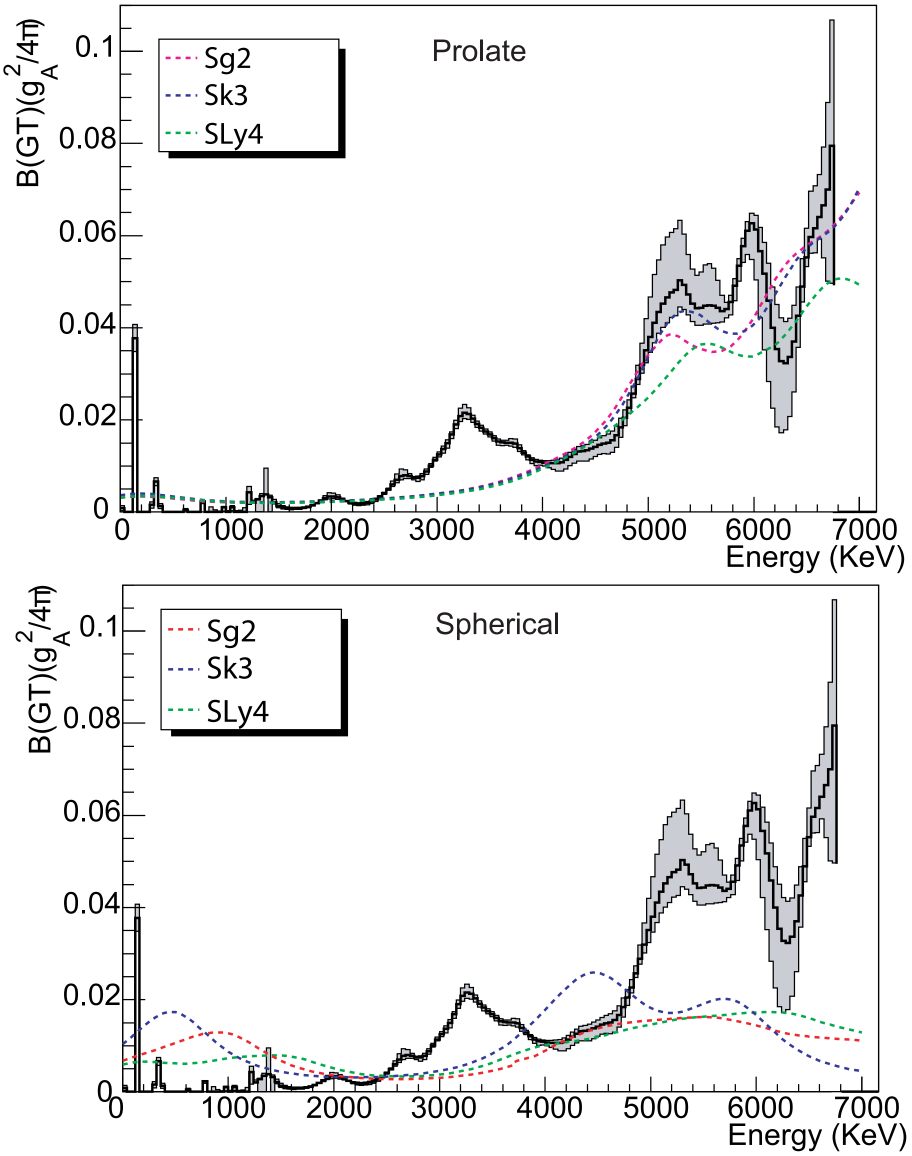

Figure 7.20: Gamow-Teller strength transitions in the beta-decay of ^{77}Sr as a function of the excitation energy of the daughter nucleus. The upper panel shows the comparison with HF+BCS+QRPA calculations using the Skyrme forces SG2, Sk3 and SLy4 for a prolate shape while the bottom panel corresponds to the same for a spherical shape. A gaussian of width Γ=1 MeV has been used for the representation of the theoretical calculations in contrast to Fig. 7.19.

can be compared to the decay in the even-even case since the only difference is the blocked neutron orbital excluded in the process and the expected excitation energy. In fact, both strength distributions are very similar, as shown in Fig. 7.22. For the

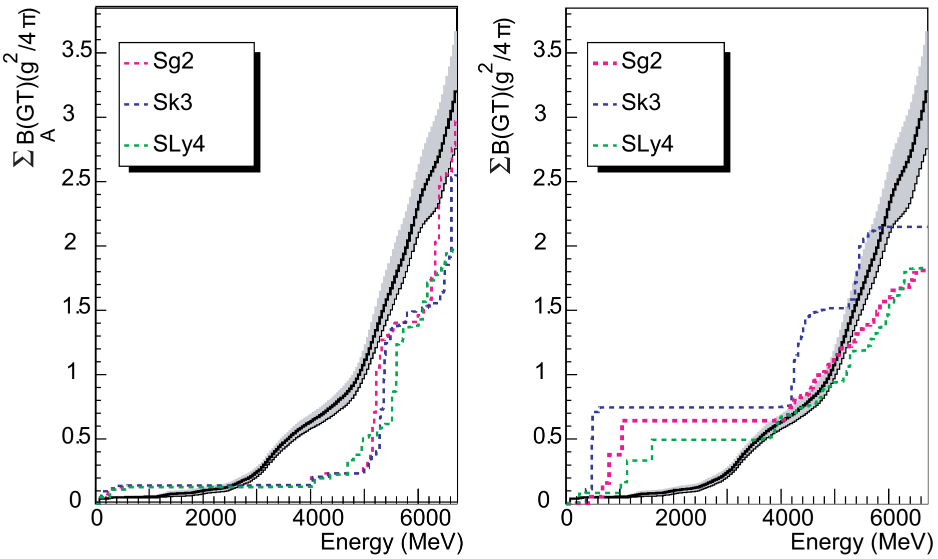

Figure 7.21: Accumulated B(GT) distribution resulting from this work (solid line) compared with QRPA calculations for prolate (left) and spherical (right) shapes using the SG2, SK3 and SLy4 Skyrme forces in ^{77}Sr.

comparison the strength of the even-even case, ^{78}Sr, has been shifted by 2×Δ ∼2.4 MeV.

In summary, the nucleus ^{77}Sr provides another test of HF+BCS+QRPA calculations in the region where the theory succeeds in reproducing the experimental results, only available if the TAS method is used. This provides the first example of the comparison between the B(GT) results obtained experimentally with a TAS and the theory for an odd-nucleus. Therefore, it opens new opportunities to study ground state deformations for odd-mass nuclei in the region.

Finally, it should be mentioned here that a very interesting case is the decay of ^{72}Kr where shape-coexistence is expected. This case was measured in the same set of experiments but the results are not presented in this PhD. thesis.

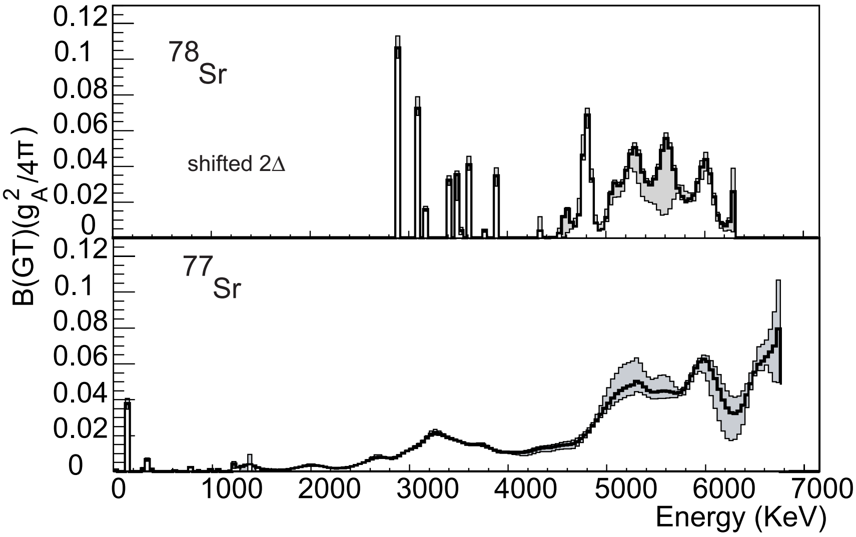

Figure 7.22: Comparison between the B(GT) distribution of ^{78}Sr (upper panel) and ^{77}Sr (lower panel). The former has been shifted by 2.4 MeV which is approximately twice the pairing gap.

7.7 Discussion of the B(GT) distributions for masses 76 and 78

We will now discuss the B(GT) distributions obtained for the decay of ^{76,78}Sr and ^{76,78}Rb with the Total Absorption technique. Figure 7.23 shows the accumulated B(GT) distributions for the four cases. The data for ^{76}Sr were analysed previously and the results published in [44]. The first point to note is that the total strength in ^{76}Sr is larger than in any of the other three cases. If we compare ^{76}Sr and ^{78}Sr, then we might anticipate naively that, since the only change is a couple of extra neutrons, the B(GT) distributions should be similar. This is indeed the case up to 3.7 MeV excitation in the daughter nucleus, the Q$_{EC}$-value in ^{78}Sr, as shown in Fig. 7.24. Above 3.7 MeV, there is strong feeding at 4-5 MeV in the decay of ^{76}Sr, whereas in ^{78}Sr this energy range is cut off by the Q$_{EC}$-window.

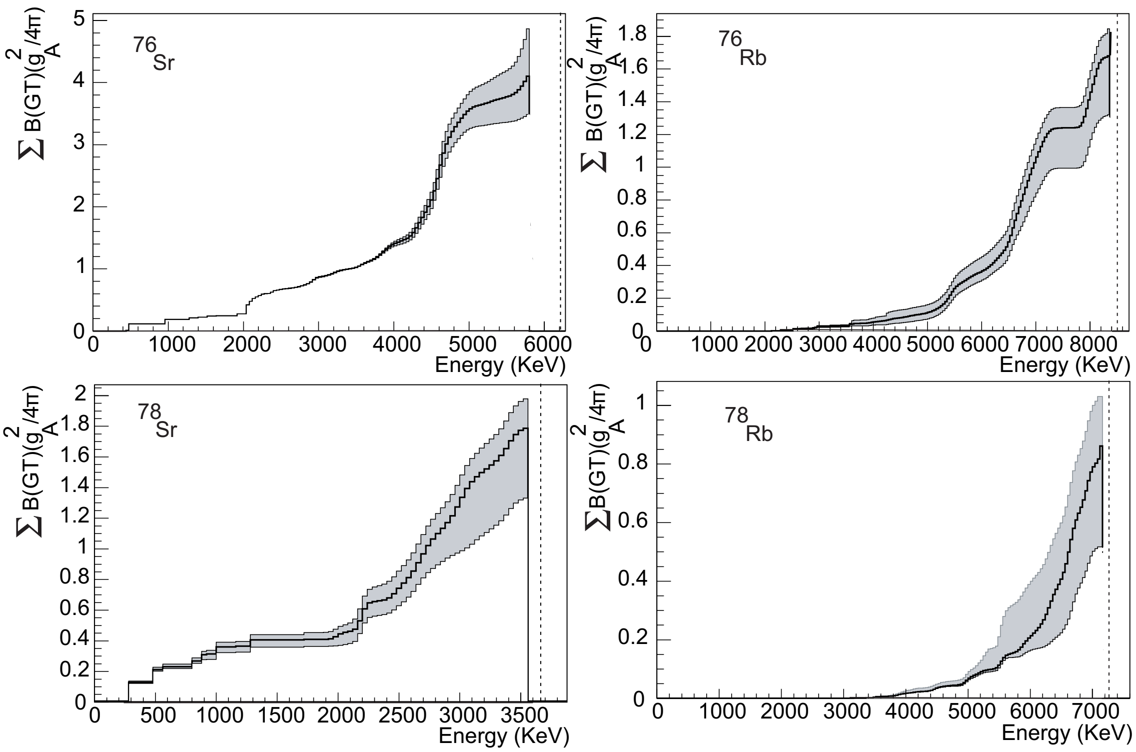

Figure 7.23: Accumulated B(GT) for ^{76}Sr [44], ^{76}Rb, ^{78}Sr and ^{78}Rb as a function of the excitation energy in the daughter nucleus using the TAS method. The vertical dotted line indicates the position of the Q$_{EC}$ value.

In the previous section, we have compared our results for ^{78}Sr with the theoretical calculations. The same is done in [44] for the ^{76}Sr case. Unfortunately there are

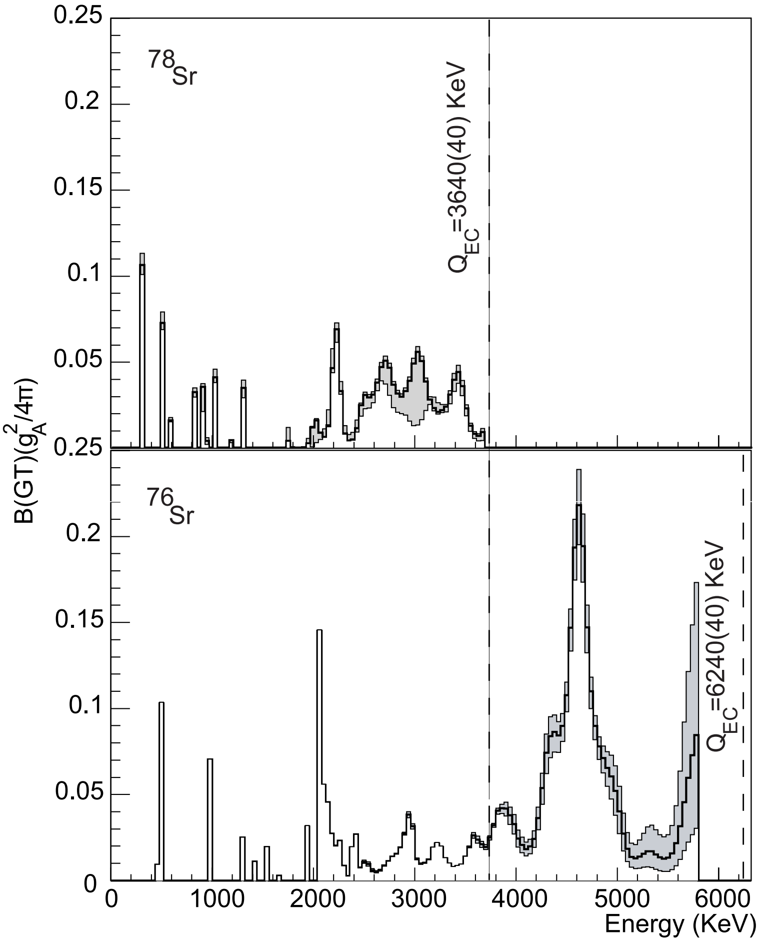

Figure 7.24: Comparison of B(GT) for the decay of ^{76}Sr and ^{78}Sr. The vertical dashed lines indicate the Q_{EC}-values for the two nuclei [67].

no similar theoretical calculations for the decay of the odd-odd nuclei. We will try to draw some conclusions from the comparison of their B(GT) distributions with their corresponding even-even case. As an aid to our understanding we can use the simple schematic diagram shown in Fig. 7.25. In the upper right side of the figure we show the decay of the even-even case into the odd-odd daughter nucleus (diagram (a)). This case involves the transformation of one proton in an occupied orbital into a neutron in an empty orbital. Note that in the present case, since we are talking about Nilsson orbitals which can be occupied by two particles at most, there is no difference between a "particle" and a "hole". We will use this terminology since it is easier to explain what happens in β-decay. The final state is a proton hole-neutron particle state in the odd-odd nucleus and the excitation energy of the state populated is essentially the single particle orbit energy difference of the two valence particles with respect to the ground state.

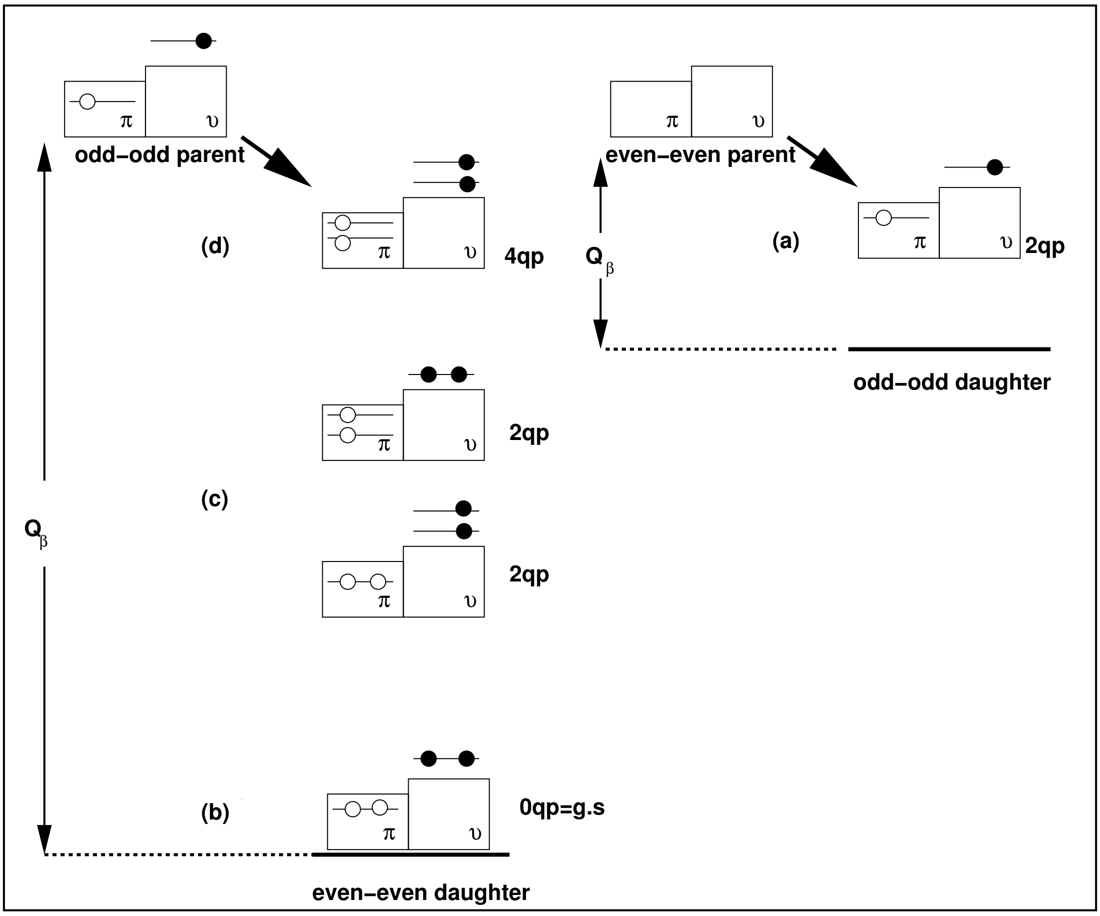

Figure 7.25: Possible β-decays in an odd-odd and even-even nucleus shown in an schematic way.

In the odd-odd decay there are three different possibilities which are expected to lie at three different excitation energies:

- Diagram (b) considers the transformation of the unpaired proton in the parent nucleus into a neutron in the daughter which occupies the same orbital as that of the odd neutron in the parent. In this case the final state results in two protons and two neutrons coupled to zero in the even-even daughter nucleus. This final state corresponds to the ground state in the even-even daughter nucleus. In the ^{76}Rb case, the parent ground state has a $(\pi[301]3/2^- - \nu[422]5/2^+)1^-$ configuration [144] and therefore this decay is not possible. On the other hand, ^{78}Rb is assumed to have a $(\pi[312]3/2^- \text{-} \nu[301]3/2^-)0^+$ configuration, as concluded in Chapter 4, and in principle the decay drawn in this diagram is possible. However, since ^{78}Kr also has a 0^+ ground state, this decay would be isospin-forbidden unless isospin mixing in the parent ground state was considered. The results from the analysis of the TAS data for ^{78}Rb confirm no strength in the gs-gs β-decay. Therefore the decay considered in diagram (b) is not possible for ^{78}Rb either.

- Diagram (*c*) shows two possible decays: Either the transformation of the odd proton from the parent ground state into a neutron in a different orbital from the ground state or the proton from a different orbital from the ground state into a neutron in the same orbital occupied by the odd neutron in the parent state. This results in a final state of two particle character (two valence protons or neutrons not coupled to zero in the daughter nucleus). Relative to the daughter ground state, these states require enough energy to break the proton or the neutron pair plus the excitation energy of the nucleons involved. Therefore they are expected at around 2-3 MeV excitation roughly if we consider the values given in Sec. 4.8 for the neutron and proton gap for ^{78}Sr. In general we will assume a pairing gap value ranging within 1.1-1.4 MeV for masses 76 and 78.
- Diagram (d) shows the case in which the valence proton and neutron in the parent ground state act as spectators in the decay. One proton from a different orbital from the parent ground state gets transformed into a neutron occupying an orbital also different from the parent ground state. Relative to the even-even ground state this is a four-particle excitation with two unpaired protons and two unpaired neutrons and requires the energy to break two pairs plus the corresponding single particle energies. From the point of view of the transformation of the parent ground state, the beta-decay is identical to figure (a). Consequently this decay should lie at the same energy below the parent ground state or from another point of view, at around four times the pairing gap.

Once this simple picture is presented, our aim is to deduce some information for the odd-odd cases. Figure 7.26 shows the B(GT) strength of ^{76}Sr and ^{76}Rb in the upper panel and ^{78}Sr and ^{78}Rb in the lower panel, with the B(GT) of both Sr isotopes shifted by the energy required to break two pairs (between 4-5 MeV depending on the nucleus). As explained above, the decay shown in diagram (b) is not possible for either ^{76}Rb nor ^{78}Rb. In both cases most of the strength lies at high energies, which corresponds to the process schematically drawn in diagram (d). This is what one would expect since the number of possible orbitals on the neutron side for an allowed G-T transition is much larger than in the case represented by diagram (*c*). In what follows we will discuss the decays corresponding to diagram (*c*):

- ^{78}Rb:
  1. Transformation of a proton from an orbital with K=1/2, 3/2 and 5/2 and negative parity into a neutron in the valence neutron orbital of the parent ground state (ν[301]3/2$^-$).

2. Transformation from a valence proton in the parent ground state ($\pi[301]3/2^-$) into a neutron in an orbital with K=1/2, 3/2 and 5/2 and negative parity.

- ^{76}Rb:

  1. Transformation of a proton from an orbital with K=3/2, 5/2 and 7/2 and positive parity into a neutron in the valence neutron orbital of the parent ground state ($\nu[422]5/2^+$).
  2. Transformation from a valence proton in the parent ground state ($\pi[312]3/2^-$) into a neutron in an orbital with K=1/2, 3/2 and 5/2 and negative parity.

In addition, it can be observed that the strength due to the process described with diagram (c), which is expected around 2-3 MeV, seems larger in the decay of ^{76}Rb than in ^{78}Rb. This must be due to differences in the orbital configuration for the two cases. Since there are no microscopical calculations, no more conclusions can be drawn here.

Using the lower panel of Fig. 7.26, one can compare the decays of ^{78}Sr and ^{78}Rb and check whether the strength observed in ^{78}Sr, corresponding to the diagram (a), is similar to the strength observed in ^{78}Rb decay at high energy in diagram (d). It can be seen that indeed the shape of the strength is similar in the range 5.5 to 7 MeV. However the strength of ^{78}Rb lying within that region is smaller, which can be explained as caused by the blocking of the spectator orbitals in the case of the odd-odd decay, namely the valence proton and neutron in the parent state. What can be concluded from this comparison is that in general terms the structure of ^{78}Sr, ^{78}Rb and also ^{78}Kr are similar. The same kind of comparison is not so conclusive in the ^{76}Rb case though, as seen in the upper graph of Fig. 7.26. However, we can clearly conclude that most of the strength observed is due to the decay represented by diagram (d).

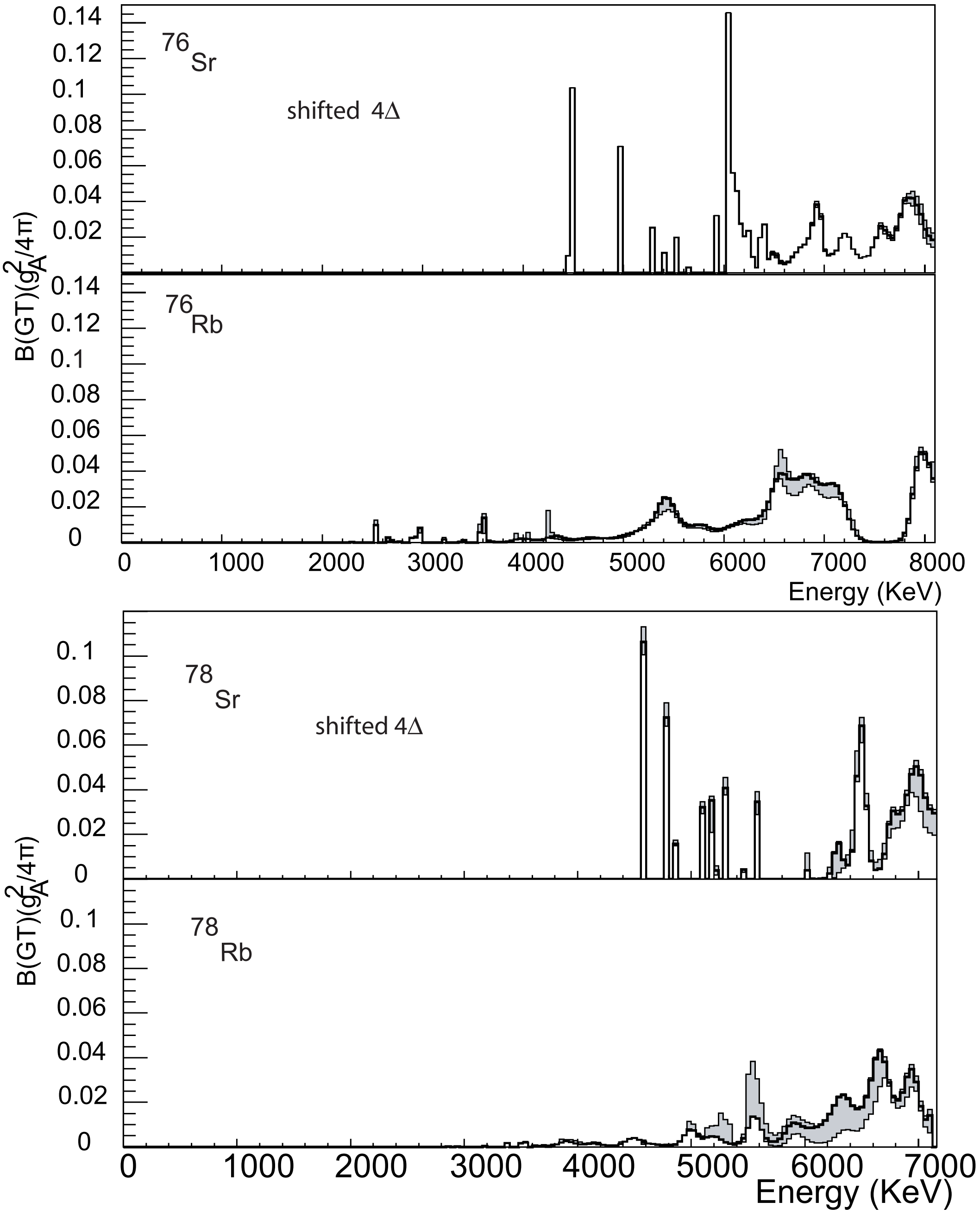

Figure 7.26: The upper graph shows a comparison between the B(GT) distribution of ^{76}Rb and ^{76}Sr. The latter has been shifted ~4.5 MeV which is approximately the energy required to break two pairs. The lower graph shows the same for the ^{78}Sr and ^{78}Rb cases.

Chapter 8

Summary

8.1 High Resolution measurements

We have studied the β^+/EC decay of ^{77,78}Sr and ^{76,78}Rb in this work. We have carried out measurements of the energies and intensities of the emitted gamma-rays and conversion electrons as well as γ-γ and γ-X-ray coincidences in the decays of ^{77,78}Sr, which have extended our knowledge of their decay schemes including spin and parity assignments to the levels populated in the daughter nucleus, ^{77}Rb and ^{78}Rb respectively.

For the decay of ^{78}Sr, we have confirmed the 7 excited levels observed by Mukai et al. [79] and the 15 transitions observed by Grawel et al [91]. Moreover, ten of the levels seen in the present work were also observed in the in-beam study by Kaye et al. [96]. In total 16 new levels and 44 new γ-ray transitions have been identified. The very much improved experimental knowledge of the ^{78}Rb levels populated in the decay and the strong link between the parent and the daughter states has allowed us to infer some possible level configurations. The structure of odd-odd nuclei is, in general, difficult to interpret and even more so in this part of the nuclear chart, where shape co-existence is common. Although a simple calculation based on a mean-field approach does not always permit us to associate an observed excited state with a definite configuration we believe that the results of the β-decay study of ^{78}Sr and the comparison with HF+BCS calculations using the SG2 Skyrme force has allowed us to make a more advanced interpretation for this difficult case.

For the decay of ^{77}Sr, we have confirmed 3 of the levels and 5 of the gamma-ray transitions observed by Lister et al [80]. In addition, 8 of the gamma-ray transitions and 6 of the levels observed in the present study were also seen in the in-beam experiment by Harder et al [121]. In total 9 new levels and 15 new gamma-ray transitions have been identified. The levels in the low energy part of the level scheme have been discussed in terms of HF+BCS+QRPA calculations leading to an interpretation of their structure.

8.2 Total Absorption measurements

In addition, a study of the β-decay of ^{77,78}Sr and ^{76,78}Rb using the LUCRECIA spectrometer at ISOLDE has been carried out. Information was required on the discrete level schemes of these nuclei for the analysis of the TAS data. Here we have relied on published data for the β-decays of ^{76}Rb and ^{78}Rb and on the decay schemes obtained from our high resolution experiments for ^{77}Sr and ^{78}Sr. The β intensity and B(GT) distributions have been deduced from the analysis of the TAS data. The comparison of the B(GT) distribution of the decay ^{78}Sr with theoretical calculations has confirmed the prolate shape, with β=0.42, of the ground state of ^{78}Sr in agreement with the proposed large deformation based on previous isotope shift measurements [113] and the measured B(E2;$2^+ \rightarrow 0^+$) values for its ground state band [26]. The B(GT) distribution of ^{77}Sr has been interpreted using a very simple decay picture. The theoretical results using a large prolate deformation for the ground state of ^{77}Sr are found to reproduce well the TAS results. Their β value, namely β=0.4, is also in agreement with the large measured spectroscopic quadrupole moment of ^{77}Sr from a previous study [122]. In summary, our study of ^{77}Sr and ^{78}Sr has provided other examples, in addition to the ^{74}Kr [45] and ^{76}Sr [44] cases, that confirm the validity of the HF+BCS+QRPA theoretical calculations in the region. They have also validated the method of extracting the deformation of the parent ground state by comparing the experimental B(GT) with that calculated. General conclusions have been inferred for the odd-odd nuclei, ^{76}Rb and ^{78}Rb, based on a comparison with their corresponding even-even nuclei. ^{76}Sr and ^{78}Sr are found to have similar B(GT) distributions up to the Q_{EC} window available in the decay of ^{78}Sr, and thus a similar structure. This is not surprising since they only differ in a couple of extra neutrons. In general terms, the structure of ^{78}Sr, ^{78}Rb and also ^{78}Kr seems to be similar from a comparison of the experimental B(GT) distributions for the decays of ^{78}Sr and ^{78}Rb. Here we rely on the assumption that the parent state and the states populated in the decay in the daughter nucleus have the same deformation. The same kind of comparison is not so conclusive in the ^{76}Rb case though.

Chapter 9

Resumen en castellano

En este último capítulo se incluye un resumen de la tesis doctoral en castellano.

9.1 Antecedentes

El proceso de la desintegración beta, que tiene lugar en el interior de núcleo y es debido a la interacción débil, consiste en la conversión de un protón en un neutrón o viceversa y la emisión de un ν_e o un $\bar{\nu}_e$ respectivamente. Como consecuencia de dicho proceso el número atómico Z desciende o aumenta en una unidad, conservándose el número de nucleones A.

Según la teoría de Fermi, el elemento de matriz H$_{fi}$=⟨f|H|i⟩, que contiene el Hamiltoniano de la interacción débil, puede dividirse en dos partes: una parte que gobierna las desintegraciones Fermi y otra las Gamow-Teller.

$$|H_{fi}|^2 = g_F|M_{fi}^F|^2 + g_{GT}|M_{fi}^{GT}|^2 \tag{9.1}$$

El primer modo viene mediado por el operador vectorial O$_F$=$\tau^{\pm}$ que aumenta o disminuye la tercera componente de isospín en una unidad, es independiente del espín nuclear y no transporta momento angular. El segundo modo, la desintegración Gamow-Teller (GT), incluye el operador axial de Pauli O$_{GT}$=$\sigma\tau^{\pm}$ que es causante del cambio de espín pero no del momento angular.

La probabilidad de la desintegración beta viene caracterizada por el valor ft derivado de la regla de oro de Fermi y puede a su vez expresarse en términos de la llamada probabilidad de transición total beta B:

$$ft = \frac{6143.6 \pm 1.7}{B}\frac{g_V^2}{4\pi} = \frac{6143.6 \pm 1.7}{B(F) + B(GT)}\frac{g_V^2}{4\pi} \tag{9.2}$$

donde B(F) y B(GT) son la probabilidad de transición Fermi y la probabilidad de transición Gamow-Teller respectivamente. Éstas a su vez pueden definirse como:

$$B(F) = \frac{1}{2J_i+1} |\langle J_f \| \sum_k t^k_\pm \| J_i \rangle|^2 \equiv \frac{g_V^2}{4\pi} \langle \tau \rangle^2 \tag{9.3}$$

$$B(GT) = \frac{1}{2J_i+1} |\langle J_f \| \sum_k \sigma^k t^k_\pm \| J_i \rangle|^2 \equiv \frac{g_A^2}{4\pi} \langle \sigma\tau \rangle^2 \tag{9.4}$$

donde dichas funciones no son más que el elemento de matriz al cuadrado del operador correspondiente entre el estado inicial, estado fundamental o estado isoméro del núcleo padre, y los distintos estados finales del núcleo hijo.

Para el caso particular de una desintegracion pura GT, la convención es utilizar la siguiente cantidad adimensional, que se utilizará a lo largo de este trabajo, para definir la probabilidad de transición Gamow-Teller:

$$B = B(GT) = \langle \sigma\tau \rangle^2 \tag{9.5}$$

donde la B(GT) viene dada en unidades $g_A^2/4\pi$.

A diferencia de las transiciones de Fermi, donde sólo la tercera componente de isospin T_z cambia debido al operador τ y por tanto un único estado se puebla en el núcleo hijo, las transiciones GT son mediadas tanto por el operador σ como τ, por lo que diferentes estados en el núcleo hijo pueden ser poblados en la desintegración. Por tanto, este último tipo de transiciones aportan mucha más información acerca de la estructura nuclear en el núcleo hijo.

El estudio de la distribución de probabilidad Gamow-Teller y su probabilidad de transición para un núcleo dado, que es lo que nos ocupa en este trabajo, proporciona un excelente test para los modelos nucleares. Esto es debido a que los parámetros de que depende son extremadamente sensibles a los detalles de la estructura nuclear. Este tipo de estudios pueden realizarse mediante la observación de la desintegración beta o mediante reacciones de intercambio de carga (p,n) o (n,p), dado que este tipo último tipo de reacciones vienen mediadas por los mismos operadores que la desintegración beta.

El estudio de la intensidad GT con las reacciones de intercambio de carga está limitado a aquellos núcleos de elementos que permiten la construcción de blancos para la reacción, es decir, principalmente núcleos estables. La ventaja que aporta la desintegración beta frente a las reacciones de intercambio de carga radica en que éstas están libres del enorme fondo de estas últimas, es decir, permiten obtener un valor absoluto de la B(GT). A su vez no presenta ambiguëdades a la hora de las normalizaciones y permite el estudio de núcleos alejados de la línea de la estabilidad.

Sin embargo, el estudio de la desintegración beta viene limitado por la ventana de energía accesible dada por el valor de Q, donde Q es la diferencia de masas entre el núcleo inicial y el final. Por tanto, los casos de estudio han de presentar una intensidad GT que se encuentre en su mayor parte dentro de esta ventana. A pesar de que el proceso GT está prohibido en la mayoría de los casos, existen ciertas zonas, como la zona de los núcleos con N∼Z con A=70-80, donde estas condiciones se cumplen. Esta región es en la que se centra este trabajo.

9.2 La región A≃80 region a lo largo de la línea N∼Z de la tabla de núclidos

Los estudios de núclidos lejos de la línea de estabilidad han atraído especial interés durante décadas dado que proporcionan nueva información que permite ampliar los modelos teóricos existentes hasta la fecha. Este trabajo se centra en el estudio de la zona de núclidos con déficit de neutrones en la región de masa A≈80 en la línea N∼Z. De hecho, estos núclidos son los más pesados con N∼Z en los que se pueden llevar a cabo estudios tan detallados como en este trabajo se presentan. Los núcleos con N∼Z son especialmente interesantes. El hecho de que los protones y neutrones se encuentren ocupando los mismos órbitales dentro del núcleo en esta zona, junto con la predicción teórica de que el esquema de niveles de Nilsson presenta una serie de 'huecos' ("gaps") para los números 34, 36, 38 y 40 de protones o neutrones (véase la Fig. 9.1), da lugar a que las propiedades nucleares cambien rápidamente cuando sustraemos o a*ñ*adimos un sólo nucleón. Esta es la razón por la que se observan las siguientes propiedades en esta zona:

- Cambios drásticos de forma del estado fundamental conforme aadimos un nucleón.
- Coexistencia de forma prolata y oblata dentro del mismo núcleo ("shape-coexistence").
- Mezcla de forma en un mismo estado ("shape mixing").

En esta región, la desintegración beta está permitida dado que los orbitales neutrónicos libres poseen los mismos números cuánticos que los protones de valencia alrededor de la superficie de Fermi. Como consecuencia, se espera que una gran parte de la intensidad GT esté contenida dentro de la ventana enérgetica limitada por el Q_{EC} de la desintegración.

De acuerdo con una idea original de Hamamoto et al. [47] y después seguida por Sarriguren et al. [48], la distribución de intensidad de la desintegración beta puede ser usada para extraer información acerca de la forma del núcleo padre en

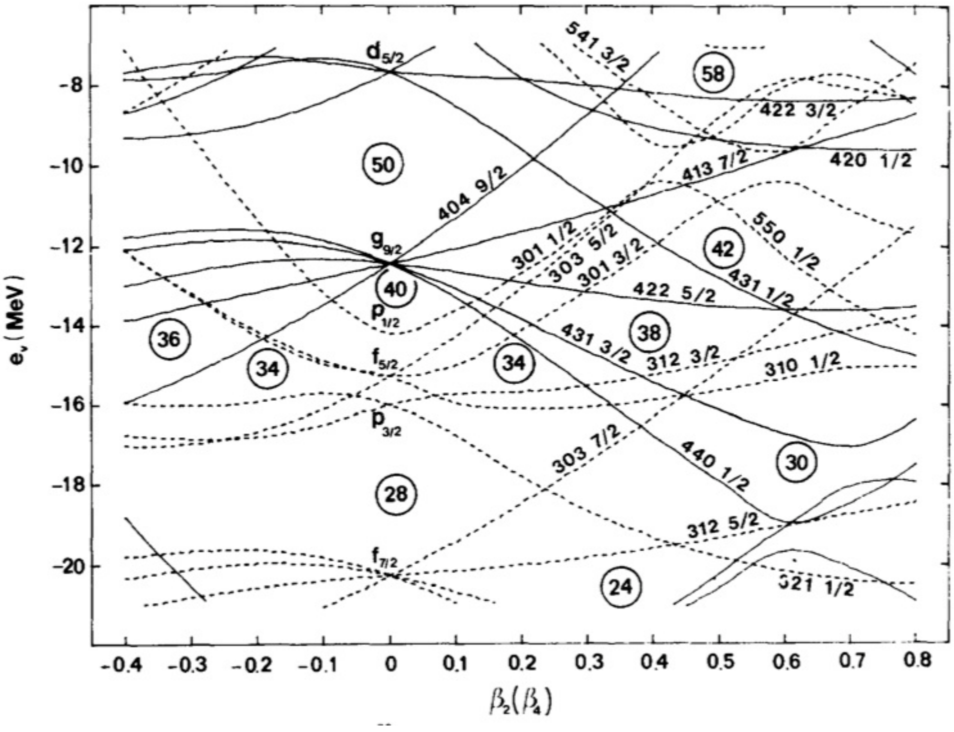

Figure 9.1: Cálculos de niveles de mono-partícula en la región A=80 en función de la deformación quadrupolar β_2 usando un potencial de Woods-Saxon [38]. En la figura aparecen los números cuánticos asímptoticos $[Nn_z\Lambda\Omega]$ para simplificar la identificación de los niveles individuales. Los números de partículas aparecen con un círculo.

algunos casos, dado que dichas distribuciones muestran una clara diferencia dependiendo de la forma (oblata, prolata o esférica) del estado fundamental del padre. Estos cálculos teóricos consisten en la utilización de un formalismo autoconsistente basado en un campo medio Hartree-Fock (HF) deformado obtenido con una interacción de Skyrme e incluyendo correlaciones de apareamiento en la aproximación BCS. A este campo medio se le incluye una interacción residual partículo-hueco (ph) espín isoespín derivada de la misma interacción de Skyrme así como una interacción residual partícula partícula (pp) de apareamiento neutrón protón en el canal $J^{\pi}=1^{+}$. Una vez hecho esto, las ecuaciones del movimiento se resuelven en la aproximación de Quasi-Random-Phase Aproximation (QRPA) protón-neutrón.

Uno de los problemas en los que se centra este trabajo es en el estudio de la deformación de estos núcleos. En el caso de los núcleos par-par, el hecho de que el estado fundamental tenga espín I=0 imposibilita la medida experimental de su momento quadrupolar. Es posible deducir indirectamente la deformación del es-

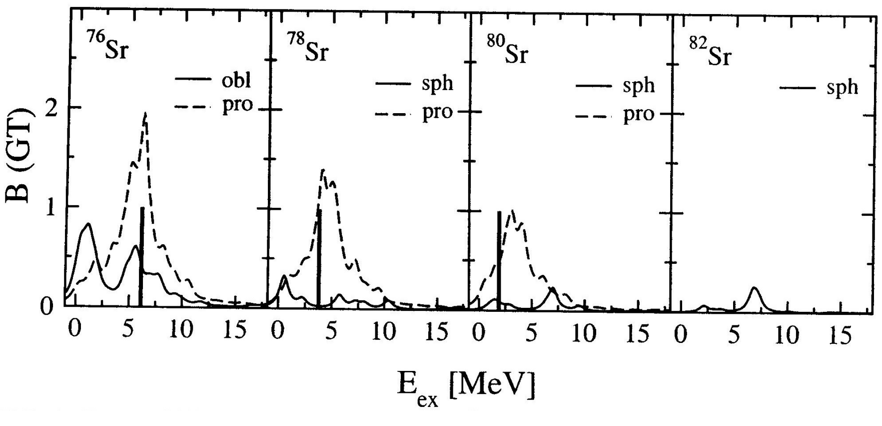

Figure 9.2: Distribuciones de probabilidad Gamow-Teller [$g_A^2/4\pi$] en función de la energía de excitación del núcleo hijo (MeV) [49]. El cálculo teórico se ha realizado asumiendo diferentes formas para el estado fundamente del núcleo padre. Las líneas verticales representan la ventana de energía accesible para la desintegración beta.

tado fundamental de estos núcleos a partir de medidas de probabilidad de transición B(E2;$2^+ \rightarrow 0^+$) o medidas de isotope shift [111]. Así mismo, la fórmula fenomenológica de Grodzin nos permite deducir la deformación β_2 a partir de la energía de excitación del primer estado excitado 2^+, E(2^+):

$$\beta_2 = [\frac{204}{(\hbar^2/2I)A^{7/3}}]^{1/2} \tag{9.6}$$

donde $\hbar^2$/2I=(1/6)E(2^+) dependiente e I es el momento de inercia. Sin embargo, ninguno de estos métodos permite obtener el signo de la formación, es decir, diferenciar entre un núcleo prolado u oblado. Esta deformación es una de las aportaciones principales de esta tesis.

Este trabajo se centra en el estudio de la distribución de B(GT) para los núcleos ^{77,78}Sr y ^{76,78}Rb. En particular, el núcleo ^{78}Sr es un núcleo par-par y existe un especial interés en determinar su deformación. La figura 9.2 muestra los cálculos teóricos para ciertos isótopos par-par del Sr [49]. En el caso del ^{78}Sr, éstos presentan una distribución B(GT) muy diferente según su estado fundamental sea prolado o esférico. Trabajos anteriores para el ^{76}Sr [44] y el ^{74}Kr [45] usando la técnica de espectroscopía de absorción total (TAS) para la determinación de la B(GT), demostraron que era posible deducir la deformación del estado fundamental del núcleo padre midiendo la B(GT) y comparando con estos cálculos. A partir de esta comparación se pudo deducir el carácter prolado y la mezcla oblada-prolada del ^{76}Sr y ^{74}Kr respectivamente. Nuestro objetivo se basa en comparar nuestros resultados experimentales con estos cálculos teóricos, al igual que se hizo para estos núcleos, y deducir la deformación del ^{78}Sr. Del mismo modo, se pretende comparar los resultados experimentales del ^{77}Sr, núcleo par-impar, con los cálculos teóricos existentes y asıobtener información sobre su estructura. Este caso es especialmente importante porque es la primera vez que se hace este tipo de estudio para un núcleo impar y en donde se utiliza la técnica del TAS. Para el caso de los núcleos par-par, en particular los núcleos ^{76,78}Rb, no existen cálculos teóricos. Nuestro objetivo será deducir información acerca de la estructura de estos núcleos en base a a la comparación de su B(GT) con aquella de los núcleos par-par, ^{76}Sr y ^{78}Sr. Para ello se utilizarán los resultados experimentales obtenidos para el ^{76}Sr de la ref. [44].

9.3 Medida experimental de la distribución de B(GT)

Desde el punto de vista experimental, la B(GT) se puede expresar en función de parámetros medibles. La probabilidad de transición GT a un estado de energía E de excitación en el núcleo hijo puede ser derivada de las medidas de su intensidad beta o población beta a ese estado, I(E), la vida media del núcleo padre, $T_{1/2}$, y la integral de la función de Fermi dependiente de la energía de la transición, Q_{EC}-E, donde Q_{EC} es la diferencia de masas entre el núcleo inicial y el final:

$$B^E(GT) = S_\beta(E) = \frac{K \quad I(E)}{(g_A/g_V)^2 f(Q_{EC}-E)T_{1/2}} \tag{9.7}$$

siendo K=6143.6±1.7 [5] y g_A/g_V=-1.270(3) [4]. Dado el carácter continuo del espectro beta, la población a un estado particular del núcleo hijo se suele medir a través de la detección de la cascada de rayos gamma (energías discretas) emitida desde ese estado al fundamental después del proceso beta. El problema radica en que, en general, tales estados pueden ser poblados bien por la desintegración beta o bien por transiciones electromagnéticas de estados poblados a más alta energía de excitación. Para obtener la intensidad beta que puebla cada nivel excitado en el núcleo hijo se ha de emplear el balance de intensidades. Esto consiste en sumar las intensidades de las transiciones gamma que desexcitan cada nivel y a esta cantidad restarle la suma de las transiciones gamma que pueblan ese mismo nivel.

$$I_\beta(E_i) = I_T^{salida}(E_i) - I_T^{entrada}(E_i) \tag{9.8}$$

De la diferencia se obtiene la intensidad beta.

Tradicionalmente siempre se han utilizado detectores de germanio para el estudio de este tipo de desintegraciones. Sin embargo, un problema para la determinación de la B(GT) es la baja eficiencia de detección de estos detectores para gammas de alta energía. Esto conduce a una pérdida de aquellos gammas que proceden de niveles a alta energía y se desintegran a niveles más bajos. Por tanto, dependiendo de la energía del gamma y de la fragmentación de la intensidad de población gamma del nivel, es posible que seamos incapaces de medir con precisión la intensidad gamma a dicho nivel. Si esto ocurre, existe un efecto acumulativo que mueve la población aparente de los estados a más energía de excitación a los niveles de baja energía. Este efecto resulta bastante evidente para valores altos de Q debido a la fragmentación de la intensidad beta. A esto se le conoce como efecto *Pandemonium* [57]. Ello da lugar a la determinación de probabilidades de transición erróneas cuando se usan detectores de germanio. Por esta razón, se hace patente la necesidad de utilizar otra técnica para poder realizar una medida precisa de la intensidad beta. La espectroscopía de absorción total (TAS), basada en el uso de grandes cristales centelleadores con gran eficiencia, resuelve este problema ya que mide cascadas de gamma enteras y no gammas individuales. Esto permite el estudio de núcleos con un Q relativamente grande y determinar con precisión su distribución de B(GT).

9.4 Experimento

El objetivo del experimento IS398 se centró en la producción de isótopos de Sr y Rb en la zona N$\sim$Z para la investigación de las formas nucleares presentes en dicha región de la tabla de núclidos. En este trabajo se presentan los resultados obtenidos acerca de la desintegración beta de los núcleos ^{77,78}Sr y ^{76,78}Rb. Para su medida se realizaron tres experimentos en 2003, 2004 y 2006 en el CERN.

La producción de los núcleos de Sr y Rb se realizó en la instalación ISOLDE mediante una reacción de espalación con protones de 1.4 GeV provenientes del PS-Booster y un blanco de Nb de espesor 52 g/cm^2 (masas 76 y 77) o 37 g/cm^2 (masa 78). Se aplicó la técnica de fluorinización con CF$_4$ en la fuente de iones para la formación de la molécula SrF$^+$ y así la extracción y separación isotópica posterior de los isótopos del Sr. Con el proceso de fluorinización se elimina la contaminación por Rb en las medidas. Esto es imprescindible ya que el Rb posee una gran sección eficaz en esta reacción y es más fácil de extraer de la fuente de iones (paso previo a la separación isotópica). Esta técnica no se utilizó sin embargo para la producción del Rb, a excepción del ^{78}Rb. En este caso particular, el ^{78}Rb presenta dos estados a bajas energías que presentan desintegración beta y que se producen en la reacción de espalación: el estado fundamental con espín-paridad 0^+ y el isómero 4^- a 111.2 keV de energía de excitación. Sin embargo nuestro estudio se centra únicamente en el estado fundamental del ^{78}Rb y su desintegración beta. Por esta razón, el ^{78}Rb se produjo a través de la desintegración beta del ^{78}Sr exclusivamente. De este modo se garantió la producción del estado 0^+ (y no el 4^-). El haz radioactivo, en forma de molécula SrF$^+$ o Rb$^+$, se extrajo posteriormente de la fuente de iones con un potencial de 60 kV para su separación isotópica en el separador de masas GPS (masa 78) o el HRS (masas 76 y 77). De ahí fue implantado en una cinta magnética que se encargaba de mover la actividad de la fuente producida a la estación de medida.

En total se utilizaron tres estaciones de medida independientes. La primera de ellas estaba compuesta por el espectrómetro de absorción total LUCRECIA, concebido y dise*ñ*ado para el estudio de desintegraciones beta, mostrado en la figura 9.3. Este detector consta de un cilindro de NaI(Tl) de dimensiones L=∅=38 cm con un agujero transversal de ∅=7.5 cm. Por un lado del agujero entra la fuente radioactiva a estudiar implantada en cinta. Por el otro se colocan los detectores auxiliares compuestos por un centelleador plástico para detectar positrones y un telescopio de germanio cuya parte frontal es un detector en configuración planar para detectar rayos X. Con esta estación se realizaron las medidas de las masas 76, 77 y 78 en los experimentos del 2003 y 2004. Durante el experimento se tomaron varias medidas del fondo ambiental y de la actividad del núcleo hijo de cada núcleo de interés para tenerlas en cuenta en el posterior análisis de los datos. Para esta estación se utilizó un sistema de adquisición de datos dise*ñ*ado por la colaboración francesa de Estrasburgo y que registra los espectros de cada detector en dos modos distintos: singles y en coincidencia.

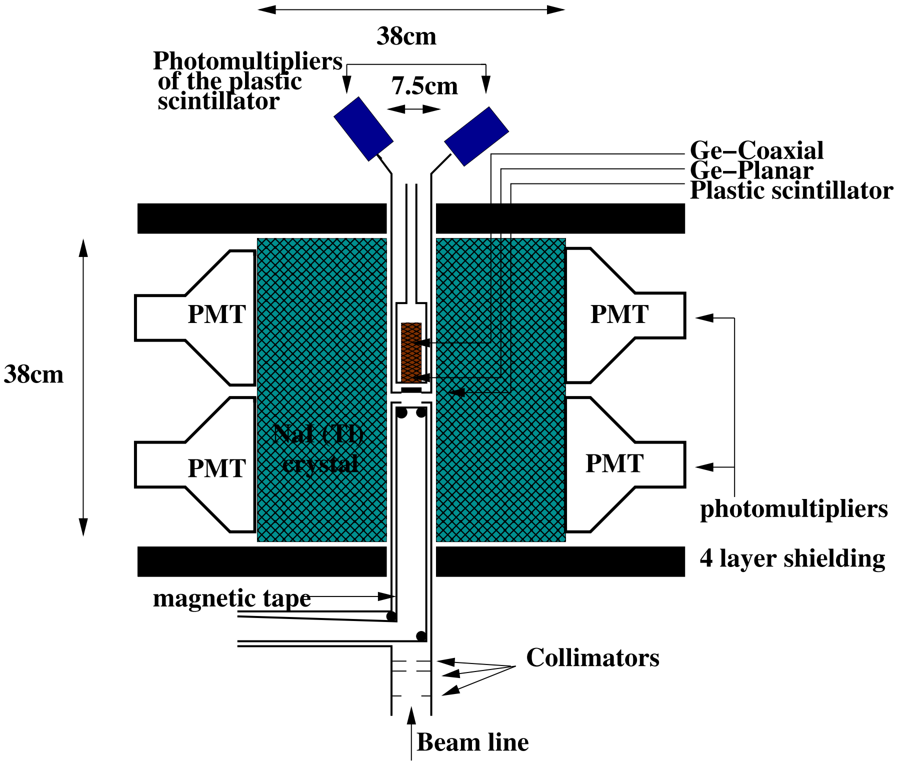

Figure 9.3: Dibujo esqumático del espectrómetro LUCRECIA.

La segunda estación se hallaba formada por tres detectores de germanio, dos de tipo coaxial y un planar para la detección de rayos X y gammas de baja energía (véase la Fig. 9.4). Esta estación de medida se montó específicamente para obtener el esquema de niveles del ^{78}Rb que se utilizaría posteriormente para el análisis de los datos del TAS para este mismo núcleo. Dicha estación permaneció interconectada a través del sistema de transporte de cinta con la estación de medida del TAS durante el experimento de 2004.

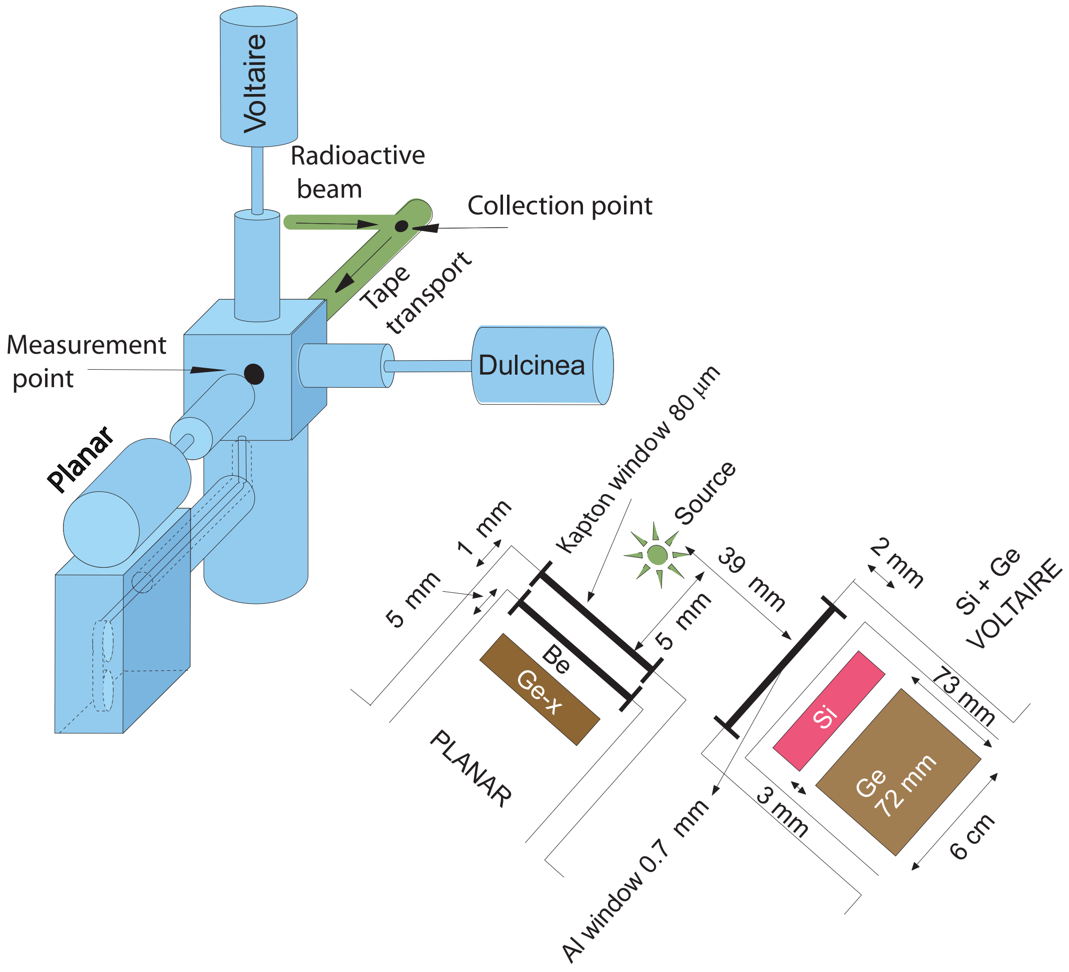

Figure 9.4: Dibujo esquemático de la segunda estación para el registro de los rayos gamma en singles y los espectros en coincidencia γ-γ and γ-X-ray. En la parte de arriba se muestra la disposición geométrica en 90 grados de los tres detectores de germanio. En la parte de abajo se presenta una vista de la sección transversal de la estación. La figura no está a escala pero el grosor de las diferentes ventanas, las dimensiones de los detectores planar y Voltaire así como las distancias desde la fuente a cada detector aparecen detalladas.

Una tercera y útima estación de medida se utilizó en el experimento de 2006. Ésta se hallaba compuesta por un espectrómetro de electrones tipo *miniorange*, construido en GSI para la medida de electrones de conversión, un telescopio de germanio (planar+coaxial), situado a 180 respecto del espectrómetro y un detector de Ge coaxial situado a 90 con respecto al resto (véase Fig. 9.5). Esta estación se utilizó para la determinación del esquema de niveles de la desintegración del ^{77}Sr y la medida de los electrones de conversión en la desintegración del ^{77,78}Sr. En estas dos últimas estaciones de medida se utilizó el sistema de adquisición del grupo de espectroscopía del IFIC y de igual modo se registraron singles y espectros en coincidencia para su posterior análisis off-line.

9.5 Análisis de los datos de alta resolución: obtención de los esquemas de niveles en la desintegración beta del ^{77}Sr y ^{78}Sr

El análisis de los sucesos en coincidencia en la parte de alta resolución es esencial para la construcción del esquema de niveles del núcleo hijo a partir de la desintegración beta de su núcleo padre. La adquisición de los datos en coincidencia se registra suceso a suceso y se escribe de manera continua en cinta. Sin embargo, el gran tama*ñ*o de los ficheros que contienen estos datos (∼Gbytes) y la necesidad de establecer correlaciones entre las diferentes variables suceso a suceso requieren de un método de almacenamiento que permita un acceso rápido a los datos guardando este tipo de correlaciones. Para ello los datos se almacenaron en ntuplas mediante el entorno gráfico ROOT [104]. Esto permitió crear proyecciones, de 1 o más dimensiones de las n variables de cada uno de los eventos, estableciendo previamente condiciones sobre éstas.

9.5.1 Estudio de las transiciones gamma

Para la construcción del esquema de niveles se crearon espectros bidimensiones llamados 'matrices' de coincidencia γ-γ entre pares de detectores: Dulcinea$\otimes$Voltaire, Dulcinea$\otimes$Planar y Voltaire$\otimes$Planar para el análisis del ^{78}Sr (experimento 2004); Planar$\otimes$DaVinci y Coaxial$\otimes$DaVinci para el ^{77}Sr (experimento 2006). El procedimiento para el estudio de coincidencias es el siguiente: se coloca una ventana en uno de los picos (transición gamma) de uno de los ejes de la matriz y la proyección en el otro eje mostrará aquellas transiciones gamma que se encuentran en coincidencia con la transición seleccionada. La substracción del fondo (fundamentalmente fondo Compton procedente de transiciones a más alta energía de excitación) se realiza poniendo ventanas a la derecha e izquierda del pico. Del

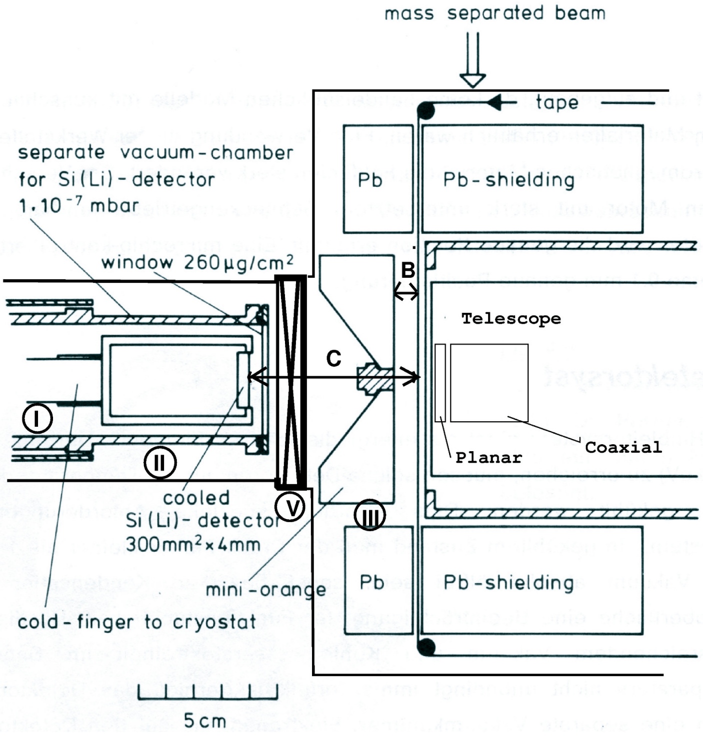

Figure 9.5: Esquema de la sección transversal de la tercera estación de medida para el estudio de los electrones de conversión con un espectrómetro de tipo mini-orange [81]. La fuente separada isotópicamente es depositada sobre la cinta magnética la cual se encarga de mover dicha fuente periódicamente hasta la parte frontal del mini-orange y el telescopio de germanio donde se realiza la medida. La fuente es depositada en el medio de ambos detectores. Un detector co-axial de germanio se encuentra sobre la fuente, a 90 grados respecto del telescopio, aunque no aparece en la figura. Las distancias B y C corresponden a las distancias desde la fuente a la parte frontal del mini-orange y el detector de Si(Li) respectivamente. Esta nomenclatura es la utilizada para clasificar las diferentes configuraciones del mini-orange que se usaron en el experimento. Los volúmenes independientes del dispositivo aparecen marcados como I, II y III respectivamente. Existe una válvula entre I y II que no aparece en la figura y una válvula marcada como V que se utiliza para aislar los volúmenes II y III, es decir, la cámara principal del mini-orange.

análisis de las distintas coincidencias se construye el esquema de niveles. Una vez conocida la eficiencia de los detectores a partir de los singles y del uso de fuentes gamma estándar, es posible obtener la intensidad gamma de cada una de las transiciones observadas. La figura 9.6 muestra alguna de las proyecciones de las ventanas de coincidencia principales en la desintegración del ^{78}Sr. Los rayos X, procedentes del proceso de captura electrónica (EC) o conversión interna de los electrones en el núcleo hijo, permiten a su vez identificar aquellas transiciones que pertenecen al esquema de niveles de interés mediante la colocación de una ventana de coincidencia en éstos. En general las energías e intensidades se dedujeron a partir de los valores medios de los picos observados en los distintos singles. Se emplearon a su vez métodos de corrección del "summing" en el planar de ambos experimentos. Para ello se realizaron simulaciones de los detectores planares con GEANT4. Posteriormente se aplicacó un algoritmo de corrección del summing teniendo en cuenta la eficiencia de fotocopico y la eficiencia total de los gammas en dichos detectores así como el esquema de niveles a estudiar.

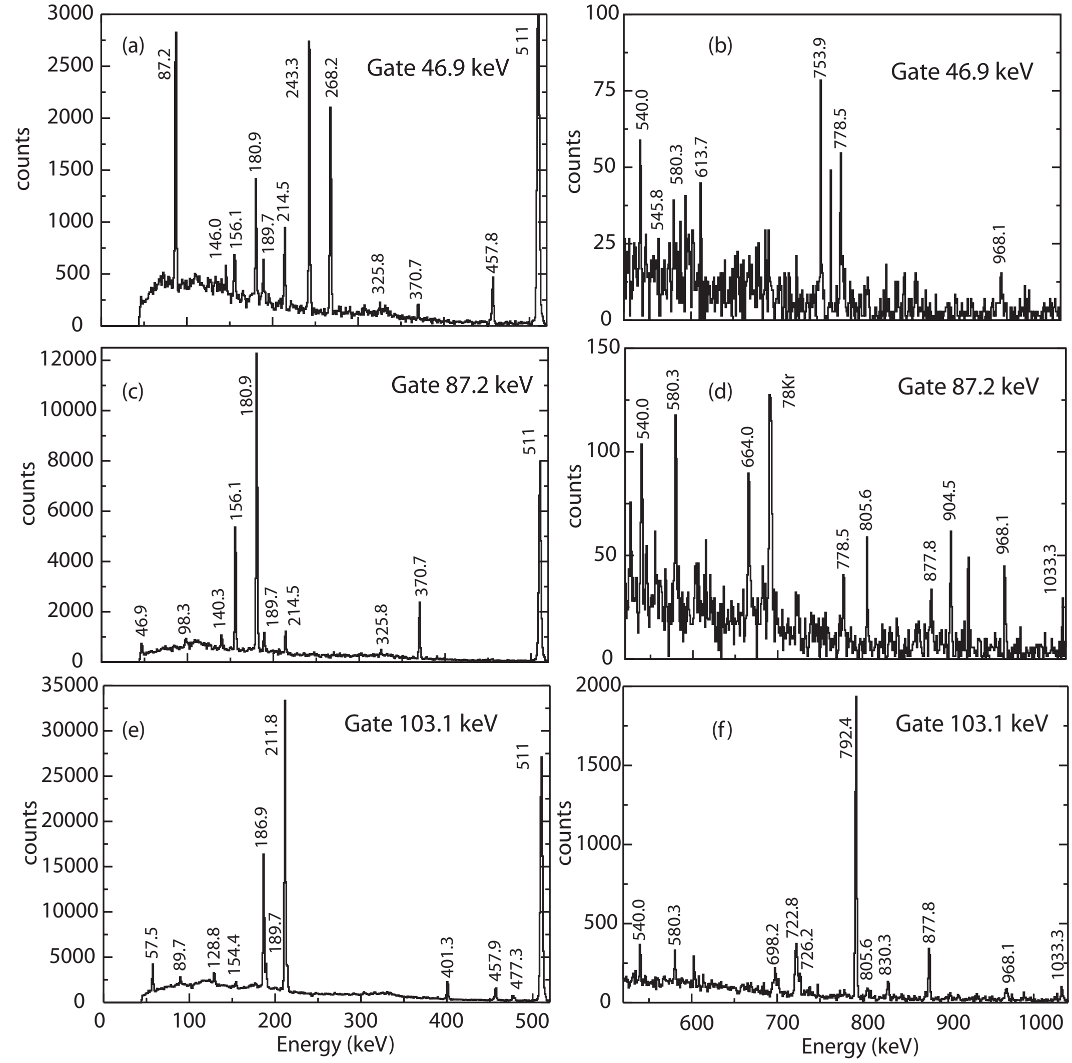

Figure 9.6: Projecciones de los espectros en Dulcinea obtenidos a partir de la colocación de una ventana de coincidencia en las líneas de 46.9 keV (a y b), 87.2 keV (c y d) y 103.1 keV (e y f) en el detector planar en la segunda estación de medida.

En este trabajo, se han determinado en total 16 nuevos niveles e identificado 44 nuevas transiciones gamma en la desintegración del ^{78}Sr. A su vez, se han determinado 9 nuevos niveles y 15 transiciones gamma para el caso del ^{77}Sr. Estos dos resultados suponen una mejora notable con respecto a lo que se conocía previamente acerca de la desintegración beta de estos núcleos.

9.5.2 Estudio de los electrones de conversión

El proceso de conversión interna compite con el de emisión de fotones, contribuyendo por tanto a la desexcitación entre dos niveles. Es por ello por lo que es necesario tenerlo en cuenta en el balance total de intensidades para obtener correctamente la intensidad beta a cada uno de los niveles poblados en la desintegración. Así mismo, es también importante en la determinación del espín y paridad de cada uno de los niveles del esquema de desintegración. Los coeficientes de conversión dependen del carácter (magnético o eléctrico) y multipolaricad de la transición(L=1,2,..). En este trabajo se han deducido los coeficientes de conversión de algunas de las transiciones de baja energía para el ^{77}Sr y ^{78}Sr mediante el uso de la tercera estación de medida descrita. Se utilizaron 4 combinaciones de imanes y distancias en el espectrómetro mini-orange para la medida de los coeficientes. Dichas configuraciones se clasificaron como A/B/C donde A es en número de imanes, B es la distancia desde la fuente radioactiva hasta la parte frontal del mini-orange y C es la distancia desde la fuente hasta el detector de Si(Li). La parte de arriba de la Fig. 9.7 muestra las curvas de transmisión de cada una de las configuraciones utilizadas. Éstas se obtuvieron a partir de fuentes estándard abiertas así como de fuentes producidas en el experimento, ^{77}Rb, ^{79}Sr y ^{79}Rb [80, 87, 86], de las que se conocen sus intensidades gamma y algunos valores de coeficientes de conversión. Para el análisis se utilizaron únicamente los singles. Conocidas las curvas de transmisión para cada configuración y haciendo uso de los valores teóricos de los coeficientes de conversión para Z=38 se obtuvo la multipolaridad de diversas transiciones en el esquema de niveles del ^{77}Sr y ^{78}Sr. En la Fig. 9.8 se muestran los resultados obtenidos para el ^{78}Sr. La información obtenida resultó relevante para la asignación de espines y el cálculo de la intensidad beta para cada núcleo de estudio.

9.5.3 Vida media del ^{78}Sr

La vida media de la desintegración del ^{78}Sr se determinó a partir de los datos de la segunda estación de medida utilizada. Los espectros gamma del detector planar fueron grabados en pasos de tiempo de 65 ms registrados por un reloj interno del sistema de acquisición. Éste reloj se ponía a cero con cada movimiento de la cinta de transporte. Los datos se dividieron en intervalos de tiempo correspondientes a 20 pasos del reloj. Para la determinación de la vida media se utilizó la línea de 103.1 keV cuya área se determinó para cada intervalo de tiempo en el planar. La

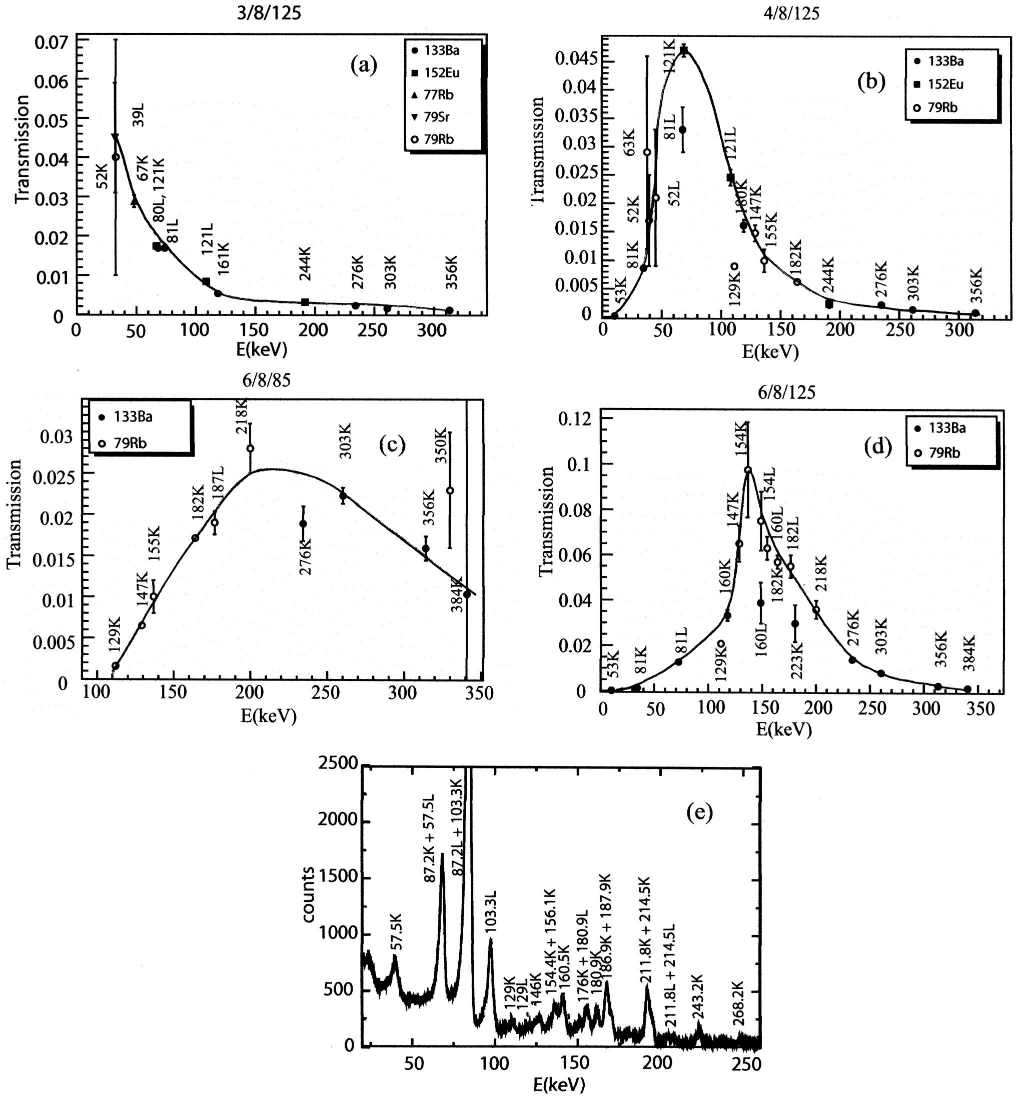

Figure 9.7: Las cuatro gráficas de arriba muestran las curvas de transmisión de las cuatro configuraciones del mini-orange utilizadas. La figura de abajo muestra el espectro de electrones medido con la configuración 6/8/125. Las líneas de conversion de electrones aparecen marcadas con las energiás de la transición electromagnética a la que corresponden y la capa atómica en donde tiene lugar la conversión. Todas corresponden a transiciones en el ^{78}Rb. Nótese que las energias de enlace de las capas K, L1 y L2 son 15.2, 2.07 y 1.87 respectivamente.

curva resultante del área del pico de dicha transición frente al tiempo se ajustó a una función exponencial resultando un valor de 155(3) s para la vida media. Similares resultados se obtuvieron utilizando otras líneas más débiles. Este valor obtenido está de acuerdo con los valores de 150(20) s, 170(30) s and 159 (8) s dados por Liang et al. [92], Hagebø et al. [105] y Grawel et al. [91], respectivamente.

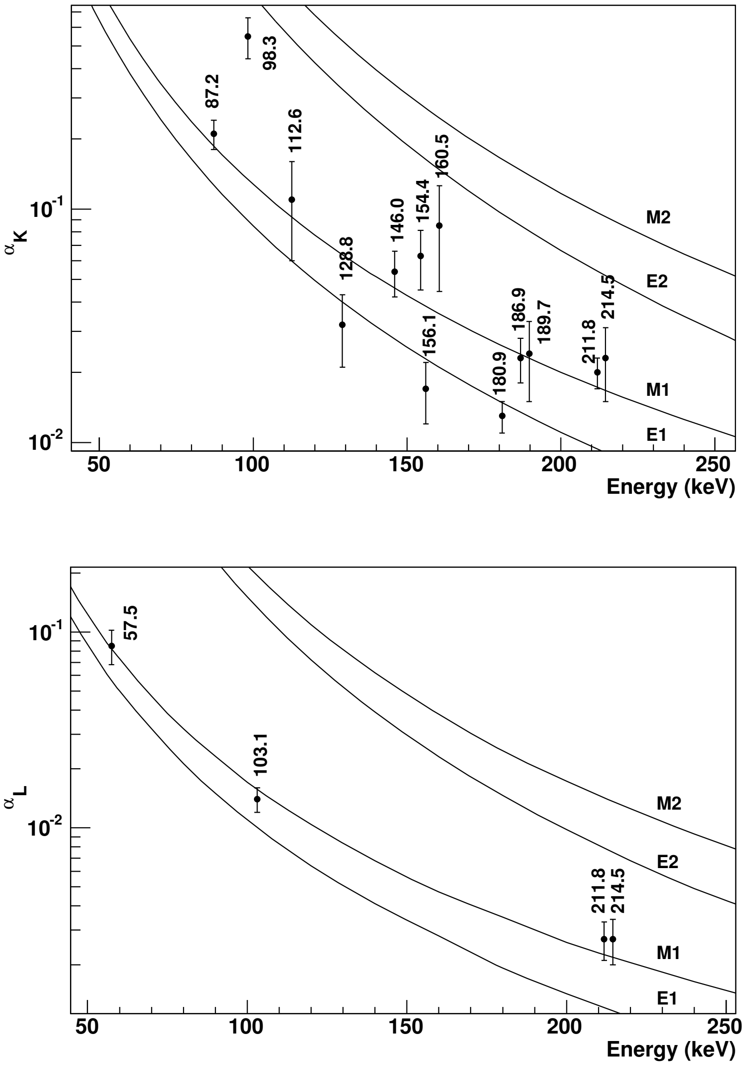

Figure 9.8: Coeficientes de conversion obtenidos para las transiciones medidas en el ^{78}Rb durante el estudio de su desintegración beta. La gráfica de arriba muestra la componente K de los coeficientes de conversión y la de abajo la componente L o L-M en el caso de que no se puedan resolver. Para cada punto se muestra la capa donde la conversión tiene lugar así como la energía de la transición.

9.5.4 Determinación de la intensidad beta, valores de log ft y B(GT)

Una vez construido el esquema de niveles a partir del estudio de las coincidencias, es posible calcular las relaciones de intensidad entre las distintas transiciones que pueblan y desexcitan un nivel y así determinar la alimentación directa procedente

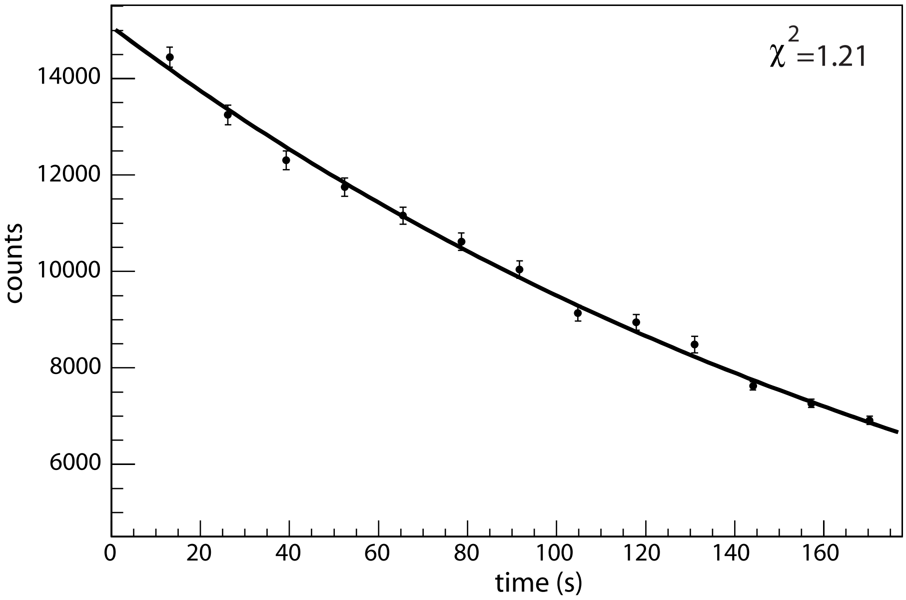

Figure 9.9: Gráfica del área bajo el pico correspondiente a la transición gamma de 103 keV en función del tiempo de medida con el detector planar. La curva corresponde al mejor ajuste posible. El resultado es una vida media de 155(3) s con un χ^2 de 1.21 tras el ajuste.

de la desintegración beta a cada uno de los niveles. Para el cálculo de la intensidad beta hay que realizar el balance de intensidades, descrito en la sección 9.3, que se resumen en la siguiente ecuación:

$$I_\beta(E_i) = I_T^{salida}(E_i) - I_T^{entrada}(E_i) \tag{9.9}$$

Esta diferencia nos proporciona la distribución de la desintegración beta a cada nivel poblado en la desintegración beta. Haciendo uso de las tablas tabuladas de la función de Fermi por Gove y Martin [3], se obtuvieron los valores de log ft. A partir de la ecuación y dado que se conocen los valores de Q$_{EC}$ y de la vida media tanto para el ^{77}Sr como el ^{78}Sr (este último determinado en este trabajo), se determinó la distribución de B(GT) para la desintegración de cada núcleo.

9.5.5 Interpretación de los niveles del ^{78}Rb y ^{77}Rb

La estructura de los núcleos impar-impar es en general difícil de interpretar y más aún en esta parte de la tabla de núclidos donde aparecen fenómenos de coexistencia de forma. En este trabajo se ha podido interpretar la estructura de los diferentes niveles de energía del ^{78}Rb en base a sus asignaciones de espín e intensidad beta haciendo uso de cálculos microscópicos HF+BCS con la fuerza de Skyrme SG2 para el ^{78}Sr [123]. Esto mismo se ha hecho para el caso del ^{77}Sr donde se han tenido a su vez en cuenta en el cálculo los diferentes miembros de cada banda rotacional [123].

9.6 Análisis de los datos de absorpción total: obtención de la B(GT) para los núcleos ^{77,78}Sr y ^{76,78}Rb

El análisis de los datos del TAS es una parte delicada. El hecho de que un espectrómetro TAS tenga una resolución y eficiencia limitadas hace que el espectro medido tenga que ser procesado. El análisis de los datos adquiere una gran complejidad ya que los datos medidos, d, pasan a estar relacionados con la intensidad beta a cada nivel, f, a través de la respuesta del detector, R. La siguiente ecuación expresa dicha relación:

$$d = R.f \tag{9.10}$$

La primera dificultad en este punto radica en determinar la respuesta del detector. Cano et al. [75] demostraron la posibilidad de construir dicha matriz de respuesta del detector R a través de simulaciones Montecarlo. En este trabajo se ha utilizado el código *GEANT4* del CERN para la obtención de dicha respuesta. Por otra parte, es necesario conocer el esquema de niveles del núcleo hijo procedente de la desintegración beta del núcleo padre para poder proceder con la construcción de R. El esquema de niveles que se tenía hasta la fecha acerca de los núcleos ^{77}Sr y ^{78}Sr era muy pobre antes de este trabajo. Esto explica la necesidad de haberlos medido con métodos de espectroscopía de alta resolución primeramente para así determinar sus esquemas de desintegración. Para el resto de núcleos en estudio, hemos hecho uso de la información de sus esquemas de niveles procedentes de la literatura [78, 77]. Un rasgo común de todos ellos es que el esquema de niveles se conoce únicamente para bajas energías de excitación. Para completar la información a altas energías (téngase en cuenta que para núcleos lejos de la estabilidad, como es el caso, la densidad de niveles puede llegar a ser del orden de $10^4 - 10^5$) se ha utilizado en este trabajo un modelo estadístico. Dicho modelo hace uso del modelo "back-shifted Fermi gas model" [131] para la determinación de la densidad de niveles. Posteriormente utiliza las parametrizaciones de las referencias [138, 139, 140] para el cálculo de los ”branching ratios” para las transiciones E1, M1 y E2 respectivamente.

Por otra parte, el problema inverso planteado por la ecuación 9.10 está mal condicionado, es decir, diferentes soluciones, algunas de ellas completamente inverosímiles , son capaces de reproducir los datos experimentales. Diversos algoritmos se han propuesto para la resolución del problema inverso planteado [66]. En este trabajo se hace uso del método de Maximización de la Expectación (EM) que consiste básicamente en aplicar de manera iterativa la fórmula de Bayes. Como información a priori se utilizan los datos experimentales y la función de respuesta del detector a la desintegración concreta que se pretende estudiar.

9.6.1 Resultados de la distribución de B(GT)

Las gráficas superiores de la Fig. 9.10 muestran la comparación entre el espectro reconstruido y los datos experimentales incluyendo los contaminantes (fondo ambiental, solapamiento electrónico de pulsos y actividad del núcleo(s) hijo(s)) tras la aplicación del algoritmo de deconvolución. Los paneles inferiores presentan la desviación entre el espectro reconstruido y los datos respecto a estos últimos. Esta representación permite mejorar la visualización de las diferencias entre ambos espectros dado que los paneles superiores se encuentran en escala logarítmica. Se puede observar un gran acuerdo entre ambos espectros.

Una vez aplicado el algoritmo de deconvolución de los datos se obtuvo la intensidad beta de cada una de las desintegraciones en estudio, mostradas en la Fig. 9.11 en trazo continuo. En esta figura aparecen a su vez representados en rojo la intensidad beta obtenida con técnicas de espectroscopía de alta resolución según las referencias [78, 77] y los resultados de alta resolución obtenidos en nuestro trabajo. En general se observa un claro desplazamiento de la distribución de intensidad hacia bajas energías en los datos de alta resolución debido al efecto Pandemonium antes comentado.

Una vez conocida la intensidad beta y aplicando la ecuación 9.4 se obtuvo la distribución de B(GT) que se muestra en la figura 9.12. La zona sombreada en color gris representa la incertidumbre debida al error asociado al Q de la reacción y la vida media (véase Eq. 9.4), los errores que conlleva la estimación de las constantes de normalización de los contaminantes y a su vez los posibles esquemas de niveles utilizados para la construcción de la matriz de respuesta del detector. Nótese que para esto último, se han asumido diferentes espines y paridades para ciertos niveles de los que se desconoce dicha información. Además se ha aplicado el modelo estadístico

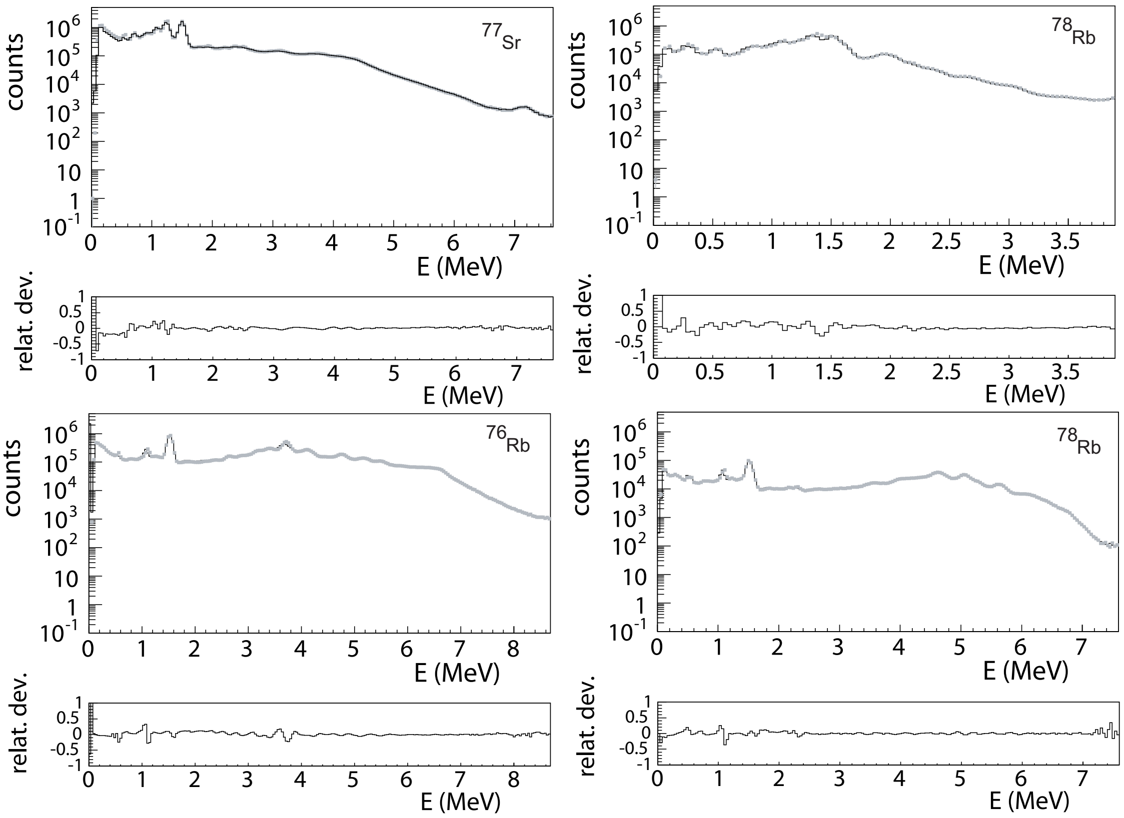

Figure 9.10: Las gráficas superiores muestran el espectro experimental del TAS (línea negra continua) con contaminantes. El espectro reconstruido tras el análisis aparece a su vez representado (línea gris discontinua). Las gráficas inferiores muestran la desviación de los datos experimentales respecto al espectro reconstruido normalizado al primero.

a partir de distintas energías de excitación para cada núcleo. De los resultados obtenidos puede observarse que una buena parte de la B(GT) se encuentra a altas energías de excitación. Los resultados de alta resolución sin embargo no permiten detectar B(GT) en esa zona y los resultados derivados de éstos difieren notablemente respecto a los obtenidos con el TAS. Esto, junto con los errores derivados del efecto Pandemonium [57], hace patente la necesidad de utilizar medidas de absorción total para este tipo de medidas.

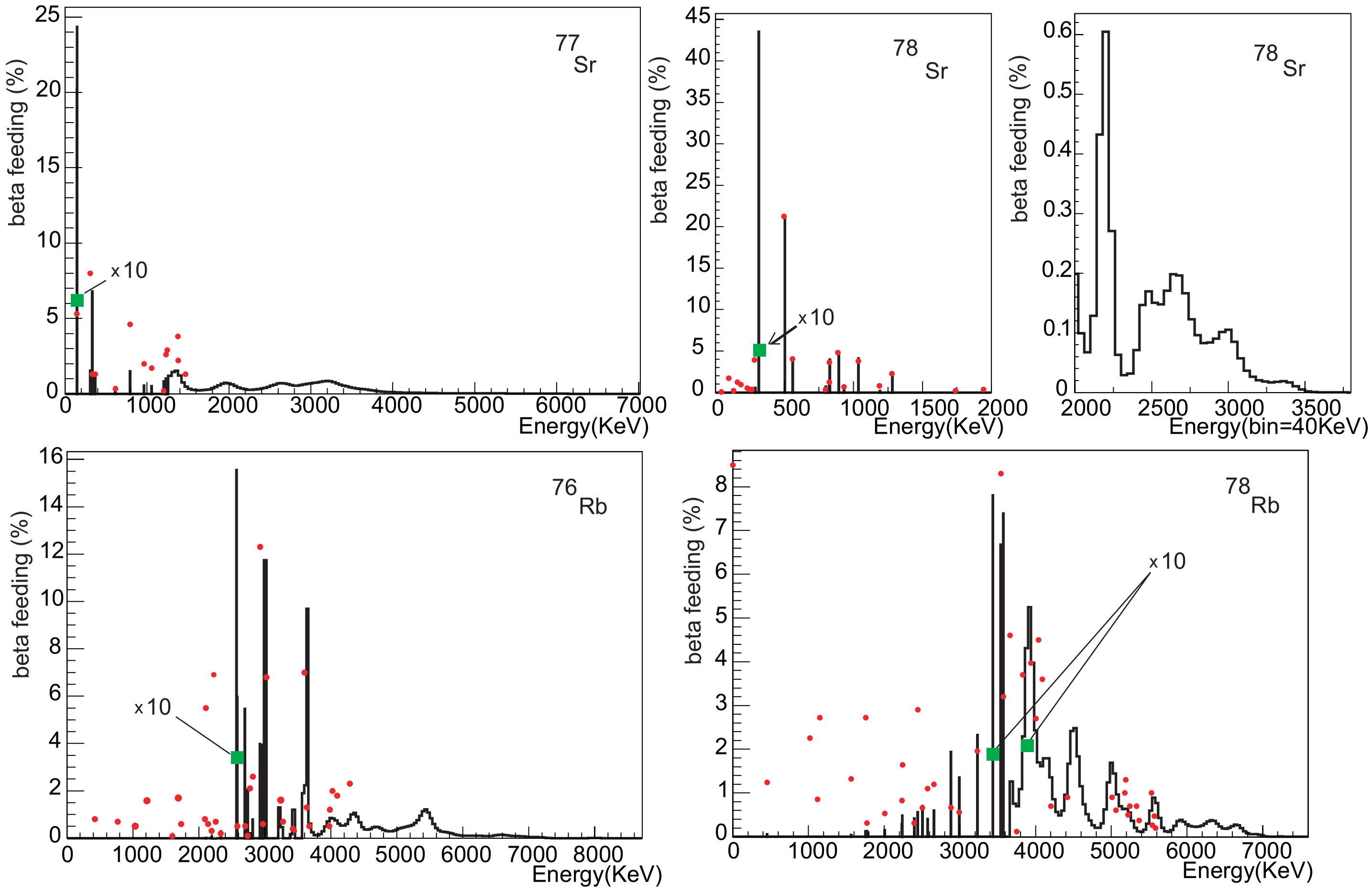

Figure 9.11: Comparación de la intensidad beta obtenida a partir de los datos del TAS (línea contínua) y los datos de alta resolución (puntos rojos). Los valores de intensidad beta que aparecen representados por un cuadrado han sido reducidos en un factor 10 para que aparezcan dentro de la gráfica [78, 77].

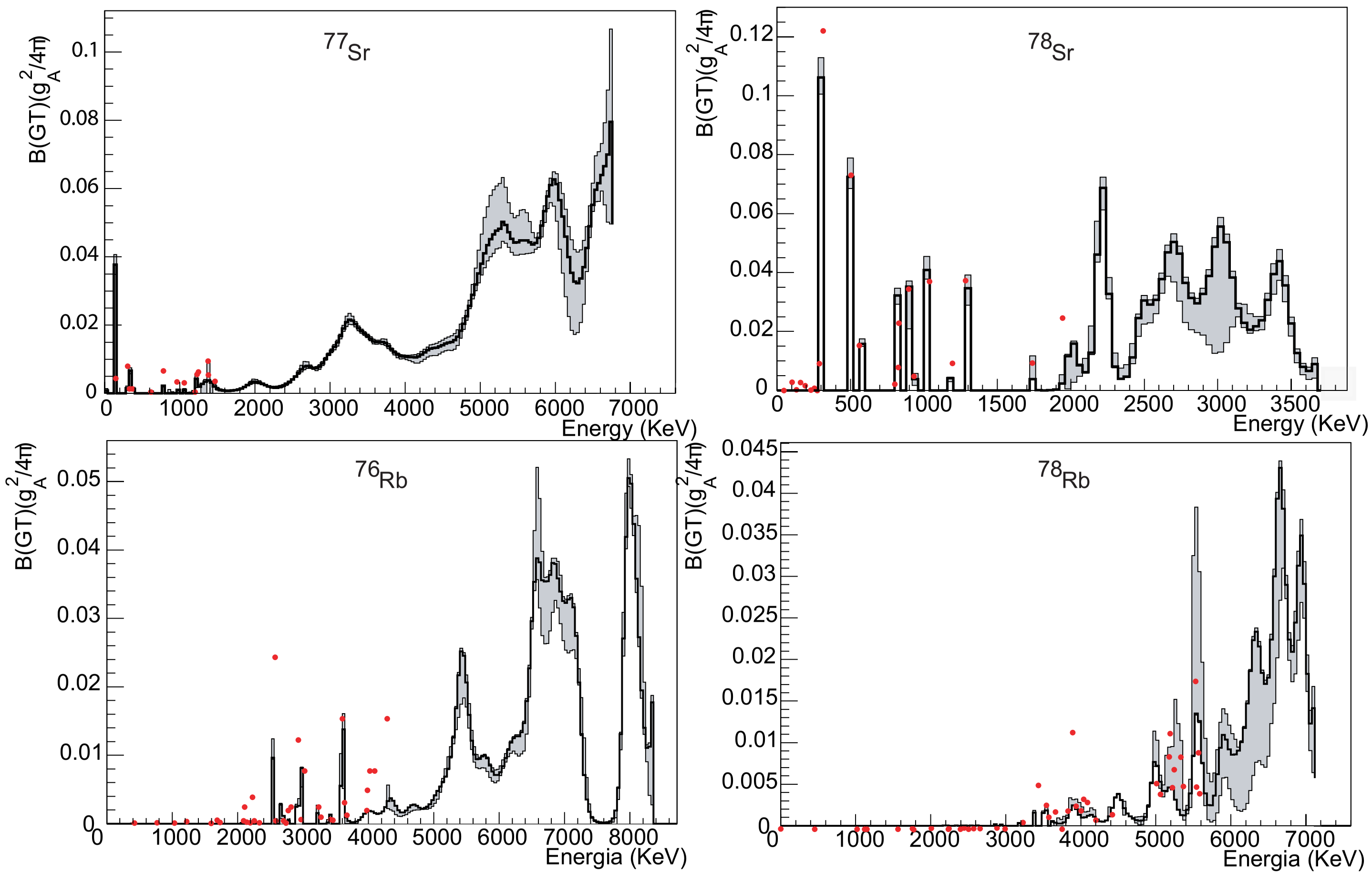

Figure 9.12: Distribución B(GT) en función de la energía de excitación en el núcleo hijo para el ^{77}Sr y ^{78}Sr (paneles de arriba) y ^{76}Rb y ^{78}Rb (paneles de abajo) obtenida a partir del análisis del TAS. Como puntos en rojo aparece la distribución B(GT) obtenida a partir de métodos de alta resolución [78, 77].

9.6.2 Deformación del estado fundamental del ^{78}Sr

El principal objetivo de los experimentos realizados fue la determinación de la deformación del estado fundamental del ^{78}Sr. Dado que es un núcleo par-par, no es posible determinar experimentalmente su momento quadrupolar y por consiguiente, su deformación. Diversos estudios [26, 113, 112] proponen una gran deformación para este núcleo, del orden de β_2 ~0.4. Sin embargo, no ha sido posible evaluar hasta la fecha el signo de dicha deformación. Motivados por el éxito en la comparación entre los datos experimentales del ^{76}Sr y ^{74}Kr [44, 45] y los cálculos teóricos HF+BCS+QRPA de los que se pudo deducir su deformación, se ha hecho una comparación similar en este trabajo. En este caso, los cálculos teóricos predicen dos mínimos de energía cuando se minimiza la energía HF fijando la deformación: uno prolado con β=0.42 y otro esférico. Para los cálculos se utilizaron 3 fuerzas de Skyrme diferentes (SG2, SK3 y SLy2), las cuales dieron resultados similares con pequeñas diferencias a niveles del detalle. En los cálculos teóricos se asumió que tanto el padre como los estados poblados en el núcleo hijo poseen la misma deformación. En este tipo de cálculos QRPA la energía calculada para los estados excitados no suele coincidir con la energía real de una manera precisa. Es por ello que para realizar la comparación, se representó la B(GT) acumulada, es decir, para cada energía de excitación se representó la suma de la B(GT) desde 0 hasta dicha energía. De la comparación, se observa claramente que los cálculos teóricos para un estado fundamental prolado reproducen muy bien nuestros datos experimentales (véase Fig. 9.13). Por el contrario, los cálculos asumiendo un estado fundamental oblado predicen una gran parte de la B(GT) a bajar energías de excitación, hecho que no se observa experimentalmente. Con ello se confirma la deformación prolada para el estado fundamental del ^{78}Sr, en acuerdo con lo predicho por [26, 113, 112], y se validan de nuevo los cálculos teóricos para esta región.

9.6.3 Interpretación de la B(GT) del ^{77}Sr

En el caso general de un núcleo impar, como es el ^{77}Sr, se esperan dos regiones diferentes en su distribución de B(GT).Una primera región a baja energía de excitación que corresponde a excitaciones de 1 quasipartícula (qp) donde las excitaciones vienen determinadas por el protón desapareado. La segunda región, a energías por encima de la energía de apareamiento (~2-3 MeV), proceden de las excitaciones de 3qp donde el neutrón desapareado en el núcleo padre actúa como espectador. Véase la figura 9.14 para entender estas dos regiones debidas a los dos modos posibles de desintegración. En la primera región sólo un número muy limitado de excitaciones puede tener lugar mientras que para la región por encima de 2-3 MeV, la B(GT) contenida ha de ser mucho mayor dado que existen muchas más excitaciones posibles que pueden contribuir. Ello se ve claramente en la Fig. 9.12 donde se observan ambas regiones.

Haciendo uso de la B(GT) obtenida a partir de los cálculos teóricos

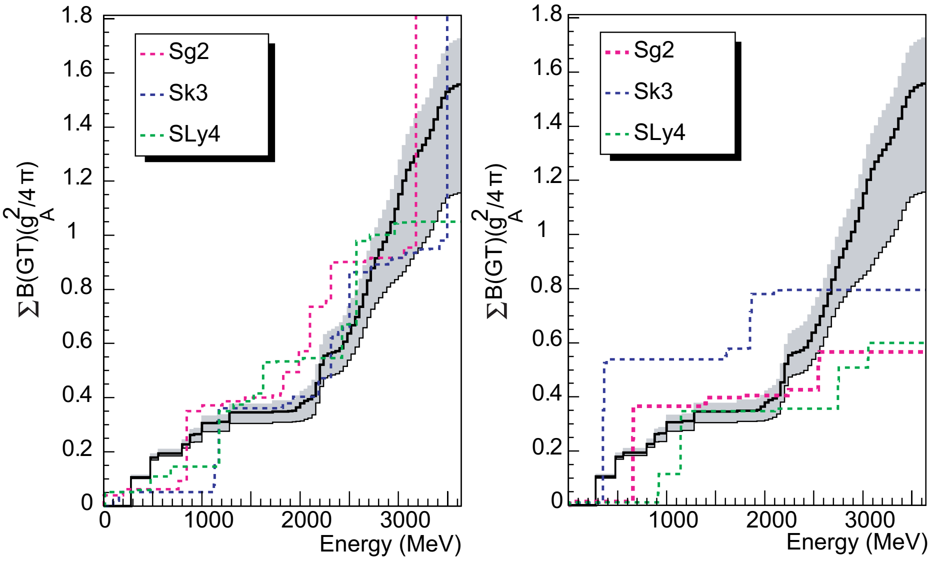

Figure 9.13: Comparación de la distribución de B(GT) acumulada obtenida en este trabajo (línea contínua) con los cálculos QRPA para una deformación prolada (izquierda) y una esférica (derecha) en el ^{78}Sr. Para los cálculos se han usado diferentes fuerzas de Skyrme SG2, SK3 y SLy4 [50] que aparecen diferenciadas en las figuras.

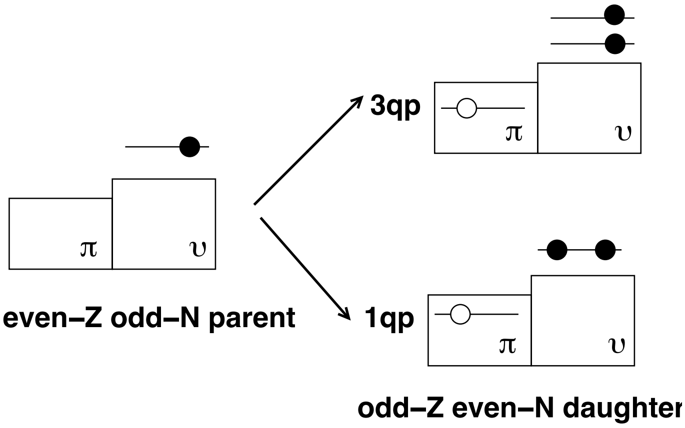

Figure 9.14: Dibujo esquemático para representar las posibles desintegraciones que tienen lugar en un núcleo par-impar en el modelo monoparticular extremo.

HF+BCS+QRPA realizados con la fuerza SG2 [123], ha sido posible deducir la configuración en términos de orbitales de Nilsson para las dos excitaciones 1qp que se observan claramente a baja energía de excitación asumiendo una deformación prolada. Por otra parte, y al igual que se hizo para el ^{78}Sr, se ha representado la B(GT) acumulada obtenida experimentalmente junto con los cálculos teóricos realizados con las fuerzas de Skyrme SK3, SG2 y SLy4 para los dos mínimos de energía obtenidos tras la minimización de la energía HF, uno prolado con β=0.42 y otro esférico (véase la Fig. 9.15). Claramente se puede ver que los resultados experimentales se ajustan muy bien a los cálculos para la deformación prolada. Ello concuerda con el valor medido del momento espectroscópico por Lievens et al [122] para el estado fundamental del ^{77}Sr. Por tanto, estos resultados de nuevo proporcionan otro ejemplo de la buena reproducción de estos cálculos teóricos para la región en cuestión. Así mismo cabe resaltar que este es el primer caso en el que se valida el método en un núcleo impar utilizando resultados de TAS.

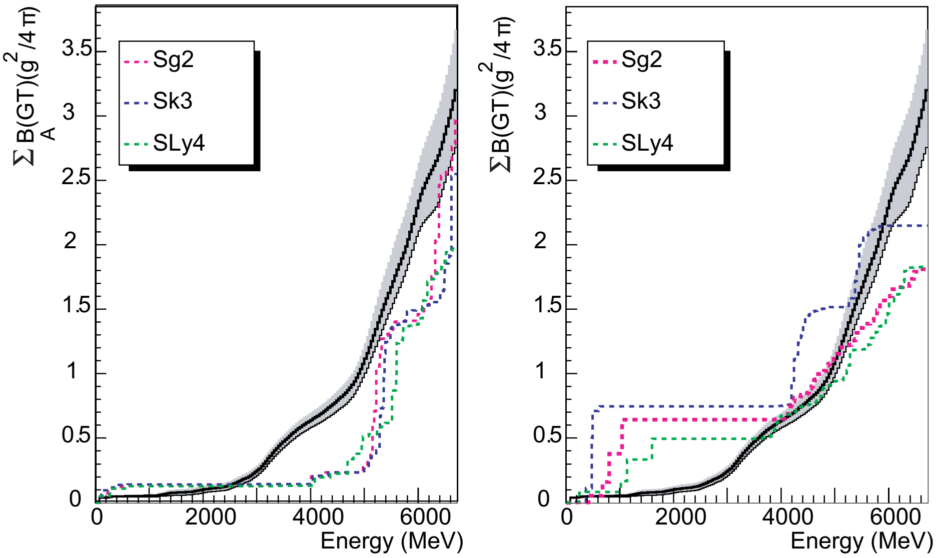

Figure 9.15: Comparación de la distribución de B(GT) acumulada obtenida en este trabajo (línea contínua) con los cálculos QRPA para una deformación prolada (izquierda) y una esférica (derecha) en el ^{77}Sr. Para los cálculos se han usado diferentes fuerzas de Skyrme SG2, SK3 y SLy4 [50] que aparecen diferenciadas en las figuras.

9.6.4 Interpretación de los núcleos impar-impar

Se han derivado conclusiones generales para los casos impar-impar, ^{76}Rb y ^{78}Rb, basándonos en su comparación con los núcleos par-par de los que poseemos información gracias a los cálculos teóricos. Para ello se ha utilizado un esquema muy simple de las posibles vías que puede seguir la desintegración beta para un núcleo par-par o impar-impar, mostrado en Fig. 9.16. En términos generales se ha podido concluir que la estructura de los núcleos ^{78}Sr, ^{78}Rb y ^{78}Kr ha de ser similar dado que la distribución de B(GT) de las desintegraciones beta del ^{78}Sr y ^{78}Rb presentan grandes similitudes. Por otra parte, se observan también similitudes entre la B(GT) de los núcleos ^{76}Sr y ^{78}Sr dentro de los primeros 3.8 MeV (ventana de energía accesible para la desintegración del ^{78}Sr). Esto es de esperar dado que la única diferencia entre ambos radica en un par de neutrones extra. En cuanto al ^{76}Rb no se pudieron llegar a resultados muy concluyentes.

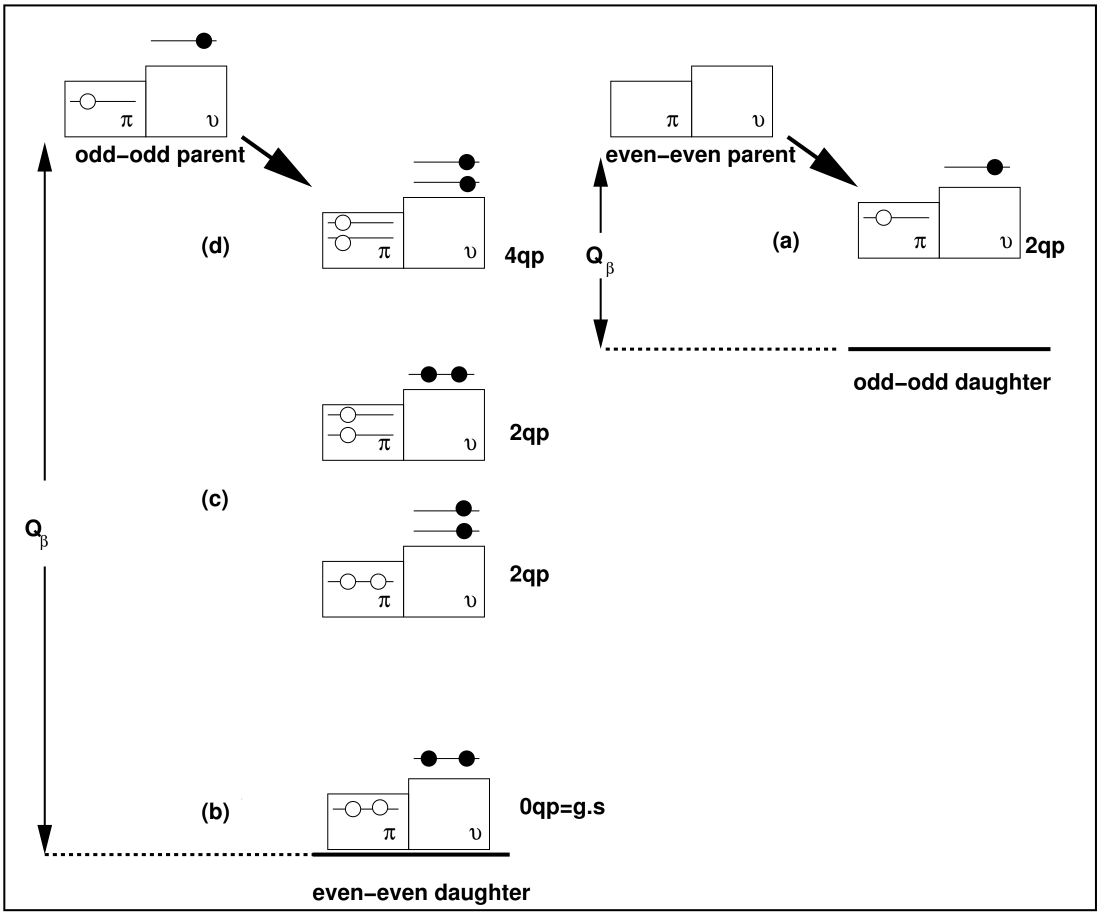

Figure 9.16: Dibujo esquemático para representar las posibles desintegraciones que tienen lugar en un núcleo par-par e impar-impar en el modelo monoparticular extremo.

9.7 Conclusión

En conclusión podemos decir que en este trabajo se ha progresado sustancialmente en el conocimiento experimental de las desintegraciones beta de los núcleos

^{77}Sr, ^{78}Sr, ^{76}Rb y ^{78}Rb. Además, a pesar de la complejidad en esta zona de la tabla de núclidos, se han podido interpretar las observaciones experimentales comparando los resultados experimentales con cálculos HF+BCS+QRPA, lo que ha contribuido a conocer mejor la estructura de estos núcleos.

Valencia, Enero de 2012.

Bibliography

[1] Antoine Henri Becquerel, "On the rays emitted by phosphorescence," Comptes Rendus 122, 420(1896)

[2] E. Fermi, Z. Physik 88, 161 (1934)

[3] N.B. Gove and M.J. Martin, log-f tables for beta decay, Nuclear Data Tables Vol.10, Number 3 (1971)

[4] J.C. Hardy and I.S. Towner, Nucl. Phys. New 16, 11 (2006)

[5] J.C. Hardy and I.S. Towner, Phys. Rev. C70, 055502 (2009)

[6] K. Ikeda, S. Fujii and J.J. Fujita, Phys. Lett. 3, 271 (1963)

[7] G. Gamow and E. Teller, Phys. Rev. 49, 895 (1936)

[8] Carl Gaarde, Nucl. Phys. A396, 127c (1983)

[9] R.R. Doering et al., Phys. Rev. Lett. 35, 1691 (1975)

[10] A. Galonsky et al., Phys. Lett. B74, 176 (1978)

[11] D. Ovazza et al., Phys. Rev. C 18, 2438 (1978)

[12] T. Wakasa, J. Sakai et al, Phys. Rev. C55, 2909 (1997)

[13] G.F. Bertsch and I. Hamamoto, Phys. Rev. C26, 1323 (1982)

[14] Vetterli et al., Phys. Rev. Lett. 59, 439 (1987)

[15] J. Rapaport et al., Nucl. Phys. A410, 371 (1983)

[16] A. Algora et al., Phys. Rev. Lett. 105, 202501 (2010)

[17] P.J. Nolan and P.J. Twin, Ann. Rev. Nucl. Part. Sci. 38, 533 (1998)

[18] J. Blons, Nucl. Phys. A502, 121c (1989)

[19] I. Ahmad and P. Butler, Ann. Rev. Nucl. Part. Sci 47, 71 (1993)

[20] W. Greiner and J.A. Maruhn, Nuclear Models, Springer, p.109, (1996)

[21] R.B. Firestone and V.S. Shirley (Eds), Table of Isotopes 8th ed., John Wiley and Sons (1996)

[22] K.S. Krane, "Introductory Nuclear Physics", John Wiley and Sons (1988)

[23] R. Neugart 16, G. Neyens, "Nuclear Moments", The Euroschool Lectures on Physics with Exotic Beams,Vol. II, Lect. Notes Phys. 700, Springer, Berlin Heidelberg (2006)

[24] W. Gelletly, Nuovo Cimento 111, 757 (1988)

[25] S.G. Nilsson, Dan. Mat. Fys. medd. 29, N0. 16 (1955)

[26] C. J. Lister et al., Phys. Rev. C42, 1191 (1990)

[27] W. Gelletly et al, Phys. Lett. B 253, 287 (1991)

[28] R.F. Casten, Nucl. Phys. A 443, 1 (1985)

[29] R.F. Casten, D.S. Brenner, and P.E. Haustein, Phys. Rev. Lett. 58, 658 (1987)

[30] S.L. Tabor, Phys. Rev. C34, 311 (1986)

[31] R.B. Piercey et al., Phys. Rev. Lett. 47, 1514 (1981)

[32] C. Chandler et al., Phys. Rev. C56, 2924(R) (1997)

[33] F. Becker et al., Eur. Phys. J. A4, 103 (1999)

[34] E. Bouchez et al., Phys. Rev. Lett. 90, 082502 (2003)

[35] E. Clément et al., Phys. Rev. C 75, 054313 (2007)

[36] Y. Aboussir et al., Atomic Data and Nucleare Data Tables 61, 127 (1995)

[37] P. Möller et al., Nucl. Data Tables 59, 185 (1995)

[38] W. Nazarewicz et al., Nucl. Phys. A435, 397 (1985)

[39] P. Bonche et al., Nucl. Phys. A443, 39 (1985)

[40] M. Bender, P. Bonche, and P.-H. Heenen, Phys. Rev. C74, 024312 (2006)

[41] S. Hilaire and M. Girod, Eur. Phys. J. A33, 237 (2007)

[42] G..A. Lalazissis and M.M. Sharma, Nucl. Phys. A586, 201 (1995)

[43] A. Petrovici, K. W. Schmid, and A. Faessler, Nucl. Phys. A605, 290 (1996); ibid 665, 333 (2000)

[44] E. Nacher et al, Phys.Rev.Lett. 92, 232501 (2004)

[45] E. Poirier et al., Phys. Rev. C 69, 034307 (2004)

[46] B. Rubio et al., J. Phys. G: Nucl. Part. Phys. 31, S1477 (2005)

[47] I. Hamamoto and X.Z. Zhang, Z. Phys. A353, 145 (1995)

[48] P. Sarriguren, E. Moya de Guerra, A. Escuderos, and A.C. Carrizo, Nucl. Phys. A635, 55 (1998)

[49] P. Sarriguren et al, Nucl. Phys. A658, 13 (1999)

[50] P. Sarriguren, Phys. Rev. C79, 044315 (2009)

[51] P. Sarriguren, private communication

[52] M. Beiner, H. Flocar, N. Van Giai, and P. Quentin, Nucl. Phys. A238, 29 (1975)

[53] N. Van Giai and H. Sagawa, Phys. Lett. B106, 379 (1981)

[54] E. Chabanat et al., Nucl. Phys. A627, 710 (1997)

[55] C.L. Duke et al., Nucl. Phys. A151, 609 (1970)

[56] W. Gelletly and J. Eberth, The Euroschool Lectures on Physics with Exotic Beams, Vol. II p.79, Springer, Berlin Heidelberg New York (2006)

[57] J.C. Hardy et al., Phys. Lett. B71, 307 (1977)

[58] W. Korten, Eur. Phys. J. A20, 5 (2003)

[59] A. Algora et al., Phys. Rev. C68, 034301 (2003)

[60] K.H. Johansen et al., Nucl. Phys. A203, 481 (1973)

[61] Alkhazov et al., Phys. Lett B157, 35 (1985)

[62] R.C.Greenwood et al., Nucl. Inst. Meth. A314, 514 (1992)

[63] M. Karny et al., Nucl. Instr. Meth. B126, 411 (1997)

[64] M.E. Aguado, Universitat de Valencia, Ph.D. in preparation.

[65] E. Valencia, Universitat de Valencia, Ph.D. in preparation.

[66] J.L Tain, D. Cano-Ott, Nucl. Instr. Meth. A571, 728 (2007)

[67] G. Audi et al., Nucl. Phys. A729, 337 (2003)

[68] G. Audi et al., Nucl. Phys. A729, 3 (2003)

[69] E. Kugler, Nucl. Inst. and Meth. B79, 322 (1993)

[70] C.F. Liang and P. Paris, Z. Phys. A - Atoms and Nuclei 309, 185 (1982)

[71] H.L. Ravn et al., Nuclear Inst. and Meth. 123, 131 (1975)

[72] R. Eder et al., Nucl. Inst. and Meth. B62, 535 (1992)

[73] E. Kugler et al., Nucl. Inst. and Meth. B70, 41 (1992)

[74] O.C. Johnsson et al, Nucl. Inst. and Meth. B70, 541 (1992)

[75] D. Cano-Ott et al., Nucl. Inst. and Meth. A430, 488 (1999)

[76] P. Dessagne et al., Eur. Phys. J. A20, 405 (2004)

[77] A. Giannatiempo et al., Phys. Rev. C72, 044308 (2005)

[78] G.K. Bavaria et al., Z. Phys. A - Atoms and Nuclei 30, 329-341 (1981)

[79] J. Mukai et al., Z. Phys. A356, 367 (1997)

[80] C.J. Lister et al., Phys. Rev. C 28, 2127 (1983)

[81] R. Barden, "Isomerie und Betazerfall: Konversionselektronen und Gammaspektroscopie von neutronenarmen Kernen um ^{100}Sn und ^{146}Gd", Ph.D. thesis, Johannes-Gutenberg Universitaet Mainz, (1988)

[82] J. van Klinken and K. Wisshak, Nucl. Instr. and Meth. 98, 1 (1972)

[83] J. van Klinken, S.J. Feenstra, K. Wisshak, and H. Faust, Nucl. Instr. and Meth. 130, 427 (1975)

[84] J. van Klinken, S.J. Feenstra, and G. Dumont, Nucl. Instr. and Meth. 151, 433 (1978)

[85] J. Bea Gilabert, 'Estudio de la estructura del nucleo ^{75}Br producido por la desintegración β^+ del ^{75}Kr, Ph.D. thesis, Universitat de Valencia, (1995)

[86] J. Liptak and J. Kristek, Nucl. Phys. A311, 421 (1978)

[87] C.J. Lister, P.E. Haustein, D.E. Alburger and J.W. Olness, Phys. Rev. C24, 260 (1981)

[88] E. Nolte and P. Vogt, Z. Phys. A275, 33 (1975)

[89] F. Marechal, SAM2000 Data Acquisition System User's Guide, edition 3.0, May 2004

[90] C. Ekström et al, Nucl. Phys. A311, 269 (1978)

[91] H. Grawel et al., Z. Phys. A 341, 247 (1992). Note that the correct name of the first author is H. Grawe but it appears as H. Grawel in this journal.

[92] C.F. Liang et al. Z. Phys. A 309, 185 (1982)

[93] H. Grawe and H. Haas, Annual Report 1981, HMI-B 373, 89 (1982)

[94] J.H. McNeill et al., Manchester University Progress report 1987, p. 20 (1988)

[95] R.A. Kaye et al., Phys. Rev C54, 1038 (1996)

[96] R.A. Kaye et al., L.A. Riley, G.Z. Solomon, and S.L. Tabor, Phys. Rev. C58, 3228 (1998)

[97] Computer Package PD/LNL Analysis Programs, Padova-Legnaro, $http://gasp.lnl.infn.it$

[98] $www.ikp.uni-koeln.de/misc/doc/Tv_user-manual/archive/Tv_user-manual.pdf$

[99] B. Jäckel et al., Nucl. Inst. and Meth. 112, 501 (1973)

[100] K. Debertin and R.G. Helmer, "Gamma and X-ray spectrometry with semiconductor detectors", pg. 164, North Holland, 1988

[101] D. S. Andreev, K. I. Erokhina, V. S. Zvonov and I. Kh. Lemberg, Instr. Expt. Techn. 25, 1358 (1972)

[102] X-ray and Gamma-ray Standards for Detector Calibration, report by the Co-ordinated Research IAEA Programme, IAEA- TECDOC-619 (1991)

[103] L.M. Fraile, private communication

[104] $http://root.cern.ch/$

[105] E. Hagebø et al., Proceedings of the Workshop Nuclear Structure of Light Nuclei Far from Stability, Experiment and Theory, Obernai, France, 1989, edited by G. Klotz, p. 241 (1989).

[106] J. Gulyás, computer code `ELEVEN` (MTA Atowki, Debrecen, unpublished).

[107] F. Roesel, H.M. Fries, K. Alder and H.C. Pauli, Atom. Data Nucl. Data Tables 21 (1978) 291

[108] T. Kibédi et al., Nucl. Instr. and Met. A589, 202 (2008)

[109] S. Raman and N.B. Gove, Phys. Rev. C7, 1995 (1973)

[110] P.M. Endt, Atomic Data and Nuclear Data Tables 23, 547 (1979)

[111] C. Thibault et al., Phys. Rev C23, 2720 (1981)

[112] P. Möller, J.R. Nix, W.D. Myers, and W.J. Swiatecki, At. Data Nucl. Data Tables 59, 185 (1995).

[113] F. Buchinger *et al.*, Phys. Rev C41, 2883 (1990)

[114] Nucl. Data Sheets 96, 1 (2002)

[115] M. Keim et al. Nucl. Phys. A586, 219 (1995)

[116] C. J. Gallagher, Jr., Phys. Rev. 111, 1982 (1958)

[117] L. W. Nordheim, Phys. Rev. 78, 294 (1950)

[118] B. R. Mottelson and S. G. Nilsson, Phys. Rev. 99, 1615 (1955)

[119] N.D. Newby, Phys. Rev. 125, 2063 (1962)

[120] C.J. Lister, B.J. Varley, H. G. Price, and J. W. Olness, Phys. Rev. Lett. 49, 308 (1982).

[121] A. Harder et al., Phys. Rev. C55, 1680 (1997)

[122] P. Lievens et al., Phys. Rev. C46, 707 (1992)

[123] P. Sarriguren, E. Moya, and A. Escuderos, Phys. Rev C64, 064306 (2001)

[124] A. Bohr and B. Mottelson, Nuclear Structure, Benjamin, NewYork (1975)

[125] N. A. Jelley, Fundamentals of Nuclear Physics, p. 250, Cambridge University Press (1990)

[126] E. Nacher, "Beta decay studies in the N$\simeq$Z and the rare-earth regions using Total Absorption Spectroscopy techniques", Ph.D. thesis, Universitat de Valencia, 1988

[127] P. Iredale, Nucl. Instr. and Meth. 11, 336 (1961)

[128] P. Iredale, Nucl. Instr. and Meth. 11, 340 (1961)

[129] D. Cano-Ott et al., Nucl. Instr. Meth. A430, 333 (1999)

[130] B. R. Erdal y G. Rudstam, Nucl. Instr. and Meth. 104 (1972) 263

[131] W. Dilg et al, Nucl. Phys. A217, 269 (1973)

[132] J.L. Tain, private communication

[133] $www - nds.iaea.org/ripl - 2$

[134] Korten et al., Nucl. Phys. A746, 90c (2004)

[135] M. Bender, P. Bonce, and P.-H. Heenen, Phys. Rev. C79, 024312 (2006)

[136] F. Becker et al., Nucl. Phys. A770, 107 (2006)

[137] G.A. Bartholomew et al., Adv. Nucl. Phys. 7, 229 (1973)

[138] J.C. Hardy et al., Phys. Lett. B109, 242 (1982)

[139] J. Kopecky et al, Phys. Rev. C41, 1941 (1990)

[140] W.V. Prestwich et al., Z. Phys. A315, 103 (1984)

[141] $http : //www - nds.iaea.org/ripl/gamma/recommended/kopecky - readme.htm$

[142] J.L. Tain, D. Cano-Ott, Nucl. Instr. Meth. A571, 719 (2007)

[143] A. Giannatiempo et al., Phys. Rev. C 52, 2444 (1995)

[144] A. Harder et al., Phys. Rev. C 51, 2932 (1995)

Acknowledgments

En primer lugar me gustaría agradecer a mi directora de tesis, Berta Rubio, por darme la oportunidad de entrar en su grupo y por su apoyo constante a lo largo de estos años. Gracias por tu paciencia, tu tiempo dedicado y por todas las cosas aprendidas a tu lado. También agradecerte los innumerable fines de semana en los que me has hecho un hueco, a espensas de estar con tu familia, para poder avanzar en la tesis. Sin tu ayuda no hubiera llegado hasta aquí.

My endless gratitude to Bill Gelletly whose encouragement and believe in me have made this thesis come to an end. He has had the infinite patience to read every single bit of this thesis and corrected the English. Thanks for those weekends of discussions with Berta and me in which you made the effort to come exclusively to Valencia to make our work on ^{78}Sr move forward. Your ”interesting” sense of humor has brightened me up even during my difficult moments.

También he de agradecer a José Luis Taín del que he aprendido infinidad de cosas y que me ha ayudado a resolver muchas dudas acerca del TAS. Guardo muy buenos recuerdos de aquellos momentos sentados alrededor de la mesa del laboratorio con sus mendrugos de pan y su té. Gracias, Kike, por tu espíritu optimista y alegre que animaba a todos los que estaban a tu alrededor. Agradecerte tus buenos consejos, explicaciones y ayuda cuando lo necesité. También agradecer al resto de compañeros de grupo en el IFIC: Alejandro, César, Jorge, Loli y Pancho.

Thanks to Charlie and Wilfried for the fun time spent in the cold Jyväskylä. I also keep a very good memory of those moments with Charly at CERN and GSI, in particular our great lunches with lots of cheese in the French restaurant near our hotel. He certainly helped me a lot during our experiments.

He de mencionar también a mis compañeros de facultad que siguieron como yo en esta tarea del doctorado dentro del IFIC (Carlos, Vicent, Paco) . Ahí han estado como amigos a los que consultar, contar las penas y pasar un buen rato. También agradezco a José Gimeno (el radiofísico que supo huir a tiempo) por nuestras tardes de ocio en el cine o simplemente comiendo juntos, que me hacían olvidar mis frustraciones con el Sr.

Gracias a Pedro Sarriguren por hacer el esfuerzo de realizar muchos de los cálculos teóricos que aquí se presentan en tiempo récord y que fueron indispensables para la finalización de algunas de las partes de esta tesis.

A Laura y Vicent porque amigos así no se encuentran todos los días y que han estado siempre ahí cuando los he necesitado. Desde nuestros comienzos juntos en alemán, hay que ver cómo ha pasado el tiempo. Gracias también a Juan y María Luisa, que aunque lejanos, siempre han hecho el esfuerzo de cruzar el charco para visitarme.

A mis amigos de TECNATOM, durante mi etapa en la industria, con los que compartí momentos muy buenos y que siguen ahí, a pesar de la distancia. Gracias Sergio, Rafa, María Dolores, Aurora, Cristina y César. Thanks to all the friends I have met during my last stage in North America for two years (Anke, Christian, Soledad, Alejandro, María, José, Mariela y Rodrigo.) and who have helped me immensely in everything, which has been hard work indeed. I have been very lucky to find you on my path.

Un agradecimiento muy especial a Víctor, que me animó y apoyó constantemente en la elaboración de esta tesis. Él ha estado ahí para los buenos y malos momentos dándome siempre ánimos. Si estoy aquí se lo debo en especial a él. Muchísimas gracias.

A María, mi hija, que a pesar de ser muy pequeña aún, ha hecho revivir el espíritu luchador de su madre y hacerme además mejor persona cada día.

Y finalmente a mis padres, a mi abuela, a mis tíos y primos maternos por saber que siempre estarán ahí aunque no entiendan mucho de lo que hace la friki de la familia. A mi abuelo al que seguro le hubiera encantado ver que al final he concluído esta tesis. Va por ti.

Valencia, Enero de 2012.